

Advanced Technologies for Next Generation Optical Transceivers in Long Haul Transport Links and Short Reach Interconnects



Mohamed Osman

Department of Electrical & Computer Engineering
McGill University
Montréal, Canada

May 2015

A thesis submitted to McGill University in partial fulfillment of
the requirements of the degree of Doctor of Philosophy

© 2015 Mohamed Osman

About the Author

Mohamed Osman received the B.S. and M.S. degrees from Alexandria University, Alexandria, Egypt, in 2006 and 2009, respectively. Since 2010, he joined the Electrical and Computer Engineering department at McGill University, as a Research Assistant where he is currently working towards the completion of the Ph.D. at the Photonics Systems Group (PSG) under the supervision of Prof. David Plant.

His current research interests include digital signal processing (DSP) for high-speed transport, access and short reach optical communications. Also, his interests include optical burst switched networks (OBSNs), optical code-division multiple-access (OCDMA) networks, media access control (MAC) protocols in optical networks. He has authored and co-authored 31 peer-reviewed journal papers (8 as the first author) and 28 conference papers (8 as first author) including a prestigious post-deadline paper at the 2014 European Conference on Optical Communications (ECOC). These papers have been cited by more than 248 times. He serves as a reviewer for Optics Express, IEEE Photonics Technology Letters, IEEE/OSA Journal of Lightwave Technology and Optics Communications.

Mr. Osman is a student member of the IEEE Photonics Society and SPIE. He is the recipient of the prestigious 2014 IEEE Photonics Society Best Graduate Student Fellowship. Also, he is the recipient of the 2014 SPIE Graduate Scholarship in Optics and Photonics. He was also awarded the McGill Engineering Doctoral Award (MEDA) for the period 2010-2012. In addition, he was awarded the 2006 Prof. Abdelsalame Mustafa prize for being the top student in the Department of Electrical Engineering, Alexandria University during the academic years 2002-2003 to 2005-2006.

Abstract

The burgeoning capacity demand for both optical transport links over metro / long-haul distances (> 100km) and short reach optical interconnects (100m-20km) for inter- and intra-datacenter networking is driving the notion of a digital signal processing (DSP) based optical transceiver. In optical transport, flexible optical transceivers employ coherent detection and DSP to enable mitigating various fiber transmission impairments such as chromatic dispersion (CD), polarization mode dispersion (PMD), Kerr nonlinearity, laser phase noise and frequency offset. In addition, these flexible transceivers need to be agile enough to adapt to the increasingly dynamic network traffic needs (e.g. varying capacity and reach requirements, dynamic wavelength assignments). On the short reach side, cheap and power efficient optics is a necessity for datacenter applications and hence intensity modulation / direct-detection (IM/DD) prevails over coherent detection. For such IM/DD transceivers, photonic integration is envisioned to play a significant role in reducing the cost along with DSP that potentially allows increasing the delivered bit rates with cheap electronics and reduced number of optical components (and consequently footprint).

In the first part of the thesis, we propose and verify, both analytically and experimentally, a myriad of DSP algorithms suitable for implementation in flexible optical coherent transceivers for transport networks. The proposed DSP algorithms tackle impairments such as laser phase noise, frequency offset, polarization rotation, fiber Kerr nonlinearity and sampling frequency offset. For each of the proposed algorithms, we provide a performance comparison with the standard counterparts in the literature highlighting the advantages of our approaches together with the underlying tradeoffs. Next, we develop and experimentally verify a rigorously derived analytical model for performance evaluation of a flexible coherent optical front-end that can operate colorlessly in a wavelength division multiplexing (WDM) scenario, i.e. without the need for a WDM demultiplexing filter prior to the receiver. The accuracy of the developed model was proved by finding a close match between model predictions and experimental results. We finally show that the model can be used as a useful system design tool to predict the system performance at various operating scenarios.

In the last part of the thesis, we propose a DSP algorithm to enable polarization division multiplexing (PDM) in IM/DD transceivers for short reach optical interconnects. This doubles the achievable bit rate with the same speed of the electronic components and with the same number of light sources by exploiting the two orthogonal polarization states per source. The proposed DSP algorithm is based on a multiple-input and multiple-output (MIMO) finite impulse response (FIR) filter that operates on the Stokes parameters of the received field, which can be obtained via a direct-detection receiver front-end, to invert the random rotations that occurred along the fiber. The proposed DSP was verified experimentally using an IM/DD transceiver that employs a single 1310 nm laser whose both polarizations were modulated by a packaged silicon photonic (SiP) intensity modulator. A record bit rate of 224 Gb/s was transmitted over 10 km with a BER below the forward-error-correcting (FEC) threshold.

Résumé

La demande de capacité fleurissante des liens de transport optique sur distance métropolitaine et de longue portée (> 100 km) ainsi que les interconnexions optiques de courte portée (100m-20km) pour le réseautage entre centre de données et à l'intérieur de ceux-ci pousse la notion de transceiver basé sur le traitement de signaux numérique (TSN). Lors de transport optique, les transceurs optique flexible utilisent la détection cohérente le TSN pour permettre d'amoinrir divers impacts de la transmission par fibre, tel que la dispersion chromatique (DC), la dispersion par mode de polarisation (DMP), l'effet nonlinéaire Kerr, le bruit de phase du laser et le décalage fréquentielle. En plus, ces transceurs flexible doivent être assez agile pour s'adapter aux besoins de plus en plus dynamiques du trafic des réseaux. (e.g. la demande variable de capacité et de portée, l'assignement dynamique des longueurs d'ondes). Du côté 'courte-portée', des composantes optique abordables et à faible consommation sont une nécessité pour les applications de centres de données, et c'est pour cette raison que la modulation par intensité avec détection directe (MI/DD) l'emporte sur la détection cohérente. Pour de tels transceurs MI/DD, l'intégration photonique joue un rôle significatif dans la réduction des coûts, de concert avec le TSN qui peut potentiellement accroître le taux binaire en utilisant de l'électronique bon marché et un nombre réduit de composante optique (et conséquemment une empreinte réduite).

Dans la première partie de cette thèse, nous proposons et vérifions de façons analytique et expérimentale une myriade d'algorithmes de TSN convenable à l'implémentation dans les transceurs optique cohérent flexible pour les réseaux de transport. Les algorithmes de TSN proposés s'attaquent aux détériorations telles que le bruit de phase du laser, la déviation fréquentielle, la rotation de la polarisation, l'effet nonlinéaire Kerr et la déviation de la fréquence d'échantillonnage. Pour chacun des algorithmes proposés, nous fournissons une comparaison des performances avec celles des algorithmes standards de la littérature, en faisant ressortir les avantages de nos approches ainsi que les contre-coûts sous-jacents. Ensuite, nous développons et vérifions expérimentalement un modèle analytique rigoureusement dérivé pour l'évaluation des performances de l'interface frontale de receveur optique cohérent flexible opérant sur un spectre de multiplexage fréquentielle (MF) sans filtre optique pour isoler et démultiplexer une couleur. La fidélité du modèle développé fût prouvée en trouvant un accord très juste entre les prédictions

du modèle et les résultats expérimentales. Finalement, nous démontrons que le modèle peut être utilisé comme outil utile pour la conception de systèmes, permettant de prédire les performances de celui-ci dans divers scénarios d'opérations.

Dans la dernière partie de cette thèse, nous proposons un algorithme de TSN permettant le multiplexage en polarisation (MP) pour transceiver MI/DD pour les interconnexions optique de courtes portée. Cette dernière double le taux binaire atteignable tout en utilisant des composantes électroniques de même vitesse ainsi que le même nombre de source lumineuse en exploitant les deux axes orthogonaux de polarisation d'une même source. L'algorithme de TSN est basé sur un filtre à réponse impulsionnelle finie (RIF) de multiple-entrées–multiple-sorties (MEMS), opérant sur les paramètres Stokes du champ reçu, qui peuvent être obtenus à l'aide d'un receveur frontale à détection directe, permettant d'inverser la rotation aléatoire de la polarisation dans la fibre. Le TSN proposé fût vérifié expérimentalement en utilisant un transceiver MI/DD opérant à 1310 nm où les deux polarisations furent modulé par un modulateur en intensité en Silice sur Photonique (SsP) assemblé. Un taux binaire record de 224 Gb/s fût transmit sur 10 km, affichant un taux d'erreur binaire sous le seuil du correcteur d'erreur.

Acknowledgments

First, I would like to thank my advisor and dear friend *Prof. David V. Plant* for his academic advice, constant encouragement, guidance, and support since starting my Ph.D. Reflecting back on the years I spent at McGill under his supervision, I feel extremely privileged for being part of his research group. I also thank him especially for the trust he has always given to me since my first day at McGill which gave me a much needed confidence particularly at the early stage of my Ph.D. Throughout the years, I learnt so much from his technical expertise especially his experimental skills given that I had zero experimental experience when I joined the group, as well as his supreme talent in predicting the future trends in the field of optical communications. I always admired him having this “big picture” in mind which I hope I can have one day. In short, I am extremely grateful to Prof. Plant for being an exceptionally humble human being before being such a remarkably talented advisor.

Also, I would like to express my gratitude to many talented individuals who helped me throughout the course of my Ph.D. Many thanks to *Mathieu Chagnon* my lab mate with whom I spent countless hours in the lab over the years. His fingerprints are all over this thesis since I did most of my experimental work with him. I had so much fun working with him and forming what *Prof. Plant* calls the M² duo. Also, many thanks to *Dr. Qunbi Zhuge*, an extremely talented researcher with whom I had so many fruitful discussions that often led to good ideas for potential future work for both of us. Also, many thanks to *Xian Xu* and *Dr. Mohammad Pasandi* who helped a lot in building our first generation of the experimental test-bed. Finally, so many special thanks to *Dr. Michel Poulin* for his technical advice and very fruitful discussion that usually stimulated me to explore and generate new ideas. I still remember he was the first person who asked me if we can transmit two polarizations using intensity modulation / direct detection which then led to a major contribution in this thesis. With *Dr. Poulin*, *Dr. Yves Painchaud* and the rest of the team at TeraXion, I had a very productive collaboration in the second half of my Ph.D.

Next, I would like to express my deep appreciation and pay humble respects to my parents *Dr. Omsia Elgendy* and *Eng. Hamdy Osman* for their support and guidance since my early years at school. Without their limitless support, extreme sacrifice and honest prayers, this journey could have never become possible. They were the first persons to believe in my skills and

motivate me to pursue an engineering career and later on further chase a research-oriented career upon completion of my undergraduate years. I still remember the days where my father used to sit down and help me with the Mathematics assignments in early school grades. He always explained things clearly and motivated me to think differently.

I would also like to thank my two beautiful angels: *Farida Osman* and *Laila Osman*. Since they came into our life, success has become the norm in my career. Looking at their beautiful and priceless smiles everyday just gives me all the positive energy I need to keep working hard towards my goals.

Finally, my lovely wife, *Heba Tamazin*. Since we got married in 2010 and she joined me in Canada, I felt complete with her beside me. She has been always a source of inspiration for me. Right after we got married, I got my first ECOC paper accepted which was just the beginning of the long journey. She always stood by me during the ups and downs of my Ph.D. Her share of success in this thesis is just as mine if not more. I feel extremely blessed to have her beside me during my Ph.D. and wish to keep her always standing by me for the rest of my life.

In the end, this thesis, with all its worth, is dedicated to my wife, my parents and my two little angels.

Mohamed Osman

April 2015

Associated Publications

The original contributions of the research work in this thesis is recognized by the community through the following 15 papers [1-15] (8 journal and 7 conference papers out of which 3 are invited). The contribution of the co-authors is stated for each paper below. In addition, I also published 45 co-authored journal and conference papers [16-60] through the collaborations with other professors, researchers and students, leading to significant contributions to the field of optical communication as well.

Journal Articles Related to the Thesis

1. **(Invited) M. Morsy-Osman**, M. Chagnon, M. Poulin, S. Lessard, and D. V. Plant, “224 Gb/s 10 km Transmission of PDM PAM-4 at 1.3 μm Using a Single Intensity-Modulated Laser and a Direct-Detection MIMO DSP-based Receiver,” *Journal of Lightwave Technology* **33**, 1417-1424 (2015).

I conceived the idea, performed the simulation and experiment, and wrote the paper. The co-authors contributed in building the experimental setup and discussing the idea.

2. Mathieu Chagnon, **Mohamed Morsy-Osman**, Michel Poulin, Christine Latrasse, Jean-Frederic Gagne, Yves Painchaud, Carl Paquet, Stephane Lessard, and David Plant, “Experimental study of 112 Gb/s short reach transmission employing PAM formats and SiP intensity modulator at 1.3 μm ,” *Opt. Express* **22**, 21018-21036 (2014).

The first author and I conceived the idea, performed simulations and experiment. The first author then wrote the paper and I helped editing it.

3. **Mohamed Morsy-Osman**, Mathieu Chagnon, Xian Xu, Qunbi Zhuge, Michel Poulin, Yves Painchaud, Martin Pelletier, Carl Paquet, David V. Plant, “Analytical and experimental performance evaluation of an integrated Si-photonics balanced coherent receiver in a colorless scenario,” *Opt. Express* **22**, 5693–5730 (2014).

I conceived the idea, performed the simulation and experiment, and wrote the paper. The co-authors contributed in building the experimental setup and discussing the idea.

4. **(Invited) Alan Pak Tao Lau**, Yuliang Gao, Qi Sui, Dawei Wang, Qunbi Zhuge, **Mohamed Morsy-Osman**, Mathieu Chagnon, Xian Xu, Chao Lu, and David V. Plant, “Beyond 100 Gb/s: Advanced DSP Techniques Enabling High Spectral Efficiency and Flexible Optical Communications,” *IEEE Signal Processing Magazine* **31** (2), 82-92 (2014).

I wrote a section in this invited paper that highlights some of the results of my own ideas. This invited paper presented a lengthy survey on a collection of ideas belonging to each of the co-authors.

5. **Mohamed Morsy-Osman**, Mathieu Chagnon, Xian Xu, Qunbi Zhuge, Michel Poulin, Yves Painchaud, Martin Pelletier, Carl Paquet, David V. Plant, “Colorless and Preamplifierless Reception Using an Integrated Si-Photonic Coherent Receiver,” *IEEE Photonics Technology Letters* **25** (11), 1027-1030 (2013).

I conceived the idea, performed the simulation and experiment, and wrote the paper. The co-authors contributed in building the experimental setup and discussing the idea.

6. **M. Morsy-Osman**, Mathieu Chagnon, Qunbi Zhuge, Xian Xu, Mohammad E. Mousa-Pasandi, Ziad A. El-Sahn, and David V. Plant, “Ultrafast and low overhead training symbol based channel estimation in coherent M-QAM single-carrier transmission systems,” *Opt. Express* **20**, B171-B180 (2012).

I conceived the idea, performed the simulation and experiment, and wrote the paper. The co-authors contributed in building the experimental setup and discussing the idea.

7. **Mohamed Morsy-Osman**, Qunbi Zhuge, Lawrence R. Chen, David V. Plant, “Joint mitigation of laser phase noise and fiber nonlinearity for polarization-multiplexed QPSK and 16-QAM coherent transmission systems,” *Optics Express* **19**, B329-B336 (2011).

I conceived the idea, performed the simulation and experiment, and wrote the paper. The co-authors contributed in building the experimental setup and discussing the idea.

8. **Mohamed Morsy-Osman**, Q. Zhuge, Lawrence R. Chen, David V. Plant, “Feedforward carrier recovery via pilot-aided transmission for single-carrier systems with arbitrary M-QAM constellations,” *Optics Express* **19**, 24331-24343 (2011).

I conceived the idea, performed the simulation and experiment, and wrote the paper. The co-authors contributed in building the experimental setup and discussing the idea.

Conference Articles Related to the Thesis

9. **M. Morsy-Osman**, M. Chagnon, M. Poulin, S. Lessard, and D. Plant, “ $1\lambda \times 224$ Gb/s 10 km Transmission of Polarization Division Multiplexed PAM-4 Signals Using 1.3 μm SiP Intensity Modulator and a Direct-Detection MIMO-based Receiver,” in Post-deadline session of European Conference on Optical Communications (ECOC), paper PD.4.4, 2014.

I conceived the idea, performed the simulation and experiment, and wrote the paper. The co-authors contributed in building the experimental setup and discussing the idea.

10. M. Poulin, C. Latrassé, J.-F. Gagne, Y. Painchaud, M. Cyr, C. Paquet, **M. Morsy-Osman**, M. Chagnon, S. Lessard, and D. V. Plant, “107 Gb/s PAM-4 Transmission over 10 km Using a SiP Series Push-Pull Modulator at 1310 nm,” in European Conference on Optical Communications (ECOC), 2014.

The co-authors ahead of me on the list built the device used later in the system-level experiment. Then I did the experiment with the help of the author next to me on the list, generated the results and helped writing the paper.

11. **Mohamed Morsy-Osman**, M. Chagnon, Q. Zhuge, X. Xu, and D. V. Plant, “Non-Data-Aided Feedforward Timing Recovery for Flexible Transceivers Employing PDM-MQAM Modulations,” Optical Fiber Communications (OFC) Conference, paper W3B.4, 2014.

I conceived the idea, performed the simulation and experiment, and wrote the paper. The co-authors contributed in building the experimental setup and discussing the idea.

12. **M. Morsy-Osman**, Q. Zhuge, M. Chagnon, X. Xu, D. V. Plant, “Experimental Demonstration of Pilot-Aided Polarization Recovery, Frequency Offset and Phase Noise Mitigation,” in Optical Fiber Communications (OFC) Conference, 2013, paper OTu3I.6.

I conceived the idea, performed the simulation and experiment, and wrote the paper. The co-authors contributed in building the experimental setup and discussing the idea.

13. **(Invited)** D. V. Plant, Q. Zhuge, **M. Morsy-Osman**, M. Chagnon, X. Xu, M. Qiu, “Flexible transceivers using adaptive digital signal processing for single carrier and OFDM,” in Optical Fiber Communications (OFC) Conference, 2013, paper OTu2I.5.

I wrote a section in this invited paper that highlights some of the results of my own ideas. This invited paper presented a survey on a collection of ideas from our research group.

14. **M. Morsy-Osman**, M. Chagnon, Q. Zhuge, X. Xu, M. E. Mousa-Pasandi, Z. A. El-Sahn, D. V. Plant, “Training Symbol Based Channel Estimation for Ultrafast Polarization Demultiplexing in Coherent Single-Carrier Transmission Systems with M-QAM Constellations,” in European Conference on Optical Communications (ECOC), 2012, paper Mo.1.A.4.

I conceived the idea, performed the simulation and experiment, and wrote the paper. The co-authors contributed in building the experimental setup and discussing the idea.

15. **M. H. Morsy-Osman**, L. Chen, D. V. Plant, “Joint mitigation of laser phase noise and fiber nonlinearity using pilot-aided transmission for single-carrier systems,” European Conference and Exposition on Optical Communications (ECOC), 2011, paper Tu.3.A.3.

I conceived the idea, performed the simulation and experiment, and wrote the paper. The co-authors contributed in building the experimental setup and discussing the idea.

Journal Articles Not Directly Related to the Thesis

16. Yuliang Gao, Qunbi Zhuge, Wei Wang, Xian Xu, Jonathan M. Buset, Meng Qiu, **Mohamed Morsy-Osman**, Mathieu Chagnon, Feng Li, Liang Wang, Chao Lu, Alan Pak Tao Lau, and David V. Plant, “40 Gb/s CAP32 short reach transmission over 80 km single mode fiber,” *Opt. Express* **23**, 11412-11423 (2015).
17. M. Chagnon, **M. Morsy-Osman**, M. Poulin, C. Paquet, S. Lessard, and D. V. Plant, “Experimental Parametric Study of a Silicon Photonic Modulator Enabled 112-Gb/s PAM Transmission System With a DAC and ADC,” *Journal of Lightwave Technology*, **33**, 1380-1387 (2015).
18. Xian Xu, Qunbi Zhuge, Benoît Châtelain, Mathieu Chagnon, **Mohamed Morsy-Osman**, Mahdi Malekiha, Meng Qiu, Yuliang Gao, Wei Wang, and David V. Plant, “Experimental investigation on the nonlinear tolerance of root M-shaped pulse in spectrally efficient coherent transmissions,” *Opt. Express* **23**, 882-894 (2015).
19. Wei Wang, Qunbi Zhuge, **Mohamed Morsy-Osman**, Yuliang Gao, Xian Xu, Mathieu Chagnon, Meng Qiu, Minh Thang Hoang, Fangyuan Zhang, Rui Li, and David V. Plant, “Decision-aided sampling frequency offset compensation for reduced-guard-interval coherent optical OFDM systems,” *Opt. Express* **22**, 27553-27564 (2014).
20. Wei Wang, Qunbi Zhuge, Yuliang Gao, Meng Qiu, **Mohamed Morsy-Osman**, Xian Xu, Mathieu Chagnon, and David V. Plant, “Low Overhead and Nonlinear-Tolerant Adaptive Zero-Guard-Interval CO-OFDM,” *Opt. Express* **22**, 17810-17822 (2014).
21. Meng Qiu, Qunbi Zhuge, Mathieu Chagnon, Yuliang Gao, Xian Xu, **Mohamed Morsy-Osman**, and David V. Plant, “Digital subcarrier multiplexing for fiber nonlinearity mitigation in coherent optical communication systems,” *Opt. Express* **22**, 18770-18777 (2014).

22. Qunbi Zhuge, **Mohamed Morsy-Osman**, Mathieu Chagnon, Xian Xu, Meng Qiu, and David V. Plant, "Terabit bandwidth-adaptive transmission using low-complexity format-transparent digital signal processing," *Opt. Express* **22**, 2278-2288 (2014).
23. Xian Xu, Qunbi Zhuge, Benoît Châtelain, **Mohamed Morsy-Osman**, Mathieu Chagnon, Meng Qiu, and David V. Plant, "A nonlinearity-tolerant frequency domain root M-shaped pulse for coherent optical communication systems," *Opt. Express* **21**, 31966-31982 (2013).
24. Mathieu Chagnon, **Mohamed Osman**, Qunbi Zhuge, Xian Xu, and David V. Plant, "Analysis and experimental demonstration of novel 8PolSK-QPSK modulation at 5 bits/symbol for passive mitigation of nonlinear impairments," *Opt. Express* **21**, 30204-30220 (2013).
25. Qunbi Zhuge, **Mohamed Morsy-Osman**, Xian Xu, Mathieu Chagnon, Meng Qiu, David V. Plant, "Spectral Efficiency-Adaptive Optical Transmission Using Time Domain Hybrid QAM for Agile Optical Networks," *Journal of Lightwave Technology* **31**(15), 2621-2628 (2013).
26. Qunbi Zhuge, **Mohamed Morsy-Osman**, David V. Plant, "Low Overhead Intra-Symbol Carrier Phase Recovery for Reduced-Guard-Interval CO-OFDM," *Journal of Lightwave Technology* **31**(8), 1158-1169 (2013).
27. Meng Qiu, Qunbi Zhuge, Xian Xu, Mathieu Chagnon, **Mohamed Morsy-Osman**, and David V. Plant, "Simple and efficient frequency offset tracking and carrier phase recovery algorithms in single carrier transmission systems," *Opt. Express* **21**, 8157-8165 (2013).
28. Qunbi Zhuge, Xian Xu, Mohammad E. Mousa-Pasandi, **Mohamed Morsy-Osman**, Mathieu Chagnon, Ziad El-Sahn, David V. Plant, "Experimental Study of the Intra-Channel Nonlinearity Influence on Single-Band 100G Coherent Optical OFDM Systems," *IEEE Photonics Technology Letters* **25**(6), 553-555 (2013).
29. Qunbi Zhuge, **Mohamed Morsy-Osman**, Mohammad E. Mousa-Pasandi, Xian Xu, Mathieu Chagnon, Ziad A. El-Sahn, Chen Chen, and David V. Plant, "Single channel and WDM transmission of 28 Gbaud zero-guard-interval CO-OFDM," *Opt. Express* **20**, B439-B444 (2012).
30. Mathieu Chagnon, **Mohamed Osman**, Xian Xu, Qunbi Zhuge, and David V. Plant, "Blind, fast and SOP independent polarization recovery for square dual polarization-MQAM formats and optical coherent receivers," *Opt. Express* **20**, 27847-27865 (2012).

31. **Mohamed Morsy-Osman**, M. Y. S. Sowailem, A. I. Abd El-Rahman, and H. M. H. Shalaby, "Performance Evaluation of an Optical Burst Switched Core Node With Generalized Arrivals and Partial Wavelength Conversion Capability," *Journal of Optical Communications and Networking* **4**(12), 997-1007 (2012).
32. Qunbi Zhuge, Mohammad E. Mousa-Pasandi, **Mohamed Morsy-Osman**, Xian Xu, Mathieu Chagnon, Ziad A. El-Sahn, David V. Plant, "Demonstration of Dispersion-Enhanced Phase Noise in RGI CO-OFDM Systems," *IEEE Photonics Technology Letters* **24**(16), 1446-1449 (2012).
33. Qunbi Zhuge, **Mohamed Morsy-Osman**, Xian Xu, Mohammad E. Mousa-Pasandi, Mathieu Chagnon, Ziad A. El-Sahn, and David V. Plant, "Pilot-aided carrier phase recovery for M-QAM using superscalar parallelization based PLL," *Opt. Express* **20**, 19599-19609 (2012).
34. Mohammad E. Mousa-Pasandi, Qunbi Zhuge, Xian Xu, **Mohamed Morsy-Osman**, Mathieu Chagnon, and David V. Plant, "Experimental Study of a novel adaptive decision-directed channel equalizer in 28 GBaud RGI-DP-CO-OFDM transport systems," *Opt. Express* **20**, 17017-17028 (2012).
35. Mohammad E. Mousa-Pasandi, Qunbi Zhuge, Xian Xu, **Mohamed Morsy-Osman**, Ziad A. El-Sahn, Mathieu Chagnon, and David V. Plant, "Experimental demonstration of non-iterative interpolation-based partial ICI compensation in 100G RGI-DP-CO-OFDM transport systems," *Opt. Express* **20**, 14825-14832 (2012).
36. Q. Zhuge, Xian Xu, Ziad A. El-Sahn, Mohammad E. Mousa-Pasandi, **Mohamed Morsy-Osman**, Mathieu Chagnon, Meng Qiu, David V. Plant, "Experimental investigation of the equalization-enhanced phase noise in long haul 56 Gbaud DP-QPSK systems," *Optics Express* **20**, 13841-13846 (2012).
37. Qunbi Zhuge, **Mohamed Morsy-Osman**, and David V. Plant, "Analysis of dispersion-enhanced phase noise in CO-OFDM systems with RF-pilot phase compensation," *Opt. Express* **19**, 24030-24036 (2011).
38. M. Y. Sowailem, **M. H. Morsy**, and Hossam M. H. Shalaby, "Employing Code Domain for Contention Resolution in Optical Burst Switched Networks with Detailed Performance Analysis", *Journal of Lightwave Technology* **27**(23), 5284-5294 (2009).

39. **M. H. Morsy**, M. Y. Sowailem and Hossam M. H. Shalaby, “An Enhanced Mathematical Model for Performance Evaluation of Optical Burst Switched Networks”, *SPIE Journal of Optical Engineering* **48**(8), 085003-085003-10 (2009).

Conference Articles Not Directly Related to the Thesis

40. David Patel, Venkat Veerasubramanian, Alireza Samani, Samir Ghosh, Mathieu Chagnon, **Mohamed Osman**, and David Plant, “A 41 GHz Slow-Wave Series Push-Pull Silicon Photonic Modulator,” in proceedings of Conference on Lasers and Electro-Optics (CLEO), paper SW3N.3, 2015.
41. M. Chagnon, **M. Osman**, D. Patel, V. Veerasubramanian, A. Samani, and D.V. Plant, “1 λ , 6 bits/symbol, 280 and 350 Gb/s Direct Detection Transceiver using Intensity Modulation, Polarization Multiplexing, and Inter-Polarization Phase Modulation,” in Post-deadline session of Optical Fiber Communications (OFC) Conference, paper Th5B.2, 2015.
42. X. Xu, Q. Zhuge, **M. Morsy-Osman**, B. Châtelain, M. Qiu, M. Chagnon, W. Wang, and D. V. Plant, “Nonlinearity-Tolerant Frequency Domain Root M-shaped Pulse for Spectrally Efficient Coherent Transmissions,” Optical Fiber Communications (OFC) Conference, paper W1G.3, 2014.
43. M. Qiu, Q. Zhuge, X. Xu, M. Chagnon, **M. Osman**, and D. V. Plant, “Subcarrier Multiplexing Using DACs for Fiber Nonlinearity Mitigation in Coherent Optical Communication Systems,” Optical Fiber Communications (OFC) Conference, paper Tu3J.2, 2014.
44. W. Wang, Q. Zhuge, X. Xu, **M. Osman**, M. Chagnon, M. Qiu, and D. V. Plant, “Nonlinear-Tolerant Adaptive Zero-Guard-Interval COOFDM for Highly Spectral Efficient Optical Transmission,” Optical Fiber Communications (OFC) Conference, paper Tu3G.3, 2014.
45. Y. Painchaud, M. Poulin, F. Pelletier, C. Latrasse, J.-F. Gagne, S. Savard, G. Robidoux, M.-J. Picard, S. Paquet, C.-A. Davidson, M. Pelletier, M. Cyr, C. Paquet, M. Guy, **M. Morsy-Osman**, M. Chagnon, and D. V. Plant, “Silicon-based products and solutions,” SPIE Photonics West 2014, paper 8988-20 (Invited).
46. Q. Zhuge, **M. Morsy-Osman**, X. Xu, M. Chagnon, M. Qiu and D. V. Plant, “Flexible Transceiver with Format-Transparent Digital Signal Processing for Ultra-large Data-rate Transmissions,” in in Signal Processing in Photonic Communications (SPPCom) 2013, paper NT2C.3.

47. Y. Painchaud, M. Poulin, M. Pelletier, F. Pelletier, C. Latrasse, G. Robidoux, S. Savard, J.-F. Gagne, V. Trudel, M.-J. Picard, P. Poulin, P. Sirois, F. D'Amours, D. Asselin, S. Paquet, C. Paquet, M. Cyr, M. Guy, **M. Morsy-Osman**, M. Chagnon, Q. Zhuge, X. Xu, D. V. Plant, "A small form factor Si-based coherent receiver," in IEEE Optical Interconnects Conference, 2013, 5-8 May 2013.
48. M. Qiu, Q. Zhuge, X. Xu, M. Chagnon, **M. Morsy-Osman**, and D. Plant, "Wide-Range, Low-Complexity Frequency Offset Tracking Technique for Single Carrier Transmission Systems," in Optical Fiber Communication (OFC) Conference 2013, paper OTu3I.8.
49. X. Xu, B. Châtelain, Q. Zhuge, **M. Morsy-Osman**, M. Chagnon, M. Qiu, and D. V. Plant, "Frequency Domain M-shaped Pulse for SPM Nonlinearity Mitigation in Coherent Optical Communications," in Optical Fiber Communications (OFC) Conference, 2013, paper JTh2A.38.
50. Q. Zhuge, X. Xu, **M. Morsy-Osman**, M. Chagnon, M. Qiu, and D. V. Plant, "Time domain hybrid QAM based rate-adaptive optical transmissions using high speed DACs," Optical Fiber Communications (OFC) Conference, 2013, paper OTh4E.6.
51. M. Chagnon, **M. Osman**, Q. Zhuge, X. Xu, M. Poulin, Y. Painchaud, M. Pelletier, C. Paquet and D. V. Plant, "Experimental Colorless Reception of $16 \times DP-16QAM$ at 28 and 30 Gbaud Using a Si-Integrated Coherent Receiver," Optical Fiber Communications (OFC) Conference, 2013, paper OTh3C.5.
52. Y. Painchaud, M. Pelletier, M. Poulin, F. Pelletier, C. Latrasse, G. Robidoux, S. Savard, J.-F. Gagné, V. Trudel, M.-J. Picard, P. Poulin, P. Sirois, F. D'Amours, D. Asselin, S. Paquet, C. Paquet, M. Cyr, M. Guy, **M. Morsy-Osman**, Q. Zhuge, X. Xu, M. Chagnon and D. V. Plant, "Ultra-Compact Coherent Receiver Based on Hybrid Integration on Silicon," Optical Fiber Communications (OFC) Conference, 2013, paper OM2J.2.
53. Qunbi Zhuge, Xian Xu, M. E. Mousa-Pasandi, **M. Morsy-Osman**, Z. A. El-Sahn, M. Chagnon, D. V. Plant, " 8×256 Gb/s WDM transmission over 2880 km of SSMF with 64 Gbaud DP-QPSK signals," in Asia Communications and Photonics Conference (ACP), 2012, 7-10 Nov. 2012, paper ATh2C.1.
54. Q. Zhuge, **M. Morsy-Osman**, M. E. Mousa-Pasandi, X. Xu, M. Chagnon, Z. A. El-Sahn, C. Chen, D. V. Plant, "Experimental Demonstration of 28 Gbaud QPSK and 16-QAM Zero-

- Guard-Interval CO-OFDM Transmissions,” European Conference on Optical Communications (ECOC), 2012, paper Tu.4.C.2.
55. Q. Zhuge, M. E. Mousa-Pasandi, **M. Morsy-Osman**, X. Xu, M. Chagnon, Z. A. Elsahn, D. V. Plant, “High Performance, Low Overhead CO-OFDM for Next Generation Fiber Transmission Systems,” in Signal Processing in Photonic Communications (SPPCom), 2012, paper SpTu2A.4.
56. Q. Zhuge, M. E. Mousa-Pasandi, X. Xu, B. Chatelain, Z. Pan, **M. Osman**, and D. V. Plant, "Linewidth-Tolerant Low Complexity Pilot-Aided Carrier Phase Recovery for M-QAM using Superscalar Parallelization," in Optical Fiber Communication Conference, OSA Technical Digest (Optical Society of America, 2012), paper OTu2G.2.
57. **M. H. Morsy**, M. Y. Sowailem and Hossam M. H. Shalaby, “Upper and Lower Bounds of Burst Loss Probability for a Core Node in an Optical Burst Switched Network with Pareto distributed arrivals”, 2010 IEEE 17th International Conference on Telecommunications (ICT), pp.523-527, 4-7 April 2010.
58. **M. H. Morsy**, M. Y. Sowailem and Hossam M. H. Shalaby, “Performance analysis of a core node equipped with wavelength converter pool in an Optical Burst Switched network”, 2010 IEEE 17th International Conference on Telecommunications (ICT), pp.516-522, 4-7 April 2010.
59. M. Y. Sowailem, **M. H. Morsy** and Hossam M. H. Shalaby, “Contention Resolution in Optical Burst Switched Networks using Spectral-Amplitude-Coding Optical Code Division Multiple Access”, IEEE Global Telecommunications Conference, GLOBECOM 2009, Optical Networks and Systems Symposium, Nov. 30 2009-Dec. 4 2009.
60. **M. H. Morsy**, M. Y. Sowailem and Hossam M. H. Shalaby, “An Enhanced Mathematical Model for Performance Evaluation of Optical Burst Switched Networks”, IEEE Global Telecommunications Conference, GLOBECOM 2008, Optical Networks and Systems Symposium, Nov. 30 2008-Dec. 4 2008.

Contents

About the Author	i
Abstract.....	ii
Résumé.....	iv
Acknowledgments	vi
Associated Publications	viii
List of Figures.....	xx
List of Tables	xxv
List of Acronyms	xxvi
Chapter 1	
Introduction.....	1
1.1 Overview.....	1
1.2 Motivation.....	2
1.2.1 Flexible optical coherent transceivers for optical transport.....	2
1.2.2 IM/DD transceivers for short reach optical interconnects	4
1.3 Thesis organization	5
1.4 Original contributions	6
Chapter 2	
Fundamentals of Fiber Optical Fiber Communication Enabled by either Direct-Detection or Coherent Reception.....	9
2.1 Overview.....	9
2.2 Intensity modulation direct-detection optical transmission system architecture	11
2.3 Coherent optical transmission system architecture.....	13
2.4 System impairments for a coherent transmission system	17
2.4.1 Transceiver related impairments.....	17
2.4.2 Fiber channel impairments	22
2.4.3 Classic DSP stacks for a coherent transceiver.....	33
2.5 System impairments for a short reach IM/DD link.....	38

Chapter 3

DSP Algorithms for Flexible Coherent Optical Transceivers	40
3.1 Overview.....	40
3.2 Pilot aided (PA-) DSP for joint carrier recovery, fiber nonlinearity mitigation and polarization demultiplexing	40
3.2.1 Introduction.....	40
3.2.2 Principles of PA-DSP for joint carrier recovery, fiber nonlinearity mitigation and polarization demultiplexing	42
3.2.3 Simulation study of PA-DSP.....	51
3.2.4 Proof-of-concept experimental verification of PA-DSP.....	58
3.3 Low overhead and ultrafast training symbol based polarization demultiplexing	63
3.3.1 Introduction.....	63
3.3.2 Principle of proposed algorithm	64
3.3.3 Experimental setup and offline DSP.....	66
3.3.4 Results and discussion	69
3.4 Non data-aided feedforward timing recovery scheme for arbitrary M-QAM modulation	73
3.4.1 Introduction.....	73
3.4.2 Principles of the timing error estimator and interpolator control	74
3.4.3 Experimental setup, offline DSP, results and discussion	76
3.5 Conclusions.....	79

Chapter 4

Performance Evaluation of a Colorless Coherent Optical Front-End in a WDM System ..	80
4.1 Overview.....	80
4.2 SiP balanced coherent receiver design and characterization	83
4.3 Theoretical performance evaluation of a colorless coherent receiver	85
4.4 Single channel experiment, results and discussion	93
4.4.1 Experimental setup and offline DSP.....	93
4.4.2 Results and discussion	94
4.5 WDM experiment, results and discussion	96
4.5.1 Experimental setup and offline DSP.....	97
4.5.2 Results and discussion	99
4.6 Verification of experimental results using the analytical SNR model.....	110
4.7 Conclusion	115
4.8 Appendix A: Derivation of ACFs, PSDs and powers of various terms in the differential photocurrent	116
4.8.1 Derivation of ACF, PSD and power of the LO-SIG and LO-ON beating terms in the differential photocurrent	116
4.8.2 Derivation of ACF, PSD and power of the residual SIG-SIG beating term in the differential photocurrent	122

4.8.3	Power of thermal and shot noise contributions in the photocurrent difference	128
4.8.4	Expressions of PSDs of the LO-LO, SIG-ON and ON-ON beating contributions in the final differential photocurrent	129
4.9	Appendix B: Dependence of the scaling factor of the SIG-SIG beating photocurrent on the residual CD and polarization orientation	130
Chapter 5		
Polarization-Division-Multiplexing in Intensity-Modulation / Direct-Detection Systems Enabled by MIMO DSP		
		133
5.1	Overview	133
5.2	Principle of Stokes space polarization demultiplexing for PDM IM/DD systems	136
5.3	Experimental setup, DSP stacks and results	139
5.3.1	Experimental setup	139
5.3.2	Offline DSP at transmitter and receiver sides	140
5.3.3	Experimental results	141
5.4	Simulation study of the impact of the coupler splitting ratio	144
5.5	Conclusion	146
Chapter 6		
Conclusion		147
6.1	Overview	147
6.2	Summary of original contributions	147
6.2.1	DSP algorithms for flexible coherent optical transceivers	148
6.2.2	Performance of a colorless coherent optical front-end	149
6.2.3	MIMO DSP enabling a PDM IM/DD system	150
6.3	Future research avenues	151
Bibliography		154

List of Figures

Fig. 2.1. Architecture of an N channel WDM IM/DD transmission system showing two configurations of the Tx: a directly modulated laser (DML) or an externally modulated laser. The insets on the bottom right show a Mach-Zhender modulator structure (MZM) together with its transfer function of the field and intensity.....	12
Fig. 2.2. Architecture of a DSP-based N channel WDM coherent transmission system.....	15
Fig. 2.3. Architectire of: (a) dual-polarization IQ (DP-IQ) modulator, (b) coherent front-end....	15
Fig. 2.4. Constellation diagrams showing 28Gbaud QPSK symbols: (a) before adding laser PN and FO, (b) with laser PN and FO with $\Delta F = 10$ MHz and $\Delta f = 1$ MHz for both Tx and LO lasers, (c) Instaneous phase versus time showing three curves: FO only, PN only and the combined FO+PN process.....	20
Fig. 2.5. Constellation diagrams showing QPSK symbols in the following cases: (a) under various amounts of quadrature error (θ_{qe}) of 0° (blue), 10° (red) and 20° (black) , (b) SPO of 0.3, and (c) SFO of 1000 ppm assuming an RC pulse with a roll-off factor of 1.....	21
Fig. 2.6. Effect of GVD on an input RC pulse with a roll-off factor of 1 in the following cases: (a) $L = 80$ km and $R = 28$ Gbaud, (b) $L = 80$ km and $R = 56$ Gbaud, and (c) $L = 1600$ km and $R = 28$ Gbaud.....	29
Fig. 2.7. An illustrative drawing showing the breaking of a fiber with random birefringence fluctuations into multiple sections each with constant birefringence magnitude and orientation.....	30
Fig. 2.8. Conventional DSP stacks at: (a) Tx side and (b) Rx side, showing various functions that may or may not be implemented.....	34
Fig. 2.9. Raised cosine pulse with different roll-off factors in: (a) time domain, (b) frequency domain.....	36
Fig. 3.1. DSP tasks for PA scheme for single-polarization (SP) signal at: a) Tx side aided with illustrative example constellations for data and pilot, and b) Rx side assuming back-to-back configuration and focusing on PA carrier recovery with an without ML phase estimation.....	43
Fig. 3.2. Spectrum of in-phase portion of a 28 Gbaud SP 16-QAM signal a) At Tx before SSB, b) At Tx after SSB and pilot insertion with $f_{sc} = 500$ MHz and $PSR = -14$ dB, c) Zoomed version	

of pilot spectral gap at Tx, d) At Rx with laser PN ($\Delta f = 2\text{MHz}$) and noise loaded (OSNR = 16.7 dB), e) Zoomed version of pilot spectral gap at Rx together with a Gaussian LPF with $B_{LPF} = 80\text{ MHz}$	46
Fig. 3.3. a) BER surface versus the pilot-to-signal power ratio and the bandwidth of the pilot LPF at two different laser linewidths for 16-QAM at OSNR = 16.7 dB, and linewidth tolerance of various CR schemes against laser phase noise for b) QPSK, c) 16-QAM, and d) 64-QAM constellations.....	52
Fig. 3.4. Performance of PA-FFCR with ML for different M-QAM formats with finite bit resolution of (a) DACs, and (b) ADCs.	54
Fig. 3.5. Required OSNR versus launch power to achieve a BER = 3.8×10^{-3} assuming noise loading at Rx side for: a) 28Gbaud PDM-QPSK system with L = 1600 km, and b) 14 Gbaud PDM 16-QAM system with L = 1200 km.	56
Fig. 3.6. Maximum system reach versus launch power to achieve a BER = 3.8×10^{-3} assuming the noise figure of inline EDFAs = 7 dB and no noise loading at Rx side for: a) 28 Gbaud PDM-QPSK system, and b) 14 Gbaud PDM 16-QAM system.....	57
Fig. 3.7. Effect of finite DAC resolution on required OSNR versus launch power to achieve a BER = 3.8×10^{-3} assuming noise loading at Rx side for 14 Gbaud PDM 16-QAM system with L = 1200 km.....	57
Fig. 3.8. PA-DSP used for the experiment at a) Tx-side, b) Rx-side.....	60
Fig. 3.9. a) Experimental setup: insets show optical spectra of PA system at PSR = -18 and -6 dB with a 0.05 nm resolution BW, b) transmitted data and pilot frames, c) back-to-back BER versus OSNR for theory, non-PA and PA systems with and w/o MLPE and PSR optimization for PA and PA-ML systems at OSNR = 14.5 dB.....	61
Fig. 3.10. a) BER versus distance for both non-PA and PA system with MLPE, b) back-to-back BER versus FO for PA system with different FFT block lengths at OSNR = 14.5 dB: insets show the electrical spectra of the received signal for FO = -12 and 0 GHz, c) back-to-back BER versus OSNR for PA system with and without MLPE using an ECL or 2.3 MHz DFB in homodyne configuration.	62
Fig. 3.11. (a) Experimental setup, (b) Training symbols and framing synchronization header. ..	67
Fig. 3.12. (a) Steady-state BER versus distance for all algorithms for both PDM-QPSK and PDM-16QAM, (b) Constellations after 320 km transmission for both PDM-QPSK and PDM-	

16QAM obtained by merely applying the inverse Jones matrix obtained by TS-EST,	
(c) Constellations of the same case in (b) after the butterfly filter updated using DD-LMS and carrier recovery using DD-PLL.	69
Fig. 3.13. Transient BER for all algorithms for (a) PDM-QPSK, (b) PDM-16QAM.	69
Fig. 3.14. BER for the TS-EST algorithm for PDM-QPSK in both high phase noise and high launch power scenarios for: (a) steady-state, (b) transient cases.	71
Fig. 3.15. (a) Periodic training symbols for SOP tracking, (b) Steady-state BER versus SOP angular frequency for different algorithms for 14 Gbaud PDM-16QAM, (c) Steady-state BER versus SOP angular frequency for different algorithms for 28 Gbaud PDM-16QAM.	72
Fig. 3.16. a) Experimental setup, b) Time evolution of the fractional delay μ_n (blue) and the increment in the base index $m_{n+1}-m_n$ (red) for back-to-back PDM-QPSK with $N = 64$ and $SFO = 1000$ (left) and 4000 ppm (right), c) Back-to-back constellations.	77
Fig. 3.17. a) Back-to-back BER versus OSNR for all modulation formats at various SFO levels: insets show the BER variation with the block size of the algorithm for different formats at fixed OSNRs, b) BER versus transmission distance at different SFO levels for all formats.	78
Fig. 4.1. (a) Picture of the PIC of the CRx showing the main building blocks, (b) Overall frequency response of the Si-photonic CRx assembly.	84
Fig. 4.2. CMRR versus frequency curves measured at 192.9 THz at the four output RF ports of the CRx when light is applied at the (a) signal port, (b) LO port.	84
Fig. 4.3. Single channel experimental setup.	94
Fig. 4.4. Single channel 28 Gbaud PDM-QPSK and PDM-16QAM comparison between colorless / preamplifierless and filtered / preamplified strategies at 320 mVpp target swing: (a) Q^2 factor versus P_{SIG} , (b) back-to-back BER versus OSNR at different P_{SIG} , (c) required OSNR to achieve the FEC threshold versus P_{SIG} for back-to-back and transmission scenarios, (d) BER versus transmission distance with no noise loading at various P_{SIG}	95
Fig. 4.5. Experimental setup for WDM experiments.	98
Fig. 4.6. BER for all WDM channels using fully colorless and preamplifierless reception at different transmission distances and at per channel received signal power of -3 and -21 dBm. Insets show the received WDM spectra in back-to-back and after 3200 km transmission where we observe a fairly flat spectrum due to the gain flattening waveshaper in the loop.	100

- Fig. 4.7. Measurement results of channel 9: (a) BER versus transmission distance, (b) SNR evaluated after offline DSP versus distance, (c) BER versus SNR using both experimental results and theory where the experimental SNR corresponding to FEC threshold is marked. 101
- Fig. 4.8. SNR of channel 9 versus received signal power per channel P_{SIG} after 0, 1600, 3200 and 4800 km transmission with varying number of channels presented to the CRx at an LO power of: (a) 15.5 dBm, (b) 12 dBm, (c) 9 dBm, (d) 6 dBm, (e) 3 dBm, (f) 0 dBm. In each subfigure, different colors represent different number of channels N_{ch} according to the legend. Also, SNR evaluated after 0, 1600, 3200 and 4800 km transmission are shown in each subfigure where the top set of four curves in each subfigure is evaluated in back-to-back and the bottom set is after 4800 km transmission. 103
- Fig. 4.9. SNR of channel 9 versus N_{ch} at $P_{SIG} = 0$ dBm after 0, 1600, 3200 and 4800 km transmission at P_{LO} of (a) 15.5 dBm, (b) 12 dBm, (c) 9 dBm, (d) 6 dBm, (e) 3 dBm, (f) 0 dBm. 104
- Fig. 4.10. SNR of channel 9 versus N_{ch} at $P_{SIG} = -12$ dBm after 0, 1600, 3200 and 4800 km transmission at P_{LO} of (a) 15.5 dBm, (b) 12 dBm, (c) 9 dBm, (d) 6 dBm, (e) 3 dBm, (f) 0 dBm. 106
- Fig. 4.11. SNR of channel 9 versus P_{LO} after 0, 1600, 3200 and 4800 km transmission at various N_{ch} and at P_{SIG} of: (a) 0 dBm, (b) -15 dBm..... 107
- Fig. 4.12. Color coded 2-D plots of SNR versus both P_{SIG} and P_{LO} for (a) back-to-back and $N_{ch} = 1$, (b) back-to-back and $N_{ch} = 16$, (c) 1600 km transmission and $N_{ch} = 1$, (d) 1600 km transmission and $N_{ch} = 16$, (e) 3200 km transmission and $N_{ch} = 1$, (f) 3200 km transmission and $N_{ch} = 16$, (g) 4800 km transmission and $N_{ch} = 1$, and (h) 4800 km transmission and $N_{ch} = 16$.. 108
- Fig. 4.13. SNR versus P_{SIG} comparing both experimental data points with the points evaluated from the fitted SNR analytical model after 0, 1600, 3200 and 4800 km at the following operating conditions: (a) $P_{LO} = 12$ dBm and $N_{ch} = 1$, (b) $P_{LO} = 12$ dBm and $N_{ch} = 16$, (c) $P_{LO} = 3$ dBm and $N_{ch} = 1$, and (d) $P_{LO} = 3$ dBm and $N_{ch} = 16$ 113
- Fig. 4.14. SNR versus N_{ch} comparing the experimental data points with the points evaluated from the fitted SNR analytical model after 0, 1600, 3200 and 4800 km at the following operating conditions: (a) $P_{LO} = 12$ dBm and $P_{SIG} = 0$ dBm, (b) $P_{LO} = 12$ dBm and $P_{SIG} = -12$ dBm, (c) $P_{LO} = 3$ dBm and $P_{SIG} = 0$ dBm, and (d) $P_{LO} = 3$ dBm and $P_{SIG} = -12$ dBm..... 114

Fig. 4.15. (a) Simulated intensity eyediagram of the single polarization QPSK signal using NRZ pulse shape, (b) experimental intensity eyediagram obtained after the single polarization IQ modulator, (c) scaling factor (β) versus the amount of residual CD for various polarization rotation angles (θ) obtained from simulations and theory on a 28 Gbaud PDM-QPSK signal..	131
Fig. 5.1. Block diagram of the PDM IM/DD system including (a) transmitter, (b) receiver front-end and (c) MIMO DSP to perform polarization demultiplexing using direct-detected Stokes parameters, (PBS: polarization beam splitter, PBC: polarization beam combiner).....	137
Fig. 5.2. a) Experimental setup, b) and c) Eye diagram after DSP for the X-polarization of a 56 Gbaud PDM PAM-4 signal after 2 km and steady-state MIMO filter taps when received SOP is at 0° (left) and 45° (right) relative to receiver PBS axis.....	140
Fig. 5.3. Offline DSP stack employed at a) Transmitter, b) receiver.	140
Fig. 5.4. a) BER versus bit rate for PDM PAM-2 and PAM-4 after various distances, b) BER versus baud rate for PDM PAM-4 and single polarization PAM-4, c) BER versus received signal power for 112 Gb/s PDM PAM-4 and PAM-2 in back-to-back.....	142
Fig. 5.5. BER versus received signal power when the received SOP was at 0° , 30° and 45° relative to the receiver PBS for both (a) 56 Gbaud PDM PAM-2, (b) 28 Gbaud PDM PAM-4.	144
Fig. 5.6. Simulation results for 28 Gbaud PDM-PAM4 system showing: a) BER versus received power for different SOPs and for two different splitting ratios, b) BER versus coupler splitting ratio for different SOPs and at different received powers.	146
Fig. 6.1. Summary of the original contributions of the thesis.....	148

List of Tables

Table 2.1. Explanation of impairments related to various terms of Manakov equation.	25
Table 2.2. <i>M</i> -QAM Constellations and number of achievable bits per symbol.....	35
Table 3.1. Linewidth tolerance of various CR schemes for different <i>M</i> -QAM formats	53

List of Acronyms

ADC	Analog-to-digital converter
ASE	Amplified spontaneous emission
ASIC	Application specific integrated circuit
AWG	Arrayed waveguide grating
AWGN	Additive white Gaussian noise
BER	Bit error rate
BPS	Blind phase search
CD	Chromatic dispersion
CMA	Constant modulus algorithm
CMOS	Complementary metal-oxide semiconductor
CMRR	Common mode rejection ratio
CR	Carrier recovery
CR _x	Coherent receiver
CW	Continuous wave
DAC	Digital-to-analog converter
DD	Direct detection
DFB	Distributed feedback
DGD	Differential group delay
DML	Directly modulated laser
DP	Dual-polarization
DPLL	Digital phase-locked loop
DSP	Digital signal processing

DWDM	Dense wavelength division multiplexing
EAM	Electro-absorption modulator
ECL	External-cavity laser
EDFA	Erbium doped fiber amplifier
EEPON	Equalization-enhanced phase noise
EML	Electro-absorption modulated laser
FDE	Frequency domain equalizer
FEC	Forward error correction
FFCR	Feedforward carrier recovery
FFT	Fast Fourier transform
FIR	Finite impulse response
FO	Frequency offset
FPGA	Field-programmable gate array
FT	Fourier transform
FTTC	Fiber to the curb
FTTH	Fiber to the home
GVD	Group velocity dispersion
IFFT	Inverse fast Fourier transform
IM	Intensity modulation
IM/DD	Intensity modulation / direction detection
IP	Internet protocol
IQ	Inphase and quadrature
ISI	Inter-symbol interference
LAN	Local area network

LMS	Least-mean square
LO	Local oscillator
MIMO	Multiple-input and multiple-output
MISO	Multiple-input and single-output
ML	Maximum-likelihood
MLPE	Maximum-likelihood phase estimation
MZM	Mach-Zehnder modulator
NDA	Non-data-aided
NL	Fiber Kerr nonlinearity
NRZ	Non-return-to-zero
OFDM	Orthogonal frequency division multiplexing
OOK	On-off keying
OSNR	Optical signal-to-noise ratio
PA	Pilot aided
PAM	Pulse amplitude modulation
PAPR	Peak-to-average power ratio
PBC/ PBS	Polarization beam combiner/splitter
PC	Polarization controller
PD	Photodetector
PDL	Polarization dependent loss
PDM	Polarization division multiplexing
PLL	Phase-locked loop
PMD	Polarization mode dispersion
PN	Laser phase noise

PPG	Pulse pattern generator
PSD	Power spectral density
PSM	Parallel single mode fiber
PSR	Pilot-to-signal power ratio
QAM	Quadrature amplitude modulation
QPSK	Quadrature phase shift keying
RF	Radio frequency
RC	Raised cosine
RRC	Root raised cosine
Rx	Receiver
RZ	Return-to-zero
SC	Single carrier
SE	Spectral efficiency
SFO	Sampling frequency offset
SiP	Silicon photonic
SISO	Single-input and single-output
SMF	Single mode fiber
SNR	Signal-to-noise ratio
SOP	State of polarization
SP	Single polarization
SPO	Sampling phase offset
SSB	Single sideband
SSFM	Split-step Fourier method
SSMF	Standard single mode fiber

SW	Optical switch
TIA	Transimpedance amplifier
TS	Training symbol
TS-EST	Training symbol based channel estimation
Tx	Transmitter
VVPE	Viterbi and Viterbi phase estimation
WDM	Wavelength-division multiplexing

Chapter 1

Introduction

1.1 Overview

The dominating and proliferating role of the Internet in every facet of nowadays society is indisputable. The spurring bandwidth demand across the Internet is propelled by the fast growing bandwidth intensive applications for social networking (e.g. Facebook), e-commerce (e.g. Amazon and eBay) and cloud computing and storage (e.g. Google and Dropbox). In addition, the growing bandwidth demand also stems from the expanding sectors of mobile networking and content delivery networks that provide streaming online multimedia. According to Cisco Visual Networking Index [1], the global internet protocol (IP) traffic has increased more than fivefold over the last five years, and is forecasted to triple over the following 5 years.

The aforesaid bandwidth demand is the impetus of the growing capacity demand from today's optical networks which is imposing new challenges on all domains of the network namely, core (backbone), metro and access parts of the network. Traditionally, optical fiber communications has been the prevailing technology adopted for core and metro networks with reach ranging from ~100 km (regional links) to thousands of kilometers (submarine links) because of the low loss and wide bandwidth offered by the optical fiber medium compared to other transmission media, e.g. copper. More recently, fiber optical communications has migrated into the access networks (or last mile networks) replacing copper links from central offices to residential customers, e.g. fiber to the curb (FTTC) and fiber to the home (FTTH) technologies [2].

Over the last decade, coherent technology together with digital signal processing (DSP) has replaced classic intensity modulation and direct detection (IM/DD) and become the predominant technology for fiber transmission systems deployed over core and metro networks. Currently, 200 Gb/s coherent transceivers are commercially available, e.g. WaveLogic3 Extreme from Ciena which is capable of packing 200 Gb/s in a dense wavelength division multiplexing (DWDM) 50 GHz channel [3]. Along with commercial products, the research literature is full of hero experiments that target extreme capacities and record spectral efficiencies, e.g. [4-8].

Moving forward, both academia and industry are confronted to further increase the achievable capacities by coherent transceivers while extending their reach. Together with that, the major

challenge is to achieve the aforesaid goals while at the same time: 1) reducing the cost per bit, 2) making the transceivers flexible enough to meet the growing demand of having fully agile optical networks to cope with dynamic and varying patterns of the Internet traffic. Photonic integration is widely agreed to be the key technology that potentially cuts the cost of coherent transceivers due to cost reduction associated with volume production. In addition, innovative designs and implementations of DSP algorithms as well as more adaptive optics are still required to realize fully flexible coherent transceivers for future agile networks.

Along with the capacity and agility demands in transport networks, optical fiber communications has migrated further to the shorter reach links. The need for faster and inexpensive short reach (< 20 km) optical interconnects for inter- and intra-datacenter communication is growing rapidly propelled by the burgeoning spread of cloud services offered by modern data centers.

The objective of this thesis is to develop advanced technologies for future flexible coherent transceivers; a key enabling technology for future agile transport networks, and introduce novel IM/DD transceiver technologies for short reach optical interconnects necessary in modern datacenters.

1.2 Motivation

1.2.1 Flexible optical coherent transceivers for optical transport

As mentioned in section 1.1, the incessantly growing capacity demand in optical transport networks has been driving a wide range of research efforts in the realm of coherent optical technology [9-23]. Indeed, coherent detection linearly maps the in-phase (I) and quadrature (Q) components on two orthogonal polarization states of the received optical field into the electrical domain by beating the received field with that of a local oscillator (LO) laser which enables the exploitation of the four available degrees of freedom on the optical carrier. Consequently, this facilitates the use of complex modulation formats, e.g. M -ary quadrature amplitude modulation (M -QAM), that deliver a higher number of bits per symbol compared to the conventional intensity modulation (IM). In addition, the use of polarization division multiplexing (PDM) essentially doubles the overall number of bits per symbol. Employing complex modulation formats in conjunction with PDM in coherent optical systems offers superior spectral efficiency (SE) compared to traditional IM / direct-detection (DD) systems;

a very desirable asset to cope with the ever-increasing need for SE in future optical transport [1].

In addition to providing higher SE, the coherent optical technology aided with high speed digital-to-analog converters (DACs) and analog-to-digital converters (ADCs) at the transmitter and receiver sides, respectively, enables pre-compensation and post-compensation of various fiber transmission impairments using digital signal processing (DSP) [9-11, 19, 21]. More specifically, a DSP-based coherent transceiver has the power to pre-compensate and post-compensate various linear impairments acquired along the fiber channel such as chromatic dispersion (CD), random polarization rotation and polarization mode dispersion (PMD). In addition, it is capable of mitigating nonlinear impairments such as nonlinearity-induced impairments due to the Kerr effect in the optical fiber as well as impairments related to the transmit and LO lasers, e.g. laser phase noise (PN) and laser frequency offset (FO).

However, it still remains a challenge to meet the relentless growing network traffic demand. A promising technological candidate for deployment in conjunction with optical coherent technology is the notion of agile/flexible software-defined optical networks [17, 24]. In the envisioned agile networks, flexible coherent transceivers, that are capable of adapting to dynamic traffic needs and thus maximizing the network capacity, are key elements that need to be installed at ingress / egress nodes. The combination of flexible transceivers, a flexible grid unlike the classic fixed 50G or 100G WDM grids, and intelligent client nodes enables a new “elastic” networking paradigm, allowing service providers to address the increasing needs of the network without frequently overhauling it [25, 26]. These flexible transceivers need to be smart, data-rate and modulation format agile and impairment aware/tolerant [17]. In addition, the notion of agility necessitates the ability of the transceiver to transmit / receive at any optical frequency in order to adapt to the dynamic nature of the network. To achieve this, a coherent receiver needs to operate in a colorless fashion by utilizing the LO laser for channel selection. Such a scheme mandates removing the WDM demultiplexing optical filter that precedes the receiver which is beneficial on one hand as it reduces cost and footprint besides offering the desired transceiver flexibility, but on the other hand, it may degrade the receiver performance depending on various system parameters such as the number of WDM channels, LO power, received signal power etc.

In the first half of this thesis, we propose various novel DSP algorithms for mitigating a myriad of transmission impairments namely, laser PN and FO, fiber-induced Kerr nonlinearity,

random polarization rotation and sampling frequency offset. All proposed DSP algorithms are transparent to modulation format and hence, are suitable for deployment in a flexible coherent transceiver; a key component in the envisioned future agile optical network. In addition to proposing novel DSP algorithms, we also present the results of a thorough theoretical and experimental study of the performance limits of a coherent receiver when employed in a WDM colorless configuration.

1.2.2 IM/DD transceivers for short reach optical interconnects

As highlighted in section 1.1, there is a growing demand for faster and low-cost short reach (< 20 km) optical interconnects for inter- and intra-datacenter communication. For an equal bit rate, modulating a single wavelength from a single laser provides a solution that is more cost effective than a multiplexed counterpart that involves the use of multiple wavelengths, i.e. WDM, or fiber lanes, to achieve the total desired bit rate. In addition, the single wavelength approach is the more scalable solution to cope with the ever-increasing capacity demand. For these short reach applications, IM/DD prevails over coherent technology as the more cost effective technology suitable for deployment.

Although 100 Gb/s transmission of Ethernet frames over SMF has been standardized as 100GBASE-LR4 by using 4×25 Gb/s in a WDM setting employing four colors in the 1300 nm band [27], it is widely agreed that achieving 100 Gb/s on a single wavelength using inexpensive and power efficient components is a mandatory building block in order to realize the envisioned 400 Gb/s and 1 Tb/s future plateaus [28]. Recently, many demonstrations of 100 Gb/s per wavelength were reported using various modulation formats [29-33], where the experiments in [31, 32] employed polarization division multiplexing (PDM) to halve the baud rate required to reach 100 Gb/s with the demultiplexing done optically with a polarization controller.

In parallel with determining the proper signaling format for these short reach optical interconnects, Silicon photonics (SiP) is rapidly emerging as an inexpensive technology platform for cheap large scale integration of various electro-optic, optical and optoelectronic components [34] which are very appealing features for these intra-datacenter interconnects. Silicon is a very useful host material for fabrication because of its low cost, high yield, large scale integration, and CMOS compatibility, enabling the integration of modulators and photodiodes with the RF drivers [35].

In the second half of this thesis, we propose a novel multiple-input and multiple-output (MIMO) DSP algorithm together with a direct-detection (DD) optical front-end that enables polarization division multiplexing (PDM) in an IM/DD system which allows either doubling the achievable bit rate per wavelength or halving the baud rate required to achieve the same bit rate in a single polarization system. We experimentally demonstrate for the first time 224 Gb/s transmission over 10 km using a single 1310 nm laser and a fully packaged SiP intensity modulator using the novel MIMO DSP after the DD receiver.

1.3 Thesis organization

After the current introductory chapter, the remainder of the thesis is organized as follows.

In **Chapter 2**, the architecture and theory of optical modulation and detection are introduced, covering both the legacy intensity modulation / direct detection (IM/DD) systems as well as the modern in-phase and quadrature (IQ) modulation / coherent detection schemes. Next, the typical and relevant optical channel impairments including CD, PMD, fiber nonlinearities, laser phase noise and sampling frequency offset are reviewed with the focus on their physical manifestations on the signal and mathematical models together with the classic DSP algorithms to mitigate them.

In **Chapter 3**, we propose and verify experimentally the performance of three DSP algorithms for coherent transmission systems. The proposed algorithms are transparent to modulation format and hence suitable for deployment in flexible coherent transceivers. We first propose pilot-aided DSP (PA-DSP) that mitigates jointly laser phase noise and frequency offset, random polarization rotation in addition to partially alleviating fiber nonlinearity. The performance of the proposed PA-DSP is verified via both simulations and experiment. Secondly, we propose a training symbol based channel estimation (TS-EST) method that enables polarization demultiplexing by inverting the random polarization rotation that occurred through the fiber. The proposed TS-EST, which utilizes a very low bandwidth overhead, is both tested in simulation and experimentally demonstrated. Thirdly, we propose and experimentally investigate a non-data-aided (NDA) feedforward timing recovery scheme to mitigate sampling frequency offset between transmitter and receiver clocks for arbitrary QAM constellations.

Chapter 4 presents a thorough study from theoretical and experimental standpoints of the performance limits of a silicon (Si-) photonic coherent receiver (CRx) when employed in a

WDM colorless configuration. The architecture of the Si-photonic CRx under study is depicted. Furthermore, we develop rigorously an analytical expression of the SNR at the CRx output in the case of colorless reception. Next, a full parametric system-level WDM experimental study is conducted using the Si-photonic CRx to validate the accuracy of the derived model.

In **Chapter 5**, we propose a novel MIMO DSP that operates in the Stokes space after a DD receiver which enables a PDM IM/DD scheme. The proposed PDM IM/DD scheme is a competitive and viable solution for short reach optical interconnects in future datacenter applications since it halves the number of required laser sources to achieve a certain target bit rate. We experimentally demonstrate 224 Gb/s transmission over 10 km using a single 1310 nm laser and Si-photonic IM by employing 56 Gbaud PAM-4 signal in conjunction with PDM.

Chapter 6 concludes the thesis summarizing the key contributions made and provides some potential directions for the future work.

1.4 Original contributions

The original contributions of this thesis are summarized hereafter.

DSP Algorithms for flexible coherent optical transceivers

We propose three DSP algorithms in the context of coherent transmission systems to mitigate a myriad of impairments. All DSP algorithms introduced are transparent to modulation format and hence, appropriate for deployment in a flexible coherent transceiver; a key enabling technology in the envisioned agile / flexible optical transport network. Below, we summarize the three propounded DSP algorithms highlighting the targeted impairment(s) to mitigate by each algorithm together with the key results achieved.

- We propose a novel pilot-aided (PA) DSP scheme for single carrier coherent transmission systems. The proposed PA-DSP is a hybrid pre- and post-compensation DSP that requires DSP tasks at both transmitter and receiver sides, respectively. We show how the received pilot can be employed to mitigate *jointly*: a) laser phase noise (PN) from transmitter (Tx) and receiver (Rx) lasers, b) frequency offset (FO) between the two lasers, c) fiber Kerr nonlinearity (NL) induced phase shift, and d) random polarization rotation along the fiber channel. The effectiveness of PA-DSP in compensating laser PN and fiber nonlinearity is verified by simulations in [36-38]. In addition, a proof-of-concept experimental verification of PA-DSP is carried out in [39] demonstrating the benefit of PA-DSP for a

28 Gbaud PDM-QPSK signal in mitigating laser PN and FO in addition to estimating and inverting the random polarization rotation along the fiber.

- We present a novel modulation format transparent TS based channel estimation (TS-EST) algorithm that utilizes a very small TS overhead to estimate the random rotation over the fiber channel in a non-adaptive way thus allowing for ultrafast polarization tracking. Our algorithm was experimentally verified in [40] for both 112 Gbps PDM-QPSK and 224 Gbps PDM-16QAM signals. Finally, we showed by simulation in [41] that the superior tracking speed of the TS-EST algorithm allows not only for initial polarization tracking but also for tracking very fast polarization transients during steady-state operation.
- We present a non-data-aided (NDA) feedforward timing recovery scheme for PDM M -QAM signals. The proposed estimator operates at 2 samples/symbol and is entirely transparent to modulation format. The proposed timing recovery is experimentally verified in [42] on 28 Gbaud PDM-QPSK, PDM-16QAM and 7 Gbaud PDM-64QAM signals in back-to-back and transmission scenarios.

Performance of a colorless coherent optical front-end

We perform a profound study from theoretical and experimental standpoints of the performance limits of a Si-photonic coherent receiver (CRx) when employed in a WDM colorless configuration. We first introduce the building blocks and key characterization results of the CRx under test. Secondly, we develop rigorously an analytical expression of the SNR at the CRx output in case of colorless reception taking into consideration all sources of noise specific to this scenario. Unlike prior art, this analytical model that we presented in [43] is the first model that is meticulously derived while considering all sources of noise and finally verified by an exhaustive set of experimental measurements to prove its validity and accuracy. The experiments performed on the CRx were done initially in [44] on a single channel and later in [43] with a WDM signal to verify the model. After the derived model was verified, it was extrapolated to predict the performance of the CRx for colorless selection of the one channel out of a fully populated WDM spectrum.

MIMO DSP enabling a PDM IM/DD system

We propose a novel MIMO DSP that operates in the Stokes space after a DD receiver to invert the polarization rotation along the fiber and achieve polarization demultiplexing. The proposed DSP enables a PDM IM/DD system where the transmitted bit rate is potentially doubled while using the same number of laser sources. In [45], we report 224 Gb/s transmission of a 56 Gbaud PDM PAM-4 signal over 10 km using a single 1310 nm laser and a SiP IM with the polarization demultiplexing done at the receiver using our novel DSP. At the time of the experiment, this was the world's highest bit rate reported for IM/DD short reach links. In [46], we performed a more comprehensive simulation-based study of the DD front-end of [45] and draw some important conclusions on how to modify the design of the front-end to make the receiver performance agnostic to the received state of polarization.

Chapter 2

Fundamentals of Fiber Optical Fiber Communication Enabled by either Direct-Detection or Coherent Reception

2.1 Overview

Historically, the invention of the laser as a coherent light source [47] and the proposal of using the optical fiber as a transmission medium in the 1960s [48, 49] were the two groundbreaking milestones that commenced the emergence of the field of high speed fiber-optic communication systems. Throughout the years, the dominant signaling format in fiber-optic communication systems was based on intensity modulation / direct-detection (IM/DD) meaning the information to be transmitted, be it analog or digital, is modulated onto the intensity of a light source and at the end of the fiber, the received light field is launched onto a photodetector that maps the intensity of the received field into a photocurrent carrying a distorted version of the transmitted data. In the language of digital communications, the transmitted bits are imprinted into the intensity in an On-Off keying (OOK) fashion and received via a photodetector resulting in a signaling rate (or symbol rate) equal to the information bit rate, i.e. a spectral efficiency equal to 1 bit/symbol. Unlike wireless communications, the classic IM/DD OOK modulation, which exploits only one degree of freedom of the optical carrier, has prevailed over the years due to being both simple to implement and sufficient to meet the capacity demand in the past.

IM/DD OOK signaling has remained the dominant technology along the years and the increasing capacity demand was met by other emerging technologies such as wavelength-division-multiplexing (WDM) and optical amplification. The combination of the vast bandwidth and low propagation loss offered by a single mode fiber and the invention of the Erbium doped fiber amplifier (EDFA) with its ability to boost a very broad spectrum [50, 51] followed by its commercialization in the 1990s allows multiplexing many carriers at different wavelengths, each carrying a single OOK signal and more recently a differential phase shift keying (DPSK) signal, resulting in large capacities length products being reported from 1990 to early 2000's [52-54].

In the middle of 2000s, the increasing capacity demand due to the evolving role of the Internet mandated utilizing other degrees of freedom available on the optical carrier to increase the spectral efficiency beyond 1 bit/symbol and hence, achieve higher capacity per channel (wavelength). This can be achieved via coherent detection which, instead of providing the intensity as in direct-detection, gives the full optical field information, i.e. amplitude and phase, by the use of phase diversity. If polarization diversity is used in addition to phase diversity, a coherent receiver provides the amplitude and phase on two orthogonal polarization states of the optical carrier, i.e. this enables modulating four degrees of freedom as opposed to only one in DD using formats such as OOK or DPSK.

Historically, optical coherent detection was studied extensively in the 1980s [55-57] due to its superior sensitivity but was later abandoned after the invention of an EDFA. The main driver behind reviving the interest in optical coherent detection since the middle of 2000s is the growth in the electronic speeds at which application specific integrated circuits (ASICs) can operate [9, 10, 13, 58, 59]. These ASICs operating at speeds commensurate with the optical line rates are capable of performing intensive DSP functionalities that allows phase and polarization tracking in addition to mitigating fiber transmission impairments if employed after an optical coherent receiver [9, 11]. For the past ten years, a tremendous amount of research has been done in this area which pushed the capacity and reach to unprecedented values (e.g. record capacity achievements using advanced modulation formats and coding combined with wavelength, space and/or mode division multiplexing in the following hero experiments [4-8]).

In this chapter, we present the background information upon which the remainder of the thesis is based. We review the generic system architecture of both the classic IM/DD and coherent optical transmission systems in sections 2.2 and 2.3, respectively focusing on the key enabling components for both schemes. In section 2.4, we list the main impairments in a coherent transmission system focusing on the mathematical modeling and the underlying signal distortions caused by each of the impairments as well as the standard DSP tasks to mitigate them. Finally in section 2.5, we highlight the impairments that are relevant and important in a short reach IM/DD optical link.

2.2 Intensity modulation direct-detection optical transmission system architecture

A generic architecture of an N channel WDM Intensity modulation direct-detection (IM/DD) transmission system is viewed in Fig. 2.1. It comprises N transmitters (Tx) at different wavelengths, an optical fiber channel having N_{spans} periodically amplified spans and N receivers (Rx). The architecture is totally generic as it accommodates any number of WDM channels, WDM grid (channel separation) and any transmitter / receiver technology as will be explained below.

At the Tx side, we show two possible strategies to perform intensity modulation: a) direct modulation, and b) external modulation. In case of a directly modulated laser (DML), the information is modulated onto the laser driving current which then switches on and off the light emerging from the laser leading to OOK modulation (see IM Tx 1 in Fig. 2.1). DMLs have the advantage of being compact and cheap hence suitable for dense integration in small form factor pluggable, e.g. SFP and XFP standard packages [60]. DMLs are widely available commercially for speeds up to 10 Gb/s and research demonstrations up to ~ 40 Gb/s [60]. The reason behind the modulation speed limitation of DMLs is the inherent chirp that is the residual unwanted phase modulation resulting from modulating the carrier density within the laser cavity which slightly changes the refractive index of the active medium [61]. Although the photodetector is transparent to phase modulation and should not be affected by this chirp, the limitation is due to the spectrum broadening due to chirp which makes chromatic dispersion along the fiber more severe.

The second strategy to modulate the intensity is to use external electro-optic modulators (see IM Tx 2 in Fig. 2.1) to reduce or eliminate the chirp problem. Two technologies of external modulators are available in the literature: electro-absorption modulators (EAMs) and Mach-Zhender modulators (MZMs). EAMs are built from a semiconductor material whose absorption characteristics change with the applied voltage and hence providing intensity modulation. The advantage of EAMs is the potential to be co-integrated in one package with the laser source and the lack of need for an interferometric structure and hence the smaller insertion loss compared to MZMs. However, like DMLs there is some residual unwanted chirp that limits modulation speeds to ~ 25 Gb/s commercially and ~ 40 Gb/s for research purposes [60]. On the other hand, MZMs are built in an interferometric structure to convert phase modulation in its arms into

amplitude (or intensity) modulation (see inset at the bottom right of Fig. 2.1). Phase modulation in each arm is based on the Pockels effect that describes how the refractive index of some materials (e.g. Lithium Niobate) changes linearly with the applied electric field (and hence voltage) [61]. Given the MZM is driven differentially in a push pull fashion, i.e. $V_+ = -V_-$, zero chirp operation is achieved and the resulting field and intensity transfer functions, i.e. $\frac{E_{out}}{E_{in}}$ and $\left|\frac{E_{out}}{E_{in}}\right|^2$ respectively, are both sinusoidal [61] and are shown in the inset at the bottom right corner of Fig. 2.1 where V_π is the voltage that needs to be applied at either arm to produce a π phase shift. Given that the bias point of the MZM is adjusted properly (done via the thermal phase shifters at the two arms) at the half power transmission point ($\left|\frac{E_{out}}{E_{in}}\right|^2 = 0.5$), a binary electrical signal with the proper swing will switch on and off the intensity of the input field to the MZM.

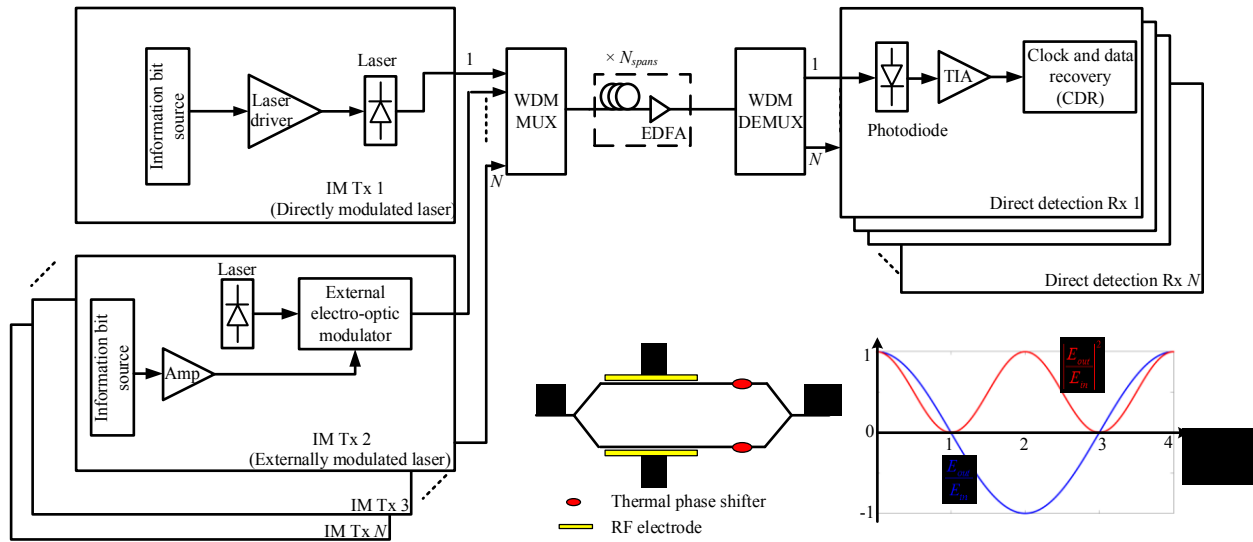


Fig. 2.1. Architecture of an N channel WDM IM/DD transmission system showing two configurations of the Tx: a directly modulated laser (DML) or an externally modulated laser. The insets on the bottom right show a Mach-Zehnder modulator structure (MZM) together with its transfer function of the field and intensity.

The Rx side is simply a photodiode that converts the intensity of one filtered WDM channel into a photocurrent. Typically, p -type/intrinsic/ n -type (PIN) photodiodes are used however avalanche photodiodes (APDs) can be sometimes preferred in special applications where superior responsivity is needed. Following the photodiode, a transimpedance amplifier (TIA) is

mostly used to convert the photocurrent into an amplified voltage which improves the overall sensitivity of the photoreceiver that contains the PIN+TIA combination. The last block is a clock and data recovery (CDR) unit that first determines the proper sampling instants, samples the data, and provides hard decisions on the received bits.

2.3 Coherent optical transmission system architecture

A DSP-based single carrier dual polarization N channel WDM coherent transmission system is shown in Fig. 2.2. It comprises N transmitters (Tx) at different wavelengths, an optical fiber channel having N_{spans} periodically amplified spans and N receivers (Rx). It should be noted that the architecture in Fig. 2.2 is totally generic in the sense that it can accommodate any modulation format, pulse shape, baud rate, number of WDM channels and channel separation (WDM grid).

In Fig. 2.2, the Tx-DSP tasks may vary from one system to another to the extent that it can be entirely omitted if we were not to pre-process the transmitted symbols before transmission. Indeed, early generations of coherent transceivers did not employ application specific integrated circuits (ASICs) to perform DSP and did not include high speed digital-to-analog converters (DACs) at the Tx side. Instead, high speed binary data streams were fed directly after amplification to the electro-optic modulator to generate simple modulation formats such as quadrature phase shift keying (QPSK) and even 16-ary quadrature amplitude modulation (16QAM) with non-return-to-zero (NRZ) and return-to-zero (RZ) pulse shapes [62-64]. This would reduce the overall complexity of the system; however, it will also deteriorate the system performance by reducing the flexibility of being able to perform some pre-processing at the Tx-side. Therefore, Tx-DSP and DACs have become indispensable in current generations of flexible coherent transceivers. For example, Tx-DSP may perform pulse shaping for the transmitted symbols which allows to spectrally engineer the transmitted spectrum to improve the performance and increase the spectral efficiency by reducing the channel separation in a WDM system [65]. A raised cosine (RC) pulse shape provides a compact spectrum with minimum out-of-band power and zero intersymbol interference (ISI) [21]. Often, the RC pulse shaping filter is split into two matched root-raised cosine (RRC) filters at the Tx and Rx DSPs to maximize the signal-to-noise-ratio (SNR) assuming an additive white Gaussian noise (AWGN) channel [66]. In addition to pulse shaping, the Tx-DSP may partially pre-compensate some of the fiber channel transmission impairments, e.g., chromatic dispersion (CD) and fiber nonlinearity [18, 67].

Finally, other Tx-DSP tasks might include pre-equalization of the frequency response of the DACs and the electro-optic modulator. In subsection 2.4.3, we highlight in more details the variety of Tx-DSP functions.

After the Tx-DSP, the four electrical signals from the DACs are fed after being amplified by radio frequency (RF) amplifiers (not shown in Fig. 2.2) to a dual-polarization IQ (DP-IQ) modulator that modulates four degrees of freedom of a continuous wave (CW) from an external laser source namely: the amplitude and phase on two orthogonal polarization states. The internal structure of the dual-polarization IQ modulator is detailed in Fig. 2.3(a). It comprises a 3 dB power splitter whose outputs are fed to two outer parent Mach-Zhender modulators (MZMs), i.e. one for each polarization, with each parent MZM having two child MZMs in its arms in a nested structure. Finally, the two outputs of the parent MZMs are fed to a polarization beam combiner (PBC) after one of them is passed through a 90° polarization rotator. Looking carefully at Fig. 2.3(a), there are 12 thermal phase shifters needed to ensure the biasing of the four child MZMs is set at null and the two parent MZMs are set to guarantee the two fields out of the child MZMs are in quadrature. Depending on whether single-drive or dual-drive configuration is adopted, either four or eight (four differential pairs) driving RF signals are applied to the RF electrodes shown around the arms of the child MZMs in Fig. 2.3(a) to perform modulation. Provided the bias points of all child and parent MZMs are adjusted properly and the swing of the applied RF signals are set carefully within the linear portion of the sinusoidal field transfer function of the child MZMs around the null point (depending on the halfwave voltage V_π as previously depicted in Fig. 2.1), the DP-IQ modulator produces linear mapping from the four RF signals I^X, Q^X, I^Y, Q^Y into the two quadrature components of two orthogonal polarization states of the optical field.

The resulting PDM signal is multiplexed with its WDM neighbors and the resulting aggregated WDM signal is launched into the transmission system. The transmission system comprises N spans of single mode fiber (SMF) where each span is followed by an inline Erbium doped fiber amplifier (EDFA) that compensates for the losses encountered in each span after propagation. Without loss of generality, the entire research work in this thesis is focused on dispersion-unmanaged links which consist of fiber spans and EDFAs only as shown in Fig. 2.2, i.e. no inline optical CD compensation is employed which not only reduces the cost but also improves the system performance [12]. In addition, the entire focus of the thesis on EDFA only

systems, i.e. systems based on Raman or hybrid Raman-EDFA amplification are not considered. Although a Raman amplifier can achieve a lower noise figure than an EDFA, it is rarely deployed in real systems due to its need for high power pumps [68]. Other components such as reconfigurable optical add-drop multiplexers (ROADMs) are omitted for simplicity. Inside the fiber, the signal will experience various impairments such as CD, fiber nonlinearities, PMD, attenuation and so forth, which are all detailed in subsection 2.4.2.

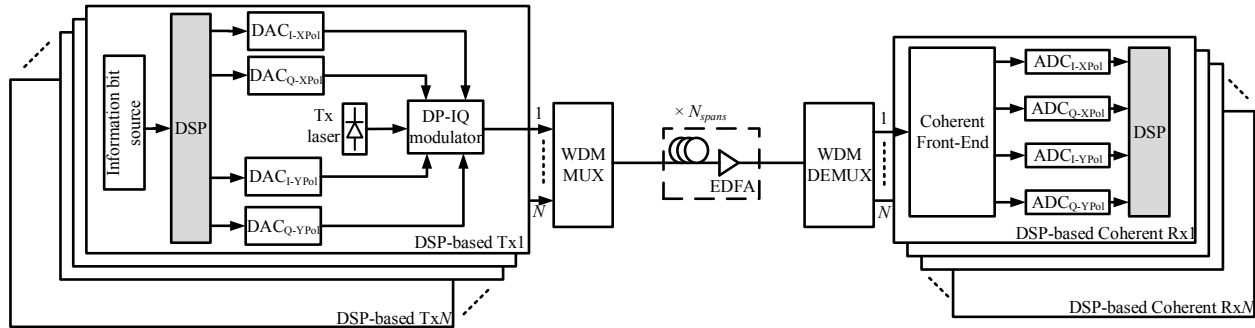


Fig. 2.2. Architecture of a DSP-based N channel WDM coherent transmission system.

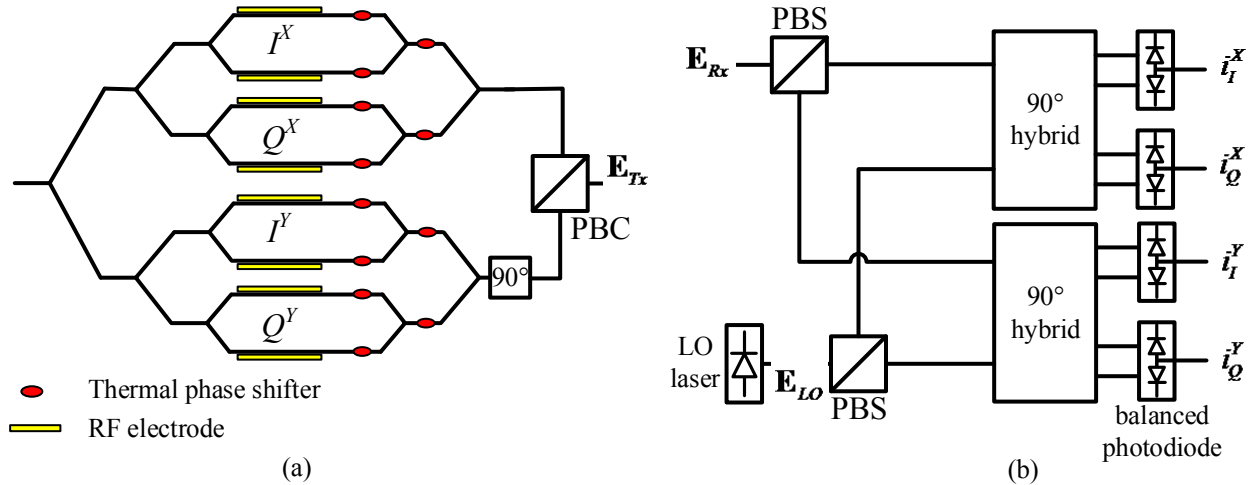


Fig. 2.3. Architecture of: (a) dual-polarization IQ (DP-IQ) modulator, (b) coherent front-end.

At the Rx, a coherent receiver (CRx) front-end integrates polarization beam splitters (PBSs), two single-polarization 90° optical hybrids, a local oscillator (LO) laser and four balanced photodetector pairs to provide four signals corresponding to the I and Q components on both polarizations of the received optical field. The detailed architecture of the CRx front-end is depicted in Fig. 2.3(b).

The four baseband signals provided by the CRx front-end are then sampled by analog-to-digital converters (ADCs) and processed by the Rx-DSP. The Rx-DSP compensates for any imperfections in the Rx optical front-end, fiber channel transmission impairments (e.g., residual CD, polarization mode dispersion (PMD)) and fiber NL impairments. It also performs matched filtering if pulse shaping is done at the Tx-DSP. Finally, it will perform frequency offset estimation and carrier phase recovery (CR). A detailed explanation of the various functions performed by the Rx DSP will follow in subsection 2.4.3.

For the sake of mathematical formulation of system impairments in the upcoming subsection, we adopt the Jones calculus [61] to represent dual-polarization optical fields as well as polarization related impairments along the fiber channel (e.g. PMD). Indeed, we denote the 2×1 Jones vector of the real-valued bandpass transmitted optical field at the output of the DP-IQ modulator as

$$\mathbf{E}_{Tx}(t) = \text{Re} \left\{ \begin{bmatrix} I^X(t) + jQ^X(t) \\ I^Y(t) + jQ^Y(t) \end{bmatrix} e^{j2\pi f_{SIG}t} \right\} \quad (2.1)$$

where $\text{Re}\{ \}$ denotes the real part of the quantity between the curly brackets and f_{SIG} denotes the frequency of the optical carrier, i.e. the frequency of the Tx laser. After propagation along the fiber, the field gets impaired due to CD, PMD and fiber nonlinearities which will be all detailed in subsection 2.4.2. The received field at the Rx side can be expressed as

$$\mathbf{E}_{Rx}(t) = \text{Re} \left\{ \begin{bmatrix} I'^X(t) + jQ'^X(t) \\ I'^Y(t) + jQ'^Y(t) \end{bmatrix} e^{j2\pi f_{SIG}t} \right\} \quad (2.2)$$

where I'^X, Q'^X, I'^Y, Q'^Y are the quadrature components of both polarizations of the received field which are evaluated based on how the transmission impairments impact the transmitted quadratures I^X, Q^X, I^Y, Q^Y . Then, the CRx front-end linearly maps the received optical field into the digital domain by beating the received field with a reference field originating from a LO laser defined as $\mathbf{E}_{LO}(t) = \text{Re} \left\{ \frac{1}{\sqrt{2}} \begin{bmatrix} 1 \\ 1 \end{bmatrix} e^{j2\pi f_{LO}t} \right\}$ where we assume that the polarization of the LO laser is set to have equal powers in both polarizations, i.e. into both sections of the CRx in Fig. 2.3(b). The four electrical photocurrents generated by the balanced photodetectors are then written as

$$i_I^X(t) = R \operatorname{Re} \left\{ \left(I'^X(t) + jQ'^X(t) \right) e^{j2\pi\Delta Ft} \right\} \quad (2.3)$$

$$i_Q^X(t) = R \operatorname{Im} \left\{ \left(I'^X(t) + jQ'^X(t) \right) e^{j2\pi\Delta Ft} \right\} \quad (2.4)$$

$$i_I^Y(t) = R \operatorname{Re} \left\{ \left(I'^Y(t) + jQ'^Y(t) \right) e^{j2\pi\Delta Ft} \right\} \quad (2.5)$$

$$i_Q^Y(t) = R \operatorname{Im} \left\{ \left(I'^Y(t) + jQ'^Y(t) \right) e^{j2\pi\Delta Ft} \right\} \quad (2.6)$$

where $\Delta F = f_{SIG} - f_{LO}$ is the frequency offset between the Tx and Rx lasers whose impact on the signal will be further studied in subsection 2.4.1.2. In Eqs. (2.3)-(2.6), R is a scaling factor that takes into account the photodiode responsivities and any constant factors that result from passive splitting of the signal through the CRx front-end. It is noteworthy that the details of the CRx front-end and its imperfections, e.g. responsivity mismatch between the P and N photodiodes of each balanced pair, are all studied thoroughly in Chapter 4 that is dedicated to the performance analysis of an imperfect CRx front-end.

2.4 System impairments for a coherent transmission system

In this section, we review the main system impairments that impact the performance of a coherent transmission system. We divide the discussion into two parts; we first list the impairments originating from the transceiver hardware itself in subsection 2.4.1 and secondly, we describe the impairments related to the fiber channel in subsection 2.4.2. We focus on the physical manifestations and mathematical formulation of the impairments of which we are concerned for the research work throughout the thesis. Finally, we depict in subsection 2.4.3 the standard DSP stacks for a coherent transceiver and explain how they can mitigate each of the listed impairments.

2.4.1 Transceiver related impairments

2.4.1.1 Timing skew and quadrature error

Looking at Fig. 2.2 and Fig. 2.3(b), it is noticeable that any difference in the propagation delays due to path length mismatch encountered by the four photocurrents out of the CRx front-end until they are sampled by the ADCs and fed to the Rx ASIC will lead to a time skew between the four discrete-time electrical signals fed to the Rx ASIC (the discrete sampled

version of $i_I^X, i_Q^X, i_I^Y, i_Q^Y$ in Eqs. (2.3)-(2.6)). If not corrected by a deskew algorithm in DSP, this will lead to a significant performance penalty due to the offset between the optimum sampling location for both quadrature components. In general, the time skew τ that needs to be corrected is not an integer multiple of the ADC sampling interval T_{ADC} . Hence, it can be written as $\tau = iT_{ADC} + \mu T_{ADC}$ where $i = \lfloor \tau/T_{ADC} \rfloor$ is the integer number of ADC samples equivalent to the time skew and μT_{ADC} is the fractional part. The time skew τ is either physically measured, which needs to be done uniquely for each CRx front-end, or alternatively estimated via correlating the four sampled waveforms [9]. After that, it is straightforward to correct the integer portion in the digital domain, whereas an interpolator is needed to correct the fractional part of the skew. There exist various interpolators in the literature based on polynomial approximations of the pulse shapes (e.g. linear, quadratic, etc.) [9, 69, 70]. An example of such interpolator employed later in the thesis is the piecewise-parabolic interpolator whose details are given later in section 3.4.2.

The quadrature error is another impairment that originates from the imperfection in the 90° hybrid of the CRx. This quadrature error will simply break the orthogonality between the pairs i_I^X, i_Q^X and i_I^Y, i_Q^Y leading to intolerable penalty if not corrected due to the resulting crosstalk between the two quadratures per polarization. Mathematically speaking, if the quadrature angle error is denoted by θ_{qe} meaning that hybrid has its quadrature angle away from 90° by θ_{qe} , the received photocurrents from the non-ideal CRx front-end having an imperfect hybrid can be expressed in terms of the photocurrents obtained from an ideal CRx with a perfect 90° hybrid as

$$i_{I,non\ ideal}^X = i_I^X \cos(\theta_{qe}/2) + i_Q^X \sin(\theta_{qe}/2) \quad (2.7)$$

$$i_{Q,non\ ideal}^X = i_I^X \sin(\theta_{qe}/2) + i_Q^X \cos(\theta_{qe}/2) \quad (2.8)$$

where the photocurrents of the Y polarization can be simply written exactly as Eqs. (2.7) and (2.8). For the purpose of illustrating visually how quadrature error impacts the performance, we show in Fig. 2.5(a) how a QPSK constellation is impacted by varying amounts of quadrature error where we superimpose three cases: $\theta_{qe} = 0^\circ$ (blue), $\theta_{qe} = 10^\circ$ (red) and $\theta_{qe} = 20^\circ$ (black). Looking at Fig. 2.5(a), it becomes apparent that a non-negligible performance penalty is unavoidable unless the quadrature error is estimated and removed at the Rx DSP.

Orthogonalization algorithms such as the eminently known Gram-Schmidt algorithm can be used to correct the quadrature error [9, 71]. Finally, it is also noteworthy that there may be a quadrature error that comes from imperfection in the DP-IQ modulator, i.e. a quadrature error originating from the Tx due to sub-optimum biasing of the parent MZM of Fig. 2.3(a). The Tx-related quadrature error may still be compensated by well-known orthogonalization algorithms (e.g. Gram-Schmidt algorithm) however the algorithm needs to be applied at the end of the chain of DSP algorithms at the Rx after all impairments subsequent to the Tx have already been compensated.

2.4.1.2 Laser phase noise and frequency offset

Laser frequency offset (FO) was already introduced in section 2.3 and it results from the fact that the CRx uses a free running LO laser, i.e. it is not frequency-locked to the laser used at the Tx. Hence, there will be an offset between the center frequencies of both lasers. In addition to FO, laser phase noise (PN) is also an important impairment related to the Tx and Rx lasers. Typically, all lasers have a non-zero linewidth around their center frequency due to unwanted spontaneous emission that accompany the stimulated emission process within the laser cavity [72]. Due to this non-zero linewidth, the phase of the originating optical field deviates from that of a pure sinusoidal signal which would be the case if an ideal monochromatic laser, i.e. single tone, was used. Typically, the random laser PN process $\varphi(t)$ is modeled as a Weiner process [72, 73] that is formulated as

$$\varphi(t) = \int_{-\infty}^t \zeta \quad (2.9)$$

where the time derivative of the phase ζ is a white Gaussian random process, i.e. having a flat power spectral density (PSD), with zero mean and variance $2\pi\Delta f$. It can be proved that for such a random process $\varphi(t)$, the following is the variance of its increment $\Delta\varphi(t_1, t_2) = \varphi(t_1) - \varphi(t_2)$

$$\sigma_{\Delta\varphi}^2 = 2\pi\Delta f |t_1 - t_2| \quad (2.10)$$

In addition, the spectral shape, i.e. the PSD, of the resulting optical field having the above mentioned random phase $\varphi(t)$, i.e. the field $e^{j[2\pi ft + \varphi(t)]}$, can be proved to have a Lorentzian shape around the laser center frequency f with a full width at half maximum (FWHM) Δf [72].

The joint impact of laser PN from both Tx and Rx lasers in addition to FO can be all lumped in one complex rotation term into Eqs. (2.3)-(2.6) by replacing $e^{j2\pi\Delta Ft}$ with $e^{j[2\pi\Delta Ft + \varphi_{Tx}(t) + \varphi_{LO}(t)]}$. Since the Tx and LO laser phase noises are independent processes, the variance of the phase increment $\Delta\varphi(t_1, t_2) = \varphi(t_1) - \varphi(t_2)$, where $\varphi(t) = \varphi_{Tx}(t) + \varphi_{LO}(t)$ is the sum of the two stochastic phase noise processes, is also defined similar to Eq. (2.10) with Δf now becoming the sum of the linewidths of the Tx and LO lasers.

For the purpose of illustrating how laser PN and FO affect the transmitted data, we plot in Fig. 2.4(a) and Fig. 2.4(b) the constellation diagrams of 28 Gbaud QPSK symbols before and after adding the impact of laser PN and FO, respectively. The example we picked to plot is for Tx and LO lasers each having linewidth $\Delta f = 1$ MHz and an FO of $\Delta F = 10$ MHz. Finally, we show in Fig. 2.4(c) the linearly increasing instantaneous phase due to FO, i.e. $2\pi\Delta Ft$, superimposed with the random Weiner PN process for both the Tx and LO lasers, i.e. $\varphi_{Tx}(t) + \varphi_{LO}(t)$, and the sum of all three portions. The task of carrier recovery (CR) algorithms at the Rx DSP is to compensate the sum of all unwanted phase rotations, i.e. mitigate both PN and FO, to recover the phase of the transmitted data.

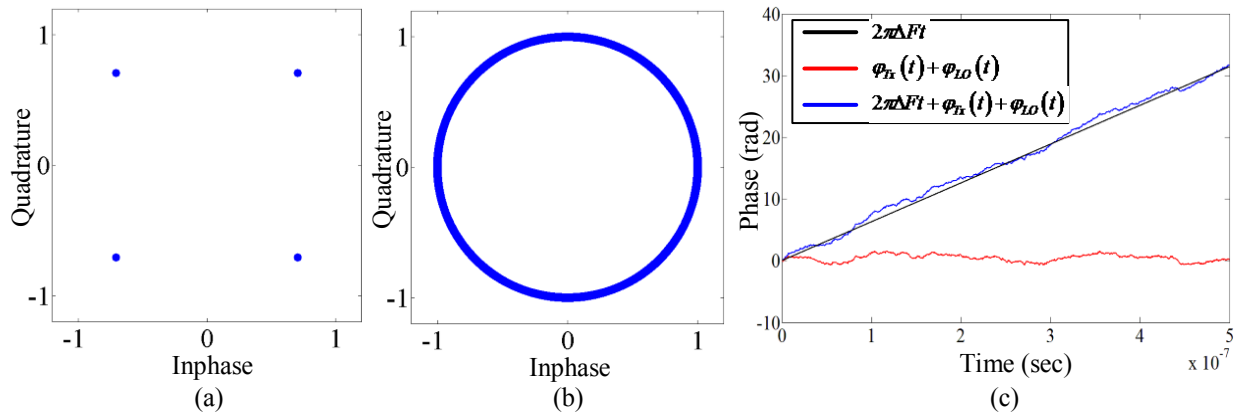


Fig. 2.4. Constellation diagrams showing 28Gbaud QPSK symbols: (a) before adding laser PN and FO, (b) with laser PN and FO with $\Delta F = 10$ MHz and $\Delta f = 1$ MHz for both Tx and LO lasers, (c) Instantaneous phase versus time showing three curves: FO only, PN only and the combined FO+PN process.

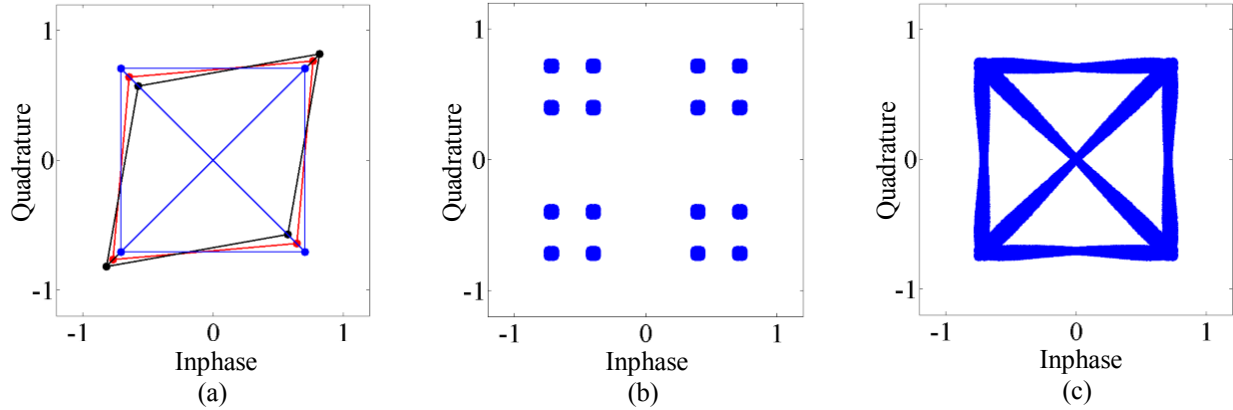


Fig. 2.5. Constellation diagrams showing QPSK symbols in the following cases: (a) under various amounts of quadrature error (θ_{qe}) of 0° (blue), 10° (red) and 20° (black) , (b) SPO of 0.3, and (c) SFO of 1000 ppm assuming an RC pulse with a roll-off factor of 1.

2.4.1.3 Sampling phase and frequency offset

Sampling phase offset (SPO) and sampling frequency offset (SFO) are two other impairments related to the transceiver imperfections. More specifically, the fact that the two sampling clocks of the Tx and Rx sides are not locked in either phase or frequency is the source of this impairment. SPO is simply the fact that the phase references of Tx and Rx clocks are not locked and hence the received discrete time samples out of the Rx ADC will be shifted away from the optimum sampling points within each transmitted symbol. In the absence of SFO, i.e. the two clocks run at exactly the same rate, SPO will remain constant over time and compensating it becomes just a matter of interpolating the discrete time samples to obtain the intermediate samples at the optimum sampling locations, i.e. similar to shifting the time origin. In this case, SPO needs to be estimated once and corrected using the interpolator over the entire received data vector. However, in case of non-zero SFO (either positive or negative depending on which clock is leading the other), the SPO will be either increasing or decreasing over time and needs to be tracked continuously and subsequently corrected.

Typically, SPO is defined relative to the symbol duration T where $SPO \in (-0.5, 0.5]$, whereas SFO is defined in parts per million (ppm) as follows

$$SFO \text{ (ppm)} = \frac{f_{ADC}/q - R}{R} \times 1000 \quad (2.11)$$

where f_{ADC} is the ADC sampling rate, q is the ADC oversampling factor, i.e. how many samples per symbol the ADC nominally provides and R is the symbol rate. An illustration of how SPO

and SFO affect the transmitted data symbols is shown in Fig. 2.5(b) and Fig. 2.5(c). We show the impact of an SPO of 0.3 in

Fig. 2.5(b) on QPSK symbols assuming an RC pulse shape with a roll-off factor of 1. We notice that due to the SPO, there is intersymbol interference (ISI) because of the offset away from the optimum sampling point at which the RC pulse satisfies the zero ISI condition. Finally in Fig. 2.5(c), we show the impact of an SFO of 1000 ppm on QPSK data where it is now clear that decoding the data becomes impossible unless the SFO is mitigated. Employing Eq. (2.11), an SFO of 1000 ppm is equivalent to the ADC sampling at 56.056 GSa/s instead of a nominal 56 GSa/s assuming that $q = 2$ and $R = 28$ Gbaud, i.e. the 56 GSa/s ADC sampling head is only 56 MHz away from its nominal value which is a practically reasonable value. The task of the timing recovery block at the Rx DSP is to mitigate both SPO and SFO. In section 3.4, we discuss in more details the mathematical formulation of SPO and SFO together with a proposed timing recovery scheme.

2.4.2 Fiber channel impairments

In this section, we begin by presenting the basic equation that governs the propagation of the electric field along a single mode fiber having a step-index profile. We quickly list the impairments encountered by the propagating field along the fiber which are all represented by distinct terms in the general propagation equation. Following that, each of the individual impairments is further studied in a more elaborate fashion in subsections 2.4.2.1 to 2.4.2.4.

Provided that the optical signal launched into the optical fiber has a wavelength λ satisfying the following single mode condition [74]

$$\lambda > \frac{2\pi}{2.405} a n_1 \sqrt{2\Delta} \quad (2.12)$$

where a is the core radius of the fiber, n_1 is the refractive index of the core, and Δ is the relative refractive index difference at the core-cladding interface. For standard single mode fibers used in modern lightwave systems operating in the 1.3-1.6 μm wavelengths bands, the core radius is set at $\sim 4 \mu\text{m}$ such that the fiber operates in single mode for $\lambda > 1.2 \mu\text{m}$ given that $n_1 = 1.45$ and $\Delta = 3 \times 10^{-3}$ satisfying the above condition in Eq. (2.12). Under such condition, the signal excites only the fundamental HE_{11} mode of the fiber whose spatial distribution (in the xy transverse

plane that is perpendicular to the z -direction of propagation) does not change during propagation, i.e. it is not function of z .

It is well-known that a single mode fiber supports two orthogonally polarized modes that, if the fiber possesses perfect cylindrical symmetry, will be degenerate and propagate with the exact same propagation constant at a given frequency [61]. To represent the propagation of the two orthogonal polarization modes, we employ the Jones formalism (similar to section 2.3) and write the Jones vector of the real-valued bandpass electric field \mathbf{E} whose center angular frequency is ω_0 as

$$\mathbf{E}(x, y, z, t) = \text{Re} \left\{ \begin{bmatrix} A^X(z, t) \\ A^Y(z, t) \end{bmatrix} F(x, y) e^{[j\beta_{av}(\omega_0)z - j\omega_0 t]} \right\} \quad (2.13)$$

where x, y, z are the spatial coordinates, t is the time variable, $F(x, y)$ is the spatial distribution of the fundamental HE_{11} mode which is independent of z , $A^X(z, t)$ and $A^Y(z, t)$ are the complex baseband envelopes of the X and Y polarization modes, $\beta_{av}(\omega_0)$ is the average propagation constant of the X and Y polarization modes at the optical carrier frequency. As will be highlighted in more detail later in this section, the assumption of perfect cylindrical symmetry for the fiber is broken in reality due to imperfect fiber manufacturing which produces slightly elliptical core. This is called fiber birefringence which results in breaking the degeneracy between the two polarization modes and hence, the two modes will have slightly different propagation constants $\beta^X(\omega)$ and $\beta^Y(\omega)$ at any given frequency with an average value of $\beta_{av}(\omega) = \frac{1}{2}[\beta^X(\omega) + \beta^Y(\omega)]$ and a difference $\Delta\beta(\omega) = \beta^X(\omega) - \beta^Y(\omega)$.

For future purposes in this section, we expand both $\beta_{av}(\omega)$ and $\Delta\beta(\omega)$ around the optical carrier frequency ω_0 using Taylor expansion as follows

$$\beta_{av}(\omega) \approx \beta_0 + \beta_1(\omega - \omega_0) + \frac{\beta_2}{2}(\omega - \omega_0)^2 + \frac{\beta_3}{6}(\omega - \omega_0)^3 \quad (2.14)$$

$$\Delta\beta(\omega) \approx \Delta\beta_0 + \Delta\beta_1(\omega - \omega_0) \quad (2.15)$$

where $\beta_n = \left. \frac{d^n \beta_{av}(\omega)}{d\omega^n} \right|_{\omega=\omega_0}$ is the n^{th} frequency derivative of the average propagation constant

evaluated at ω_0 . Physically speaking, $\beta_0 = \beta_{av}(\omega_0)$ is the value of the average propagation

constant at ω_0 , whereas $\beta_1 = \left. \frac{d\beta_{av}(\omega)}{d\omega} \right|_{\omega=\omega_0} = v_g^{-1}(\omega_0)$ is the average group delay per unit length

(or equivalently the inverse of the group velocity) at ω_0 . Also, $\beta_2 = \left. \frac{d^2 \beta_{av}(\omega)}{d\omega^2} \right|_{\omega=\omega_0}$ is called the

group velocity dispersion (GVD) parameter and represents the frequency derivative of the average group delay, i.e. it represents how fast the group delay changes with frequency. If β_2 is

larger, the transmitted signal will get severely distorted due to pulse broadening as will be further illustrated in subsection 2.4.2.2. Back to Eq. (2.15), $\Delta\beta_0 = \Delta\beta(\omega_0)$ which is the difference

between the propagation constants of the X and Y polarizations at ω_0 resulting in a differential

phase between the two propagating polarization modes. Next, $\Delta\beta_1 = \left. \frac{d\Delta\beta(\omega)}{d\omega} \right|_{\omega=\omega_0} = \beta_1^X - \beta_1^Y$ is

called the differential group delay (DGD) and it represents the group delay difference between the X and Y polarizations due to the slight difference in group velocities stemming from fiber birefringence.

Since $F(x, y)$ does not depend on z , the only quantity that varies with z is the Jones vector of the baseband complex field envelope $\mathbf{A}(z, t) = [A^X(z, t) \ A^Y(z, t)]^T$ whose evolution with z is the main concern in this section. The general equation that describes the evolution of $\mathbf{A}(z, t)$ along the fiber is called the Manakov equation [61], which is derived from the vector form of the nonlinear Shrodinger equation (NLSE) while assuming that random birefringence fluctuations occur at short length scales and its impact on the nonlinear term can be averaged. The details of such derivation is beyond the scope of the thesis and can be found in [75]. Below, we give the final form of the Manakov equation which is actually a vector form of two coupled partial differential equations governing the propagation of $A^X(z, t)$ and $A^Y(z, t)$

$$\frac{\partial \mathbf{A}}{\partial z} + \beta_1 \frac{\partial \mathbf{A}}{\partial t} + \frac{\Delta \beta_1}{2} \mathbf{M}_1 \frac{\partial \mathbf{A}}{\partial t} + \frac{j\beta_2}{2} \frac{\partial^2 \mathbf{A}}{\partial t^2} - \frac{\beta_3}{6} \frac{\partial^3 \mathbf{A}}{\partial t^3} = -\frac{\alpha}{2} \mathbf{A} + j \frac{\Delta \beta_0}{2} \mathbf{M}_1 \mathbf{A} + \frac{8}{9} j\gamma (\mathbf{A}^H \mathbf{A}) \mathbf{A} \quad (2.16)$$

where \mathbf{M}_1 is a 2×2 matrix defined as $\mathbf{M}_1 = \mathbf{R}^{-1} \sigma_1 \mathbf{R}$ where $\mathbf{R} = \begin{bmatrix} \cos \psi & \sin \psi \\ -\sin \psi & \cos \psi \end{bmatrix}$ is a random rotation matrix that varies with z to model the impact of varying birefringence axes along the fiber, i.e. ψ is randomly varying with z , and $\sigma_1 = \begin{bmatrix} 1 & 0 \\ 0 & -1 \end{bmatrix}$ is the first Pauli spin matrix [61].

At the first glance at Eq. (2.16), it becomes apparent that all terms contain linear operators applied to \mathbf{A} except for the last term $\frac{8}{9} j\gamma (\mathbf{A}^H \mathbf{A}) \mathbf{A}$ which is nonlinear. Also, the last term is the term that couples the two imbedded propagation equations of $A^X(z, t)$ and $A^Y(z, t)$ due to the inner vector product $\mathbf{A}^H \mathbf{A}$ which evaluates the total power on both polarizations, i.e. $\mathbf{A}^H \mathbf{A} = |A^X(z, t)|^2 + |A^Y(z, t)|^2$.

If we enumerate the terms in Eq. (2.16) from 1 to 8 starting at $\frac{\partial \mathbf{A}}{\partial z}$ on the left hand side until $\frac{8}{9} j\gamma (\mathbf{A}^H \mathbf{A}) \mathbf{A}$ at the right hand side, we list the physical meaning / impairment of all these individual terms in Table 2.1. We finally simplify Eq. (2.16) somewhat by noting that the second term $\beta_1 \frac{\partial \mathbf{A}}{\partial t}$ corresponds to a constant group delay experienced by the optical signal as it propagates through the fiber. Since this delay is not an impairment that impacts the signal quality in any way, it is easier to work in a reference time frame moving with the signal and hence this term will be omitted from this point on in the discussion. In the upcoming subsections, we explain in a more extensive fashion each of the underlying impairments tied with all terms listed in Table 2.1.

Table 2.1. Explanation of impairments related to various terms of Manakov equation.

Term	Expression	Physical meaning / impairment
1	$\frac{\partial \mathbf{A}}{\partial z}$	Evolution of the complex envelope \mathbf{A} with propagation
2	$\beta_1 \frac{\partial \mathbf{A}}{\partial t}$	Constant propagation delay inversely proportional to the group delay ($1/\beta_1$)

3	$\frac{\Delta\beta_1}{2} \mathbf{M}_1 \frac{\partial \mathbf{A}}{\partial t}$	Differential group delay between the X and Y polarizations leading to PMD
4	$\frac{j\beta_2}{2} \frac{\partial^2 \mathbf{A}}{\partial t^2}$	Group velocity dispersion (GVD)
5	$-\frac{\beta_3}{6} \frac{\partial^3 \mathbf{A}}{\partial t^3}$	Third-order dispersion leading to change in GVD with frequency or wavelength (typically called dispersion slope)
6	$-\frac{\alpha}{2} \mathbf{A}$	Fiber loss or attenuation
7	$j \frac{\Delta\beta_0}{2} \mathbf{M}_1 \mathbf{A}$	Differential phase shift between the X and Y polarizations leading to unitary polarization rotation
8	$\frac{8}{9} j\gamma (\mathbf{A}^H \mathbf{A}) \mathbf{A}$	Fiber Kerr nonlinearity

2.4.2.1 Fiber loss or attenuation

The simplest impairment to understand in Eq. (2.16) is fiber loss. The easiest way to understand fiber losses is to perform the following change of variables and introduce

$$\mathbf{A}(z, t) = \mathbf{B}(z, t) e^{-\alpha z/2} \quad (2.17)$$

By plugging Eq. (2.17) into Eq. (2.16), we obtain

$$\frac{\partial \mathbf{B}}{\partial z} + \frac{\Delta\beta_1}{2} \mathbf{M}_1 \frac{\partial \mathbf{B}}{\partial t} + \frac{j\beta_2}{2} \frac{\partial^2 \mathbf{B}}{\partial t^2} - \frac{\beta_3}{6} \frac{\partial^3 \mathbf{B}}{\partial t^3} = j \frac{\Delta\beta_0}{2} \mathbf{M}_1 \mathbf{B} + \frac{8}{9} j\gamma e^{-\alpha z} (\mathbf{B}^H \mathbf{B}) \mathbf{B} \quad (2.18)$$

The new variable $\mathbf{B}(z, t)$ introduced is basically the complex field envelope without the impact of fiber loss which was separated in the decaying exponential $e^{-\alpha z/2}$. We notice that the new Eq. (2.18) has the exact same form as the Manakov equation given by Eq. (2.16) except for the nonlinear term which becomes $\frac{8}{9} j\gamma e^{-\alpha z} (\mathbf{B}^H \mathbf{B}) \mathbf{B}$ which is intuitively understood by noticing that the power profile decays exponentially as $e^{-\alpha z}$ which will in turn reduce the nonlinear effects whose strength at any given point on the fiber z is proportional to the total power at this point.

Besides that, the important outcome of Eq. (2.17) is that the power decays exponentially as $e^{-\alpha z}$ along the fiber. Historically, silica fiber was preferred over copper and other types of transmission media for metro and long-haul distances because of the low propagation loss. The majority of modern lightwave systems employ standard single mode fiber having loss coefficient of ~ 0.2 dB/km in the C band (1550 nm operating window) and ~ 0.3 dB/km in the O band

(1310 nm operating window) [61]. Typically, fiber loss is compensated by periodically amplifying the optical signal by means of optical amplifiers. This lumped amplification mechanism is the most widespread in field deployments where Erbium doped fiber amplifiers (EDFAs) are used after every fiber span (typically every ~ 80 km). Alternatively, distributed amplification by means of Raman amplifiers can be used to improve the performance over lumped amplification due to the better noise figure (NF) however Raman amplifiers are rarely used in practice due to the high power pump lasers required [68].

2.4.2.2 Group velocity dispersion (GVD) or chromatic dispersion (CD)

Looking back at Eq. (2.18), if we neglect the nonlinear term, the PMD term and the differential phase delay term, and keep only the dispersion related terms, we arrive at

$$\frac{\partial \mathbf{B}}{\partial z} + \frac{j\beta_2}{2} \frac{\partial^2 \mathbf{B}}{\partial t^2} - \frac{\beta_3}{6} \frac{\partial^3 \mathbf{B}}{\partial t^3} = 0 \quad (2.19)$$

By employing the Fourier transformation of $\mathbf{B}(z, t)$ given by

$$\tilde{\mathbf{B}} = \int_{-\infty}^{\infty} \mathbf{B}(z, t) e^{j\omega t} dt \quad (2.20)$$

and applying this FT on (2.19) followed by solving the differential equation, we obtain a closed form solution of the evolution of $\tilde{\mathbf{B}}$, i.e. the propagation of the spectrum of the field envelop,

$$\tilde{\mathbf{B}}(z, \omega) = \tilde{\mathbf{B}}(0, \omega) e^{j\left(\frac{\beta_2 \omega^2}{2} + \frac{\beta_3 \omega^3}{6}\right)z} \quad (2.21)$$

which means that the effect of GVD after distance L is modeled in the frequency domain by the following transfer function

$$H_{GVD}(L, \omega) = e^{j\left(\frac{\beta_2 \omega^2}{2} + \frac{\beta_3 \omega^3}{6}\right)L} \quad (2.22)$$

The transfer function in Eq. (2.22) has an all-pass magnitude response and a phase response comprising a quadratic and a cubic terms. The quadratic term in the phase response, i.e. $\beta_2 \omega^2 / 2$, contains the GVD parameter β_2 which represents how fast the group delay ($\beta_1 L$) changes with frequency to the first order. The physical origin behind GVD is twofold; first is material

dispersion due to the wavelength dependence of the refractive index of fiber core (hence GVD is equivalently termed chromatic dispersion (CD)) and second is waveguide dispersion that arises due to the fact that the propagation constant is dependent on fiber parameters such as the core radius and the refractive index difference between the fiber core and cladding materials. Next, the cubic term containing β_3 dictates how fast the group delay ($\beta_1 L$) changes with frequency to the second order, or equivalently how fast the GVD changes with frequency to the first order.

Typically, GVD is quantified in lightwave transmission systems using the dispersion parameter D in ps/(nm.km) which is related to β_2 as follows

$$D = \frac{d}{d\lambda} \left(\frac{1}{v_g} \right) = -\frac{2\pi c}{\lambda^2} \beta_2 \quad (2.23)$$

Also, the dispersion slope S in ps/(nm².km) is customarily used to quantify how the dispersion parameter D changes with wavelength as $D = S(\lambda - \lambda_{ZD})$ where λ_{ZD} is the zero dispersion wavelength. S is related to β_3 as follows

$$S = \frac{dD}{d\lambda} = \left(\frac{2\pi c}{\lambda^2} \right)^2 \beta_3 \quad (2.24)$$

For standard single mode fibers used in modern lightwave systems, D is ~ 17 ps/(nm.km) near 1550 nm and it becomes zero near λ_{ZD} which is ~ 1310 nm. To demonstrate visually how GVD impacts a propagating pulse, we plot in Fig. 2.6(a) the amplitude versus time (normalized with respect to symbol duration) showing an input raised cosine (RC) pulse with a roll-off factor of 1 assuming a symbol rate of 28 Gbaud (hence a symbol duration of 35.7 ps) superimposed with the real and imaginary parts of the pulse after 80 km of propagation over standard SMF with $D = 17$ ps/(nm.km). We notice that the energy of the pulse spreads quickly to interfere with nearly ~ 20 symbols after only 80 km (typically a single span). In Fig. 2.6(b), we show how the pulse spreads more (~ 70 symbols) after 80 km of propagation when the symbol rate is doubled to 56 Gbaud. Finally, we show in Fig. 2.6(c) the pulse spreading in case of a longer transmission distance of 1600 km. In this case, the pulse spreads to occupy a time span equivalent to more than 200 symbols. Clearly, GVD will cause an intolerable amount of ISI if a real pattern containing multiple neighboring pulses is transmitted. Fortunately, GVD can be compensated at the Rx DSP by means of a linear filter that inverts the frequency response given by Eq. (2.22)

since coherent detection maps the received field linearly into the digital domain. This is the main advantage that coherent detection has over legacy DD receivers after which GVD could not be compensated in the digital domain and bulky, lossy and expensive in-line optical dispersion compensation had to be used instead. On the other hand, most modern coherent transmission systems employ a dispersion unmanaged transmission strategy where no optical dispersion compensation is used and the entire GVD of the link is compensated by the Rx DSP.

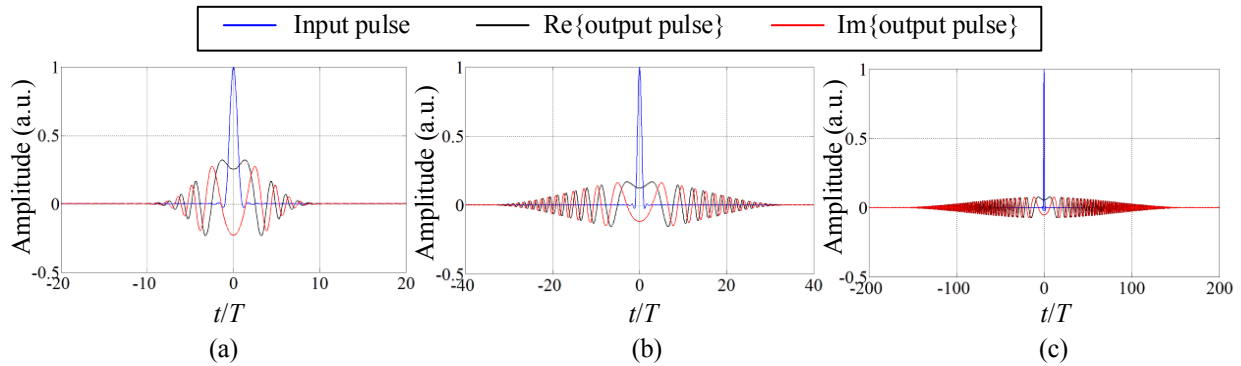


Fig. 2.6. Effect of GVD on an input RC pulse with a roll-off factor of 1 in the following cases: (a) $L = 80$ km and $R = 28$ Gbaud, (b) $L = 80$ km and $R = 56$ Gbaud, and (c) $L = 1600$ km and $R = 28$ Gbaud

2.4.2.3 Random polarization rotation and polarization mode dispersion (PMD)

If we neglect all other impairment in Eq. (2.18) and keep only the two terms containing $\Delta\beta_0$ and $\Delta\beta_1$ which originate from the difference in propagation constants of the X and Y polarizations due to fiber birefringence, we arrive at

$$\frac{\partial \mathbf{B}}{\partial z} + \frac{\Delta\beta_1}{2} \mathbf{M}_1 \frac{\partial \mathbf{B}}{\partial t} = j \frac{\Delta\beta_0}{2} \mathbf{M}_1 \mathbf{B} \quad (2.25)$$

where \mathbf{M}_1 is a 2×2 matrix defined as $\mathbf{M}_1 = \mathbf{R}^{-1} \sigma_1 \mathbf{R}$ where $\mathbf{R} = \begin{bmatrix} \cos \psi & \sin \psi \\ -\sin \psi & \cos \psi \end{bmatrix}$ is a random rotation matrix that varies with z to model the impact of varying birefringence axes along the fiber, i.e. ψ is randomly varying with z , and $\sigma_1 = \begin{bmatrix} 1 & 0 \\ 0 & -1 \end{bmatrix}$ is the first Pauli spin matrix [61].

Similar to the method used to obtain the frequency response of the GVD in Eq. (2.22), if we take the FT of Eq. (2.25) and perform the integration over z , we obtain

$$\tilde{\mathbf{M}}_1 = \begin{bmatrix} j\left[\frac{\Delta\beta_0}{2} + \frac{\Delta\beta_1\omega}{2}\right]L & \\ \\ 0 & e^{-j\left[\frac{\Delta\nu_0}{2} + \frac{\Delta\nu_1\omega}{2}\right]L} \end{bmatrix} \quad (2.26)$$

where we neglect the z dependence of \mathbf{M}_1 . This is directly understood for fibers with constant birefringence where the principle axes (slow and fast axes) as well as the magnitude of birefringence, i.e. DGD, do not change over distance. In this case, the rotation matrix \mathbf{R} in Eq. (2.26) projects the input field onto the principle axes of the fiber and then the following 2×2 matrix applies the differential phase terms (including both the constant differential phase and the frequency dependent one) on both polarizations before rotating back to the input coordinates of the input signal by the matrix \mathbf{R}^{-1} . One example of fibers with constant birefringence is polarization maintaining fibers (PMFs) in which the degeneracy between both polarizations is intentionally broken and its fast and slow axes are known in advance [61].

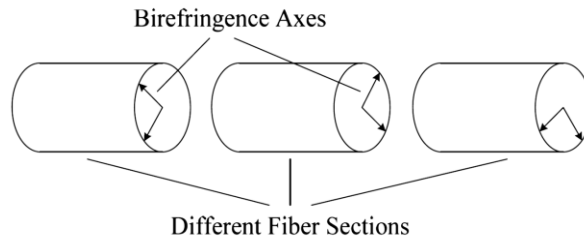


Fig. 2.7. An illustrative drawing showing the breaking of a fiber with random birefringence fluctuations into multiple sections each with constant birefringence magnitude and orientation.

For fibers with random birefringence, the magnitude and orientation of birefringence vary along the fiber on a length scale of ~ 10 m which is called the correlation length [61]. The standard approach to model such situation is to break the fiber into small sections (shorter than the correlation length) as shown in Fig. 2.7 within which the birefringence is assumed constant in both magnitude and orientation. It turns out that such a fiber still has two principle states of polarization (PSPs) that, when a pulse is launched onto one of them, its corresponding output SOP does not change with frequency to the first order meaning the pulse remains undistorted [76]. The two input PSPs are orthogonal as well as their corresponding output SOPs and are in general elliptical. These PSPs are analogous to slow and fast axes in case of a fiber with constant birefringence except for one fundamental difference, the PSPs in case of fibers

with random birefringence are not related to any local intentionally induced birefringence but rather depend on the collective effects of the birefringence over the entire fiber length. Hence, these PSPs will change with fiber length and will even vary from one fiber to another having the same length because of the random nature of these birefringence fluctuations within an ensemble of fibers having the same length.

Hence, Eq. (2.26) still applies for fibers with random birefringence except for the fact that the rotation matrix \mathbf{R} now rotates the input signal to the PSPs of the fiber. Finally, we should note that Eq. (2.26) should be re-written for a coherent transmission system where another rotation matrix \mathbf{R}_2 is left multiplied to take into account the misalignment in the polarization axes at the Tx and Rx sides, i.e. the reference axes of the PBC at the Tx side and those of the PBS at the CRx front-end are not necessarily aligned. This leads to

$$\tilde{\mathbf{R}} = \begin{bmatrix} j \left[\frac{\Delta\beta_0}{2} + \frac{\Delta\beta_1\omega}{2} \right] L & 0 \\ 0 & e^{-j \left[\frac{\Delta\nu_0}{2} + \frac{\Delta\nu_1\omega}{2} \right] L} \end{bmatrix} \quad (2.27)$$

It is clear from Eq.(2.27) that polarization related impairments can be modeled as one unitary 2×2 rotation matrix that is in general frequency dependent because of DGD. However, for modern fibers with very low DGD values [61], $\Delta\beta_1$ can be neglected and the overall 2×2 rotation matrix representing the fiber becomes frequency independent. Whether the overall unitary rotation is frequency dependent or not, the fiber is similar to a 2×2 multiple-input and multiple-output (MIMO) system. At the Rx DSP, a 2×2 MIMO butterfly linear filter will be needed to invert Eq. (2.27). If DGD is negligible and the rotation matrix is independent of frequency, the 2×2 butterfly filter does not need to have a temporal length, i.e. it can have only 4 single taps. This will be revisited in section 3.3 in which we assume the fiber is modeled as a frequency independent 2×2 rotation matrix and use a novel TS based scheme to estimate it.

2.4.2.4 Kerr nonlinear effects

If we look back at Eq. (2.18) and neglect all terms leaving only the GVD and nonlinear terms, we have

$$\frac{\partial \mathbf{B}}{\partial z} + \frac{j\beta_2}{2} \frac{\partial^2 \mathbf{B}}{\partial t^2} = \frac{8}{9} j\gamma e^{-\alpha z} (\mathbf{B}^H \mathbf{B}) \mathbf{B} \quad (2.28)$$

which can be written in the following compact form

$$\frac{\partial \mathbf{B}}{\partial z} = (\hat{D} + \hat{N}) \mathbf{B} \quad (2.29)$$

where $\hat{D} = -\frac{j\beta_2}{2} \frac{\partial^2}{\partial t^2}$ and $\hat{N} = \frac{8}{9} j\gamma e^{-\alpha z} (\mathbf{B}^H \mathbf{B})$ are the linear and nonlinear operators representing the GVD and Kerr nonlinearity, respectively. The physical origin behind Kerr nonlinearity is the dependence of the refractive index on the light intensity which is why \hat{N} includes $e^{-\alpha z} (\mathbf{B}^H \mathbf{B})$ which is the total power on both polarizations at any given position on the fiber z . Furthermore, \hat{N} includes the nonlinear coefficient γ that is defined as

$$\gamma = \frac{2\pi n_2}{\lambda_0 A_{eff}} \quad (2.30)$$

where n_2 is a constant in the order of $2.6 \times 10^{-20} \text{ m}^2/\text{W}$, λ_0 denotes the carrier wavelength and A_{eff} is the effective area of the fiber core (typically $\sim 80 \mu\text{m}^2$ for standard SMF).

If we examine carefully Eq. (2.29), we notice that the dispersion and nonlinear operators, i.e. \hat{D} and \hat{N} , cannot be commuted or applied separately. This can be understood by the fact that \hat{N} includes $e^{-\alpha z} (\mathbf{B}^H(z, t) \mathbf{B}(z, t))$ which depends on the total power profile of the field along the fiber. If the dispersion was negligible, applying \hat{N} to the input signal $\mathbf{B}(0, t)$ would merely be done by applying a phase shift $\int_0^L \hat{N}(z) dz$ to obtain $\mathbf{B}(L, t)$ after a propagation length L .

However, since dispersion is non negligible, \hat{D} distorts the envelope of the signal $\mathbf{B}^H(z, t) \mathbf{B}(z, t)$ along the fiber hence interacting with \hat{N} and thus, the operators \hat{D} and \hat{N} cannot be separated in general. This is the reason why Eq. (2.29) does not have a closed form analytical solution.

The standard way to solve Eq. (2.29) across the literature is to use a numerical method called the split step Fourier method (SSFM) [14]. The principle of the SSFM is to assume that over a small distance h the dispersive and nonlinear effects can be applied independently as follows

$$\mathbf{B}(z+h, t) \approx e^{(h\hat{D})} e^{(h\hat{N}(z))} \mathbf{B}(z, t) \quad (2.31)$$

In Eq. (2.31), we obtain $\mathbf{B}(z+h, t)$ from the field $\mathbf{B}(z, t)$ by applying first the nonlinear operator, which is performed as a phase shift in the time domain, followed by the dispersion operator, which is applied in the frequency domain as discussed in subsection 2.4.2.2. Hence each step in the SSFM method requires a fast Fourier transform (FFT) and an inverse FFT (IFFT) to apply both \hat{D} and \hat{N} . Although using the SSFM in either the forward propagation direction (to simulate fiber propagation) or in the backward propagation direction (to recover the transmitted signal from a received signal distorted by both dispersive and nonlinear effects) produce very accurate results, the number of operations required to perform an FFT/IFFT pair per SSFM step is usually prohibitive for real life implementations [77].

Another method to approximate the solution of Eq. (2.29), that is receiving a lot of interest in the literature, is based on the first order perturbation theory [67, 78, 79]. The main idea of this method is to write down the solution of Eq. (2.29) in two parts; the first is the linear solution obtained by neglecting the nonlinear operator and the second is an additive noise (small perturbation) added to the signal due to the nonlinearity [80]. The advantage of the perturbation based nonlinearity compensation over backward propagation SSFM is that it requires much less computational complexity and is applied at the Tx DSP side at the symbol rate [78].

Finally, it is noteworthy that the discussion about fiber nonlinearity in this section was confined to only intra-channel nonlinear effects that is the nonlinear phase shift impacting the signal depends on the power of the signal itself. However, in case of WDM transmission, inter-channel nonlinear effects is also a major source of impairment that leads to a nonlinear phase shift induced by not only the channel's own power, but also by the power of the other channels. Fortunately, the dispersion induced walk-off limits the efficiency of inter-channel nonlinear effects due to the field averaging. Therefore, only close WDM neighbors cause a detrimental impact nonlinear phase shift.

2.4.3 Classic DSP stacks for a coherent transceiver

After explaining in the two previous subsections the major impairments suffered by the signal in a coherent transmission system, we turn the discussion in this section to the functions carried out by the Tx and Rx DSPs; two main components of the system that was depicted in Fig. 2.2.

In Fig. 2.8(a)-Fig. 2.8(b), we show the typical DSP stacks at the Tx and Rx sides of a coherent transceiver, respectively, listing the most widely employed DSP functions. We confine the

discussion in this section to single carrier (SC) systems, which is the scheme adopted for the entire thesis, rather than multiple carrier schemes that rely on dividing the signal into multiple low bit rate streams on orthogonal subcarriers, generated either in the electrical or optical domains, such as coherent optical orthogonal frequency division multiplexing (CO-OFDM) [81].

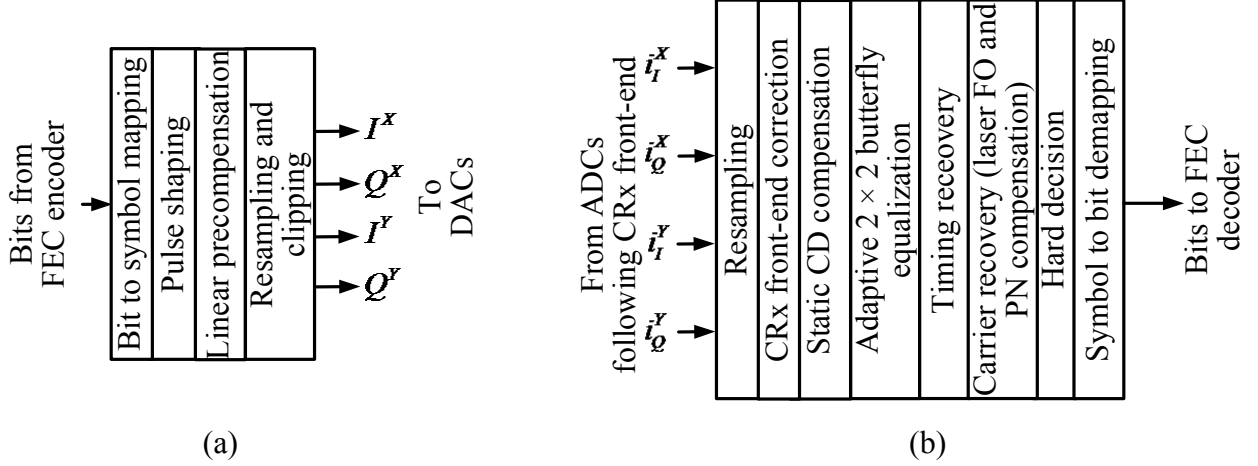
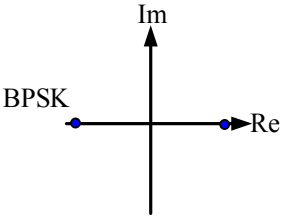
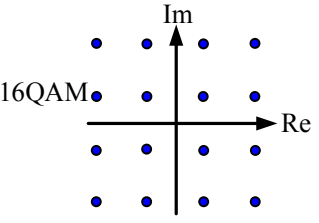
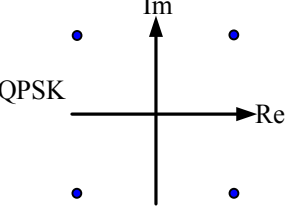
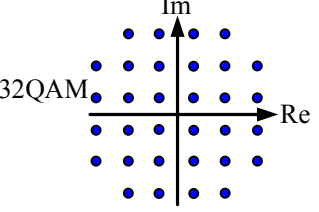
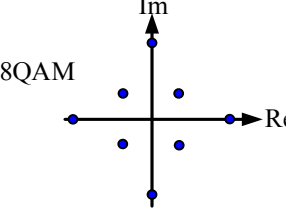
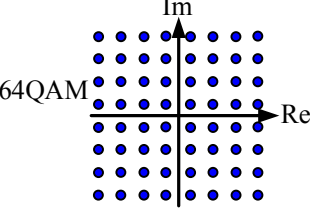


Fig. 2.8. Conventional DSP stacks at: (a) Tx side and (b) Rx side, showing various functions that may or may not be implemented.

2.4.3.1 Tx side DSP

At the Tx side, the bit stream fed from the forward error correction (FEC) encoder is mapped into symbols on both X and Y polarizations. If we denote by $\mathbf{s}_k = [s_k^X \ s_k^Y]^T$ the 2×1 Jones vector including the transmitted symbols on both polarizations where the mapping into the symbols $s_k^X = s_{r,k}^X + js_{i,k}^X$ and $s_k^Y = s_{r,k}^Y + js_{i,k}^Y$ is done depending on the modulation format used. For example, if M -ary quadrature amplitude modulation (e.g. 4QAM (QPSK) and 16QAM) is employed, the real and imaginary parts of the symbols will be drawn from the following set of possible values $s_{r,k}^X, s_{i,k}^X, s_{r,k}^Y, s_{i,k}^Y \in \{-\sqrt{M}+1, \dots, -1, 1, \dots, \sqrt{M}-1\}$. If the transmitted bit rate is denoted by R_b , the transmitted symbol rate (or baud rate) will be $R = R_b / (p \log_2(M))$ where $p = 2$ or 1 depending on whether PDM is used or not, and $\log_2(M)$ is the number of bits encoded into each symbol per polarization for M -QAM format which defines the resulting spectral efficiency (SE) of the transmission system. Table 2.2 shows the constellation diagrams of some M -QAM formats together with the number of bits per symbol achieved.

Table 2.2. M -QAM Constellations and number of achievable bits per symbol.

Constellation	bit/symbol	Constellation	bit/symbol
 <p>BPSK</p>	1	 <p>16QAM</p>	4
 <p>QPSK</p>	2	 <p>32QAM</p>	5
 <p>8QAM</p>	3	 <p>64QAM</p>	6

Following the bit to symbol mapping, the symbols are filtered by a pulse shape $h_{ps}(t)$ and the resulting time domain signal that represents the complex baseband envelope of the transmitted signal can now be written as

$$\mathbf{S}(t) = \sum_{k=-\infty}^{\infty} \mathbf{s}_k h_{ps}(t - kT) \quad (2.32)$$

As previously mentioned in section 2.3, Tx DSP is not mandatory and simple analog circuits can be used to generate the desired QAM formats with pulse shapes such as NRZ and return-to-zero (RZ). However, using Tx DSP allows to implement $h_{ps}(t)$ in Eq. (2.32) as a digital finite impulse response (FIR) filter and use bandlimited pulses instead of NRZ and RZ pulses which improves the spectral efficiency as will be highlighted shortly. A typical pulse shape that is widely used is the so-called raised cosine (RC) pulse which satisfies the Nyquist zero ISI criterion [66]. The impulse response of the RC pulse and its frequency response are

$$h_{ps,RC}(t) = \frac{\sin(\pi t/T)}{\pi t/T} \frac{\cos(\pi \alpha t/T)}{1 - (2\alpha t/T)^2} \quad (2.33)$$

$$H_{ps,RC}(f) = \begin{cases} T, & |f| \leq \frac{1-\alpha}{2T} \\ \frac{T}{2} \left[1 + \cos \left(\frac{\pi T}{\alpha} \left[|f| - \frac{1-\alpha}{2T} \right] \right) \right], & \frac{1-\alpha}{2T} < |f| \leq \frac{1+\alpha}{2T} \\ 0, & |f| > \frac{1+\alpha}{2T} \end{cases} \quad (2.34)$$

where α is the roll-off factor parameter of the pulse which defines the excess bandwidth, i.e. the bandwidth occupied beyond the Nyquist bandwidth of $1/2T$. Fig. 2.9 shows the RC impulse response and frequency response for various roll-off factors where we can see that the least bandwidth is occupied when $\alpha = 0$. However, for any α the RC pulse in Fig. 2.9(a) clearly satisfies the zero ISI criterion, i.e. $h_{ps,RC}(nT) = 0$ when n is an integer not equal to 0. Typically, the frequency response of the RC pulse in Eq. (2.34) is split equally between the Tx and Rx meaning that a square root raised cosine (RRC) pulse having $H_{ps,RRC}(f) = \sqrt{H_{ps,RC}(f)}$ is used at the Tx to pulse shape the data and an identical RRC filter is used as a matched filter at the Rx to maximize the signal to noise ratio (assuming an AWGN channel) while still maintaining a zero ISI overall pulse shape.

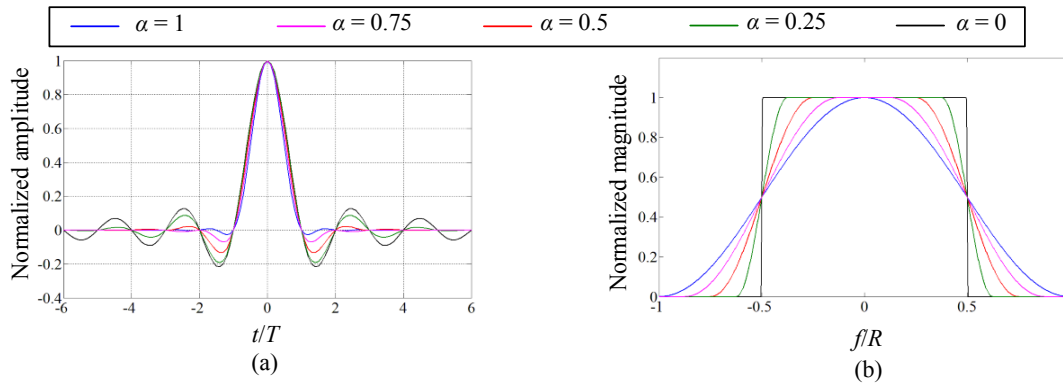


Fig. 2.9. Raised cosine pulse with different roll-off factors in: (a) time domain, (b) frequency domain.

After pulse shaping, the transmitted samples may be further filtered to precompensate some of the linear system impairments such as CD and limited frequency response of the DAC and the DP-IQ modulator. Finally, the transmitted samples may need to be resampled before being applied to the DACs in case the sampling rate of the DAC differs from the sampling rate of the data out of the Tx DSP. Also, clipping is sometimes needed to reduce the peak to average power

ratio (PAPR) of the signal and avoid degrading the performance due to limited bit resolution of the DACs.

2.4.3.2 Rx side DSP

Fig. 2.8(b) shows the sequence of DSP function performed by the Rx DSP which are detailed below:

- Resampling may be needed if the ADC sampling rate does not match the sampling rate adopted for Rx DSP. Typically, an oversampling factor of 2, i.e. two samples per symbol, is used in the Rx DSP.
- Correction of any CRx front-end imperfections. As discussed in detail in subsection 2.4.1, these imperfections include timing skew and quadrature error. The Rx DSP utilizes deskew algorithm to correct the timing skew by means of an interpolator after estimating the skew. Also, an orthogonalization algorithm such as the Gram-Shmidt algorithm is used to correct the quadrature error (see Eqs. (2.7) and (2.8)).
- CD or GVD compensation by means of a static, i.e. non adaptive, equalizer that simply inverts Eq. (2.22). Usually the CD equalizer is implemented in the frequency domain using either overlap-add or overlap-save methods [82] since implementing such an equalizer in the time domain will require a huge prohibitive computational complexity as the number of taps needed can be quite large especially for long propagation lengths (see Fig. 2.6(c)). In practical systems, the length of the fiber link might be unknown to the receiver, leading to the necessity of CD estimation for which various estimation algorithms have been proposed [83].
- Adaptive 2×2 MIMO butterfly equalizer to undo the random polarization rotation and mitigate PMD. This equalizer simply uses one of the well-known tap adaptation algorithms (e.g. the constant modulus algorithm (CMA) for QPSK [9] or the least-mean-squares (LMS) algorithm for any QAM format [84]) to update the taps of the equalizer to invert Eq. (2.27).
- Timing recovery to correct any sampling frequency and phase offset as discussed in subsection 2.4.1. A typical timing recovery algorithm consists of a timing error detector or a timing estimator in conjunction with an interpolator that uses the estimated timing error to interpolate the asynchronous samples and obtain synchronous samples. The

Gardner algorithm [85] is the most widely known timing error detector which works well for a BPSK or a QPSK signal. Also, the digital square and filter timing estimator in [86] and its less computationally intensive version in [87] are two algorithms that can operate for any M -QAM format.

- Carrier recovery including both laser PN and FO compensation which were both presented in detail in subsection 2.4.1. Various algorithms exist in the literature to compensate laser PN such as the Viterbi and Viterbi algorithm [88], first order digital phase locked loop (DPLL) [89], binary phase search (BPS) [73, 90], etc. For FO correction, the periodogram method [91] is one widely acclaimed method and the second order DPLL [92] is another method that can simultaneously compensate PN and FO.
- Hard decision or slicing the soft values of the symbols which depends on the modulation format. Finally, the decided symbols can be fed back to the some of the DSP blocks that operate in a decision directed (DD) mode. For example, the LMS adaptation algorithm [84] in the 2×2 MIMO equalizer as well as the DPLL utilize the current decision to update itself for the future symbols. The final step is to de-map the symbols into bits which are finally fed to the FEC decoder. It is finally noteworthy that the separation of the bit to symbol mapping and de-mapping blocks from the FEC encoder/decoder blocks is because we assume hard decision FEC is used however, if soft decision FEC is utilized to improve the coding gain and boost the system performance, these blocks merge.

2.5 System impairments for a short reach IM/DD link

In the previous section, we gave a detailed review of the impairments that distort the signal in a coherent transmission system originating from both the transceiver hardware imperfections and the fiber channel itself. In this section, we re-visit these impairments with the objective of highlighting the impairments that are relevant and detrimental for a short reach IM/DD link with a reach < 20 km, which is the topic of the last part of the thesis (Chapter 5).

We begin with the transceiver related impairments discussed in subsection 2.4.1. A typical IM/DD link will not suffer from timing skew and quadrature error because the receiver front-end is merely a photodiode and has no 90° hybrid. In addition, since the photodiode is completely insensitive to phase, the IM/DD system will not be impacted by laser phase noise. Although laser

phase noise can be converted into intensity noise by CD, which can be detrimental for long haul IM/DD links with large residual CD [93], the residual CD after short distances will not be large enough and the resulting laser phase noise to intensity noise conversion will be negligible.

Next, sampling phase and frequency offsets are still two important impairments for a short reach IM/DD link. Hence, we showed in Fig. 2.1 that a clock and data recovery (CDR) unit is a mandatory component for a DD receiver since it extracts the timing information from the received data which allows then to sample at the proper sampling phase and with the proper sampling period leading to the optimum decision instants.

Then, we move on to discuss the fiber channel impairments that were explained in subsection 2.4.2. Intuitively, fiber loss will still be detrimental for such IM/DD short reach links especially that these links need to ultimately operate without the need for any optical amplifiers. Regarding dispersion as discussed in subsection 2.4.2.2, the significance of the impact of GVD on the signal depends on three parameters: a) the operating wavelength, b) the distance and c) the symbol rate. Since the IEEE 802.3ba standard for 100G Ethernet defines 1310 nm as the operating wavelength of short reach optics [27], GVD becomes negligible for such systems operating near the zero dispersion wavelength. Regarding random polarization rotation, the photodiode at the Rx is completely insensitive to the received state of polarization and hence random polarization rotation is not an issue for a classic DD receiver. Finally, PMD and Kerr nonlinearity are negligible at these length scales for short reach optics.

Based on the previous discussion, we can simply conclude that a classic IM/DD short reach link typically does not need to employ any DSP to mitigate impairments, which is the case for commercial classic IM/DD transceivers. However, the novel IM/DD system that will be presented in this thesis in Chapter 5, which involves using two polarizations of a laser source, will be impacted by additional impairments, e.g. polarization rotation, and hence DSP will be mandatory.

Chapter 3

DSP Algorithms for Flexible Coherent Optical Transceivers

3.1 Overview

In this chapter, we propose three DSP algorithms for flexible coherent transceivers to mitigate various impairments. The performance of the algorithms is tested via both simulations and experiments and compared to standard algorithms in the literature. All three DSP schemes presented are transparent to modulation format, and hence suited for flexible transceivers in future agile networks as highlighted in section 1.2.1.

The remainder of the chapter is organized as follows. In section 3.2, we present pilot-aided (PA-) DSP for joint carrier recovery, fiber nonlinearity mitigation and polarization demultiplexing. Next, section 3.3 is reserved for our novel training symbol based channel estimation (TS-EST) which achieves ultrafast and low overhead polarization demultiplexing and tracking. Afterwards in section 3.4, we present a non-data-aided feedforward timing recovery for mitigating sampling frequency offset for any QAM order. Finally, we conclude the chapter in section 3.5

3.2 Pilot aided (PA-) DSP for joint carrier recovery, fiber nonlinearity mitigation and polarization demultiplexing

3.2.1 Introduction

As clearly highlighted in section 1.2, in order to fulfill the need for higher capacity in optical transport networks, increasing the constellation size is a viable solution that enables mapping more bits per each symbol and hence increases the spectral efficiency. However, these highly dense M -QAM constellations have, in addition to the high optical signal to noise ratio (OSNR) requirement, an inherent stringent laser linewidth requirement because of the small distances between adjacent constellation points and hence, high performance linewidth tolerant carrier recovery (CR) algorithms are needed. As shown in [73], feedback-based CR schemes cannot fulfill these linewidth requirements because of inevitable feedback delays when the algorithm is

implemented in a parallelized and pipelined architecture for real-time operation. Thus, the authors in [73] proposed a feed-forward carrier recovery (FFCR) scheme based on a blind phase search (BPS) algorithm for M -QAM constellations. BPS provides one of the best known linewidth tolerances in the literature at the expense of high computation complexity. Moreover, the algorithm's complexity increases as the QAM order (M) increases. Other FFCR algorithms with less complexity also exist in the literature (e.g., Viterbi and Viterbi phase estimation (VVPE) for QPSK [88] and QPSK partitioning for 16-QAM [94]), but with reduced linewidth tolerance as well as being not transparent to modulation format.

In addition to carrier recovery, which implies both laser PN and FO compensation, polarization demultiplexing (or recovery) is a mandatory task of the Rx-DSP (see Fig. 2.8(b) for the typical Rx-DSP stack) using a 2×2 MIMO butterfly equalizer to undo the random polarization rotation that occurred along the fiber. Several algorithms have been proposed in the literature for adapting the taps of the butterfly equalizer. Data-aided schemes are widely used because of their transparency to modulation format order, where training symbols (TS) are sent and used at the receiver for tap adaptation using the least mean squares (LMS) algorithm [11]. Such TS based schemes reduce throughput due to the relatively large TS overhead required and also suffer from synchronization problems needed to locate the TS frame within the received data. In addition, data-aided schemes also suffer from stability problems at steady-state tap adaptation because of the linewidth tolerance of the CR scheme used, which affects the decisions used for calculating the error signal used for tap update at steady state, i.e. while operating in decision directed (DD) mode. Alternatively, blind techniques, e.g. the constant modulus algorithm (CMA) [9], that exploit special data properties are sometimes used but they suffer, among other problems, from being not transparent to the QAM order.

In the current section 3.2, we propose the use of pilot-aided (PA) transmission to compensate jointly laser phase noise (PN) and laser frequency offset (FO) in addition to polarization demultiplexing in a coherent transmission system. In addition to the aforementioned set of impairments, we show that the proposed PA-DSP also partially mitigates fiber Kerr nonlinearity and boosts the maximum system reach. The proposed PA-DSP is fully transparent to modulation format and has the advantage that it de-couples CR from polarization demultiplexing, i.e. PN and FO can be compensated before polarization demultiplexing and hence there is no stability issues at steady-state DD operation. In addition, the novel PA-DSP does not require synchronization to

locate the pilot and eliminates the cycle slip problem when the pilot is used for CR. The pilot tone is electrically inserted in a middle spectral gap based on our work in [36-38] by single-sideband (SSB) subcarrier modulation of the in-phase (I) and quadrature (Q) signals at the transmitter side DSP. We presented the results of our study in [36] of the tolerance of the proposed PA-DSP to laser linewidth for various QAM orders in comparison to other CR schemes in the literature. In addition, we showed our proof-of-concept experimental results obtained in [39] that used the PA-DSP for joint compensation of laser PN, FO and for polarization demultiplexing by estimating the 2×2 Jones channel matrix. The excellent PN and FO tolerance was experimentally demonstrated for a 28 Gbaud PDM-QPSK signal.

3.2.2 Principles of PA-DSP for joint carrier recovery, fiber nonlinearity mitigation and polarization demultiplexing

The main idea behind the proposed PA scheme is to insert a pilot tone at the middle of the transmitted spectrum of the single-carrier (SC) PDM signal. After transmission along the classic coherent transmission system previously depicted in Fig. 2.2, the pilot tone will be impacted by the following set of impairments: a) laser phase noise (PN) from transmitter (Tx) and receiver (Rx) lasers, b) frequency offset (FO) between the two lasers, c) fiber Kerr nonlinearity (NL) induced phase shift, and d) random polarization rotation along the fiber channel. At the receiver, the pilot tone is filtered out of the received spectrum to separate it from the data. Given the knowledge of the originally transmitted pilot, the joint impact of the aforementioned impairments on the pilot tone is evaluated and used to mitigate the impact of these impairments on the corresponding data symbols.

In the next subsections, we show the detailed DSP tasks at both Tx and Rx DSPs which are needed to enable PA-DSP. Next we show how the received pilot can be used for joint carrier recovery, fiber nonlinearity mitigation and polarization demultiplexing. Prior to the detailed analysis, it should be noted that the proposed PA scheme does not require any extra hardware added to the standard architecture of the coherent transmission system shown in Fig. 2.2; however, different / additional DSP tasks will be carried out by Tx and Rx DSPs as will be depicted in details hereafter.

3.2.2.1 Transmitter and receiver DSP stacks for pilot-tone insertion / extraction

We start by considering only one field polarization and show in Fig. 3.1 a block diagram representation of the tasks performed by the transmitter (Tx) and receiver (Rx) DSPs in the proposed PA scheme for a single polarization (SP) signal. Initially, we employ the simpler single polarization case to explain the pilot insertion / extraction tasks and to show how the phase information of the received pilot can be used for carrier recovery, i.e. laser PN mitigation and FO compensation, in addition to partially mitigating fiber Kerr nonlinearity. Later in the following subsection, we extend the mathematical formulation of the PA scheme to consider a polarization-division-multiplexed (PDM) signal having two transmitted orthogonal polarizations and show how the pilot insertion and extraction tasks explained here can be easily extended to the case of a PDM signal. Furthermore, we also show how the received pilot information can be additionally used to perform polarization demultiplexing, i.e. to estimate and invert the random polarization rotation that occurs along the fiber channel.

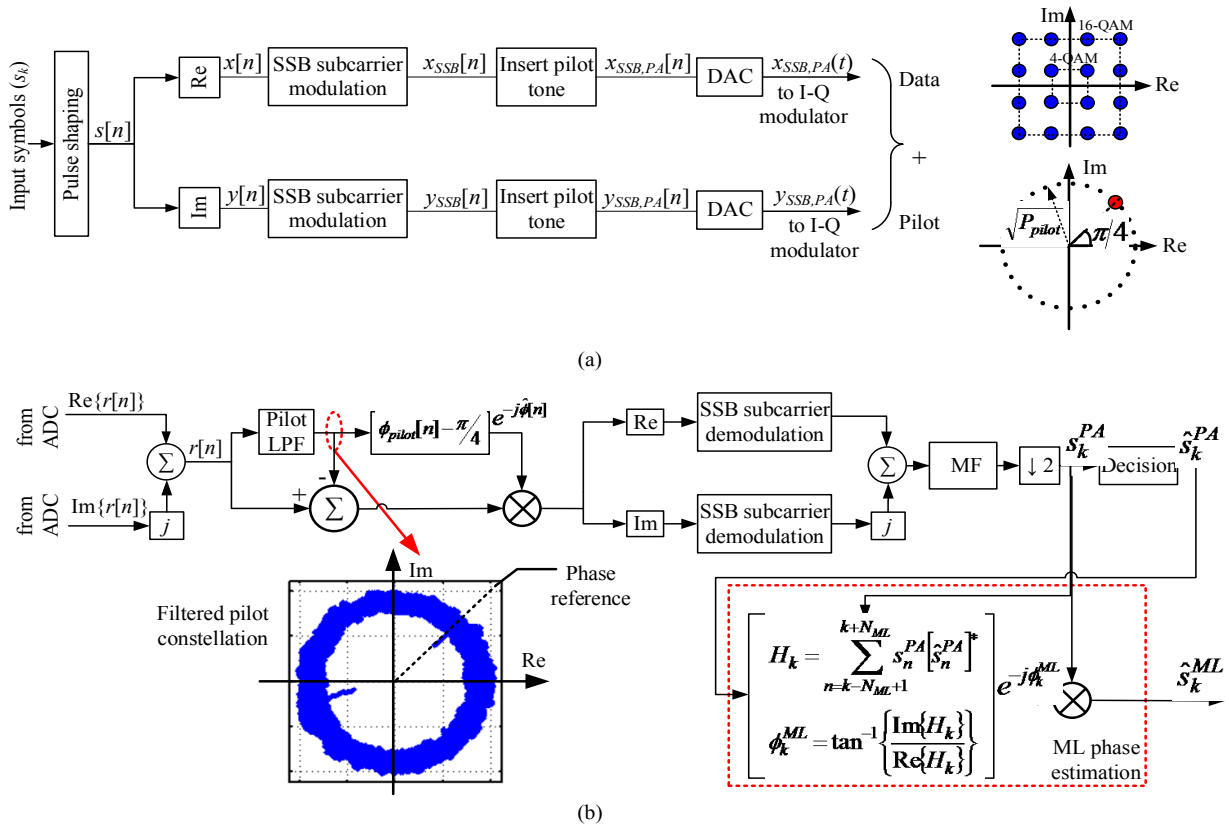


Fig. 3.1. DSP tasks for PA scheme for single-polarization (SP) signal at: a) Tx side aided with illustrative example constellations for data and pilot, and b) Rx side assuming back-to-back configuration and focusing on PA carrier recovery with an without ML phase estimation.

In Fig. 3.1, a discrete-time index n is adopted while we use a continuous-time variable t throughout the mathematical formulation hereafter. This is justified by the fact that discrete-time processing at the Nyquist rate is equivalent to continuous-time processing [82]. In the following discussion, we refer to the conventional coherent transceiver that uses standard DSP stacks, which were depicted in Fig. 2.8, as the “non-PA” system to distinguish it from the proposed system that relies on PA-DSP.

In Fig. 3.1(a), the Tx-DSP first applies a bandlimited pulse shaping filter with impulse response $h_{ps}(t)$ to the complex transmitted symbols s_k , where $s_k = x_k + jy_k$ and $x_k, y_k \in \{-\sqrt{M} + 1, \dots, -1, 1, \dots, \sqrt{M} - 1\}$ are the real and imaginary parts for square M -QAM constellations. Without loss of generality, an RRC pulse shaping filter with a roll-off factor α (see subsection 2.4.3.1 for more details on the RRC pulse) is assumed in all our simulations and experimental work; however, the proposed PA-DSP scheme should work equally well for other pulse shapes. An example is shown in Fig. 3.2(a) where we show the spectrum of the real part of a 28 Gbaud 16QAM signal after being filtered with a root raised cosine (RRC) filter with a roll-off factor of 1. Then, in order to enable the pilot insertion, a spectral gap is opened at the middle of the spectrum of the SC signal. First, both quadrature signals (which are real-valued) $x(t) = \sum_{k=-\infty}^{\infty} x_k h_{ps}(t - kT)$ and $y(t) = \sum_{k=-\infty}^{\infty} y_k h_{ps}(t - kT)$, where T is the symbol duration and $h_{ps}(t)$ is the pulse shaping filter's impulse response, are separately single sideband (SSB) modulated on an electrical subcarrier having a frequency f_{sc} as follows:

$$x_{SSB}(t) = \text{Re}\{x^+(t)e^{j2\pi f_{sc}t}\}, \quad y_{SSB}(t) = \text{Re}\{y^+(t)e^{j2\pi f_{sc}t}\} \quad (3.1)$$

where the complex analytic signals $x^+(t)$ and $y^+(t)$ having one sided spectra are obtained by

$$x^+(t) = x(t) + j\hat{x}(t), \quad y^+(t) = y(t) + j\hat{y}(t) \quad (3.2)$$

In Eq. (3.2), $\hat{x}(t)$ and $\hat{y}(t)$ are obtained by passing $x(t)$ and $y(t)$, respectively, through a Hilbert transformer with an impulse response $h_{Hilbert}(t) = \frac{1}{\pi t}$, $-\infty < t < \infty$, and a frequency response $H_{Hilbert}(f)$ given by

$$H_{\text{Hilbert}}(f) = \begin{cases} -j, & f > 0 \\ 0, & f = 0 \\ j, & f < 0 \end{cases} \quad (3.3)$$

Then, the spectra of the two SSB modulated signals $x_{SSB}(t)$ and $y_{SSB}(t)$ can be easily written in terms of the baseband spectra $X(f)$ and $Y(f)$, and the unit-step function $u(f)$ as

$$X_{SSB}(f) = X(f - f_{sc})u(f - f_{sc}) + X(f + f_{sc})u(-f - f_{sc}) \quad (3.4)$$

$$Y_{SSB}(f) = Y(f - f_{sc})u(f - f_{sc}) + Y(f + f_{sc})u(-f - f_{sc}) \quad (3.5)$$

Following SSB subcarrier modulation, the Tx-DSP adds the pilot tone at zero frequency to both $x_{SSB}(t)$ and $y_{SSB}(t)$, which fits in the gap at the middle of their spectra. The two signals after pilot insertion, denoted by $x_{SSB,PA}(t)$ and $y_{SSB,PA}(t)$, are written in terms of $x_{SSB}(t)$ and $y_{SSB}(t)$ as

$$x_{SSB,PA}(t) = x_{SSB}(t) + \sqrt{P_{\text{pilot}}/2}, \quad y_{SSB,PA}(t) = y_{SSB}(t) + \sqrt{P_{\text{pilot}}/2} \quad (3.6)$$

where P_{pilot} is the pilot tone power which is a design parameter set according to the required pilot-to-signal power ratio (PSR) defined as $PSR(\text{dB}) = 10\log_{10}(P_{\text{pilot}} / P_{\text{signal}})$. For illustration, Fig. 3.2(b) shows the spectrum of the 28 Gbaud 16-QAM signal whose spectrum was shown in Fig. 3.2(a), after SSB subcarrier modulation with $f_{sc} = 500$ MHz (1.7% bandwidth overhead) and an inserted pilot with $PSR = -14$ dB. Also, a zoomed version of the spectral region around the pilot is shown in Fig. 3.2(c). Then, $x_{SSB,PA}(t)$ and $y_{SSB,PA}(t)$ drive the two arms of the I-Q modulator where the complex transmitted signal $s_{tr}(t) = x_{SSB,PA}(t) + jy_{SSB,PA}(t)$ can be written as

$$s_{tr}(t) = [x_{SSB}(t) + jy_{SSB}(t)] + \sqrt{P_{\text{pilot}}/2} \times (1 + j) \quad (3.7)$$

Hence, $s_{tr}(t)$ comprises data symbols and a frequency multiplexed pilot, that is continuously transmitted, as can be seen by the illustrative constellations in Fig. 3.1(a). It should be noted that the inserted pilot is assumed at DC, i.e. zero frequency, initially in our mathematical formulation however, it can be inserted away from DC as long as it still lies within the spectral gap created by the SSB modulation to enable separating the pilot from the data at the Rx. This will be the case later on in our experiment where the pilot tone had to be shifted away from DC to avoid getting blocked by the AC coupled transmitter.

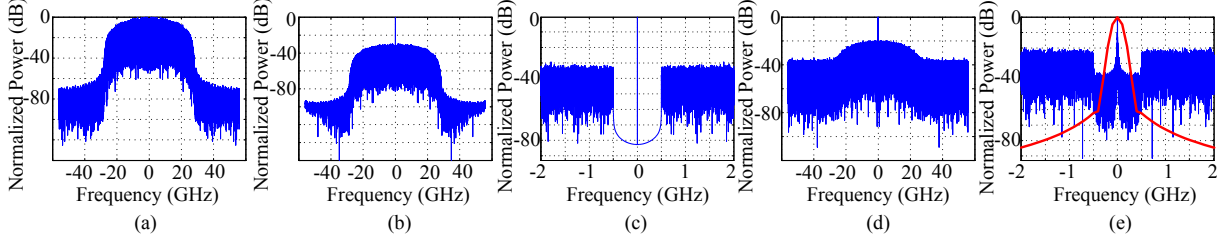


Fig. 3.2. Spectrum of in-phase portion of a 28 Gbaud SP 16-QAM signal a) At Tx before SSB, b) At Tx after SSB and pilot insertion with $f_{sc} = 500$ MHz and $PSR = -14$ dB, c) Zoomed version of pilot spectral gap at Tx, d) At Rx with laser PN ($\Delta f = 2$ MHz) and noise loaded (OSNR = 16.7 dB), e) Zoomed version of pilot spectral gap at Rx together with a Gaussian LPF with $B_{LPF} = 80$ MHz.

3.2.2.2 PA-DSP for carrier recovery and fiber nonlinearity mitigation

We initially assume a back-to-back configuration where there is neither chromatic dispersion nor fiber nonlinearity. Referring back to Eq. (3.7), one can see that both data and pilot terms in $s_{tr}(t)$ will acquire the same combined instantaneous phase due to: a) PN from Tx and Rx lasers, b) FO between both lasers. Hence, the received signal $r(t)$ after coherent reception in this back-to-back setting can be written as

$$\begin{aligned} r(t) &= \left(s_{tr}(t) e^{j\phi_{Tx}(t)} + N(t) \right) \times e^{j(\phi_{Rx}(t) + 2\pi\Delta Ft)} \\ &= \left[x_{SSB}(t) + jy_{SSB}(t) \right] \times e^{j[\phi_{Tx}(t) + \phi_{Rx}(t) + 2\pi\Delta Ft]} + \sqrt{P_{pilot}/2} \times (1 + j) \times e^{j[\phi_{Tx}(t) + \phi_{Rx}(t) + 2\pi\Delta Ft]} + N'(t) \end{aligned} \quad (3.8)$$

where $\phi_{Tx}(t)$, $\phi_{Rx}(t)$ are the instantaneous phase noises of the Tx and Rx lasers, respectively, and ΔF is the frequency offset between both lasers. At the Rx, the pilot tone is filtered using a Gaussian low-pass filter (LPF), which was found to produce best results among other LPF shapes, having a 3 dB bandwidth B_{LPF} . As long as f_{sc} and B_{LPF} are carefully chosen, there will be no spectral overlap between the pilot tone and the SSB subcarrier modulated data. Hence, the output of the LPF will be equal to the pilot term in Eq. (3.16) in addition to some filtered noise. Then, the instantaneous phase of the filtered pilot $\phi_{pilot}(t)$ can be written as follows

$$\begin{aligned} \phi_{pilot}(t) &= \phi_{Tx}(t) + \phi_{Rx}(t) + 2\pi\Delta Ft + \pi/4 + \phi_n(t) \\ &= \phi(t) + \pi/4 + \phi_n(t) \end{aligned} \quad (3.9)$$

where $\phi_n(t)$ is due to the filtered noise and $\phi(t)$ is the combined instantaneous phase due to the lumped effect of Tx and Rx laser PN and FO. For illustration, the spectrum of the received pilot-aided 28 Gbaud 16-QAM signal after being impaired by laser PN with combined linewidth of $\Delta f = 2$ MHz and a frequency offset $\Delta F = 0$ is shown in Fig. 3.2(d), where noise loading is

performed to set the OSNR level to 16.7 dB (corresponding to 1 dB penalty at $\text{BER} = 3.8 \times 10^{-3}$). To further clarify how PN broadens the spectrum of the pilot, a zoomed version of the pilot spectral gap is shown in Fig. 3.2(e), where we also show the response of a Gaussian LPF with $B_{LPF} = 80$ MHz. In Fig. 3.1(b), we show the corresponding constellation of the filtered pilot tone impaired by laser PN. The Rx can now easily use $\phi_{\text{pilot}}(t) - \pi/4$ as an estimate $\phi(t)$ for the combined phase due to laser PN and FO $\phi(t)$, where the estimation error depends on $\phi_n(t)$. Then, the Rx de-rotates the data term in Eq. (3.16) using $\phi(t)$ as shown in Fig. 3.1(b). The following tasks are fairly straightforward and involve SSB subcarrier demodulation of the de-rotated data signal, matched filtering, picking one sample per symbol to produce the received symbols after pilot phase compensation s_k^{PA} , and symbol decision to produce an estimate \hat{s}_k depending on which M -QAM constellation employed. Up to this point, PA-FFCR has been completed and \hat{s}_k are the final symbol decisions.

Next, as shown in Fig. 3.1(b), a further possible performance improvement can be achieved by employing maximum likelihood (ML) phase estimation to provide more accurate symbol decisions by refining the phase estimate obtained from the noisy received pilot. In order to refine the estimate $\phi(t)$ obtained from the pilot phase, the decided symbol \hat{s}_k after pilot phase compensation along with the symbol s_k^{PA} before the decision are fed into a second stage where ML phase estimation is employed. The ML phase estimate is calculated as shown by the block enclosed by dotted lines in Fig. 3.1(b). It evaluates an estimate ϕ_k^{ML} for the residual phase uncompensated by the pilot phase as follows:

$$H_k = \sum_{n=k-N_{ML}+1}^{k+N_{ML}} s_n^{PA} [\hat{s}_n^{PA}]^* \quad (3.10)$$

$$\phi_k^{ML} = \tan^{-1} \left\{ \frac{\text{Im}\{H_k\}}{\text{Re}\{H_k\}} \right\} \quad (3.11)$$

Theoretical details of ML phase estimation can be found in [66, 95]. As seen in Eqs. (3.10) and (3.11), the ML estimate is calculated based on how much the original symbols after pilot phase compensation s_k^{PA} are rotated from their designated constellation points \hat{s}_k found after decision where averaging over $2N_{ML}$ symbols is done to reduce the estimation noise. The ML

phase estimation works well because most of the PN has been already compensated by the pilot phase, and hence the decided symbols \hat{s} are most likely correct. As will be supported by the results in upcoming subsections, the ML stage significantly improves the linewidth tolerance over the case where only pilot phase is used for carrier recovery.

Finally, we revisit the assumption made at the beginning of subsection 3.2.2.2 that we study a back-to-back configuration. Looking back carefully at Eq. (3.8), we notice that in case of fiber transmission, the transmitted signal portion $s_{tr}(t)e^{j\phi_{Tx}(t)}$ in Eq. (3.8), which contains the transmitted data together with the inserted pilot impaired by the Tx laser phase noise, passes first through the fiber channel which impacts the signal by both chromatic dispersion (CD) and Kerr nonlinearity (NL) accurately modeled by the operators D and N using the SSFM as discussed earlier in Chapter 2 (see Eq. (2.29)). At the end of the fiber and after coherent reception, the effect of Rx laser phase noise and FO should then impact the output signal in a way similar to the term $e^{j(\phi_{Rx}(t)+2\pi\Delta Ft)}$ in Eq. (3.8). However in the transmission case, it is noticeable that it is not mathematically valid to lump the impact of Tx and Rx PN and FO in one single complex rotation as in the second line of Eq. (3.8) because this will require commuting this term $e^{j(\phi_{Rx}(t)+2\pi\Delta Ft)}$ with the D and N operators modeling the fiber transmission.

As discussed earlier in Chapter 2, the D and N operators can only be applied separately over short distances of fiber where the interplay between CD and NL is negligible. However, if we still neglect this interplay and separate the D and N operators over the whole fiber channel, we can re-write Eq. (3.8) as

$$\begin{aligned} r(t) &\approx \left[s_{tr}(t)e^{j\phi_{Tx}(t)} \otimes h_{CD}(t) \right] \times e^{j\phi_{NL}(t)} \times e^{j(\phi_{Rx}(t)+2\pi\Delta Ft)} \\ &\approx s_{tr}(t)e^{j[\phi_{Tx}(t)+\phi_{NL}(t)+\phi_{Rx}(t)+2\pi\Delta Ft]} \otimes h_{CD}(t) \end{aligned} \quad (3.12)$$

where $\phi_{NL}(t)$ is the NL induced phase shift that is proportional to the instantaneous envelope of the propagating signal and is introduced by applying the operator N . In the second line of Eq. (3.12), we made a simplifying approximation by commuting the complex rotation operators with the convolution operator representing the fiber CD which enabled us to lump all the phase shifts induced by laser PN, FO and fiber NL in a single complex rotation. It is also easily noticeable that the received pilot phase will contain contributions from all these individual

complex rotations and can be estimated and applied back to de-rotate the data symbols similar to the way described in the back-to-back case. This explains how PA-DSP is effective for carrier recovery as well as NL partial mitigation.

Looking back at the simplifying assumptions that led to Eq. (3.12), we notice two limitations:

- Separating the D and N operators and neglecting the interplay between CD and NL will limit the effectiveness of using the pilot phase to mitigate fiber nonlinearity. This will finally make the proposed PA-DSP only partially mitigates fiber nonlinearity. This can be further inferred from the fact that the data and pilot get impacted by the D and N operators differently. Since the pilot tone has a very narrow bandwidth (almost negligible relative to the data spectrum), it does not get spread by CD and only acquires the NL induced phase shift whereas, the data symbols gets spread by CD and at the same time, the NL induced phase shift affects the signal based on the instantaneous intensity of the propagating field at a certain position along the fiber. This mismatch in the impact of fiber transmission on both the pilot and data is the main underlying reason why PA-DSP only partially mitigates fiber nonlinearity.
- Commuting the complex rotation $e^{j\phi_{NL}(t)} \times e^{j(\phi_{Rx}(t)+2\pi\Delta Ft)}$ with the convolution with the CD impulse response $\otimes h_{CD}(t)$ will also limit the effectiveness of the PA laser PN mitigation. In fact, this approximation allows the Rx to compensate CD and perform carrier recovery separately. This is a common approximation in all conventional carrier recovery schemes in standard Rx DSP, i.e. non-PA DSP, where the laser PN of both Tx and Rx lasers are assumed lumped in one complex rotation which implies commuting the convolution operator with the CD impulse response and the complex rotation. This leads to an impairment known as equalization enhanced phase noise (EEPN) that was thoroughly studied in [96, 97]. The effect of EEPN on reducing the laser PN tolerance of our PA carrier recovery was not major because the baud rates tested in both simulation and experiment (~ 28 Gbaud), propagation distances considered (< 5000 km), and laser linewidths studied (few MHz) were insufficient to make the impact of EEPN more prominent.

3.2.2.3 PA-DSP for polarization demultiplexing

In this subsection, we extend the mathematical formulation of the PA scheme to consider a polarization-division-multiplexed (PDM) signal and show how the received pilot can be used to perform polarization demultiplexing, i.e. to estimate and invert the random polarization rotation that occurs along the fiber channel, besides carrier recovery and nonlinearity mitigation.

For a PDM signal, all DSP tasks that were shown in Fig. 3.1 for a SP signal will still be performed for both field polarizations except for pilot insertion which will be only inserted on one polarization and not the other. SSB subcarrier modulation will still be performed for both polarizations on the data symbols. Looking back at Eq. (3.7) and focusing only on the pilot term in the PDM case, we can write the transmitted Jones vector of the pilot tone $\mathbf{P}_{Tx}(t)$ as

$$\mathbf{P}_{Tx}(t) = \begin{bmatrix} e^{j2\pi f_{pilot}t} \\ 0 \end{bmatrix} \quad (3.13)$$

where f_{pilot} is the frequency at which the pilot tone is inserted. In all previous discussions, the pilot was assumed at DC, i.e. $f_{pilot} = 0$, however we now generalize the mathematical formulation to the case where the transmitted pilot is shifted away from DC but still lies within the spectral gap. As will be stated later, this was mandatory during our experiment to avoid getting the pilot blocked by the AC coupled transmitter. Now, the received Jones vector of the pilot can be written as

$$\mathbf{P}_{Rx}(t) = e^{j[\phi_{Tx}(t) + \phi_{Tx}(t) + 2\pi\Delta Ft]} \mathbf{J} \mathbf{P}_{Tx}(t) = e^{j[\phi_{Tx}(t) + \phi_{Tx}(t) + 2\pi\Delta Ft + 2\pi f_{pilot}t]} \begin{bmatrix} a \\ -b^* \end{bmatrix} \quad (3.14)$$

where \mathbf{J} is a unitary 2×2 Jones matrix that models the random polarization rotation along the fiber and is given by (see subsection 2.4.2.3 for more detail)

$$\mathbf{J} = \begin{bmatrix} a & b \\ -b^* & a^* \end{bmatrix} \quad (3.15)$$

From Eq. (3.14), the phase of the received pilot can be used as before for carrier recovery even when there is random polarization rotation. In addition, the received pilot on both polarizations can be used to estimate $|a|$, $|b|$ and $\theta = \arg\{a\} + \arg\{b\}$. Then, we left multiply the inverse of a matrix $\mathbf{J}_e = \begin{bmatrix} |a| & |b|e^{j\theta} \\ -|b|e^{-j\theta} & |a| \end{bmatrix}$, where ; separates the two matrix rows, by pilot and data symbols to remove polarization crosstalk and achieve polarization demultiplexing.

3.2.3 Simulation study of PA-DSP

3.2.3.1 PA-DSP for carrier recovery

We divide this subsection into three parts. In the first, we present the parameters used for our simulation that was conducted on MATLAB. We also show how some design parameters (e.g., PSR and B_{LPF}) should be optimized to guarantee the best performance from the proposed PA-FFCR scheme. Secondly, we show the linewidth tolerance results of both PA-FFCR and PA-FFCR with ML compared to other CR schemes. Finally, we investigate how the finite bit resolution of both DACs and ADCs affects the performance.

(a) Simulation parameters and optimization

In our simulations, a fixed baud rate of 28 Gbaud is used for all M -QAM formats which corresponds to a bit rate of $(28 \times p \times \log_2 M)$ Gb/s where $p = 2$ or 1 depending on whether or not PDM is used. Hence, when $\Delta f T$ is needed to be swept, we sweep Δf while maintaining the symbol duration constant. All our BER measurements are based on the simulation of 240,000 symbols. Furthermore, noise loading is used at the Rx to control the OSNR level. As mentioned earlier, two RRC filters with roll-off factors of 1 are used at the Tx and Rx. Each RRC filter is implemented in the time domain as a 32-tap FIR filter with $T/2$ tap spacing. Finally, OSNR penalties for all M -QAM formats are evaluated from the difference between the actual and theoretical required OSNR, obtained as in [73], to achieve a $BER = 3.8 \times 10^{-3}$. All OSNR values are evaluated based on a 0.1 nm reference bandwidth.

For the design parameters of PA-FFCR, we set the subcarrier frequency f_{sc} to 500 MHz in all our simulations, which corresponds to 1.7% bandwidth overhead. f_{sc} is an important parameter that has to be properly set to ensure that PA-FFCR performs well while maintaining a low bandwidth overhead. $f_{sc} = 500$ MHz is a good value since it is large enough so that data and pilot symbols do not spectrally overlap while at the same time, it results in a small bandwidth overhead and ensures that the filtered noise after the Gaussian LPF is not too high to adversely affect the estimate $\hat{\phi}(t)$. The two remaining design parameters, namely PSR and B_{LPF} , are also crucial and should be optimized in order to guarantee an optimum performance. First, PSR determines how much power is allocated for the pilot tone. It should be chosen large enough to ensure that noise does not severely mask the pilot while at the same time, it should be small

enough to maintain a sufficient signal power compared to noise. Second, B_{LPF} needs to be small enough to ensure that the filtered noise does not adversely affect $\hat{\phi}(t)$ while at the same time, it should be large enough to pass the useful pilot phase information. Fig. 3.3(a) illustrates how the values of PSR and B_{LPF} affect the performance of the system: two surfaces of the BER values versus both PSR and B_{LPF} are shown for $\Delta f.T = 3 \times 10^{-5}$ (lower surface) and 1×10^{-4} (upper surface). For the two surfaces, 16-QAM is taken as an example and a 16.7 dB OSNR (corresponding to 1 dB penalty) is used. For the lower surface, optimum values of PSR and B_{LPF} are found to be -17 dB and 50 MHz, respectively, resulting in $BER = 2.1 \times 10^{-3}$. For the top surface, optimum values of PSR and B_{LPF} are -15 dB and 120 MHz, respectively, resulting in a $BER = 3 \times 10^{-3}$. The main observation from Fig. 3.3(a) is that as $\Delta f.T$ increases, the optimum PSR and B_{LPF} also increase. This is justified by the fact that as $\Delta f.T$ increases, the pilot tone will carry more useful information about the increased PN and its spectrum will be broader; hence, larger PSR and B_{LPF} are required. Thus all upcoming results always use optimum PSR and B_{LPF} .

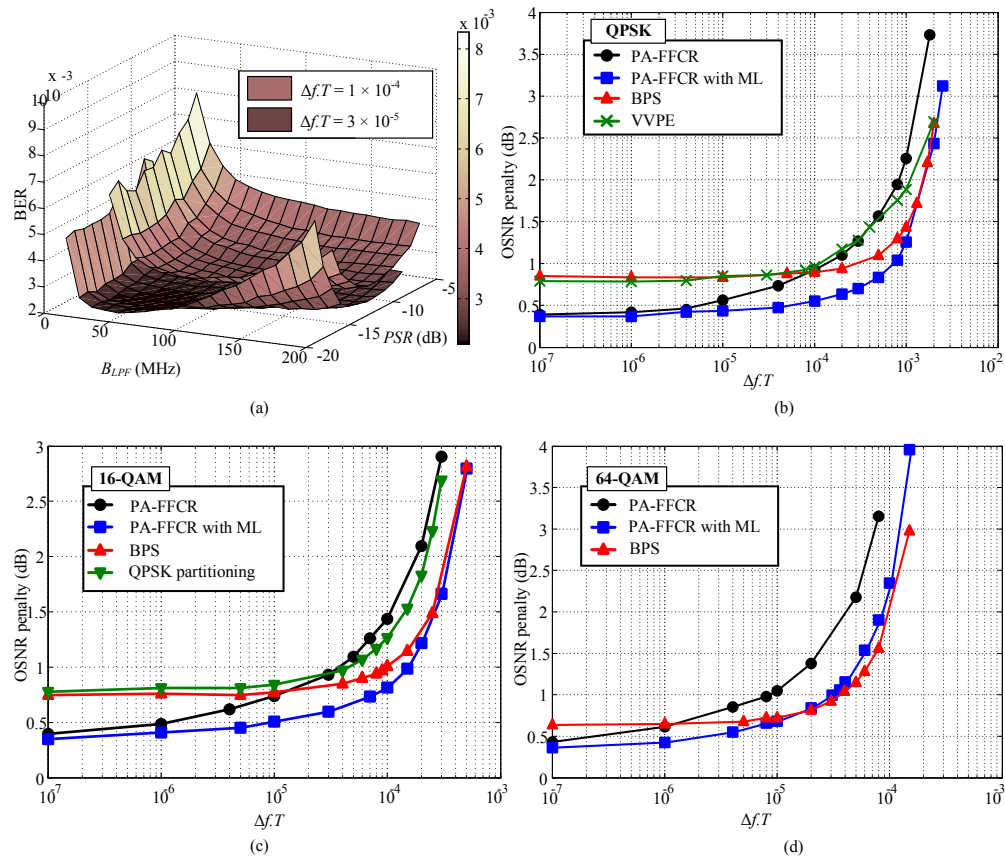


Fig. 3.3. a) BER surface versus the pilot-to-signal power ratio and the bandwidth of the pilot LPF at two different laser linewidths for 16-QAM at OSNR = 16.7 dB, and linewidth tolerance of various CR schemes against laser phase noise for b) QPSK, c) 16-QAM, and d) 64-QAM constellations.

(b) Phase noise tolerance

In this subsection, the performance of both PA-FFCR and PA-FFCR with ML is assessed and compared to other CR schemes in terms of linewidth tolerance for M -QAM constellations. Fig. 3.3(b)-Fig. 3.3(d) show the OSNR penalty as a function of $\Delta f \cdot T$ for QPSK, 16-QAM and 64-QAM respectively. The CR schemes we compare are PA-FFCR, PA-FFCR with ML and BPS [73] for all M -QAM formats, whereas VVPE [88] and QPSK partitioning [94] work only for QPSK and 16-QAM, respectively. As noticed in all three figures, PA-FFCR with or without ML outperforms the other techniques for small values of $\Delta f \cdot T$ since at these PN levels, most of the OSNR penalty in case of BPS, VVPE and QPSK partitioning is imposed by differential encoding used to remove the $\pi/4$ angle ambiguity. On the other hand, there is no need to differentially encode the data in a PA system because there is no angle ambiguity. Also, as $\Delta f \cdot T$ increases, it is clear how much the ML phase estimation improves the linewidth tolerance when added to PA-FFCR. Table 3.1 shows the maximum tolerable $\Delta f \cdot T$, defined as the tolerable $\Delta f \cdot T$ at 1 dB OSNR penalty, for all techniques and corresponding tolerable linewidth values Δf at 28 Gbaud. Clearly, either PA-FFCR, PA-FFCR with ML or BPS provide excellent linewidth tolerance and allow all M -QAM formats up to 64-QAM to be implemented with inexpensive DFB lasers. As also observed from Table 3.1 or the three figures, PA-FFCR with ML always performs better than BPS (or similar in case of 64-QAM) which provides the best known linewidth tolerance in the literature. This excellent performance of PA-FFCR with ML comes with less computation complexity compared to BPS as will be explained in the next section.

Table 3.1. Linewidth tolerance of various CR schemes for different M-QAM formats

CR scheme	QPSK		16-QAM		64-QAM	
	$(\Delta f \cdot T)_{\max}$	Δf_{\max} at 28 Gbaud	$(\Delta f \cdot T)_{\max}$	Δf_{\max} at 28 Gbaud	$(\Delta f \cdot T)_{\max}$	Δf_{\max} at 28 Gbaud
PA-FFCR	1.5×10^{-4}	4.2 MHz	4×10^{-5}	1.12 MHz	1×10^{-5}	280 KHz
PA-FFCR with ML	7.5×10^{-4}	21 MHz	1.8×10^{-4}	5.04 MHz	3.5×10^{-5}	980 KHz
BPS	3×10^{-4}	8.4 MHz	1×10^{-4}	2.8 MHz	3.5×10^{-5}	980 KHz
VVPE	1×10^{-4}	2.8 MHz	-	-	-	-
QPSK partitioning	-	-	4.5×10^{-5}	1.26 MHz	-	-

(c) Effect of finite resolution of DACs and ADCs on PA-FFCR

In this subsection, we study the effect of finite bit resolution of both the DACs used after the Tx-DSP to drive the I-Q modulators and the ADCs used after the Rx coherent front-end on the performance of our proposed scheme. We consider only the PA-FFCR with ML for our results. Fig. 3.4(a) shows the OSNR penalty versus $\Delta f.T$ for the PA-FFCR with ML scheme for all M -QAM formats in two cases: infinite resolution (same as the previous results in Fig. 3.3) and 6-bit DAC resolution. Similarly, Fig. 3.4(b) shows the performance when using a 6-bit ADC compared to the infinite resolution case. As expected, we observe that the OSNR penalty imposed by the finite resolution of DACs or ADCs is negligible for the QPSK case and starts to increase as the QAM order increases. Quantitatively, using a 6-bit DAC or ADC quantizes the analog voltages into 64 levels which leads to tolerable $\Delta f.T$ values of 7.5×10^{-4} for QPSK, 1.5×10^{-4} for 16-QAM and 1.3×10^{-5} for 64-QAM compared to the values in Table 3.1 for the infinite resolution case. However, it should be noted that the increasing penalty due to the finite DAC/ADC resolution as the QAM order increases originates from the inherent resolution requirement to represent the multilevel I and Q signals and not from a limitation of our scheme. This is justified by observing that the additional penalty imposed by using finite DAC/ADC resolution is not dependent on the laser PN, i.e. $\Delta f.T$, and it is even lower as $\Delta f.T$ increases which indicates that it is not caused by the CR scheme.

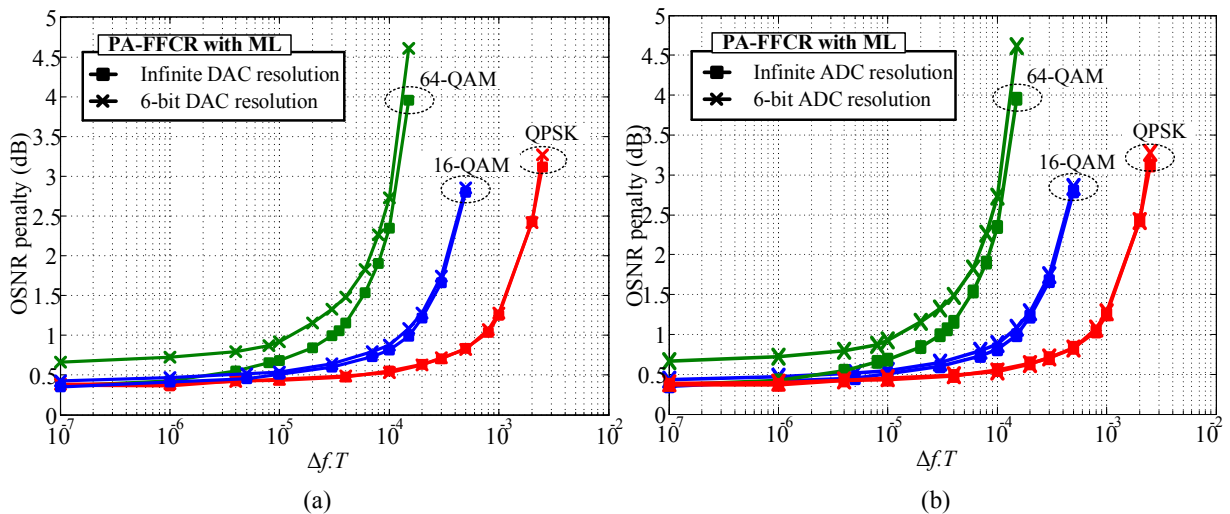


Fig. 3.4. Performance of PA-FFCR with ML for different M-QAM formats with finite bit resolution of (a) DACs, and (b) ADCs.

3.2.3.2 PA-DSP for NL mitigation

The performance improvement achieved by PA NL mitigation is verified using simulations on 28 Gbaud PDM-QPSK and 14 Gbaud PDM 16-QAM systems both delivering a 112 Gb/s. 2^{16} random symbols are generated and used for all BER calculations for both systems. All Tx-DSP tasks shown in Fig. 3.1(a) are carried out at the Nyquist rate in MATLAB. Then, the four I and Q signals on both polarizations are upsampled to 8 samples/symbol and launched into OptiSystem 9.0 to simulate the optical layer of the transmission system which includes electrical-to-optical conversion, propagation through the fiber channel, and coherent optical-to-electrical conversion. It should be noted that 8 samples/symbol are used in OptiSystem to provide enough simulation BW. For the optical layer, the Tx and Rx lasers are assumed to have a linewidth of 100 kHz each. The signal is propagated over a dispersion unmanaged SSMF with an 80 km span length, attenuation $\alpha = 0.2$ dB/km, dispersion $D = 17$ ps/(nm.km), dispersion slope $S = 0.075$ ps/(nm².km), effective area $A = 80$ μm^2 , Kerr NL parameter $n_2 = 26 \times 10^{-21}$ m²/W, and negligible PMD. An Erbium-doped fiber amplifier (EDFA) with a noise figure $NF = 7$ dB is placed after every span. Noise loading at the Rx is carried out to sweep the received OSNR level when needed for the simulation. At the Rx, the four signals out of the coherent front-end are launched back into MATLAB where they are first downsampled to their Nyquist rate and then processed as in Fig. 3.1(b). Finally, a forward error correction (FEC) threshold BER of 3.8×10^{-3} is assumed in all simulations. Both the non-PA and PA systems use CD frequency domain equalization and RRC matched filtering. For the purpose of FFCR in the non-PA system, Viterbi and Viterbi phase estimation (VVPE) [88] and QPSK partitioning [94] are used for PDM-QPSK and PDM 16-QAM systems, respectively. Also, differential encoding is used for the non-PA system to resolve the angle ambiguity. In the PA system, neither differential encoding nor a dedicated FFCR algorithm is used since laser phase noise is compensated by the pilot itself.

Fig. 3.5(a) and Fig. 3.5(b) compare the required OSNR versus launch power of the proposed PA scheme to the non-PA one for both PDM-QPSK and PDM 16-QAM systems, respectively. For the 28 Gbaud PDM-QPSK case in Fig. 3.5(a), a transmission distance of 1600 km is used. Two subcarriers of 250 MHz and 1 GHz corresponding to 0.9% and 3.6% BW overhead, respectively, are simulated for the PA system. For those curves, we assume an infinite DAC resolution. Also, optimum values of PSR and 3 dB BW of the pilot LPF are used. As a reference, theoretical results for a linear AWGN channel are also shown. Examining the curves, the two PA

systems outperform the non-PA system for small launch powers (0.3 dB less required OSNR) because of the penalty imposed by differential encoding for the non-PA system compared to absolute phase encoding for the PA system (no phase ambiguity). For such small launch powers, there is no difference between the two PA systems which suggests that using a smaller f_{sc} is clearly the better choice to reduce BW overhead. For high launch powers above 1 dBm, i.e., the NL regime, the PA system with $f_{sc} = 1$ GHz outperforms both the non-PA system and the PA system with $f_{sc} = 250$ MHz due to improved NL tolerance. Hence, we deduce that a larger pilot spectral gap provides better NL tolerance because fiber NL is a rapidly varying process compared to laser PN, and hence a large spectral gap enables the pilot to acquire the faster variations in NL phase. However, this spectral gap can be increased indefinitely. Quantitatively, the PA system with $f_{sc} = 1$ GHz allows for an increase in the allowable launch power by nearly 1 dB for OSNR levels over 14 dB compared to the non-PA system. Next, Fig. 3.5(b) compares the required OSNR versus launch power curves of the non-PA and PA systems assuming 14 Gbaud PDM 16-QAM modulation and a transmission distance of 1200 km. $f_{sc} = 1.5$ GHz is chosen for the non-PA system since there is enough room in the assumed 50 GHz channel to accommodate the pilot spectral gap. Clearly, PA transmission improves the NL tolerance of the system by allowing for more than 1.5 dB increase in the maximum launch power for OSNR levels above 19 dB.

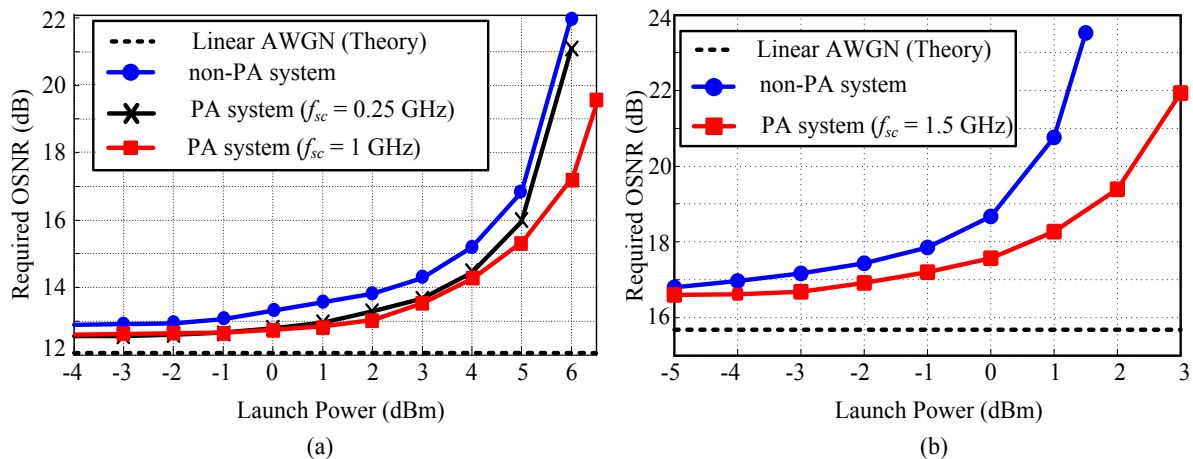


Fig. 3.5. Required OSNR versus launch power to achieve a $\text{BER} = 3.8 \times 10^{-3}$ assuming noise loading at Rx side for: a) 28Gbaud PDM-QPSK system with $L = 1600$ km, and b) 14 Gbaud PDM 16-QAM system with $L = 1200$ km.

Fig. 3.6(a) and Fig. 3.6(b) show the reach improvement achieved by using PA transmission for both PDM-QPSK and PDM 16-QAM systems, respectively. In these figures, no noise

loading is performed and the OSNR level is limited only by the contribution of in-line EDFAs. As depicted by the figure, PA transmission allows for a maximum reach increase by 720 km and 480 km for PDM-QPSK and PDM 16-QAM systems, respectively which correspond to 9% and 20% reach increase.

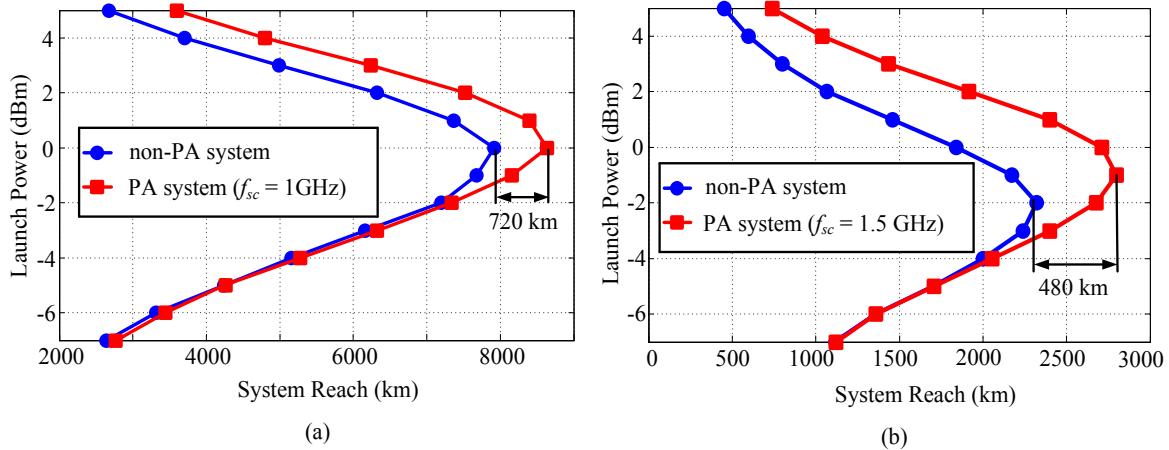


Fig. 3.6. Maximum system reach versus launch power to achieve a $\text{BER} = 3.8 \times 10^{-3}$ assuming the noise figure of inline EDFAs = 7 dB and no noise loading at Rx side for: a) 28 Gbaud PDM-QPSK system, and b) 14 Gbaud PDM 16-QAM system.

Finally, we study the impact of realistic bit resolutions of Tx side DACs on the performance of our proposed PA scheme. Since a 16-QAM signal is inherently more vulnerable to quantization effects resulting from lower bit resolution of DACs compared to a QPSK signal, we

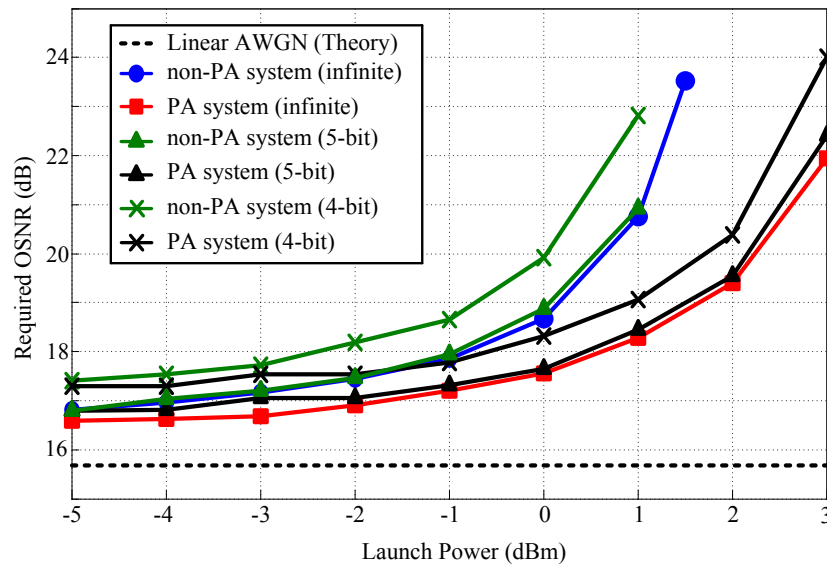


Fig. 3.7. Effect of finite DAC resolution on required OSNR versus launch power to achieve a $\text{BER} = 3.8 \times 10^{-3}$ assuming noise loading at Rx side for 14 Gbaud PDM 16-QAM system with $L = 1200$ km.

only consider how the performance of a PDM 16-QAM system is affected when finite resolution DACs are used in both PA and non-PA cases. Fig. 3.7 shows the required OSNR versus launch power curves for a 14 Gbaud PDM 16-QAM system in both PA and non-PA cases for three different DAC bit resolutions: infinite, 5, and 4. The two curves representing the infinite case are identical to the ones shown in Fig. 3.5(b). As the DAC resolution is reduced to 5 and 4, it is clear that both non-PA and PA systems are affected similarly by more stringent quantization. However, it is clearly seen that the PA scheme still outperforms the non-PA system by the same amount as the infinite DAC resolution case.

3.2.4 Proof-of-concept experimental verification of PA-DSP

In this subsection, we present the results of a proof-of-concept experiment that we carried out to verify the effectiveness of PA-DSP to jointly mitigate multiple impairments as previously explained and verified by simulations in the previous subsections. Throughout this experiment, we employ PA-DSP to: a) mitigate laser PN, b) compensate laser FO, and c) achieve polarization demultiplexing for a PDM signal. With 3.4 % bandwidth (BW) overhead, we experimentally demonstrate all PA algorithms for 28 Gbaud PDM-QPSK using a root-raised-cosine pulse shape (RRC) with 0.05 roll-off factor. Excellent back-to-back performance with 2 dB optical signal-to-noise ratio (OSNR) penalty from theory is reported. Also, error-free 5000 km transmission is achieved assuming a FEC threshold of 3.8×10^{-3} . In addition, the excellent tolerance of the PA scheme to frequency offsets up to ± 12 GHz is demonstrated. Finally, laser linewidth tolerance is experimentally verified and found to match simulation results presented in subsection 3.2.3.1.

We divide this subsection into two parts. Firstly, we give a detailed description of the DSP stacks we use specifically on the experimental data at both Tx and Rx sides focusing on the key parameters used for our DSP blocks. Secondly, the experimental setup used is depicted followed by the results obtained.

3.2.4.1 Principles and parameters of PA-DSP at Tx and Rx sides in the experiment

Fig. 3.9 Fig. 3.8(a) shows the Tx-side DSP required to create the middle spectral gap and insert the pilot similar to the concept shown in Fig. 3.1(a). The entire Tx-DSP was applied offline before loading the resulting waveforms on the memories of the DACs. First, the transmitted symbols at 28 Gbaud are pulse shaped at 2 samples/symbol by a Nyquist RRC filter with 0.05

roll-off factor. Then, resampling to the DAC sampling rate (32 GSa/s) corresponding to 1.14 oversampling factor is performed. After that, SSB subcarrier modulation is performed by means of Hilbert filtering separately on both I and Q signals (real signals). The subcarrier frequency (f_{sc}) determines the BW overhead and was chosen to be 500 MHz leading to 3.4% overhead and a 1 GHz pilot spectral gap in passband. Pre-compensation of the DAC analog frequency response then follows. As aforementioned in subsection 3.2.2.1, the pilot tone had to be moved away from DC to avoid getting blocked at the DAC outputs (AC-coupled) and hence, the pilot tone was placed at f_{pilot} equal to 250 MHz. The power of the added pilot determines the pilot-to-signal power ratio (PSR) which is an important design parameter as shown from simulation results in Fig. 3.3(a). Finally, the resulting two signals were quantized to 6-bit resolution and loaded to the DAC memories where the pattern length was 2^{17} .

Rx-side DSP is shown in Fig. 3.8(b) where the grey blocks distinguish the tasks that are specific to the PA-DSP. We start by resampling to 2 samples/symbols, CD compensation using a frequency domain equalizer (FDE). Then, a coarse FO compensation stage follows. It locates the pilot tone in the received spectrum and frequency shifts the received signal depending on the difference between the frequency of the located pilot and f_{pilot} . The FFT block length affects the accuracy of this coarse FO estimation stage and will be studied in the results, however this block provides only a rough initial FO to bring the pilot back to f_{pilot} to be filtered later. Any residual FO due to inaccuracy of this stage contributes to the pilot phase and will be compensated jointly with phase noise later. Also, this FO compensation stage might not need any additional FFT computation if it uses the FFT evaluated during FDE-based CD compensation. Since the pilot and the data are frequency multiplexed, they are easily separated by filtering the pilot. Then, we exploit the prior knowledge of the transmitted pilot for estimating the 2×2 Jones channel matrix \mathbf{J} and the frequency offset besides phase noise compensation as thoroughly explained in subsection 3.2.2. Then, SSB demodulation is performed to frequency shift the data back to baseband and matched filtering then follows. Since polarization rotation has already been mitigated by the pilot, a butterfly filter whose taps are updated using DD-LMS then removes residual inter-symbol interference (ISI) and polarization-mode-dispersion (PMD). To further improve the PN tolerance, ML phase estimation can be performed as explained in subsection 3.2.2.2 and decisions are finally made. Finally, we should note that all described PA-DSP does not depend on the modulation format except for three decision blocks needed for DD-LMS, ML

phase estimation (if used) and the final symbol decision. Also, performing PN and FO compensation prior to the butterfly filter de-couples PN compensation from the DD-LMS algorithm which makes it more stable. In addition, no frame synchronization is needed since the pilot is continuously transmitted. Also, no cycle slips can occur using PA-based PN mitigation.

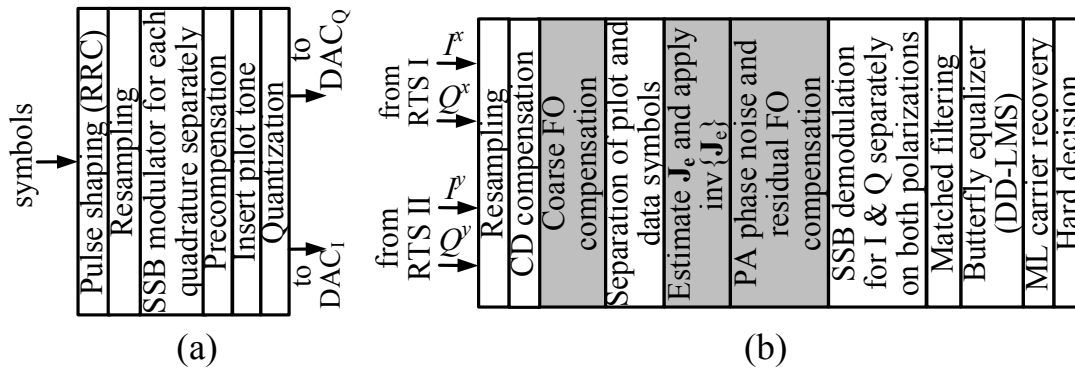


Fig. 3.8. PA-DSP used for the experiment at a) Tx-side, b) Rx-side.

3.2.4.2 Experimental setup and results

PA algorithms were verified experimentally for 28 Gbaud PDM-QPSK with an RRC pulse with 0.05 roll-off factor using the setup in Fig. 3.9(a). Components enclosed by red lines were only used for the last part of the experiment that evaluates the PN tolerance. Two 32 GSa/s MICRAM DACs drive a QAM transmitter to modulate an ECL having a linewidth less than 100 kHz. PDM was emulated with a de-correlation delay of 700 symbols. The PDM signal was launched at -2 dBm into a recirculating loop containing 4×80 km SMF-28e⁺ low-loss fiber and four EDFAs with 5 dB noise figure each. Then, the output signal from the loop is filtered by a 0.3 nm filter and pre-amplified before coherent reception using a local oscillator (LO) ECL similar to the Tx ECL. Noise loading is done whenever we needed to sweep OSNR. After balanced detection, signals were sampled by 80 GSa/s real-time scopes (RTSs) for offline processing. Since PDM is emulated, the transmitted pilot on X and Y polarizations could not be controlled independently. Hence, to send $\mathbf{P}_{Tx}(t)$ as previously defined in subsection 3.2.2.3, we used the transmitted pilot frame in Fig. 3.9(b) where we sent $e^{j2\pi f_{pilot}n}$ for the whole pattern except the last 700 zeros. After PDM emulation, we have a period of 700 symbols where we send a pilot on one polarization and zero on the other as required to estimate \mathbf{J}_e as described

earlier in subsection 3.2.2.3. It should be noted that those zeros are only transmitted within the pilot spectral gap whereas SSB modulated data symbols are sent continuously. Only for setup limitations (PDM emulation), we had to carry out frame synchronization to locate those 700 symbols and estimate \mathbf{J}_e . Otherwise in a true PDM system, frame synchronization is not needed.

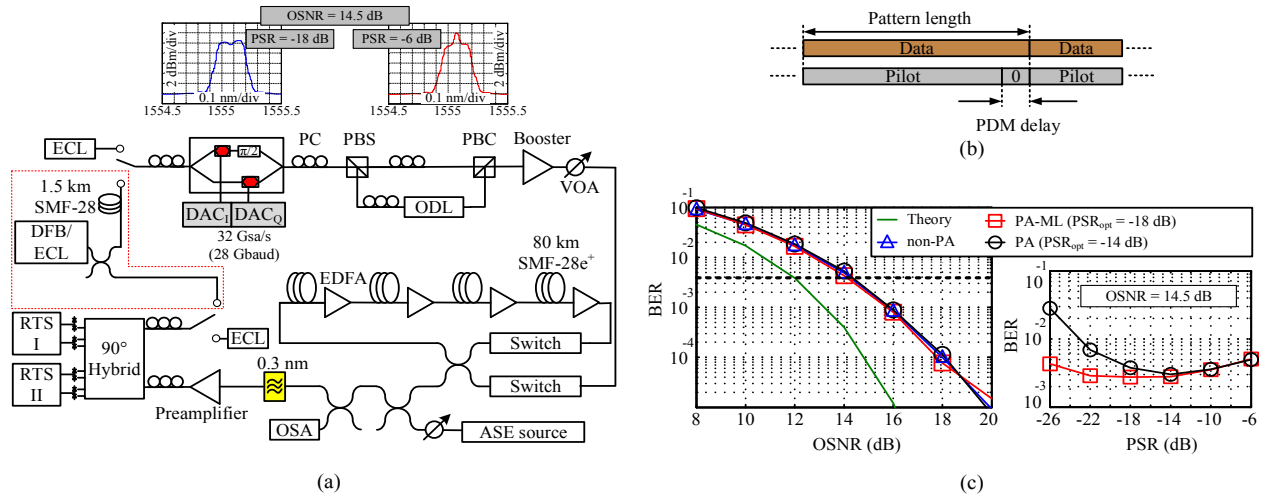


Fig. 3.9. a) Experimental setup: insets show optical spectra of PA system at $PSR = -18$ and -6 dB with a 0.05 nm resolution BW, b) transmitted data and pilot frames, c) back-to-back BER versus OSNR for theory, non-PA and PA systems with and w/o MLPE and PSR optimization for PA and PA-ML systems at $OSNR = 14.5$ dB

The left subplot of Fig. 3.9(c) shows the back-to-back bit-error-rate (BER) versus OSNR for the PA system with and without MLPE using optimum PSRs of -18 and -14 dB, respectively compared to a non-PA system and theory. For fairness in comparison, the non-PA system uses the same parameters and all Tx-side DSP blocks in Fig. 3.8(a) as the PA system except the SSB modulation and pilot insertion blocks. The non-PA system uses conventional Rx-DSP as in section 2.4.3 in addition to MLPE for fair comparison. The two systems deliver the same bit rate with 3.4% more BW for the PA case. A 2 dB OSNR penalty from theory is observed for all systems at a BER of 3.8×10^{-3} . Optimum PSRs (PSR_{opt}) for the PA system were found at an OSNR of 14.5 dB by sweeping the PSR and evaluating the BER and results are also shown in the right subplot of Fig. 3.9(c). We notice that PSR_{opt} is less when MLPE is used since it relaxes the requirement on the pilot power by compensating any residual phase noise. Next, we compare the BER versus transmission distance curves of both a PA system with MLPE using $PSR = -18$ dB and a non-PA system in Fig. 3.10(a). The PA system provides a reach of 5000 km below the FEC threshold which is slightly larger than 4700 km for the non-PA system. Next, Fig. 3.10(b)

shows the BER versus FO curves for a PA system using MLPE at a 14.5 dB OSNR. FO is swept between ± 12 GHz using a frequency fine-tuning feature in our LO ECL to set the FO required (FO_{set}) which was found to be very close to the estimated FO after offline processing. Also, we found that using an FFT block length as small as 4096 still provides a good initial FO estimate for subsequent Rx-side DSP. The small insets in Fig. 3.10(b) show the electrical spectra of the received signal for $FO = -12$ and 0 GHz. Finally, we evaluate the PN tolerance of the PA system. Since the worst DFB available in our lab had a 2.3 MHz linewidth, we used the components enclosed by the red line in Fig. 3.9(a) for homodyne detection to have a 4.6 MHz combined linewidth. The DFB output was split by a 3 dB coupler and a 1.5 km SMF-28 de-correlates the Tx and LO. For comparison with a low linewidth scenario, we lowered the power of one ECL to the same DFB output power (~ 11 dBm) and used it in the same homodyne scheme. In Fig. 3.10(c), we compare the back-to-back BER versus OSNR of the ECL and DFB cases when using PA-DSP with and without MLPE. Since PN of the ECL is small, MLPE does not provide extra PN tolerance and PA with or without MLPE requires 14.5 dB OSNR to achieve the FEC threshold which is 2.5 dB away from theory. The additional 0.5 dB OSNR penalty compared to Fig. 3.9(c) is due to the lower ECL power at Tx and LO. For the 4.6 MHz DFB case, PA with MLPE requires almost the same OSNR as in the ECL case, whereas PA without MLPE needs 0.5 dB additional OSNR due to the lower PN tolerance as shown in our simulations in subsection 3.2.3.1.

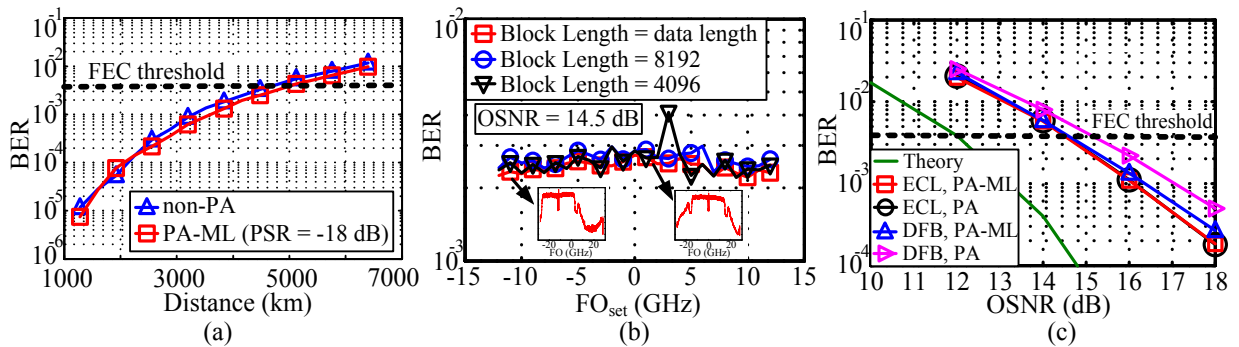


Fig. 3.10. a) BER versus distance for both non-PA and PA system with MLPE, b) back-to-back BER versus FO for PA system with different FFT block lengths at OSNR = 14.5 dB: insets show the electrical spectra of the received signal for $FO = -12$ and 0 GHz, c) back-to-back BER versus OSNR for PA system with and without MLPE using an ECL or 2.3 MHz DFB in homodyne configuration.

3.3 Low overhead and ultrafast training symbol based polarization demultiplexing

3.3.1 Introduction

As mentioned in Chapter 2, a DSP-based coherent transceiver has the additional power to post-compensate and/or pre-compensate linear and nonlinear fiber transmission impairments [9, 10, 13-15, 59, 98]. In addition, coherent detection of both in-phase (I) and quadrature (Q) signals on both field polarizations enables the use of polarization division multiplexing (PDM) as an efficient way to double spectral efficiency in optical transport systems [9, 13]. As detailed earlier in section 2.4.2, the signal suffers along the fiber from linear impairments, and in particular, from random polarization rotation and polarization mode dispersion (PMD) [9-11, 15]. Using a polarization-diversity coherent receiver, the two transmitted orthogonal polarizations are reconstructed by a 2×2 butterfly equalizer that mitigates polarization crosstalk and inter-symbol interference (ISI) due to PMD, filtering effects, and residual CD. Several algorithms have been used for adapting the taps of the butterfly equalizer. Data-aided schemes are widely used where training symbols (TS) are sent and used at the receiver for tap adaptation using the least mean squares (LMS) algorithm [11]. Such TS based schemes reduce throughput due to the relatively large TS overhead required and have synchronization issues to locate TS. Therefore, blind techniques that exploit special data properties are preferred. One example of blind schemes is the constant modulus algorithm (CMA) which is widely used for quadrature phase shift keying (QPSK) modulation [9, 10]. Even for high order quadrature amplitude modulations (QAMs) having non constant modulus, e.g. 16QAM, CMA still achieves reasonable pre-convergence after which adaptation is switched to decision-directed LMS (DD-LMS) for steady-state operation [99]. However, CMA usually provides slower convergence compared to TS based approaches and also suffers from the singularity problem that happens when both output polarizations of the butterfly equalizer converge to one transmitted polarization [100]. In general, convergence speed of all adaptive algorithms depend on the state of polarization (SOP) of received light, tap initialization and the step size parameter used for updating the taps.

In the current section 3.3, we present a novel modulation format transparent TS based channel estimation (TS-EST) algorithm that utilizes a very small TS overhead to estimate the 2×2 Jones channel matrix in a non-adaptive way thus allowing for ultrafast polarization tracking. The

proposed TS-EST algorithm is based on the fact that modern fibers have very small PMD parameter (< 0.1 ps/km $^{1/2}$) [61], and hence the channel can be assumed flat in the frequency domain given that the residual ISI is small since CD is initially compensated (see subsection 2.4.2.3 for more details). The estimated 2×2 Jones channel matrix entries are then used to set the initial center taps of a butterfly equalizer. As polarization crosstalk is mitigated, initial constellations are reasonably compact such that decision-directed (DD) steady-state adaptation can be started after as few as 40 training symbols for TS-EST, thus achieving ultrafast polarization demultiplexing. Our algorithm was experimentally verified on both 112 Gbps PDM-QPSK and 224 Gbps PDM-16QAM systems and compared with TS-LMS and CMA. Results reveal that the proposed TS-EST algorithm achieves the same steady-state BER with a superior convergence speed compared to CMA and TS-LMS algorithms [40]. Finally, we showed by simulation that the superior tracking speed of the TS-EST algorithm allows not only for initial polarization tracking but also for tracking very fast polarization transients during steady-state operation. This can be done by sending four training symbols periodically with an overhead as low as 0.57% and exploiting them to periodically estimate the channel matrix and re-update the center taps of the butterfly equalizer before resuming adaptation using DD-LMS [41].

3.3.2 Principle of proposed algorithm

Assuming CD is first compensated by a static FDE, PMD and polarization dependent loss (PDL) are negligible, and fiber nonlinearity is relatively small, a fiber channel can be considered flat in the frequency domain and modeled as a unitary 2×2 Jones matrix \mathbf{J} (see subsection 2.4.2.3 for more details)

$$\mathbf{J} = \begin{bmatrix} a & b \\ -b^* & a^* \end{bmatrix} \quad (3.16)$$

$$a = e^{j\delta} \cos \theta, \quad b = e^{j\varphi} \sin \theta \quad (3.17)$$

where 2θ and φ are the azimuth and elevation rotation angles, respectively, whereas 2δ is a differential phase between the two polarizations. Assuming Nyquist pulses and using Eq. (3.16), the received signal $\mathbf{S}_{rx}[n] = [s_{rx}^x[n] \quad s_{rx}^y[n]]^T$ can be expressed as

$$\mathbf{S}_{rx}[n] = e^{j\psi[n]} \mathbf{J} \mathbf{S}_{tx}[n] = e^{j\psi[n]} \begin{bmatrix} as_{tx}^x[n] + bs_{tx}^y[n] \\ -b^* s_{tx}^x[n] + a^* s_{tx}^y[n] \end{bmatrix} \quad (3.18)$$

where $\mathbf{S}_{tx}[n] = [s_{tx}^x[n] \ s_{tx}^y[n]]^T$ is the transmitted signal and $\psi[n]$ is the instantaneous phase of the n^{th} symbol originating from laser phase noise $\psi_{pn}[n]$ and frequency offset ΔF as follows

$$\psi[n] = 2\pi\Delta FT + \psi_{pn}[n] \quad (3.19)$$

The principle of the proposed algorithm is to send short special training symbols on X and Y polarizations and use the received data to estimate \mathbf{J} regardless of laser phase noise and frequency offset. Basically, we send N training symbols $\mathbf{T}_{tx}[k]$, where $k \in [0, N-1]$, designed such that: $\mathbf{T}_{tx}[k] = ce^{j\xi} [1 \ 1]^T$ and $\mathbf{T}_{tx}[k+1] = ce^{j\xi} [1 \ -1]^T$, where $\xi \in \{\pm\pi/4, \pm3\pi/4\}$ and c is a normalization constant that is chosen depending on the modulation format such that we send one of the four constellation corner symbols on the X and Y polarizations for the training period where the phase shift between every two successive polarization multiplexed training symbols alternates between 0 and π . Using Eq. (3.18), we can write the received training symbols as

$$\mathbf{T}_{rx}[k] = ce^{j(\xi+\psi[k])} \begin{bmatrix} a+b \\ -b^* + a^* \end{bmatrix}, \quad \mathbf{T}_{rx}[k+1] = ce^{j(\xi+\psi[k+1])} \begin{bmatrix} a-b \\ -b^* - a^* \end{bmatrix} \quad (3.20)$$

Knowing that $\psi[k] \approx \psi[k+1]$ since laser phase noise is a slower process compared to the baud rate [101] and that \mathbf{J} is unitary, if we normalize the received training symbols in Eq. (3.20) to unit envelope, we can get

$$|a| \approx \sqrt{0.5 \left(1 + \frac{1}{N} \operatorname{Re} \left\{ \sum_{i=0}^{N/2-1} \left(\begin{matrix} T_{rx}^x[2i] T_{rx}^{x*}[2i+1] - \dots \\ T_{rx}^y[2i] T_{rx}^{y*}[2i+1] \end{matrix} \right) \right\} \right)} \quad (3.21)$$

$$|b| \approx \sqrt{1 - |a|^2} \quad (3.22)$$

$$\arg\{a\} + \arg\{b\} = \arg \left\{ - \sum_{i=0}^{N/2-1} \left(\begin{matrix} T_{rx}^x[2i] T_{rx}^{y*}[2i+1] + \dots \\ T_{rx}^{y*}[2i] T_{rx}^y[2i+1] \end{matrix} \right) \right\} \quad (3.23)$$

Then, if the inverse of the matrix \mathbf{J}_1 given by

$$\mathbf{J}_1 = \begin{bmatrix} |a| & |b|e^{j(\arg\{a\}+\arg\{b\})} \\ -|b|e^{-j(\arg\{a\}+\arg\{b\})} & |a| \end{bmatrix} \quad (3.24)$$

is left multiplied by \mathbf{J} , this yields zeros on the off-diagonal elements which achieves perfect polarization demultiplexing. Theoretically, the lowest number of training symbols required to perform TS-EST according to above equations is 2. However, in a noisy environment and low OSNR levels after long transmission distances, the \sum operation in Eqs. (3.21) and (3.23) is needed to average the estimates over N training symbols where $N > 2$. Furthermore, the differential phase between the two polarizations 2δ can be also estimated if we apply the inverse of \mathbf{J}_1 back to the received training symbols and estimate the common phase difference between the demultiplexed training symbols.

After polarization demultiplexing is achieved, we can use the above estimates to set the initial center taps of a standard butterfly 2×2 equalizer whose remaining job is to mitigate any residual ISI. However, since polarization crosstalk is already mitigated, the constellations obtained by merely applying the inverse channel matrix estimated in Eqs. (3.21)-(3.23) are reasonably good to the extent that decision-directed (DD) error calculation can be pursued to update the taps of the butterfly filter using the DD-LMS algorithm after the short TS period. Since TS-EST is not an adaptive algorithm, the TS period used for estimation can be very short leading to very small TS overhead and ultrafast polarization tracking. As will be experimentally demonstrated hereafter, we used N as short as 10 and 40 for PDM-QPSK and PDM-16QAM, respectively.

3.3.3 Experimental setup and offline DSP

The proposed algorithm was verified experimentally for both 28 Gbaud PDM-QPSK and PDM-16QAM systems using the setup in Fig. 3.11(a). The in-phase (I) and quadrature (Q) signals were generated from either pulse pattern generators (PPGs) for PDM-QPSK or digital-to-analog converters (DACs) for PDM-16QAM. The I and Q signals were fed to a QAM transmitter to modulate either an external cavity laser (ECL) laser having a linewidth less than 100 kHz or a distributed feedback (DFB) laser with a 2.4 MHz linewidth depending on whether low or high phase noise scenario is considered. Single polarization power eye diagrams after the QAM transmitter are shown in the insets of Fig. 3.11(a) for both QPSK and 16QAM. Using a polarization beam splitter (PBS), an optical delay line (ODL) and a polarization beam combiner

(PBC), PDM was emulated with a decorrelation delay of 324 symbols. The PDM signal was launched into an optical recirculating loop where each loop contains 4 spans of 80 km of SMF-28e⁺ low loss fiber and an erbium-doped fiber amplifier (EDFA) with 5 dB noise figure. Then, the output signal from the loop is filtered by a 0.4 nm filter, pre-amplified and re-filtered by a 0.4 nm filter before coherent reception. Coherent reception is done using a 90° optical hybrid that mixes the signal with CW light from an ECL laser similar to the one used at the transmitter. After balanced detection, the four signals were sampled by two real-time scopes each running at 80 GSa/s for offline processing.

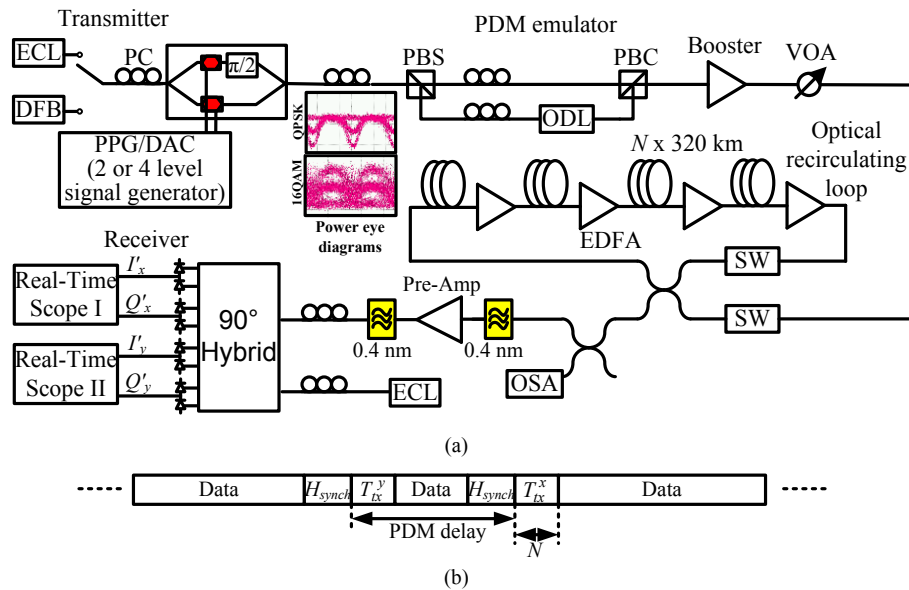


Fig. 3.11. (a) Experimental setup, (b) Training symbols and framing synchronization header.

Since PDM was emulated in our experimental setup, we could not send different data on the two polarizations. Hence, our training symbols explained in the previous sections were inserted into the transmitted data by sending N training symbols $T_{tx}^x[n]$ and $T_{tx}^y[n]$ separated in time by the decorrelation delay used for PDM emulation, i.e. 324 symbols, as explained in Fig. 3.11(b). This will result in having $T_{tx}^x[n]$ and $T_{tx}^y[n]$ aligned in time at the two transmitted orthogonal polarizations after the PDM emulator.

Offline digital signal processing (DSP) at the receiver side starts by IQ imbalance compensation, resampling to 2 samples per symbol and CD compensation using a static FDE. Since the TS-EST algorithm is a data aided approach, frequency offset compensation has to be done before polarization demultiplexing. For that reason, the periodogram method [91] was

chosen since it still works if there is polarization crosstalk prior to getting into the butterfly equalizer. Then, synchronization is performed to locate the N training symbols within the received data. Since training symbols added for polarization demultiplexing do not have good auto-correlation properties, cross-correlating the received symbols with the known TS would not produce a distinct peak to locate them. Hence, for synchronization purpose, 100 random symbols are sent in a header (H_{synch}) prior to the TS used for polarization demultiplexing as shown in Fig. 3.11(b). At the receiver side, a peak is located by cross-correlating the received symbols with the known synchronization header from which the location of the TS that follows the header is automatically found. For polarization demultiplexing, we compare our proposed training symbol based channel estimation (TS-EST) with TS-LMS and CMA to achieve initial polarization tracking. After initial convergence is achieved by either TS-EST or TS-LMS, we switch to DD-LMS for steady-state operation. In case of CMA, we keep using it for steady-state operation for PDM-QPSK, whereas we also switch to DD-LMS for PDM-16QAM depending on when CMA pre-converges to a reasonably compact constellation. We used step sizes of 1×10^{-3} , 1×10^{-3} and 4×10^{-4} for TS-LMS, CMA and DD-LMS, respectively. For TS-EST, we used 10 and 40 training symbols for PDM-QPSK and PDM-16QAM, respectively to estimate the 2×2 Jones matrix. Finally, phase noise was mitigated by a decision-directed first order phase locked loop (DD-PLL) with a loop coefficient of 0.02. The DD-PLL was either interleaved with the DD-LMS algorithms for steady-state operation or placed after the butterfly equalizer if CMA was used at steady-state in case of PDM-QPSK. Differential encoding / decoding was used to mitigate the angle ambiguity and cycle slips for all PDM-QPSK results. On the other hand, we used absolute encoding / decoding in case of PDM-16QAM to remove the penalty introduced by differential decoding. In order to resolve the angle ambiguity in case of absolute decoding, we used 100 pilot symbols at the beginning of our symbols and we did not encounter any cycle slips in all PDM-16QAM experimental data collected.

To verify how good the Jones matrix estimates provided by the proposed TS-EST algorithm are, we plot in Fig. 3.12(b) the constellations after 320 km for both PDM-QPSK and PDM-16QAM obtained by merely applying the estimated inverse Jones matrix using the proposed TS-EST scheme, *i.e.* before the butterfly equalizer and the PLL. This proves that polarization demultiplexing is indeed achieved using very low TS overhead. This allows the subsequent butterfly equalizer to operate in DD mode if initialized according to TS-EST. Fig. 3.12(c) shows

the final resulting constellations after the butterfly equalizer and the PLL. On the other hand, we always used 1500 training symbols for TS-LMS since it was the most needed to switch to DD-LMS in all collected data sets.

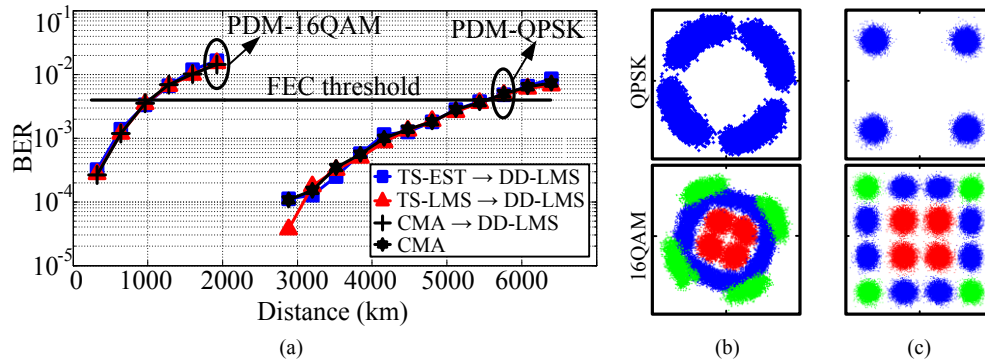


Fig. 3.12. (a) Steady-state BER versus distance for all algorithms for both PDM-QPSK and PDM-16QAM, (b) Constellations after 320 km transmission for both PDM-QPSK and PDM-16QAM obtained by merely applying the inverse Jones matrix obtained by TS-EST, (c) Constellations of the same case in (b) after the butterfly filter updated using DD-LMS and carrier recovery using DD-PLL.

3.3.4 Results and discussion

3.3.4.1 Low phase noise and optimum launch power scenario

In this subsection, we experimentally study the performance of our proposed TS-EST algorithm in a low phase noise and low launch power scenario. Throughout this subsection, ECLs were used as transmit and LO lasers and an optimum launch power of -2 dBm was set. Steady-state and transient performance of the TS-EST scheme is compared to standard adaptive algorithms used for polarization demultiplexing.

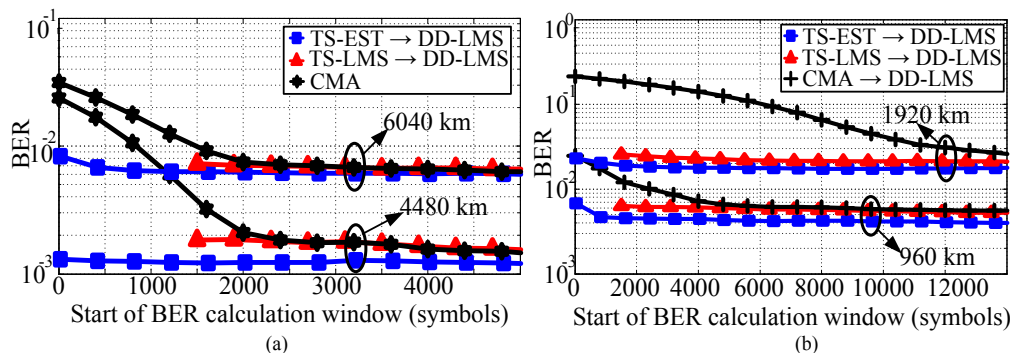


Fig. 3.13. Transient BER for all algorithms for (a) PDM-QPSK, (b) PDM-16QAM.

In Fig. 3.12(a), we first compare all the polarization demultiplexing algorithms in steady-state operation for both PDM-QPSK and PDM-16QAM. Steady-state bit-error-rates (BER) are calculated excluding the convergence period. All algorithms achieve similar steady-state BER

allowing us to transmit 5400 and 1000 km below a FEC threshold of 3.8×10^{-3} for PDM-QPSK and PDM-16QAM, respectively.

Secondly, the speed of convergence of the algorithms is compared. A smaller window of 20000 symbols over which BER is calculated is swept starting right after the training period. In case of CMA, the window was swept from the first symbol as no training is needed. Fig. 3.13(a) shows the results for PDM-QPSK at two different transmission distances of 4480 and 6080 km. Compared to TS-LMS, our proposed TS-EST scheme uses only 20 training symbols to achieve almost the same BER provided by TS-LMS using 1500 training symbols resulting in a huge reduction in TS length and very fast polarization tracking. Compared to around 2500 symbols needed by CMA, TS-EST achieves much faster convergence as well. It is also noteworthy that the speed of convergence achieved by our scheme does not depend on the SOP of the received light, whereas both TS-LMS and CMA might achieve a faster or slower convergence depending on the SOP, tap initialization and the step size parameter used for adaptation. Also, our scheme inherently does not suffer from any singularity problems and has the advantage that the transmitted X and Y polarizations are always recovered at the output X and Y polarizations, respectively. Finally, we compare all algorithms for PDM-16QAM after 960 and 1920 km. As seen in Fig. 3.13(b), TS-LMS needs 1500 symbols before switching to DD operation compared to around 3000 and 8500 symbols needed by CMA at both distances, respectively. On the other hand, since TS-EST needed only 40 training symbols before switching to steady-state DD operation, it is very difficult to visualize such a short convergence period in Fig. 3.13(b).

3.3.4.2 High phase noise and high launch power scenario

In this subsection, we experimentally study the performance of our proposed TS-EST algorithm in a high phase noise and high launch power scenario. This aims at evaluating the tolerance of the TS-EST algorithm against large phase noise and high fiber nonlinearity to validate the assumptions upon which the channel model used in subsection 3.3.2 to propose the algorithm.

In Fig. 3.14(a), we first plot the steady-state BER versus distance of the TS-EST algorithm for PDM-QPSK in the high phase noise and high launch power scenarios. For the high laser phase noise scenario, a 2.4 MHz DFB laser was used as the transmit laser while keeping an ECL as the LO in order not to add an additional penalty from equalization enhanced phase noise (EPPN) [97, 102]. For the high launch power case, 2 dBm was launched into the recirculating loop to

have high fiber nonlinearity. For comparison, we also plot the steady-state BER for the case of having -2 dBm launch power and two ECLs as transmit and LO lasers. In all scenarios, TS-EST using 10 training symbols was used for polarization demultiplexing. We notice that the TS-EST algorithm works well in both scenarios. For the high phase noise scenario, the BERs achieved are so close to the ones obtained when using an ECL as the transmit laser because the loop coefficient of the DD-PLL was optimized to mitigate the larger phase noise. However, for the 2 dBm launch power case, BERs are about an order of magnitude higher than the optimum launch power case because we did not use any nonlinearity mitigation scheme. However, this penalty does not originate from using the TS-EST algorithm for initializing the butterfly equalizer because the transient BER curves shown in Fig. 3.14(b) show that after 10 training symbols the initial BERs were very close to the steady-state BERs achieved after switching to DD-LMS steady-state operation for both 2560 and 3840 km transmission. Fig. 3.14(b) also shows that TS-EST still provides very fast convergence with very small TS overhead for both high laser phase noise and high fiber nonlinearity scenarios.

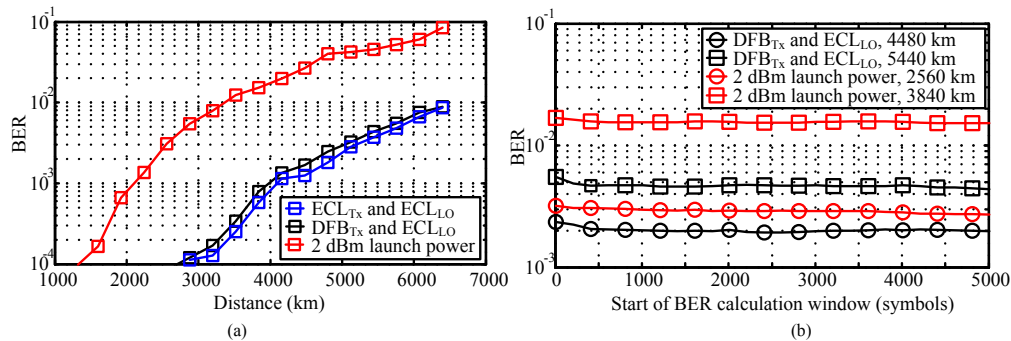


Fig. 3.14. BER for the TS-EST algorithm for PDM-QPSK in both high phase noise and high launch power scenarios for: (a) steady-state, (b) transient cases.

3.3.4.3 TS-EST algorithm for tracking fast SOP transients

In this subsection, we show by simulation that the superior tracking speed and low TS overhead (OH) required by the proposed TS-EST algorithm can not only be used for initial polarization demultiplexing at startup but also for tracking fast SOP transients at steady-state operation.

Simulations were done in an optical back-to-back configuration for both 14 Gbaud and 28 Gbaud PDM-16QAM at an OSNR level 3 dB higher than the theoretical required OSNR to achieve a FEC threshold of 3.8×10^{-3} . To study the effect of SOP transients on the steady-state BER, we multiply the Jones vector of the transmitted symbols by the Jones matrix \mathbf{J} [103]

$$\mathbf{J} = \begin{bmatrix} \cos \omega t & \sin \omega t \\ -\sin \omega t & \cos \omega t \end{bmatrix} \quad (3.25)$$

where ω is the angular frequency of the SOP changes. Multiplying by \mathbf{J} given in Eq. (3.25) simulates a continuous polarization rotation at a constant rate. Although continuous polarization rotation does not mimic the realistic random polarization rotation which occurs as random events and may lead to system outages, it is easier to model and allows verifying the DSP tracking algorithm at various deterministic rates of change of SOP rather than having to perform lengthy simulations and calculate outage probabilities in case of random SOP changes. Transmit and LO laser linewidths were 100 kHz and a total of 448000 symbols were transmitted. Since the focus in this subsection is not on the initial convergence of all polarization demultiplexing algorithms, we only calculate the steady-state BER in all cases by excluding the first 40000 symbols to allow all algorithms to converge. Steady-state BER values will depend on how each algorithm used for steady-state operation is able to track the endless time-varying SOP introduced by \mathbf{J} in Eq. (3.25). For the TS-EST algorithm to be able to track dynamically varying SOP, we transmit 4 training symbols every 700 symbols as shown in Fig. 3.15(a) which corresponds to a very small overall overhead of 0.57%. For this overhead, the TS transmission rate is 20 MHz and 40 MHz at 14 and 28 Gbaud, respectively, which allows tracking very fast SOP transients as will be shown.

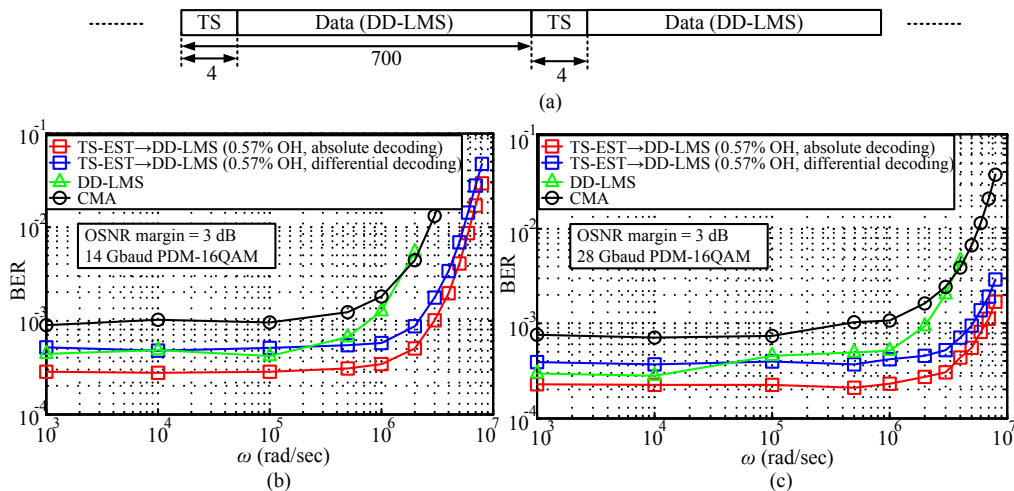


Fig. 3.15. (a) Periodic training symbols for SOP tracking, (b) Steady-state BER versus SOP angular frequency for different algorithms for 14 Gbaud PDM-16QAM, (c) Steady-state BER versus SOP angular frequency for different algorithms for 28 Gbaud PDM-16QAM.

It is noteworthy that no extra overhead is needed to perform synchronization to locate the TS within the received data since synchronization has already been achieved at startup and training

symbols are sent periodically every 700 symbols at steady-state operation. After using TS-EST every 700 symbols using the 4 training symbols, we use the newly found Jones matrix estimates to update the center taps of the butterfly equalizer and continue operating using the DD-LMS operation until the next TS period.

In Fig. 3.15(b) and Fig. 3.15(c), we plot the steady-state BER versus the SOP angular frequency (ω) for both 14 Gbaud and 28 Gbaud PDM-16QAM, respectively. Although high speed SOP transients happen as rare events in a real system and will cause system outages [104, 105], we use a fixed ω for each point on Fig. 3.15(b) and Fig. 3.15(c) to simplify the simulation as well as characterize the tracking limits of all algorithms. We compare three polarization demultiplexing algorithms at steady-state: 1) TS-EST every 700 symbols and using DD-LMS for the data symbols within the TS period, 2) DD-LMS, and 3) CMA. For the case of TS-EST, as TS are sent periodically every 700 symbols to be used for channel estimation, those TS can be also used to resolve the angle ambiguity and cycle slip problem and hence, absolute decoding can be used instead of differential decoding. Thus, we also show both cases on Fig. 3.15(b) and Fig. 3.15(c). For DD-LMS, we use TS-LMS for the initial tracking before switching to DD-LMS for steady-state operation. In both 14 and 28 Gbaud cases, our TS-EST algorithm considerably improves the tracking performance of the DD-LMS algorithm at the expense of 0.57% overhead. We should also note that if DD-LMS is used, a real system has to go back to training mode and uses TS-LMS if the adaptive equalizer loses polarization tracking and the BER deteriorates because DD-LMS is not going to be able to re-track the fast varying channel. However, the TS overhead needed for TS-LMS to re-track the channel is much larger than the TS overhead needed for our TS-EST algorithm especially because no synchronization is further needed. Finally, it is clear that CMA provides a considerably worse performance if used at steady-state for 16QAM since it is a multi ring constellation.

3.4 Non data-aided feedforward timing recovery scheme for arbitrary M-QAM modulation

3.4.1 Introduction

As mentioned in section 1.2.1, flexible digital signal processing (DSP)-based coherent transceivers that are modulation format agile are key elements in the envisioned future software-defined optical networks [17]. Therefore, algorithms that are transparent to modulation format

are attractive technology candidates for implementation in those transceivers. Among various algorithms, the task of digital timing recovery is obtaining synchronous samples commensurate with the symbol rate from the received asynchronous samples at the ADC sampling rate, i.e. it corrects the sampling frequency offset (SFO) between the transmitter and receiver clocks. Non-data-aided (NDA) (or blind) digital timing recovery algorithms are categorized into feedforward and feedback approaches. Although feedback algorithms usually require fewer computations than feedforward counterparts, they are often not transparent to modulation format. For example, the widely-known Gardner algorithm [85] operates only on BPSK and QPSK signals and also suffers from a long acquisition time until the feedback loop is locked.

In the current section 3.4, we modify the NDA feedforward timing error estimator in [87] for PDM signals. The proposed estimator operates at 2 samples/symbol and is transparent to modulation format and tolerant to polarization rotation. The timing error estimate obtained is used to control a piecewise-parabolic interpolator in order to compensate for SFO. The proposed timing recovery is experimentally verified on 28 Gbaud PDM-QPSK, PDM-16QAM and 7 Gbaud PDM-64QAM signals with up to 5000 ppm SFO being corrected at small penalties both in back-to-back and transmission scenarios [42].

3.4.2 Principles of the timing error estimator and interpolator control

Assuming CD is compensated first, polarization mode dispersion (PMD) and fiber Kerr nonlinearity are neglected, the Jones vector of the received continuous-time signal $\mathbf{r}(t)$ can be expressed in terms of the Jones vector of the transmitted symbols at the k^{th} baud (symbol) position $\mathbf{s}_k = [s_k^X \quad s_k^Y]^T$ as follows

$$\mathbf{r}(t) = \sum_k \mathbf{J} \mathbf{s}_k h(t - kT - \zeta T) \quad (3.26)$$

where X and Y denote the modulated orthogonal polarization, \mathbf{J} is a unitary 2×2 matrix that represents the overall Jones rotation, the superscript \mathbf{T} denotes the transpose operator, $h(t)$ is the transmitted pulse shape, T is the baud duration and $\zeta \in (-0.5, 0.5]$ is the normalized symbol timing delay which is the parameter to be estimated. Also, the transmitted symbols on both polarizations s_k^X and s_k^Y are independent and can be drawn from any linear and memoryless modulation, e.g. M -ary QAM with $M = \{4, 16, 32, 64, \dots\}$. Next, the real and imaginary parts of each polarization in the waveform given by Eq. (3.26) are sampled by means of four ADCs with

a sampling interval T_{ADC} that is nominally half the symbol duration, i.e. $T_{ADC} = T/2$ in case of zero SFO, leading to the following discrete-time samples

$$\mathbf{r}[n] := \mathbf{r}(nT_{ADC}) = \sum_k \mathbf{J}\mathbf{s}_k h(nT_{ADC} - kT - \zeta T) = \sum_k \mathbf{J}\mathbf{s}_k h_e[n - 2k] \quad (3.27)$$

where $h_e[n] = h(nT_{ADC} - \zeta T)$ are the samples obtained from the pulse shape $h(t)$ at a rate $1/T_{ADC}$ after time-shifting by ζT . Basically, ζ represents a sampling phase offset (SPO) resulting in the received samples being ζT away from the optimum sampling points as previously illustrated in subsection 2.4.1. If there is no SFO, ζ remains constant over the length of the received samples. However, when there is non-zero (but constant) SFO, the sampling phase offset ζ will be linearly time-varying. Over a block of received samples with length N , we can assume that ζ stays approximately constant provided that $N \ll 1/SFO$ where SFO is the sampling frequency offset in ppm was defined in Eq. (2.11). Given the above condition is met, an estimate $\hat{\zeta}_i$ of the normalized timing error within the i^{th} block of samples can be formulated by modifying the estimator in [87], which was proposed for a one-dimensional (single-polarization) signal, as follows

$$\frac{\hat{\zeta}_i}{T} = \frac{1}{2\pi} \arg \left\{ \sum_{n=iN}^{(i+1)N-1} (-1)^n \cdot \mathbf{r}^H[n] \mathbf{r}[n] + j \sum_{n=iN}^{(i+1)N-2} (-1)^n \cdot \Re \{ \mathbf{r}^H[n] \mathbf{r}[n+1] \} \right\} \quad (3.28)$$

where $\arg \{ \}$ and $\Re \{ \}$ denote the argument and real part of the quantity inside the curly brackets, respectively and the superscript \mathbf{H} denotes the Hermitian transpose operator. Different from the original estimator in [87], we evaluate the product $\mathbf{r}^H \mathbf{r}$ in the first and second terms of Eq. (3.28) which means that samples on both polarizations are used in the estimator while essentially removing the polarization crosstalk effect which improves the estimation accuracy (note that $\mathbf{J}^H \mathbf{J} = \mathbf{I}$ where \mathbf{I} is the identity matrix). The estimator in Eq. (3.28) requires 4 real multiplications per sample per polarization. It needs to be re-computed for each block of N samples and the difference between the sampling phase estimates of two successive blocks can be used to control a polynomial based interpolator. Out of various interpolating polynomials in the literature, we use the piecewise-parabolic interpolator in [70] where each synchronous sample $\mathbf{r}_{\text{interp}}[n]$ at the output is evaluated from a set of 4 asynchronous received samples at its input as

$$\begin{aligned} \mathbf{r}_{\text{interp}}[n] = & \mathbf{r}[m_n + 2] \cdot (0.5\mu_n^2 - 0.5\mu_n) + \mathbf{r}[m_n + 1] \cdot (-0.5\mu_n^2 + 1.5\mu_n) \\ & + \mathbf{r}[m_n] \cdot (-0.5\mu_n^2 - 0.5\mu_n + 1) + \mathbf{r}[m_n - 1] \cdot (0.5\mu_n^2 - 0.5\mu_n) \end{aligned} \quad (3.29)$$

where m_n represents the base index of the sample set being interpolated and μ_n is the fractional delay that determines the interpolator coefficients. Within the i^{th} block of N samples, m_n and μ_n are updated for each interpolator output sample such that m_n is incremented by 1 and μ_n stays the same within the block. As soon as m_n reaches the last sample in the i^{th} block, both m_n and μ_n are updated for the next block based on the difference between the estimated sampling phase offsets of the next and current blocks. Similar to [69], this recursion is formulated as follows

$$m_{n+1} = \begin{cases} m_n + 1, & \text{for } iN < m_n < (i+1)N - 1 \\ m_n + \left\lfloor \mu_n + 1 + \text{SAW}\left(2\hat{\zeta}_{i+1} - 2\hat{\zeta}_i\right) \right\rfloor, & \text{for } m_n = (i+1)N - 1 \end{cases} \quad (3.30)$$

$$\mu_{n+1} = \begin{cases} \mu_n, & \text{for } iN < m_n < (i+1)N - 1 \\ \left\lfloor \mu_n + 1 + \text{SAW}\left(2\hat{\zeta}_{i+1} - 2\hat{\zeta}_i\right) \right\rfloor_{\text{mod } 1}, & \text{for } m_n = (i+1)N - 1 \end{cases} \quad (3.31)$$

where $\text{SAW}(x) = 2(0.5x + 0.5) - 2\lfloor 0.5x + 0.5 \rfloor - 1$ is the sawtooth function with a period of 2 which wraps the difference between the two timing estimates of consecutive blocks. In the second line of Eq. (3.30), m_{n+1} can be either $m_n + 2$, m_n , or $m_n + 1$ meaning either a sample dropping, a sample overlap, or neither of them, is introduced between the two successive blocks, respectively. Sample dropping (or overlap) occurs when the ADC clock is running faster (or slower) than twice the baud rate. Fig. 3.16(b) shows the time evolution of μ_n and the increment $m_{n+1} - m_n$ for $N = 64$ at two SFO levels of 1000 (left) and 4000 ppm (right). In the latter case, the increments in μ_n are larger and sample dropping happens more frequently.

3.4.3 Experimental setup, offline DSP, results and discussion

The experimental setup is shown in Fig. 3.16(a). The in-phase (I) and quadrature (Q) signals, having either 2, 4 or 8 levels for various modulations, were generated from two MICRAM digital-to-analog converters (DACs) driven by two Xilinx FPGAs. The symbol clock was set at 28 Gbaud for QPSK and 16QAM and at 7 Gbaud for 64QAM. Then, the DAC outputs were fed to a QAM transmitter to modulate an external cavity laser (ECL) with linewidth less than 100 kHz. PDM was emulated and the signal was launched at the optimum launch power into a

recirculating loop containing 4×80 km of SMF-28e+ fiber, each followed by an EDFA having a noise figure of 5 dB. At the output of the loop, noise loading allows varying the OSNR. After filtering and pre-amplification, the signal is fed to a Si-photonic (SiP) coherent receiver (CRx) from TeraXion. An ECL similar to the transmitter ECL was used as an LO. The four CRx outputs were sampled and recorded by one Agilent 80 GSa/s real-time scope (RTS).

Offline processing starts by IQ imbalance and quadrature error correction, resampling to 2 samples per symbol, chromatic dispersion (CD) compensation. Then, the SFO present in the captured data, although being very small at around 30 kHz, was corrected using the proposed timing recovery where N was set to 16384 samples since the SFO being tracked is very small. Then, the data was resampled depending on the SFO under which the algorithm is desired to be tested, e.g. an SFO of 1000 ppm corresponds to resampling the data from 2 to 2.002 samples per symbol. Next, the SFO introduced was corrected using the proposed timing recovery. Next, laser frequency offset is removed using the periodogram method [91]. Polarization is then demultiplexed using a 31-tap butterfly equalizer whose taps are updated using either the constant modulus algorithm for PDM-QPSK or the least mean squares algorithm in training mode followed by decision-directed mode for PDM-16QAM and 64-QAM [9]. Phase noise was mitigated by a decision-directed phase locked loop (PLL). Finally, the BER is evaluated.

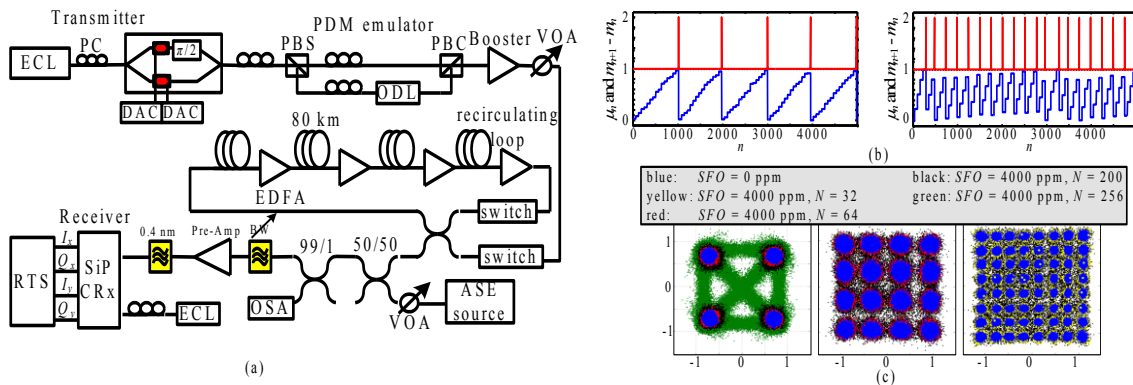


Fig. 3.16. a) Experimental setup, b) Time evolution of the fractional delay μ_n (blue) and the increment in the base index $m_{n+1} - m_n$ (red) for back-to-back PDM-QPSK with $N = 64$ and $SFO = 1000$ (left) and 4000 ppm (right), c) Back-to-back constellations.

First, we study the impact of varying N on the performance of the algorithm. In Fig. 3.16(c), we compare the back-to-back constellations (with no noise loading) of all modulations when $SFO = 4000$ ppm (for different block sizes) with the case of $SFO = 0$. We notice that under such high SFO, increasing N deteriorates the performance until the algorithm fails if $N > 1/SFO$ which is the case for the green constellation in case of QPSK where $N = 256$. On the other hand,

reducing N allows the algorithm to track larger SFO but affects the estimation accuracy especially in presence of noise. For this reason, we plot in the top insets of Fig. 3.17(a) the BER versus N for all three formats for different SFOs in back-to-back with noise loading at the OSNRs indicated on the figures. We notice that the optimum N decreases as SFO increases however, the algorithm fails when using N below 32. Also, we notice that $N = 32$ always produces the best performance for 64QAM since the OSNR level is the highest among all formats. For all forthcoming results, we fix N at 64 for both QPSK and 16QAM and at 32 for 64QAM. Next, we show in Fig. 3.17(a) the back-to-back BER versus OSNR for all three modulations at different SFO levels. As a reference, we also plot the theoretical BERs versus OSNR for all formats. Various formats are drawn with different colors whereas different SFOs are distinguished with markers. For QPSK in case of SFO = 5000 ppm, we noticed a very small OSNR penalty of 0.15 dB (measured relative to the case of zero SFO at the FEC threshold). For both 16QAM and 64QAM, the OSNR penalty in case of a large SFO of 5000 ppm increases to 1.2 and 5.5 dB, respectively. However, the OSNR penalty for both formats is still very small when the SFO is 1000 ppm and increases when SFO is 3000 ppm to only 0.5 and 1.4 dB for 16QAM and 64QAM, respectively. Finally, we evaluate the performance of the algorithm on transmitted data where we plot in Fig. 3.17(b) the BER versus distance for all formats. We notice some reduction in the reach for all formats depending on the SFO level. For example, the reach reduction was almost negligible when SFO = 1000 ppm. At SFO = 3000 ppm, the reach slightly decreases by ~ 100 and 70 km for 16QAM and 64QAM, respectively corresponding to $\sim 9\%$ and 16% relative degradation.

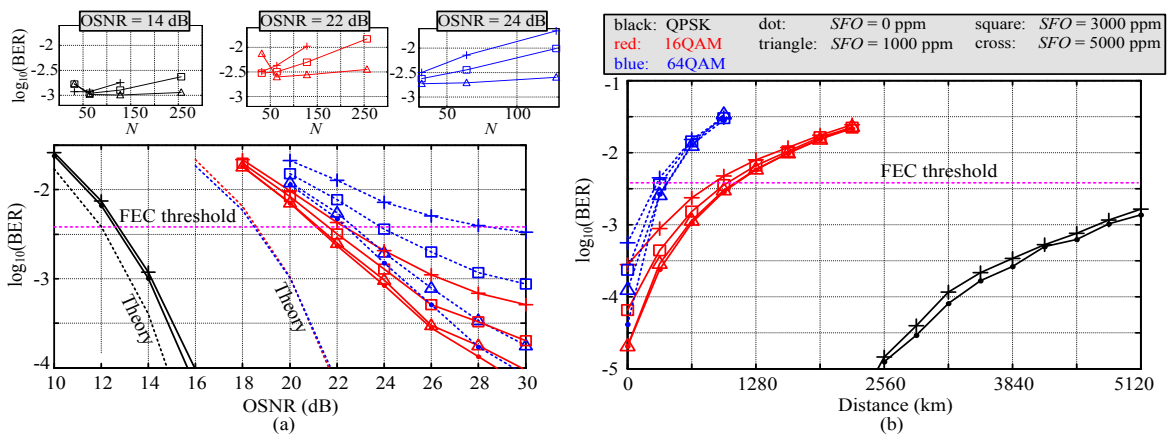


Fig. 3.17. a) Back-to-back BER versus OSNR for all modulation formats at various SFO levels: insets show the BER variation with the block size of the algorithm for different formats at fixed OSNRs, b) BER versus transmission distance at different SFO levels for all formats.

3.5 Conclusions

In this chapter, we presented three DSP schemes for flexible coherent transceivers to mitigate various impairments. Below, we provide our final concluding remarks on each of the three algorithms previously presented in sections 3.2, 3.3 and 3.4, respectively.

- PA-DSP was proposed and verified by both simulations and experiments in section 3.2 to combat jointly laser PN and FO besides polarization demultiplexing in a coherent transmission system. Also, we showed that PA-DSP also partially mitigates fiber Kerr nonlinearity and boosts the maximum system reach. The proposed PA-DSP is fully transparent to modulation format and has the following set of advantage that come at the expense of extra bandwidth overhead allocated for the inserted pilot tone: a) it de-couples CR from polarization demultiplexing, i.e. PN and FO can be compensated before polarization demultiplexing, b) it does not require synchronization to locate the pilot, and c) the cycle slip problem is eliminated when the pilot is used for CR.
- Low overhead training symbol based estimation (TS-EST) of the Jones channel matrix was proposed in section 3.3. With fewer than 40 training symbols, tap adaptation of a butterfly equalizer can be started in DD mode. The proposed scheme was experimentally verified for 28 Gbaud PDM-QPSK and PDM-16QAM and found to achieve superior convergence speed compared to standard algorithms. Also, the proposed TS-EST algorithm was verified to be tolerable to large phase noise and high fiber nonlinearity scenarios. Finally, we also showed by simulation that the superior speed and simplicity of the TS-EST algorithm can also be beneficial for tracking fast polarization transients if four training symbols are periodically sent during steady-state operation with an overhead as low as 0.57%.
- In section 3.4, we reported a NDA feedforward timing error estimator for PDM M -QAM signals. The proposed estimator operates at 2 samples/symbol and feeds timing information to a piecewise-parabolic interpolator in order to compensate for SFO. The proposed timing recovery was experimentally verified on 28 Gbaud PDM-QPSK, PDM-16QAM and 7 Gbaud PDM-64QAM signals with up to 5000 ppm SFO being corrected at small penalties both in back-to-back and transmission scenarios.

Chapter 4

Performance Evaluation of a Colorless Coherent Optical Front-End in a WDM System

4.1 Overview

As articulated in section 1.2.1, a promising and viable technological solution to meet the growing capacity demand in optical transport networks is the concept of an agile/flexible software-defined optical network [17, 24]. In the envisioned agile network, flexible coherent transceivers, that are capable of adapting to dynamic traffic needs and thus maximizing the network capacity, are key elements that need to be deployed at ingress/egress nodes. These flexible transceivers need to be smart, data-rate and modulation format agile and impairment aware/tolerant. In addition, the notion of agility necessitates the ability of the transceiver to transmit / receive at any optical frequency in order to adapt to the dynamic nature of the network [25, 26]. Since external cavity lasers (ECLs) fully tunable over the C and L bands are commercially available [106], they can be incorporated as transmitter and LO lasers and hence, in principle, enable the transceiver to operate at any wavelength. At the transmitter side, tuning the laser simply varies the transmission wavelength without any observable change in the transmitted signal quality provided that the electro-optics performs similarly across the tuning range. However on the receiver side, the situation is more complex. A CRx can in principle operate in a colorless fashion by utilizing the LO laser for channel selection. Such a scheme mandates removing the demultiplexing filter before the receiver which is beneficial on one hand as it reduces cost and footprint besides offering the desired transceiver flexibility, but on the other hand, it may degrade the performance depending on various parameters e.g., the number of channels co-incident at the receiver with the channel of interest, the LO power, etc. Colorless reception in the context of coherent optical communication was studied from a theoretical standpoint more than two decades ago [107]; however, the absence of commercial narrow linewidth lasers and high speed integrated circuits (ICs) prevented any practical implementation. Recently, there have been some reports on experimental colorless coherent reception by utilizing

either a conventional CRx front-end followed by single-ended detection [108], which suffers from limited maximum channel count and poor dynamic range due to the inability to reject the self-beat common mode noise, or a more complicated receiver front-end followed by single-ended detection to enable rejecting the self-beat noise [109]. Later in [110], Zhang et al. presented design guidelines and performance limits of colorless reception employing balanced detection based on simulation and analytical predictions. More recently in [111], the authors demonstrated experimentally the use of an integrated PLC-based balanced coherent receiver for colorless reception of one 100G channel among 80 WDM channels.

The recent tremendous progress of the photonic integration technology allows for cost effective and volume production of coherent receivers employing balanced photodetectors which are more suited for colorless operation. Recently, integrated dual-polarization phase-diversity balanced coherent receiver photonic integrated circuits (PICs) have been demonstrated in both Si [112, 113] and InP [114, 115]. Si has advantages over InP as a host material since it can be made into larger wafers allowing for lower cost chips [35]. In addition, the world of analog ICs now offers linear and differential transimpedance amplifiers (TIAs) with variable gain control and bandwidths commensurate with the baud rates at which a coherent transceiver operates. Recently, researchers reported TIAs packaged and wire bonded to the PIC in one module [113, 115, 116]. The TIAs enhance the receiver dynamic range and provide the target voltage swing required by the analog-to-digital converters (ADCs). In addition, TIAs accompanied with the high sensitivity of coherent reception potentially enable preamplifierless operation in which the optical preamplifier prior to the receiver is removed and essentially replaced by the electrical TIAs thus saving footprint and power consumption.

In this chapter, we study from theoretical and experimental standpoints the performance limits of a Si-photonic CRx when employed in a WDM colorless configuration. Firstly, we show the building blocks and introduce the key characterization results of the CRx assembly presented in [113]. Secondly, we develop rigorously an analytical expression of the SNR at the CRx output in the case of colorless reception taking into consideration all sources of noise namely, LO-ON, SIG-SIG, SIG-ON, ON-ON and LO-LO beatings as well as the receiver shot and thermal noises, where SIG stands for signal and ON stands for optical noise incoming with the signal. As will be later explained in details, the ON incoming with the signal contains contributions of both the amplified spontaneous emission (ASE) noise from in-line optical amplifiers and the fiber

nonlinearity (NL) induced noise, which can be both modeled, according to [117-119], as additive white Gaussian noise (AWGN) in the context of dispersion unmanaged transmission (UT). Compared to [110] where an analytical SNR expression was also given, the derivation performed in this manuscript, which is based on evaluating the autocorrelation functions and the power spectral densities of all terms in the differential photocurrent, is more rigorous. In addition, we propose an analytical expression for an effective common mode rejection ratio (CMRR) for the SIG-SIG beating term which takes into account the frequency dependent nature of the power imbalance and the skew mismatch between the P and N photodiodes of the CRx weighted by the power spectral density of the received signal intensity. This parameter was only arbitrarily defined in [110]. Furthermore, another distinguishing difference from the model in [110] is the inclusion of the impact of fiber nonlinearity as excess AWGN in addition to the conventional ASE noise from in-line EDFAs. Thirdly, we study experimentally the performance of the CRx in: a) preamplifierless reception of a single channel 28 Gbaud PDM-QPSK and PDM-16QAM signals, b) colorless and preamplifierless reception of 16×112 Gbps PDM-QPSK WDM channels. The above single channel and WDM experimental results were presented in [43, 44]. For the WDM experiment, we first use a maximum LO power of 15.5 dBm and evaluate the BER of each channel at various transmission distances at received powers of -3 and -21 dBm per channel. Next, we restrict our measurements to one of the center channels of the WDM spectrum and perform an extensive set of measurements where we sweep the LO power, the received signal power, the distance and the number of channels presented to the CRx. This set of measurements aims at evaluating the performance limits of the CRx when used for colorless reception. Results reveal that in the regime of high received signal power, the residual SIG-SIG beat noise from the out-of-band (OOB) channels degrades the performance especially for lower LO to signal power ratios and this degradation becomes relatively less pronounced as the transmission distance increases. In the regime of low received signal power, the shot noise and receiver thermal noise degrade the performance especially for very low LO powers and short transmission distances. Two key CRx specifications that dictate the achievable dynamic operating range are highlighted namely the responsivity and the CMRR, which impact the performance in the regimes of low and high received signal powers, respectively. Finally, we employ our experimental SNR results to fit the proposed analytical model to our experimental data using the least-squares criterion. An excellent match between experimental and analytical

SNRs is found. We finally use the model to extrapolate the SNR curves beyond our experimental capabilities and predict the SNR when the number of channels is larger than 16. We conclude that the CRx allows for colorless selection of the test channel out of a fully populated WDM spectrum with 80 channels while achieving error-free operation after 4800 km transmission provided that the LO and received signal powers are properly set [43].

This chapter is organized as follows. In section 4.2, the architecture of the SiP CRx assembly is presented and the main device-level characterization results are introduced. Section 4.3, supported by appendices A and B in sections 4.8 and 4.9, presents an analytical model for the SNR at the output of the CRx where various noise sources that impact the SNR in a colorless reception scheme are outlined. Next, section 4.4 presents the system-level single channel experimental results obtained using the SiP CRx on both 112 Gb/s PDM-QPSK and 224 Gb/s PDM-16QAM aiming at studying the CRx sensitivity limits when used without an optical preamplifier. In section 4.5, we present the system-level WDM experimental results obtained using the CRx for colorless reception of 16×112 Gb/s PDM-QPSK channels where a thorough experimental parametric study of the impact of the LO power, received signal power, number of channels and transmission distance on the performance of colorless reception is conducted. Next in section 4.6, the WDM experimental data obtained from the parametric study is compared to theoretical values predicted by the developed analytical model presented in section 4.3. Finally, concluding remarks are given in section 4.7.

4.2 SiP balanced coherent receiver design and characterization

The coherent receiver is based on silicon photonics (SiP) technology which enables a very compact design. Fig. 4.1(a) gives a view of the assembly. Strip waveguides of 220 nm (height) \times 500 nm (width) are used to convey the light in the optical chip. A single-mode and a PM fiber whose end facets are polished at an angle close to 45° are used to couple the light from the data-carrying signal and LO respectively into the SiP chip. Polarization diversity is obtained via a 2D surface grating that couples orthogonal linear polarization states from the data-carrying signal in two separate waveguides. For the LO, a 1D grating coupler is used, followed by a 1×2 multimode interference (MMI) splitter. The light from each polarization of the incoming signal is combined to the light from the split LO using 2×4 MMI couplers. The light from the two 2×4 MMI couplers is coupled out of the chip using eight 1D grating coupler and sent to two 1×4

photodiode arrays which are flip chip mounted onto the $6\text{ mm} \times 6\text{ mm}$ SiP chip. The photodiodes are used in balanced pairs and connected to TIAs. The SiP chip and TIAs are fixed onto a ceramic substrate. RF lines connect the AC-coupled differential outputs of the TIAs to eight pins on the CRx package in a GSGSG configuration. For the sake of the present experiments, an RF interface board is used to provide access to a set of four single-ended outputs (XI^+ , XQ^+ , YI^+ and YQ^+) on K connectors. The assembled CRx has a small-signal bandwidth of 22 GHz and a quadrature error of less than 3° . The effective responsivity at 192.9 THz averaged over all 8 photodiodes (PDs) is 0.025 and 0.029 A/W for the SIG and LO ports, respectively. These effective responsivities include (besides the PD responsivities) the 3 dB intrinsic loss of the polarization beam splitter (PBS) and the 6 dB intrinsic loss of the 2×4 MMI coupler in addition to their excess loss as well as coupling losses in and out of the SiP chip. Fig. 4.1(b) shows the overall small signal frequency response including the photodiodes, the TIA and the RF lines on the ceramic. The overshoot in the response is due to the TIA. Finally, Fig. 4.2(a) and Fig. 4.2(b) show the CMRR versus frequency curves for the LO and SIG ports, respectively measured at the four output ports at 192.9 THz according to the procedure described in [120]. We notice that the CRx provides a DC CMRR better than -14 and -18 dB for the LO and SIG ports, respectively.

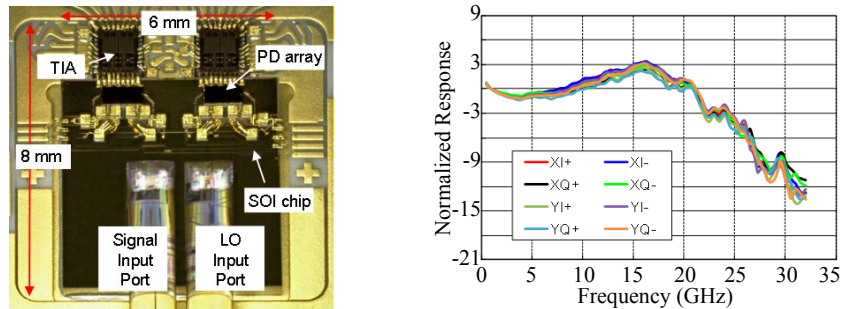


Fig. 4.1. (a) Picture of the PIC of the CRx showing the main building blocks, (b) Overall frequency response of the Si-photonic CRx assembly.

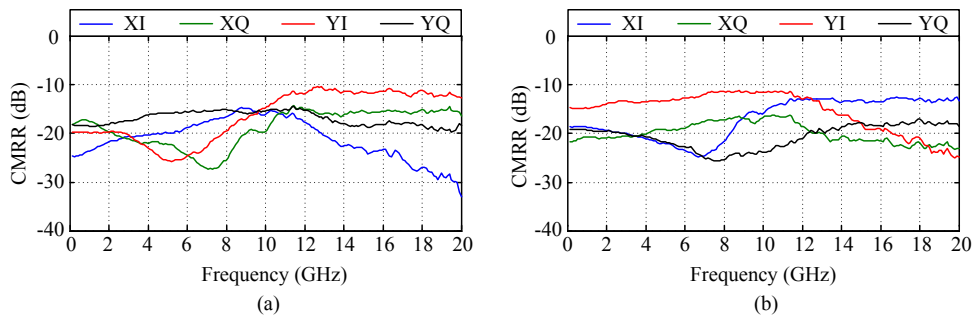


Fig. 4.2. CMRR versus frequency curves measured at 192.9 THz at the four output RF ports of the CRx when light is applied at the (a) signal port, (b) LO port.

4.3 Theoretical performance evaluation of a colorless coherent receiver

After laying out the CRx chip architecture in section 4.2, the performance of the CRx when employed for colorless coherent reception is evaluated analytically in this section. We present the various noise sources that dictate the performance of colorless CRx operation, highlighting the key CRx specifications that impact the performance. An analytical expression for the SNR at the CRx output is developed. The SNR analytical model derived will be employed later in this chapter in section 4.6 to verify the experimental results and fit the analytical model derived hereafter.

Although an analytical SNR expression for the colorless scenario when employing coherent balanced detection has been presented in [110], a more rigorous and complete approach is adopted in this manuscript. Without loss of generality, we consider one of the four CRx output ports $\{XI, XQ, YI, YQ\}$ and derive an expression of the autocorrelation function (ACF) (and then the power spectral density PSD) of the differential photocurrent after imperfect balanced detection. The desired signal term as well as various noise terms in the final differential photocurrent are identified and their respective ACFs (and PSDs) are derived methodically in terms of input fields to the CRx. Compared to [110], the expressions we obtain hereafter are more complete and the systematic approach adopted throughout the derivation leads to an expression for an “effective CMRR” which is a system parameter that quantifies the ability of balanced detection to reject the SIG-SIG beating, taking into account the frequency dependent nature of the power imbalance and the skew mismatch between the P and N photodiodes of the CRx weighted by the PSD of the received signal intensity. This quantity termed “effective CMRR” was proposed and only arbitrarily defined in [110]. Furthermore, another distinguishing difference from the work in [110] is that the optical noise incoming with the received signal assumed in our model contains the impact of not only the ASE noise from in-line EDFAs but also the induced noise due to fiber nonlinearity where both noise sources can be modeled as AWGN in the context of dispersion unmanaged transmission [117-119].

The procedure used to derive the ACFs and PSDs for various terms in the differential photocurrent follows the one outlined in [121]. We start by writing the photocurrents at the outputs of the P and N photodiodes (PDs), denoted by $i^P(t)$ and $i^N(t)$, in terms of the real electric fields of the signal (all WDM channels and their accompanying optical noise) and LO as

$$\begin{aligned}
i^P(t) &= \left[\sum_{i=1}^{N_{ch}} \sqrt{R_{SIG,i}^P} (E_{SIG,i}(t) + E_{ON,i}(t)) + \sqrt{R_{LO,s}^P} (E_{LO}(t)) \right]^2 + i_{sh}^P + i_{th}^P \\
&\approx 2\sqrt{R_{SIG,s}^P R_{LO,s}^P} [E_{SIG,s}(t)E_{LO}(t) + E_{ON,s}(t)E_{LO}(t)] \\
&\quad + \sum_{i=1}^{N_{ch}} R_{SIG,i}^P [E_{SIG,i}^2(t) + E_{ON,i}^2(t) + 2E_{SIG,i}(t)E_{ON,i}(t)] + R_{LO,s}^P E_{LO}^2(t) + i_{sh}^P + i_{th}^P, \tag{4.1}
\end{aligned}$$

$$\begin{aligned}
i^N(t) &= \left[\sum_{i=1}^{N_{ch}} \sqrt{R_{SIG,i}^N} (E_{SIG,i}(t-\delta) + E_{ON,i}(t-\delta)) - \sqrt{R_{LO,s}^N} (E_{LO}(t-\delta)) \right]^2 + i_{sh}^N + i_{th}^N \\
&\approx -2\sqrt{R_{SIG,s}^N R_{LO,s}^N} [E_{SIG,s}(t-\delta)E_{LO}(t-\delta) + E_{ON,s}(t-\delta)E_{LO}(t-\delta)] \\
&\quad + \sum_{i=1}^{N_{ch}} R_{SIG,i}^N [E_{SIG,i}^2(t-\delta) + E_{ON,i}^2(t-\delta) + 2E_{SIG,i}(t-\delta)E_{ON,i}(t-\delta)] \\
&\quad + R_{LO,s}^N E_{LO}^2(t-\delta) + i_{sh}^N + i_{th}^N, \tag{4.2}
\end{aligned}$$

where $E_{SIG,i}$, $E_{ON,i}$, E_{LO} are the real-valued electric fields of the i^{th} signal out of N_{ch} WDM signals presented to the CRx in colorless scheme, optical noise accompanying the i^{th} WDM signal, and local oscillator (LO) all measured at the input to the CRx, respectively. Without loss of generality, we assume that channel $s \in \{1, 2, \dots, N_{ch}\}$ is the desired channel in the WDM spectrum. Also, we assume that the LO frequency is tuned such that the frequency offset between the LO and the center frequency of channel s is much less than its baseband bandwidth, i.e. intradyne reception is used. Thus, the LO beating with OOB channels will lie outside the CRx bandwidth and hence was eliminated in the second equality of Eqs. (4.1) and (4.2). Also, we assume that $E_{ON,i}$ is the total incoming optical noise with the i^{th} WDM channel which contains both the ASE noise from in-line optical amplifiers and the noise induced due to fiber NL. According to [117-119], the NL-induced noise in case of dispersion uncompensated transmission can be modeled accurately as AWGN similar to ASE noise and hence, both additive noises can be combined in one total optical noise field which finally results in a worse optical signal-to-noise ratio (OSNR) governing the system performance [118]. According to [118], this modified OSNR at the CRx input is defined as $OSNR = P_{SIG}/P_{ON}$ where $P_{ON} = P_{ASE} + P_{NL}$ is the total optical noise power due to both ASE and NL contributions. As will be shown in section 4.6, both the ASE noise and the NL-induced noise scale linearly with transmission distance (assuming the NL-induced noise contributions from multiple spans are approximately summed incoherently [117, 118]) and will be indistinguishable in our experimental data since the launch

power was kept constant throughout the measured data. In addition, $R_{SIG,i}^P, R_{SIG,i}^N$ are the effective responsivities at the wavelength of the i^{th} channel measured at the P and N PDs to the optical power applied to the signal port. In addition, $R_{LO,s}^P, R_{LO,s}^N$ are the effective responsivities measured at the P and N PDs to the LO power applied at the wavelength of channel s . It is also noteworthy that the effective responsivities defined above take into account (besides the photodiode responsivities) the 3 dB intrinsic loss of the polarization beam splitter (PBS) and the 6 dB intrinsic loss of the 2×4 MMI coupler in addition to their excess loss as well as coupling losses in and out of the SiP chip. In addition, δ is the time skew between the P and N paths measured from the output of the MMI couplers up to current subtraction which occurs inside the TIA. Finally, i_{sh}^P, i_{sh}^N are the shot noise currents at the P and N photodiode outputs and i_{th}^P, i_{th}^N are the input-referred thermal noise currents at the P and N inputs of the TIA, respectively. In Eqs. (4.1) and (4.2), we also neglect the SIG-SIG beating between each WDM channel with its neighbors and consider only the beating between each signal with itself which lies within the CRx bandwidth. Although a portion of the spectral components from the beating between two adjacent WDM channels may fall inside the baseband CRx bandwidth, this portion is negligible compared to the SIG-SIG beating of each channel with itself especially after being lowpass filtered by the CRx frequency response.

Similar to [121], we express the real-valued fields in Eqs. (4.1) and (4.2) in terms of baseband complex envelopes (denoted by boldface symbols throughout the manuscript) as

$$\begin{aligned} E_{SIG,i}(t) &= \text{Re}\left\{\tilde{\mathbf{E}}_{SIG,i} e^{j2\pi\nu_{SIG,i}t}\right\}, \\ E_{LO}(t) &= \text{Re}\left\{\tilde{\mathbf{E}}_{LO} e^{j2\pi\nu_{LO}t}\right\}, \\ E_{ON,i}(t) &= \text{Re}\left\{\tilde{\mathbf{E}}_{ON,i} e^{j2\pi\nu_{SIG,i}t}\right\}, \end{aligned} \quad (4.3)$$

where $\tilde{\mathbf{E}}_k$ is the baseband complex envelope representing the real bandpass field $E_k(t)$ and $e^{j2\pi\nu_k t}$ is the complex-valued carrier at the optical frequency ν_k . Now, one can use the relation

$$\begin{aligned} E_1(t)E_2(t) &= \text{Re}\left\{\tilde{\mathbf{E}}_1 e^{j2\pi\nu_1 t} \tilde{\mathbf{E}}_2 e^{j2\pi\nu_2 t}\right\} \\ &= \frac{1}{2} \text{Re}\left\{\tilde{\mathbf{E}}_1 \tilde{\mathbf{E}}_2 e^{j2\pi(\nu_1 + \nu_2)t} + \tilde{\mathbf{E}}_1 \tilde{\mathbf{E}}_2^* e^{j2\pi(\nu_1 - \nu_2)t}\right\}, \end{aligned} \quad (4.4)$$

to re-write Eqs. (4.1) and (4.2) noting that the terms at the sum of optical frequencies will be filtered out, yielding

$$\begin{aligned}
i^P(t) &= 2\sqrt{R_{SIG,s}^P R_{LO,s}^P} \cdot \frac{1}{2} \operatorname{Re} \left\{ \tilde{\mathbf{E}}_{SIG,s} \tilde{\mathbf{E}}_{LO}^* + \tilde{\mathbf{E}}_{ON,s} \tilde{\mathbf{E}}_{LO}^* \right. \\
&\quad \left. + \frac{1}{2} \sum_{i=1}^{N_{ch}} R_{SIG,i}^P \left[\tilde{\mathbf{E}}_{SIG,i} \tilde{\mathbf{E}}_{ON,i} + \tilde{\mathbf{E}}_{SIG,i} \tilde{\mathbf{E}}_{ON,i}^* \right] \right. \\
&\quad \left. + R_{LO,s}^P \cdot \frac{1}{2} \left| \tilde{\mathbf{E}}_{LO} \right|^2 + i_{sh}^P + i_{th}^P \right\}, \tag{4.5}
\end{aligned}$$

$$\begin{aligned}
i^N(t) &= -2\sqrt{R_{SIG,s}^N R_{LO,s}^N} \cdot \frac{1}{2} \operatorname{Re} \left\{ \tilde{\mathbf{E}}_{SIG,s} \tilde{\mathbf{E}}_{LO}^* e^{j\Delta\nu(t-\delta)} \right. \\
&\quad \left. + \tilde{\mathbf{E}}_{ON,s} \tilde{\mathbf{E}}_{LO}^* e^{j\Delta\nu(t-\delta)} \right\} \\
&\quad + \frac{1}{2} \sum_{i=1}^{N_{ch}} R_{SIG,i}^N \left[\tilde{\mathbf{E}}_{SIG,i} \tilde{\mathbf{E}}_{ON,i} + \tilde{\mathbf{E}}_{SIG,i} \tilde{\mathbf{E}}_{ON,i}^* \right] \\
&\quad + R_{LO,s}^N \cdot \frac{1}{2} \left| \tilde{\mathbf{E}}_{LO} \right|^2 + i_{sh}^N + i_{th}^N, \tag{4.6}
\end{aligned}$$

where $\Delta\nu = \nu_{SIG,s} - \nu_{LO}$ is the frequency offset between the center frequency of channel s and the LO. Next, the difference between the P and N photocurrents in Eqs. (4.5) and (4.6), which represents the final differential photocurrent, can be written as

$$\begin{aligned}
\Delta i(t) &= i^P(t) \otimes h^P(t) - i^N(t) \otimes h^N(t) \\
&= \Delta i_{LO-SIG}(t) + \Delta i_{LO-ON}(t) + \Delta i_{SIG-SIG}(t) + \Delta i_{ON-ON}(t) + \Delta i_{SIG-ON}(t) \\
&\quad + \Delta i_{LO-LO}(t) + \Delta i_{sh}(t) + \Delta i_{th}(t), \tag{4.7}
\end{aligned}$$

where \otimes denotes convolution, $h^P(t)$ and $h^N(t)$ are the impulse responses of the P and N paths from the PD outputs up to current subtraction in the TIAs, i.e. they include the impact of limited bandwidth of PDs, TIA and wire bonding between them. Ideally, $h^P(t)$ and $h^N(t)$ should be the same but the slight difference between the frequency responses should be taken into account since it will impact the frequency dependence of the common mode rejection ratio of the CRx. In Eq. (4.7), we separate the individual contributions in the final photocurrent where the first term is the LO-SIG beating term which is the desired signal term resulting from subtracting the first terms of Eqs. (4.5) and (4.6) after convolving each of them with $h^P(t)$ and $h^N(t)$. The next terms in Eq. (4.7) represent all noise contributions in the final differential photocurrent due to LO-ON, SIG-SIG, ON-ON, SIG-ON, LO-LO beatings as well as shot and thermal noises which

also result from subtracting all terms subsequent to the LO-SIG term in Eqs. (4.5) and (4.6) after convolving with the P and N impulse responses.

In case of ideal balanced detection, i.e. when $R_{SIG,i}^P = R_{SIG,i}^N$, $R_{LO,s}^P = R_{LO,s}^N$, $h^P(t) = h^N(t)$ and $\delta = 0$, the SIG-SIG, ON-ON, SIG-ON and LO-LO noise terms in Eq. (4.7) cancel out since these terms are common to both the P and N PDs and will be entirely rejected. In this case, the LO-ON beating as well as the thermal and shot noises become the only noise sources contributing to the final differential photocurrent. However in reality, imperfect balanced detection due to frequency dependent power imbalance and skew mismatch between the P and N photocurrents will lead to residual noise power due to imperfect common mode rejection. For the rest of the derivation, we assume imperfect balanced detection and derive the time-averaged ACF of $\Delta i(t)$ in Eq. (4.7), which is denoted by $\bar{\Gamma}_{\Delta i}(\tau)$, as follows

$$\begin{aligned} \bar{\Gamma}_{\Delta i}(\tau) &= \overline{\langle \Delta i(t) \Delta i(t-\tau) \rangle} \\ &= \bar{\Gamma}_{\Delta i_{LO-SIG}}(\tau) + \bar{\Gamma}_{\Delta i_{LO-ON}}(\tau) + \bar{\Gamma}_{\Delta i_{SIG-SIG}}(\tau) + \bar{\Gamma}_{\Delta i_{ON-ON}}(\tau) + \bar{\Gamma}_{\Delta i_{SIG-ON}}(\tau) \\ &\quad + \bar{\Gamma}_{\Delta i_{LO-LO}}(\tau) + \bar{\Gamma}_{\Delta i_{sh}}(\tau) + \bar{\Gamma}_{\Delta i_{th}}(\tau), \end{aligned} \quad (4.8)$$

where $\langle \rangle$ denotes ensemble (statistical) averaging and the bar denotes time averaging. In deriving Eq. (4.8), all the cross correlation terms between currents from various sources can be shown to cancel out by the use of statistical independence between different fields as well as the fact that $\langle \tilde{\mathbf{E}}_i \tilde{\mathbf{E}}_j \rangle = 0$ for all fields. This finally means that the ACF of the final photocurrent is the sum of the ACFs of all individual terms in Eq. (4.7). The next step is to find the individual ACFs, i.e. each term in Eq. (4.8), in terms of the input fields as well as the CRx parameters. After that, we make use of the Wiener–Khinchine theorem for non-stationary signals¹ which states that the power spectral density (PSD) of a non-stationary signal is the Fourier transform (FT) of its time-averaged ACF $\bar{\Gamma}_E(\tau)$ which can be applied to Eq. Eq. (4.8), yielding

¹ Although both LO and signal fields are stationary in their CW form, a modulated signal field is non-stationary rendering the final photocurrent difference Δi non-stationary. Hence, we apply both ensemble and time averaging to obtain a single argument time-averaged ACF from which the PSD is obtained using the Wiener–Khinchine theorem.

$$\begin{aligned}
S_{\Delta i}(f) &= \text{FT} \{ \bar{\Gamma}_{\Delta i}(\tau) \} \\
&= S_{\Delta i_{LO-SIG}}(f) + S_{\Delta i_{LO-ON}}(f) + S_{\Delta i_{SIG-SIG}}(f) + S_{\Delta i_{ON-ON}}(f) + S_{\Delta i_{SIG-ON}}(f) \\
&\quad + S_{\Delta i_{LO-LO}}(f) + S_{\Delta i_{sh}}(f) + S_{\Delta i_{th}}(f) \\
&\approx S_{\Delta i_{LO-SIG}}(f) + S_{\Delta i_{LO-ON}}(f) + S_{\Delta i_{SIG-SIG}}(f) + S_{\Delta i_{sh}}(f) + S_{\Delta i_{th}}(f), \tag{4.9}
\end{aligned}$$

where in the last equality, we neglect the ON-ON, SIG-ON and LO-LO contributions to the overall photocurrent difference². The argument behind neglecting those three terms is that they were found to be experimentally negligible compared to the SIG-SIG beating. In fact, this experimental observation is intuitive since the SIG-SIG, ON-ON and SIG-ON beatings are proportional to P_{SIG}^2 , P_{ON}^2 and $P_{SIG}P_{ON}$, respectively, where P_{SIG}, P_{ON} are the average optical powers of the received signal and the total optical noise real-valued fields within the bandwidth of one channel. Given that the OSNR level (defined similar to [118] as the ratio between the optical signal power to the total optical noise power including both ASE and NL-induced noises) at the CRx input at which error-free operation is achieved is relatively high (e.g. > 12 dB in 0.1 nm for 28 Gbaud PDM-QPSK), we can notice that ON-ON and SIG-ON beatings are negligible compared to SIG-SIG beating. Regarding the LO-LO beating, $S_{\Delta i_{LO-LO}}(f)$ is proportional to $P_{LO}^2 RIN(f)$, where P_{LO} is the average optical power of the LO field and $RIN(f)$ is the PSD of the relative intensity noise of the LO laser. Since the LO used in experiments had a RIN of around -145 dB/Hz and the maximum LO power used throughout experiments is 15.5 dBm, the LO RIN contribution to the final photocurrent was experimentally found to be negligible.

Using Eq. (4.9), we can evaluate the SNR achieved after offline DSP if we assume that the receiver side DSP will mitigate transmission impairments by employing various algorithms, some of which involving filtering of the final sampled photocurrent. If we assume only linear equalization within the DSP, i.e. no NL mitigation algorithms, and lump all filtering performed in DSP in the transfer function $H_{rx-DSP}(f)$, one can calculate the final SNR after DSP as the total power of the useful LO-SIG term after DSP filtering divided by the total AC power from various noise sources after filtering, which yields

² Despite that we neglect the ON-ON, SIG-ON and LO-LO terms in the final SNR expression derived, we provide the final expressions of the PSDs of each of those three noise contributions in appendix A (see subsection 4.8) for completeness.

$$\begin{aligned}
SNR &= \frac{\int_{-\infty}^{\infty} S_{\Delta i_{LO-SIG}}(f) |H_{rx-DSP}(f)|^2 df}{\int_{-\infty}^{\infty} \left[S_{\Delta i_{LO-ON}}(f) + S_{\Delta i_{SIG-SIG}}(f) + S_{\Delta i_{sh}}(f) + S_{\Delta i_{th}}(f) \right]^{AC} |H_{rx-DSP}(f)|^2 df} \\
&= \frac{P_{\Delta i_{LO-SIG}}}{\sigma_{\Delta i_{LO-ON}}^2 + \sigma_{\Delta i_{SIG-SIG}}^2 + \sigma_{\Delta i_{sh}}^2 + \sigma_{\Delta i_{th}}^2}, \tag{4.10}
\end{aligned}$$

where $[]^{AC}$ denotes keeping only the AC portion of each PSD involved in the integration. To further pursue the derivation, we should evaluate the PSDs involved in the integrations in Eq. (4.10) in terms of the input fields to the CRx as well as the CRx parameters. The rigorous way to perform such a task is to find the time-averaged ACFs of each term from which the Fourier transformation leads to the PSDs in Eq. (4.10). In appendix A, we provide the complete derivation of all ACFs and PSDs from which the powers required to evaluate the SNR in Eq. (4.10) are evaluated. If we substitute Eqs. (4.29), (4.32), (4.41), (4.42) and (4.43) derived in appendix A into Eq. (4.10), we reach the following final analytical expression for the SNR of one of the four electrical photocurrents

$$SNR = \frac{2P_{LO}P_{SIG}}{2c_1P_{LO}P_{ON} + c_2(\sigma_{\Delta i_{sh}}^2 + \sigma_{\Delta i_{th}}^2) + \overline{CMRR}_{SIG}N_{ch}\beta P_{SIG}^2}, \tag{4.11}$$

where c_1 , c_2 and \overline{CMRR}_{SIG} are obtained as follows

$$c_1 = \frac{\int_{-B_{ch}/2}^{B_{ch}/2} \left| H^P(f) \sqrt{R_{SIG,s}^P R_{LO,s}^P} + H^N(f) e^{j2\pi f \delta} \sqrt{R_{SIG,s}^N R_{LO,s}^N} \right|^2 |H_{rx-DSP}(f)|^2 df}{\int_{-\infty}^{\infty} \left| H^P(f) \sqrt{R_{SIG,s}^P R_{LO,s}^P} + H^N(f) e^{j2\pi f \delta} \sqrt{R_{SIG,s}^N R_{LO,s}^N} \right|^2 |G(f)|^2 |H_{rx-DSP}(f)|^2 df} \Bigg/ \int_{-\infty}^{\infty} |G(f)|^2 df,$$

$$c_2 = \frac{1}{\int_{-\infty}^{\infty} \left| H^P(f) \sqrt{R_{SIG,s}^P R_{LO,s}^P} + H^N(f) e^{j2\pi f \delta} \sqrt{R_{SIG,s}^N R_{LO,s}^N} \right|^2 |G(f)|^2 |H_{rx-DSP}(f)|^2 df} \Bigg/ \int_{-\infty}^{\infty} |G(f)|^2 df,$$

$$\overline{CMRR}_{SIG} = \frac{\int_{-\infty}^{\infty} \left| H^P(f) R_{SIG}^P - H^N(f) e^{j2\pi f \delta} R_{SIG}^N \right|^2 S_{\Delta i_{SIG}}^{AC}(f) |H_{rx-DSP}(f)|^2 df}{\int_{-\infty}^{\infty} \left| H^P(f) \sqrt{R_{SIG}^P R_{LO}^P} + H^N(f) e^{j2\pi f \delta} \sqrt{R_{SIG}^N R_{LO}^N} \right|^2 |G(f)|^2 |H_{rx-DSP}(f)|^2 df} \Bigg/ \int_{-\infty}^{\infty} |G(f)|^2 df,$$

and $\sigma_{\Delta i_{sh}}^2, \sigma_{\Delta i_{th}}^2$ are the variances (AC power) of the shot noise and thermal noise contributions in the differential photocurrent which are expressed by Eqs. (4.42) and (4.43) in appendix A. Also, the scaling factor β is defined in appendix A as the ratio between the AC power from the filtered photocurrent generated by the field intensity of one channel and its DC electrical power. In appendix B, a more thorough study of β is performed to assess its dependence on the residual chromatic dispersion (CD) and polarization orientation of the received signal. It should be noted that Eq. (4.11) was proved by considering only one of the four outputs provided by the CRx; however, the derived SNR expression has the same form for all ports except for using the parameters of each port, e.g. responsivities and frequency responses. Hence, an overall average SNR can be calculated by averaging the SNRs calculated at the four ports.

The quantity \overline{CMRR}_{SIG} denotes the so-called ‘‘effective CMRR’’ of the SIG-SIG beating which is a system parameter (not a CRx parameter) that quantifies the ability of imperfect balanced detection to reject the common-mode SIG-SIG beating while taking into account the CRx parameters, namely, the effective responsivities, frequency responses and time skew for the P and N paths up to current subtraction inside the TIAs, as well as the system parameters, namely, the residual CD, polarization orientation and pulse shape which are imbedded in the PSD of the intensity $S_{|\tilde{E}_{SIG}|}^{AC}(f)$ (see Eq. (4.40) in appendix A). In fact, the effective CMRR definition given above contains the quantity $|H^P(f)R_{SIG}^P - H^N(f)e^{j2\pi f\delta}R_{SIG}^N|^2$ which quantifies the CRx ability to reject the common mode SIG-SIG beating incoming from the SIG port. Since this rejection ability is frequency dependent, the effective CMRR expression also weighs this quantity using the PSD of the common mode quantity being rejected, i.e. the field intensity, as represented by $S_{|\tilde{E}_{SIG}|}^{AC}(f)$ in the \overline{CMRR}_{SIG} expression. Dividing by the denominator in the effective CMRR expression means that \overline{CMRR}_{SIG} is a measure of how strong the power of the residual common mode SIG-SIG beating is compared to that of the differential LO-SIG beating. This explains why the denominator is proportional to the product of responsivities of the SIG and LO ports whereas the numerator is proportional to the square of the responsivity of the SIG port. Finally, we should note that the above expression for the effective CMRR was obtained in a systematic and rigorous manner in the derivation included in appendix A. This differs from [110] where the authors proposed the interesting concept of an effective CMRR, being a single

averaged value applied to the common mode beating and defined quite arbitrarily as the CMRR value at half the Nyquist frequency.

4.4 Single channel experiment, results and discussion

4.4.1 Experimental setup and offline DSP

The experimental setup used for the single channel transmission is shown in Fig. 4.3. For both QPSK and 16QAM, the binary or 4-level in-phase (I) and quadrature (Q) signals at 28 Gbaud were generated from two MICRAM digital-to-analog converters (DACs) driven by two Xilinx FPGAs. They were then fed to a QAM transmitter, which comprises a single polarization LiNbO₃ double-nested Mach-Zehnder modulator driven by two high-speed RF amplifiers, to modulate the light from a 15.5 dBm CW external cavity laser (ECL) having a linewidth of less than 100 kHz. Single polarization power eye diagrams are shown in the insets of Fig. 4.3 for both single polarization QPSK and 16QAM. Next, PDM was emulated with a decorrelation delay of 700 symbols. The PDM signal was launched at the optimum launch power (-1 dBm) into a recirculating loop containing 4×80 km of SMF-28e⁺ fiber, each followed by an erbium-doped fiber amplifier (EDFA) having a noise figure of 5 dB. At the output of the loop, noise loading allows to vary the OSNR and a VOA is used to sweep the received optical power P_{SIG} . In this series of single channel experiments, we compare two reception strategies: 1) filterless and preamplifierless reception in which the attenuated signal is fed directly to the signal port of the CRx module, 2) filtered and preamplified reception in which the attenuated signal first passes through an optical preamplifier inserted between a pair of 0.4 nm optical filters, prior to the receiver (see grey-shaded box in Fig. 4.3). The first and second of these optical filters remove out-of-band ASE noise from the inline EDFAs and preamplifier respectively. For fairness of the comparison, we maintain a fixed target voltage swing for the output electrical signals by adjusting either the TIA gain (G_{TIA}) in strategy (1) or the preamplifier gain (G_{PA}) in strategy (2). Throughout all experiments, a 15.5 dBm ECL was used for the LO. After the CRx, the four baseband signals were sampled and recorded by one Agilent DSOX96204Q 80 GSa/s scope.

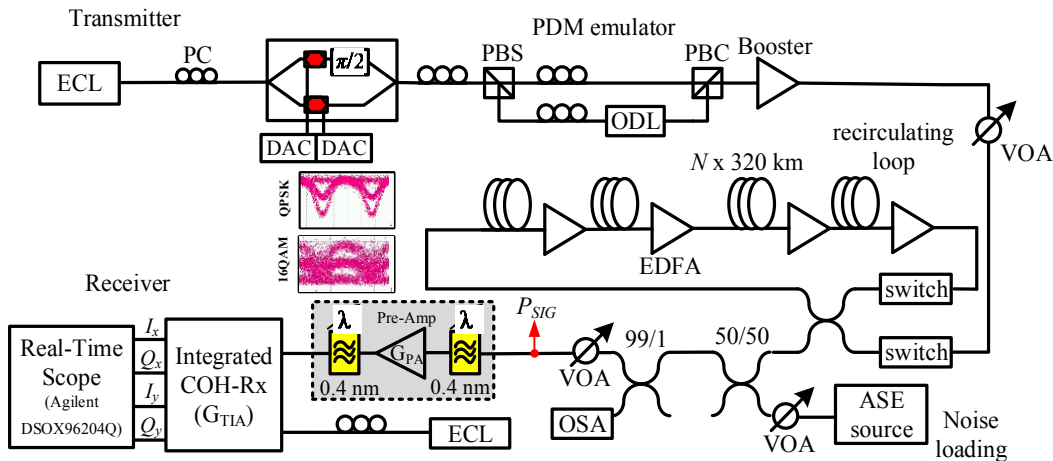


Fig. 4.3. Single channel experimental setup.

Offline processing starts by IQ imbalance and quadrature error correction, resampling to 2 samples per symbol, chromatic dispersion (CD) compensation and frequency offset removal using the periodogram method [91]. Polarization is then demultiplexed using a 31-tap butterfly equalizer. For PDM-QPSK, taps are updated using the constant modulus algorithm (CMA) with a step size of 1×10^{-3} [9]. For PDM-16QAM, taps are updated using training symbol based least mean squares algorithm with a step size of 1×10^{-3} for the first 1000 symbols before switching to decision-directed LMS (DD-LMS) with 4×10^{-4} step size at steady state. Phase noise was mitigated by a decision-directed phase locked loop. Finally, hard decision and BER estimation are performed.

4.4.2 Results and discussion

We compare the sensitivity of the filterless / preamplifierless reception with that of the filtered / preamplified reception for both single channel 28 Gbaud PDM-QPSK and PDM-16QAM at 192.9 THz with fixed target voltage swing. We start by comparing the back-to-back Q^2 factor versus received signal power P_{SIG} curves for both strategies. In the preamplifierless case, we vary the TIA gain (G_{TIA}) to achieve a 320 mVpp voltage swing (single-ended) whereas for the preamplified case, we vary the preamplifier gain (G_{PA}) to obtain the same swing. As P_{SIG} decreases in Fig. 4.4(a), we observe that the difference in Q^2 factor between both strategies in back-to-back (blue and red curves) increases to reach 4 dB for QPSK and 3 dB for 16QAM at

P_{SIG} of -23 dBm. The more likely reason for the performance difference at low P_{SIG} is the much lower optical signal power hitting the photodetectors in the preamplifierless case which makes the LO shot noise and thermal noise dominant relative to the signal-LO beat term. We also show in Fig. 4.4(a) the Q^2 factor versus P_{SIG} after transmission (dashed curves). After 4480 km QPSK transmission, preamplifierless reception achieves a Q^2 factor that is 1 dB less than preamplified reception at P_{SIG} of -23 dBm. For 640 km 16QAM transmission, the Q^2 factor difference between the two strategies is 2 dB at P_{SIG} of -23 dBm. At low P_{SIG} , the smaller difference in Q^2 factor between both strategies after transmission compared to back-to-back does not mean that the penalty due to preamplifierless reception is smaller however, it is because the ASE noise floor is much higher after transmission. For comparison, we also plot in Fig. 4.4(a) the theoretical Q^2 factor corresponding to the FEC threshold for both QPSK and 16QAM (magenta lines).

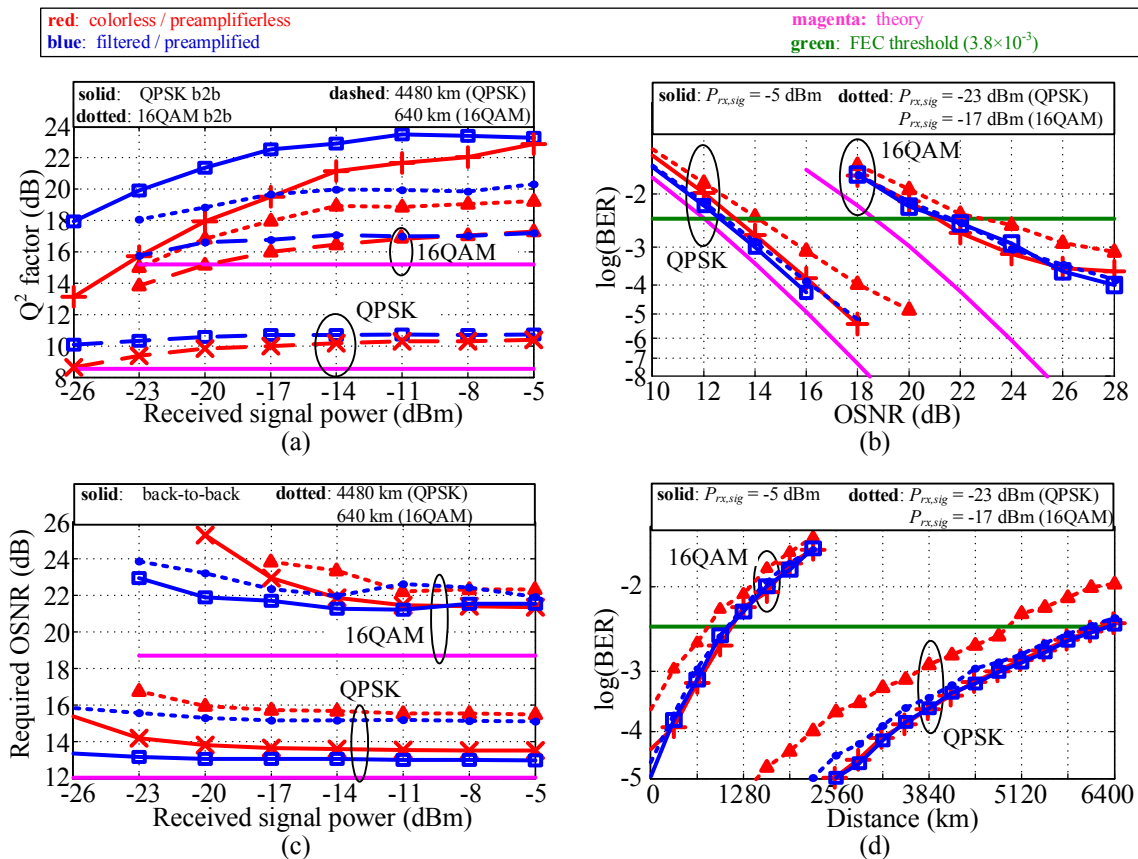


Fig. 4.4. Single channel 28 Gbaud PDM-QPSK and PDM-16QAM comparison between colorless / preamplifierless and filtered / preamplified strategies at 320 mVpp target swing: (a) Q^2 factor versus P_{SIG} , (b) back-to-back BER versus OSNR at different P_{SIG} , (c) required OSNR to achieve the FEC threshold versus P_{SIG} for back-to-back and transmission scenarios, (d) BER versus transmission distance with no noise loading at various P_{SIG} .

Next, Fig. 4.4(b) shows the back-to-back BER versus OSNR (in 0.1 nm) curves obtained with both strategies at P_{SIG} of -5 and -23 dBm for QPSK and -5 and -17 dBm for 16QAM. For QPSK at $P_{SIG} = -5$ dBm, preamplifierless reception achieves 1.5 dB OSNR penalty relative to theory at the FEC threshold (magenta curves) compared to 1 dB for the preamplified case. An additional 0.7 dB OSNR is required by the preamplifierless strategy at $P_{SIG} = -23$ dBm compared to merely 0.2 dB more OSNR needed in the preamplified case. For 16QAM at $P_{SIG} = -5$ dBm, both strategies achieve less than 3 dB OSNR penalty from theory. At $P_{SIG} = -17$ dBm, an additional 1.6 dB OSNR is required for the preamplifierless strategy compared to merely 0.2 dB more OSNR needed in the preamplified case.

Fig. 4.4(c) shows the required OSNR at the FEC threshold versus P_{SIG} for back-to-back and transmission scenarios. For QPSK (bottom set of curves), 15.1-15.5 dB OSNR is needed after 4480 km transmission at $P_{SIG} = -5$ dBm for either preamplified or preamplifierless reception which is 2 dB higher than back-to-back at the same P_{SIG} due to transmission penalty (mostly fiber nonlinearity). As P_{SIG} decreases to -23 dBm, the OSNR required increases by about 1 dB in the case of preamplifierless reception, whereas it increases slightly, by 0.5 dB, for the preamplified case. For 16QAM (upper set of curves), 0.5-1 dB additional OSNR is required by both strategies after 640 km transmission compared to back-to-back at $P_{SIG} = -5$ dBm. As P_{SIG} drops to -17 dBm, an additional 1.5 dB OSNR is required in case of preamplifierless reception compared to an extra 0.4 dB needed in the preamplified case.

In Fig. 4.4(d), we plot the BER versus transmission distance for all scenarios without noise loading, i.e. the OSNR level is dictated by the in-line EDFAs. For QPSK, as P_{SIG} is decreased from -5 to -23 dBm, the reach drops from 6080 to 4800 km in case of preamplifierless reception. A very small decrease in reach from 6080 to 5760 km is noticed for preamplified reception. For 16QAM in the case of preamplifierless reception, the reach decreases from 960 to 640 km.

4.5 WDM experiment, results and discussion

In this section, we evaluate experimentally the system-level performance of the SiP CRx module whose chip architecture was described in section 4.2. First, we introduce the experimental setup

used to assess the CRx performance using 16×112 Gbps PDM-QPSK WDM channels. Subsequently, we present the experimental results, starting with the BER for all 16 channels at different distances and received signal powers. Afterwards, we present a series of extensive measurements obtained for one of the center WDM channels where the LO power, received signal power, distance, and number of channels presented to the CRx are swept. A thorough discussion of the results is given, focusing on the major noise sources affecting the performance of the colorless operation of the CRx for different operating parameters in view of the analytical SNR expression derived in section 4.3. Finally, we use the experimental SNR data to fit the analytical SNR expression derived in section 4.3. The fitted SNR model is then used to predict the SNR at other operating parameters beyond our experimental capabilities, e.g. larger number of WDM channels.

4.5.1 Experimental setup and offline DSP

Fig. 4.5 shows the experimental setup used in various WDM measurements presented in the following subsections. CW light from 16 distributed feedback (DFB) lasers (50 GHz spaced and centered at 192.9 THz) are multiplexed using a 50 GHz arrayed waveguide grating WDM multiplexer and then bulk modulated by means of a QAM transmitter. The QAM transmitter comprises a single polarization LiNbO₃ double-nested Mach-Zehnder modulator and two high-speed RF amplifiers to drive the two quadratures. Binary I and Q electrical signals are fed to the QAM transmitter from two MICRAM DACs driven by two Xilinx FPGAs at 28 Gbaud to realize 16×112 Gbps PDM-QPSK WDM channels on a 50 GHz grid. Then, a polarization beam splitter (PBS), variable optical delay line (VODL) and polarization beam combiner (PBC) are employed for PDM emulation with a decorrelation delay between the two orthogonal polarizations equivalent to 700 symbols at 28 Gbaud. After optical amplification, odd and even WDM channels are decorrelated by ~ 7.5 ns using a 50 GHz interleaver / de-interleaver. The resulting optical signal was attenuated using a variable optical attenuator (VOA) to set the launch power at -2 dBm per channel which was experimentally found to be the optimum launch power that achieves the right balance between fiber nonlinearity and ASE noise from in-line EDFAs. At this launch power, which was kept constant throughout the experiment, both ASE and NL-induced noises are non-negligible and hence, they were both included in the SNR model presented in section 4.3. Next, the resulting signal was launched into a recirculating loop containing four

spans of 80 km of SMF-28e+ fiber, each span being followed by an erbium-doped fiber amplifier (EDFA) having a noise figure of 5 dB. In addition, an optical WaveShaper from Finisar is inserted after the second in-line EDFA for gain flattening.

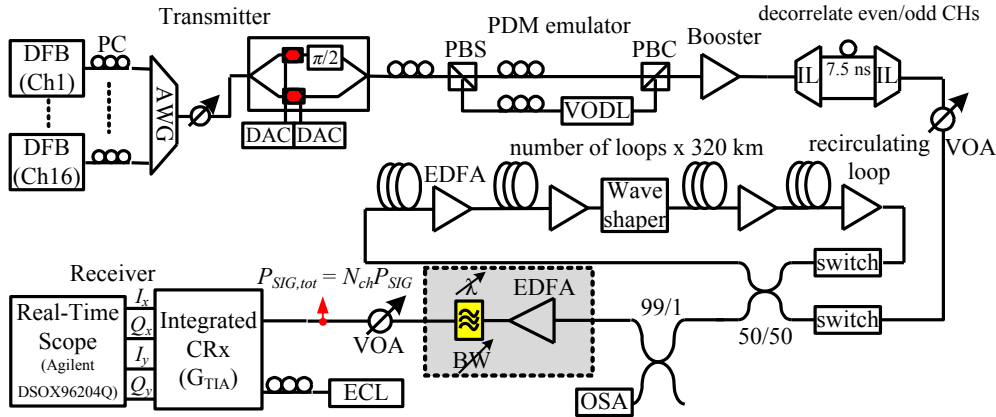


Fig. 4.5. Experimental setup for WDM experiments.

At the output of the loop, no noise loading is performed hence the OSNR is only dictated by the ASE noise from in-line EDFAs around the loop as well as the fiber NL-induced noise. We used a 99:1 coupler to monitor the WDM spectrum on an optical spectrum analyzer (OSA) and to measure the OSNR. After 1600, 3200 and 4800 km of transmission, i.e. 5, 10 and 15 loops respectively, the measured OSNRs, assuming a 0.1 nm reference bandwidth, were 21.4, 18.9 and 17.6 dB, respectively. After the 99:1 coupler, we distinguish between two reception configurations: a) fully colorless configuration in which the attenuated signal carrying all 16 channels is fed directly to the signal port of the CRx module at a total power level $P_{SIG,tot} (= N_{ch}P_{SIG})$ controlled by the VOA, i.e. elements in the grey shaded box are skipped, b) another configuration in which the WDM signal is first amplified to a constant total power of 22 dBm, subsequently filtered using a wavelength & bandwidth tunable filter, and then attenuated using a VOA to set the total received power level ($P_{SIG,tot}$) before finally entering the CRx, i.e. elements in the grey shaded box are employed. Inserting the EDFA prior to the CRx allows us to sweep $P_{SIG,tot}$, and subsequently the received power per channel (P_{SIG}), to levels larger than the received power from the loop. As will be observed in the next subsection, the sweep range of P_{SIG} extends up to 5 dBm per channel in order to evaluate the impact of colorless reception on the dynamic range of the CRx. After the EDFA, the wavelength & bandwidth tunable filter had its center frequency constantly set to that of channel 9 (with channel 1 having the smallest frequency) and its bandwidth swept to vary the number of channels presented to the CRx denoted by N_{ch} . Using

this filter, we can vary N_{ch} between 1 and 16, where the extreme cases correspond to fully filtered and fully colorless reception schemes, respectively.

In reception configuration (a), the frequency of the LO laser is swept to the center frequency of the channel desired to be selected out of the 16 available channels. However in configuration (b), the LO frequency is constantly set to channel 9 (channel of interest in this configuration) and the bandwidth of the tunable filter is set to control the number of out-of-band (OOB) WDM neighbors ($N_{ch} - 1$) co-incident on the CRx with channel 9. In both configurations, the VOA sets the received power level per channel (P_{SIG}) as desired prior to the CRx. At all received power levels, the voltage swing provided by the TIAs at the output of the CRx is maintained at a constant 320 mVpp (single-ended). Finally, the four electrical signals are sampled at 80 GSa/s using one Agilent DSOX96204Q real-time scope and stored for offline processing using a myriad of standard DSP algorithms to mitigate various impairments. All algorithms are the same as the ones explained in section 4.4.2.

4.5.2 Results and discussion

In this subsection, we present all experimental results obtained using the setup depicted in Fig. 4.5. In subsection 4.5.2.1, we show the results of reception configuration (a) in which fully colorless and preamplifierless strategy is employed. Next, subsection 4.5.2.2 presents all results collected on channel 9 employing reception configuration (b) where the EDFA and the tunable wavelength & bandwidth filter in the grey shaded box in Fig. 4.5 are inserted prior to the CRx. Using this configuration, various operating parameters such as the received signal power per channel (P_{SIG}), LO power (P_{LO}), number of channels (N_{ch}) incident on the CRx, and distance (L) are swept. Results collected from channel 9 include the SNR measured after offline DSP while sweeping the aforementioned parameters to evaluate the impact of each parameter on the performance of colorless CRx operation and to identify the dynamic range of the CRx for various number of channels. Based on the results, we also identify the key specifications of the CRx that are crucial for colorless operation. Later in section 4.6, we use the experimental SNR data at various operating parameters to fit the analytical SNR expression derived in section 4.3. The fitted SNR model is then used to predict the SNR at other operating parameters beyond our experimental capabilities, e.g. larger N_{ch} .

4.5.2.1 Configuration (a): BER for all channels at various distances using fully colorless and preamplifierless reception at either -3 dBm/ch or -21 dBm/ch

BERs of all 16 WDM channels were calculated and are plotted in Fig. 4.6 for 3200, 4480 and 4800 km transmission at two different P_{SIG} (-3 and -21 dBm per channel). All results in Fig. 4.6 are collected in the fully colorless and preamplifierless reception termed above by reception configuration (a). The LO power (P_{LO}) was set to 15.5 dBm and its frequency was tuned to select each one of the 16 channels before data was acquired. Insets at the right of Fig. 4.6 also show the WDM spectra in back-to-back and after 3200 km transmission obtained using a 0.05 nm resolution bandwidth on the OSA. We assume a 3.8×10^{-3} forward error correction (FEC) threshold, which is typical for the hard-decision FEC algorithm with 7% overhead defined in [122]. Then, if we carefully examine the BERs of all 16 channels, we can claim a 4800 km reach for all channels at P_{SIG} of -3 dBm which slightly decreases to 4160 km at -21 dBm per channel. As will be explained in upcoming subsections, the good performance (reach) achieved by the CRx for fully colorless and preamplifierless reception with very low received signal power of -21 dBm per channel is enabled by moderate CMRR and responsivity possessed by the CRx.

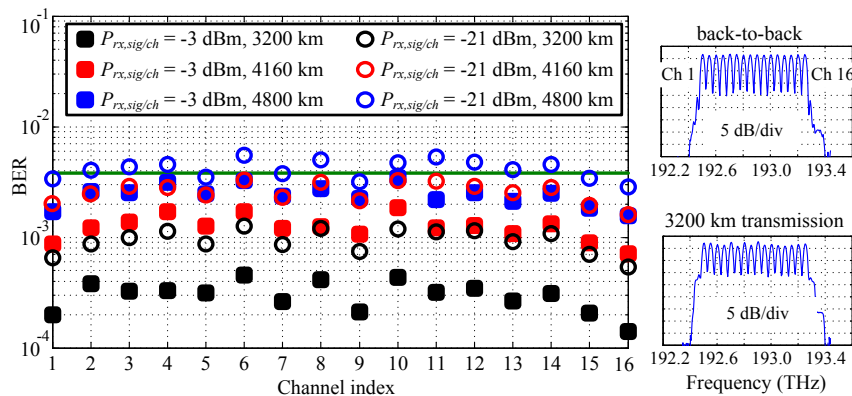


Fig. 4.6. BER for all WDM channels using fully colorless and preamplifierless reception at different transmission distances and at per channel received signal power of -3 and -21 dBm. Insets show the received WDM spectra in back-to-back and after 3200 km transmission where we observe a fairly flat spectrum due to the gain flattening waveshaper in the loop.

4.5.2.2 Configuration (b): Parametric study of SNR of channel 9 (center channel)

Having evaluated the CRx colorless / preamplifierless operation for each channel across the spectrum, we now focus on channel 9 specifically. All measurements on channel 9 presented in the upcoming subsections, which involve sweeping various experimental parameters such as P_{LO} , P_{SIG} , N_{ch} and L , will use the SNR calculated after offline DSP instead of BER as the performance metric. The reason for using SNRs instead of BERs is that SNRs allow us to assess the

performance quantitatively in back-to-back and short transmission distance scenarios when BERs are usually below 10^{-5} . Evaluating BERs in this low-error regime would require acquiring and storing a number of symbols exceeding the memory of the real-time scope used. Also, later in section 4.6, utilizing the experimental SNRs allows us to perform direct comparison with analytically predicted SNRs based on the derived SNR expression in section 4.3.

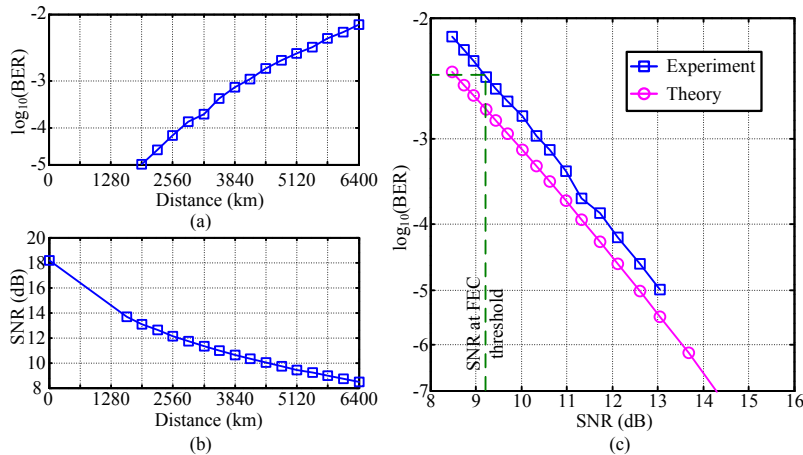


Fig. 4.7. Measurement results of channel 9: (a) BER versus transmission distance, (b) SNR evaluated after offline DSP versus distance, (c) BER versus SNR using both experimental results and theory where the experimental SNR corresponding to FEC threshold is marked.

Fig. 4.7 shows the relationship between experimentally evaluated BER and SNR for channel 9. In Fig. 4.7(a), we plot the calculated BER on a double log scale versus the transmission distance whereas Fig. 4.7(b) shows the corresponding SNR evaluated at these distances. Using both curves, we plot in Fig. 4.7(c) the BER versus SNR relationship found experimentally. We find that a 9.2 dB SNR corresponds to the 3.8×10^{-3} FEC threshold which is 0.67 dB higher than the theoretical SNR of 8.53 dB at this BER level for 28 Gbaud QPSK assuming an ideal additive white Gaussian noise (AWGN) channel [66]. By means of Fig. 4.7(c), all SNR results that will be presented in the forthcoming subsections can be mapped into BER values in a straightforward manner.

(a) Impact of received signal power and number of channels presented to the CRx on the SNR of channel 9 at various distances and LO powers

From this point forward, the entire measurements are performed only for channel 9 in the WDM spectrum. In Fig. 4.8(a)-Fig. 4.8(f), we show the SNR versus P_{SIG} at different LO powers of 15.5, 12, 9, 6, 3 and 0 dBm, respectively. In each subplot, we plot the SNR curves with different colors corresponding to various number of channels (N_{ch}) presented to the CRx where N_{ch} is set to

either 1, 5, 11 or 16 channels, ranging from fully filtered to colorless reception respectively. Also in each subplot, SNR curves measured at various transmission distances of 0, 1600, 3200 and 4800 km are plotted together where the top group of four curves always corresponds to the back-to-back case whereas the bottom set of curves represents the 4800 km transmission case. By examining Fig. 4.8(a)-Fig. 4.8(f), we notice that the sweep range of P_{SIG} starts at -24 dBm for $P_{LO} = 15.5$ and 12 dBm (see Fig. 4.8(a) and Fig. 4.8(b)), whereas for $P_{LO} = 9, 6, 3$ and 0 dBm the sweep range of P_{SIG} had to be reduced to start at -21, -18, -15 and -12 dBm, respectively (see Fig. 4.8(c)-Fig. 4.8(f)). The reason for increasing the lower end of the P_{SIG} sweep range for $P_{LO} \leq 9$ dBm is to be able to achieve the fixed target voltage swing of 320 mVpp after the TIAs at the CRx output. For that reason, at each $P_{LO} \leq 9$ dBm, the minimal value of the P_{SIG} sweep range was fixed to the least power level at which the TIAs could provide the 320 mVpp target swing when their respective gain was set to maximum (5 k Ω differential transimpedance Z_t). Since for a fixed target voltage swing, the required Z_t for the TIAs is proportional to $\sqrt{P_{LO}P_{SIG}}$, we notice in Fig. 4.8(c)-Fig. 4.8(f) that as P_{LO} is decreased by 3 dB going from one subfigure to the next, the starting point of the P_{SIG} sweep range (at maximum Z_t) increases by 3 dB agreeing with the above proportionality.

Looking at the SNR variation with P_{SIG} throughout Fig. 4.8(a)-Fig. 4.8(f), we notice that regardless of P_{LO} , L and N_{ch} , the SNR improves as P_{SIG} is increased to an extent after which the SNR starts to decrease if P_{SIG} is further increased. This means that an optimum P_{SIG} exists for each P_{LO} , L , and N_{ch} . Furthermore, if a certain target required SNR at a certain P_{LO} , L and N_{ch} is to be achieved, one can specify a dynamic range for P_{SIG} within which the target SNR is at least guaranteed. It is noticeable that the dynamic range of P_{SIG} at a given L and P_{LO} decreases as N_{ch} is increased from 1 to 16 showing the impact of colorless reception. Finally, the dynamic range of P_{SIG} at a given L and N_{ch} is also found to decrease when P_{LO} is decreased.

The two reasons for the SNR degradation at the low and high ends of P_{SIG} are distinct. At high received signal power ($P_{SIG} \sim 0$ dBm), the SNR degradation observed with a further increase of P_{SIG} is due to the residual SIG-SIG beat noise which is expressed by the last term in the denominator of Eq. (4.11). This SIG-SIG beat noise is proportional to $N_{ch}P_{SIG}^2$ which explains why the SNR degrades as P_{SIG} is increased and why this degradation is more pronounced as more channels are presented to the CRx. In fact, we can re-write Eq. (4.11) by neglecting the thermal and shot noises at high P_{SIG} and dividing by $P_{LO}P_{SIG}$, which yields

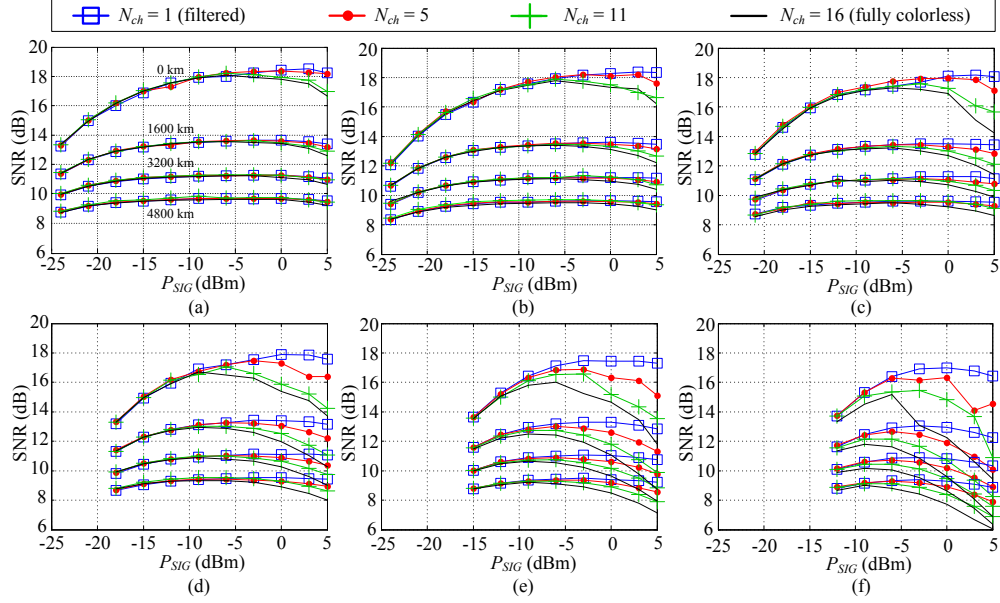


Fig. 4.8. SNR of channel 9 versus received signal power per channel P_{SIG} after 0, 1600, 3200 and 4800 km transmission with varying number of channels presented to the CRx at an LO power of: (a) 15.5 dBm, (b) 12 dBm, (c) 9 dBm, (d) 6 dBm, (e) 3 dBm, (f) 0 dBm. In each subfigure, different colors represent different number of channels N_{ch} according to the legend. Also, SNR evaluated after 0, 1600, 3200 and 4800 km transmission are shown in each subfigure where the top set of four curves in each subfigure is evaluated in back-to-back and the bottom set is after 4800 km transmission.

$$SNR = \frac{2}{2c_1 OSNR^{-1} + \frac{CMRR_{SIG} N_{ch} \beta \cdot LSR^{-1}},} \quad (4.12)$$

where LSR is the LO to signal power ratio at the CRx input. We can see from Eq. (4.12) that for a fixed OSNR, i.e. fixed distance, the SNR depends on the effective CMRR defined in section 4.3, N_{ch} and LSR . If more channels are introduced to the CRx, the SNR degrades due to larger SIG-SIG beating from the OOB neighbors. Also, the impact of the SIG-SIG beat noise can be greatly reduced if high enough LSR is employed, which is also apparent in Fig. 4.8 by observing the impact of P_{LO} on the SNR difference between the cases of $N_{ch} = 1$ and $N_{ch} = 16$, i.e. the SNR penalty due to colorless reception compared to filtered reception denoted by $\Delta SNR_{1,16}$, at a given L and at $P_{SIG} = 0$ dBm.

Since we are now interested in the high end of P_{SIG} and studying the impact of N_{ch} on SNR, we re-plot in Fig. 4.9 a portion of the results shown in Fig. 4.8 by focusing only on the SNR at $P_{SIG} = 0$ dBm. Fig. 4.9(a)-Fig. 4.9(f) show the SNR after 0, 1600, 3200 and 4800 km transmission versus N_{ch} at LO powers from 15.5 dBm down to 0 dBm, all at $P_{SIG} = 0$ dBm. This exactly corresponds to $LSRs$ ranging from 15.5 dB to 0 dB. By examining Fig. 4.9 carefully, we

notice that for $LSR \geq 9$ dB, i.e. $P_{LO} \geq 9$ dBm, $\Delta SNR_{1,16}$ in Fig. 4.9(a)-Fig. 4.9(c) is found to be < 1.2 dB at any of the various distances travelled, which is a reasonably small degradation given the transceiver flexibility and hardware savings gained in an entirely colorless reception scheme. In fact, this 1.2 dB SNR penalty due to colorless reception is only pronounced in back-to-back at $P_{LO} = 9$ dBm whereas $\Delta SNR_{1,16}$ is less after transmission. This can be explained in light of the approximate SNR expression in Eq. (4.12) by noting that the OSNR decreases as L increases and hence the SIG-SIG beat term becomes less significant relative to the first term. On the other hand for $LSR < 9$ dB, $\Delta SNR_{1,16}$ in Fig. 4.9(d)-Fig. 4.9(f) increases significantly where it becomes most apparent in Fig. 4.9(f) when $LSR = 0$ dB. In view of Eq. (4.12), it should be finally noted that the SNR degradation due to colorless reception can be greatly reduced by developing coherent receivers with improved CMRRs which results in a better rejection for the SIG-SIG beating from the OOB channels.

Looking back at Fig. 4.8 for low received signal powers ($P_{SIG} \leq -12$ dBm), we notice that the SNR degrades quickly as P_{SIG} decreases and that the SNR is independent of N_{ch} . Referring back to the general SNR expression in Eq. (4.11), we re-write the expression by neglecting the SIG-SIG beat term for low P_{SIG} and dividing by $P_{SIG}P_{LO}$, which yields

$$SNR = \frac{2}{2c_1 OSNR^{-1} + c_2 \cdot \frac{4eR_{LO}^{av}\Delta f}{P_{SIG}} + c_2 \cdot \frac{i_{TIA}^2 \Delta f}{P_{LO}P_{SIG}}}, \quad (4.13)$$

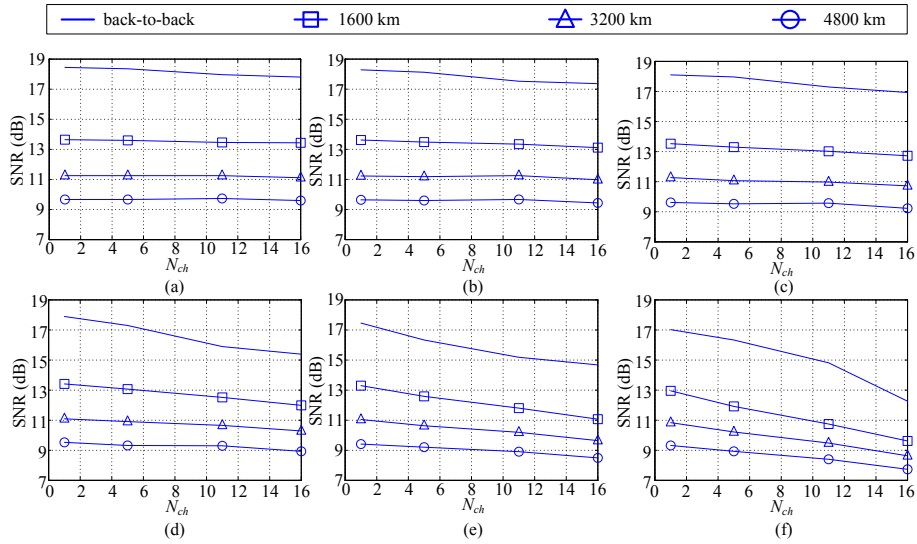


Fig. 4.9. SNR of channel 9 versus N_{ch} at $P_{SIG} = 0$ dBm after 0, 1600, 3200 and 4800 km transmission at P_{LO} of (a) 15.5 dBm, (b) 12 dBm, (c) 9 dBm, (d) 6 dBm, (e) 3 dBm, (f) 0 dBm.

where we neglected the signal contribution to the shot noise and kept only the LO shot noise term. In view of Eq. (4.13), we can easily explain the SNR trends at the low end of P_{SIG} in Fig. 4.8. First, it is clear that as P_{SIG} increases while P_{LO} is fixed, the SNR increases due to the second and third terms (shot and thermal noises) in the denominator of Eq. (4.13) being smaller which matches our observation in Fig. 4.8. In addition, we also observe in Fig. 4.8 that the impact of changing P_{SIG} is less pronounced as L increases which can be explained by the decrease in the OSNR with L , thus making the first term in the denominator of Eq. (4.13) larger compared to the second and third ones. Our next observation based on Eq. (4.13) is that increasing P_{LO} for a fixed P_{SIG} should also improve the SNR which goes along with the experimental results in Fig. 4.8. Comparing the impact of P_{SIG} and P_{LO} on the SNR in the low received signal power regime, we can observe in Fig. 4.8 that increasing P_{SIG} by 3 dB for a fixed P_{LO} results in a larger SNR improvement compared to increasing P_{LO} by 3 dB for a fixed P_{SIG} . As an example, if P_{SIG} is increased from -21 to -18 dBm at $P_{LO} = 9$ dBm, the SNR improves by 1.68 dB whereas the improvement is 1.26 dB if P_{LO} increases from 9 to 12 dBm while keeping P_{SIG} at -21 dBm. The observation that P_{SIG} has a slightly larger impact on the SNR compared to P_{LO} can also be explained in light of the denominator of Eq. (4.13) by noting that P_{SIG} affects both the second and third terms compared to P_{LO} impacting only one term. Next, we notice that the SNR in Eq. (4.13) is totally independent of N_{ch} at low P_{SIG} which agrees with Fig. 4.8. In order to further make this independence clear, we re-plot in Fig. 4.10 a portion of the results in Fig. 4.8 which are collected at $P_{SIG} = -12$ dBm. Fig. 4.10(a)-Fig. 4.10(f) show the SNR after 0, 1600, 3200 and 4800 km transmission versus N_{ch} at LO powers from 15.5 dBm down to 0 dBm, all at low P_{SIG} of -12 dBm. In Fig. 4.10, it is evident that N_{ch} has no impact on the SNR at either any distance or any P_{LO} at $P_{SIG} = -12$ dBm.

Finally, it should be also noted that the CRx responsivity is a key specification in this low P_{SIG} regime because according to Eq. (4.13) if all parameters stay the same while R_{SIG} and R_{LO} are increased, the SNR will consequently increase (note that $c_2 \propto (R_{SIG}R_{LO})^{-1}$). Physically speaking, larger responsivities translate into larger photocurrents from the PDs relative to the fundamental CRx noise. Although the CRx used in our experiments possess a moderate responsivity due to relatively high coupling losses into the SiP chip, it still allows for good performance at low P_{SIG} . For example when $P_{LO} = 12$ dBm, the SNR after 1600-4800 km

transmission degrades by < 1 dB when P_{SIG} decreases from 0 to -18 dBm while providing the same output voltage swing using the TIA gain.

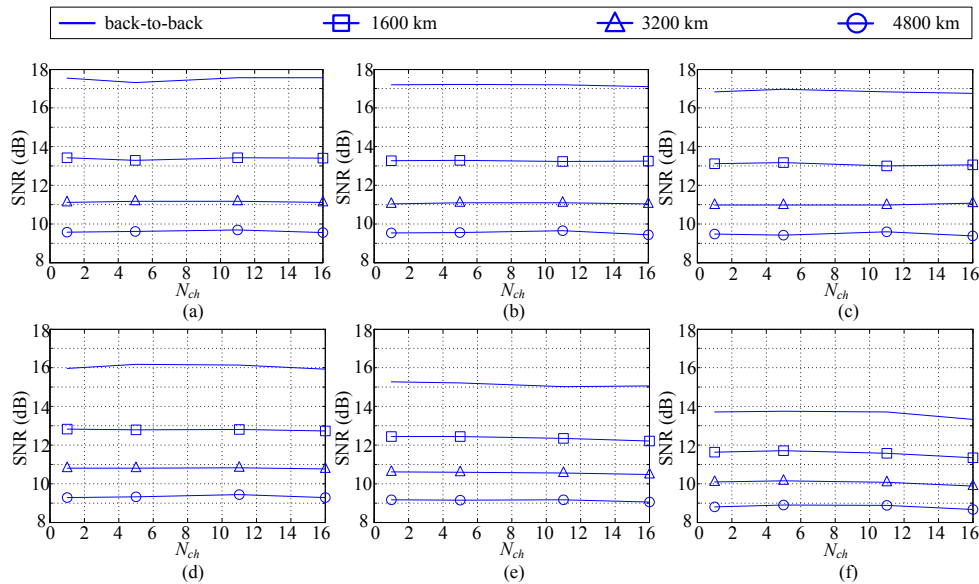


Fig. 4.10. SNR of channel 9 versus N_{ch} at $P_{SIG} = -12$ dBm after 0, 1600, 3200 and 4800 km transmission at P_{LO} of (a) 15.5 dBm, (b) 12 dBm, (c) 9 dBm, (d) 6 dBm, (e) 3 dBm, (f) 0 dBm.

(b) Impact of LO power on the SNR of channel 9 at various distances and number of channels presented to the CRx for both regimes of high and low received signal power

In this subsection, we explicitly show the impact of the LO power on the SNR of channel 9. In Fig. 4.11, we re-plot a portion of the results shown in Fig. 4.8 where we show the SNR versus P_{LO} at various distances and number of channels presented to the CRx for both regimes of high and low received signal powers ($P_{SIG} = 0$ and -15 dBm, respectively). For the $P_{SIG} = 0$ dBm case in Fig. 4.11(a), we observe how significant it is to choose a high LSR which greatly reduces the SNR penalty due to colorless reception. For example, changing the LSR from 0 to 12 dB reduces $\Delta\text{SNR}_{1,16}$ from 1.5-4.7 dB (for distances travelled from 4800 to 0 km) to 0.1-0.65 dB. This agrees with Eq. (4.12) as discussed in the previous subsection. Moving to Fig. 4.11(b) when $P_{SIG} = -15$ dBm, we notice that increasing P_{LO} improves the SNR and that the SNR is independent of N_{ch} which agrees with Eq. (4.13). As mentioned in section 4.3, the LO-LO beat noise was not observed throughout all experimental data because the RIN of our lasers is below -145 dB/Hz. However, it is noteworthy that as P_{LO} is increased beyond 15.5 dBm (maximum output power from our ECLs) at $P_{SIG} = -15$ dBm (see Fig. 4.11(b)), the LO-LO beat noise should eventually lead to SNR degradation.

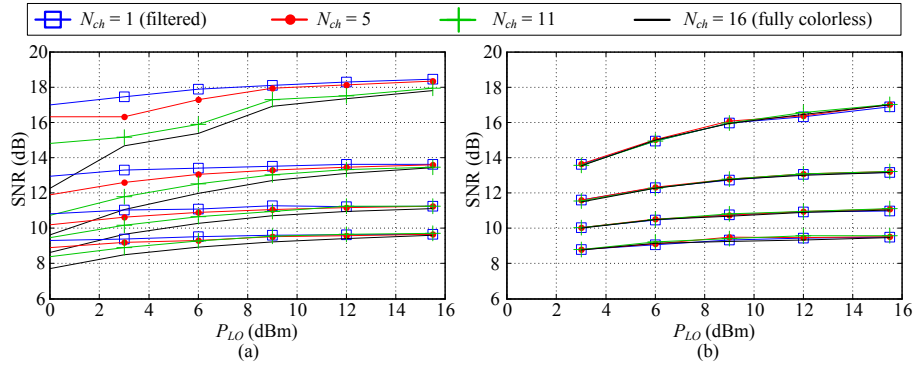


Fig. 4.11. SNR of channel 9 versus P_{LO} after 0, 1600, 3200 and 4800 km transmission at various N_{ch} and at P_{SIG} of: (a) 0 dBm, (b) -15 dBm.

(c) Two dimensional (2-D) plots of SNR of channel 9 versus LO power and received signal power at different distances in case of 1 (filtered) and 16 channels (colorless)

In this subsection, we re-present the experimental data of Fig. 4.8 corresponding to the extreme cases of $N_{ch} = 1$, i.e. filtered operation and $N_{ch} = 16$, i.e. fully colorless operation. Here, we present the SNR data as two dimensional (2-D) plots versus both P_{SIG} and P_{LO} as the two independent variables being swept. Fig. 4.12 depicts these 2-D plots where different SNR values are encoded into different colors according to the color bars beside each subfigure (red representing higher SNR whereas blue representing smaller SNR). In all Fig. 4.12(a)-Fig. 4.12(h), the small **x**'s mark the positions of experimental data points across the 2-D space (P_{SIG} , P_{LO}). All values between those points are evaluated using linear interpolation using the two nearest experimental data points resulting in continuous and smooth color-coded surfaces. The four rows of subfigures in Fig. 4.12 represent data after 0, 1600, 3200, and 4800 km transmission, respectively, whereas the left column of subfigures represent the filtered case ($N_{ch} = 1$) and the right column represent the colorless case ($N_{ch} = 16$). We should also notice that each pair of subfigures in any row share the same SNR color bar to ease the comparison within each row between the filtered and colorless scenarios. Also, we observe in all subfigures a white space at the bottom left corner where no surface is plotted. This range of (P_{SIG} , P_{LO}) has no experimental data since the target voltage swing of 320 mVpp could not be achieved within this range when both P_{SIG} and P_{LO} are small.

Also, we plot in each subfigure (if applicable) a black contour line corresponding to the parameters (P_{SIG} , P_{LO}) that achieve an SNR of 9.2 dB (FEC threshold). If we now compare Fig. 4.12(g) and Fig. 4.12(h) in the last row, we notice that the operating range where error-free

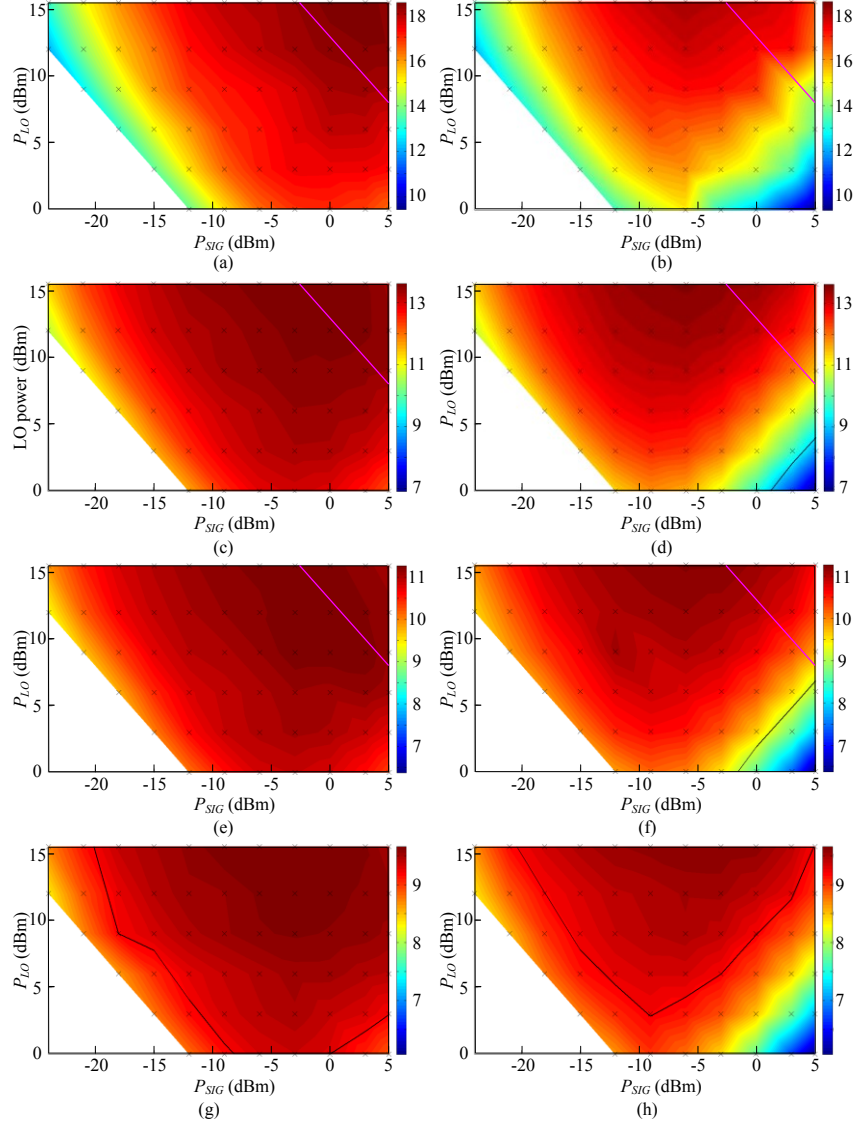


Fig. 4.12. Color coded 2-D plots of SNR versus both P_{SIG} and P_{LO} for (a) back-to-back and $N_{ch} = 1$, (b) back-to-back and $N_{ch} = 16$, (c) 1600 km transmission and $N_{ch} = 1$, (d) 1600 km transmission and $N_{ch} = 16$, (e) 3200 km transmission and $N_{ch} = 1$, (f) 3200 km transmission and $N_{ch} = 16$, (g) 4800 km transmission and $N_{ch} = 1$, and (h) 4800 km transmission and $N_{ch} = 16$.

operation is achieved, i.e. when $SNR > 9.2$ dB which is the area above the contour, is tighter in case of $N_{ch} = 16$ compared to $N_{ch} = 1$ due to the residual SIG-SIG self beat noise impact in the case of colorless reception which degrades the SNR as P_{SIG} increases and P_{LO} decreases. Within the operating range, we notice that for a fixed P_{LO} , there is a dynamic range for P_{SIG} within which error-free operation is possible and that this dynamic range gets wider as P_{LO} increases. Generally, the SNR degradation observed in the left edge of the surfaces in Fig. 4.12(g) and Fig. 4.12(h) is due to the fundamental receiver shot and thermal noises. On the other hand, we notice

a SNR degradation in the bottom right corner (where the LSR is smallest) of all subfigures in the right column representing the colorless scenario, due to the residual SIG-SIG self-beat noise due to neighboring WDM channels in this case. In fact, one should also expect SNR degradation near the top right corner of all subfigures due to saturation effects when both P_{SIG} and P_{LO} are large. In this case, the TIAs may get overloaded leading to nonlinear distortion of the signal which in turn degrades the SNR. From a system design perspective, the TIA overload problem is governed by two important parameters namely the maximum single-ended DC current (I_{DC}) and the peak-to-peak differential AC current (I_{ACppd}), which are calculated similar to [110] as follows

$$I_{DC} = R_{LO}P_{LO} + N_{ch}R_{SIG}P_{SIG}, \quad (4.14)$$

$$I_{ACppd} = 8\sqrt{R_{LO}P_{LO} \cdot PAPR \cdot R_{SIG}P_{SIG}}, \quad (4.15)$$

where $PAPR$ is the peak-to-average power ratio of the photocurrent of one WDM channel which depends on the residual CD and polarization orientation [110]. If those two currents calculated in Eqs. (4.14) and (4.15) are guaranteed to be below the maximum ratings of the TIA, TIA saturation will be avoided and linear operation will be achieved. In our experiment, the TIAs had maximum ratings of 4 mA and 3 mA for I_{DC} and I_{ACppd} , respectively. Regarding DC saturation, if we use the effective responsivities of our CRx which are 0.025 and 0.029 A/W for the signal and LO ports, respectively, we can infer from Eq. (4.14) that for the experimental point with the largest P_{LO} , P_{SIG} and N_{ch} in Fig. 4.12, i.e. when $P_{LO} = 15.5$ dBm, $P_{SIG} = 5$ dBm and $N_{ch} = 16$, I_{DC} will be 2.27 mA which is below 4 mA, meaning that no DC saturation has occurred in our experiment and that the results in Fig. 4.12 are not affected by the TIA DC overload. On the other hand, the AC overload problem affects a portion of our experimental data. If we use a $PAPR$ of 10 dB³ and the CRx responsivities defined above, we can use Eq. (4.15) to evaluate (P_{LO} , P_{SIG}) that corresponds to $I_{ACppd} = 3$ mA which yields the magenta lines plotted in Fig. 4.12(a)-Fig. 4.12(h) near the top right corner of each subfigure. This means that the experimental points above these contours were affected by TIA AC saturation whereas all points lying below these lines were not impacted by AC saturation and the TIAs were in the linear regime of operation. Finally, it is noteworthy that the two currents calculated according to Eqs. (4.14) and (4.15) are not the only key parameters that should be considered when assessing TIA saturation.

³ Although the $PAPR$ depends on the accumulated CD, polarization orientation and number of channels, we use a $PAPR$ value of 10 dB which represents an average value evaluated from the different raw waveforms captured by the real-time scope at various distances, number of channels, etc.

In fact, one should also consider the common mode AC current (which is dependent on N_{ch}). One can actually evaluate the single-ended AC current, i.e. before subtraction that takes place inside the TIA, which should include both the common mode and differential AC contributions. However, the TIA specification regarding the maximum common mode AC current was not available and hence, was not considered.

4.6 Verification of experimental results using the analytical SNR model

In this section, the goal is to verify the match between the experimental data presented in the preceding section and the behavior predicted by the analytical SNR model given by Eq. (4.11). In order to do so, the analytical SNR model in Eq. (4.11) is fitted to the experimental data. We first re-write Eq. (4.11) after re-expressing the denominator which represents the various noise sources as follows

$$SNR = \frac{P_{LO}P_{SIG}}{\alpha_1 P_{LO}P_{SIG} + \alpha_2 N_{loops} P_{LO}P_{SIG} + \alpha_3 + \alpha_4 (P_{LO} + N_{ch}P_{SIG}) + \alpha_5 N_{ch}P_{SIG}^2}, \quad (4.16)$$

where $\alpha_1, \alpha_2, \dots, \alpha_5$ are the coefficients that need to be estimated in order to fit the model in Eq. (4.16) to the experimental data. In fact, the first two terms in the denominator of Eq. (4.16) represent the LO beating with the noise coming along with the received signal which was represented by the first term (LO-ON beating) in the denominator of Eq. (4.11). Here, we split this term into two terms representing the LO beating with the noise accompanying the received signal in back-to-back and transmission scenarios, respectively. The reason to add a noise accompanying the signal in the back-to-back case is to take into account the noise due to the transmitter. This noise from the transmitter side impacts the signal even without transmission and originates from the booster EDFA, RF drivers of the IQ modulator, etc. Hence, the α_1 term in Eq. (4.16) is independent of the transmission distance. On the other hand, the α_2 term represents the LO beating with the incoming optical noise due to both ASE noise of the in-line EDFAs and NL-induced noise after dispersion uncompensated transmission. According to [118], as the number of WDM channels increases and the channel spacing gets smaller, i.e. more dense spectrum, the NL-induced noise accumulation along the link is approximately linear with the number of spans which corresponds to summing incoherently the powers of NL noise

contributions from various spans. In our experiment, we always had 16 WDM channels with 50 GHz spacing propagating along the link which results in NL accumulation approximately proportional to $N_{spans}^{1.06}$ [118], which is very close to being linear. Hence, both the ASE and NL-induced AWGNs can be safely assumed to scale linearly with the number of spans, and consequently, with the number of loops in the recirculating loop, N_{loops} . Next, by carefully comparing the first noise term in Eq. (4.11) with the first two noise terms in Eq. (4.16), we notice that the first noise term in Eq. (4.11) is expressed in terms of the product $P_{LO}P_{ON}$ whereas in Eq. (4.16), we make use of the proportionality between P_{ON} and P_{SIG} for a fixed OSNR and write both the α_1 and α_2 terms in terms of $P_{LO}P_{SIG}$ instead, i.e. the inverses of the OSNRs in back-to-back and after one loop transmission are imbedded into α_1 and α_2 , respectively. We should note that the launch power, which affects P_{ON} by changing the power of the NL-induced noise contribution, was kept constant throughout the experiment. In fact, P_{SIG} in Eq. (4.16) denotes the received signal power (not the launch power) that was swept using the VOA prior to the CRx after NL accumulation already happened along the fiber. In addition, it is noteworthy that the number of WDM channels propagating along the link in our experiment was also kept constant at 16, whereas the number of channels presented to the CRx, denoted by N_{ch} in Eq. (4.16), was swept using the tunable bandwidth optical filter at the end of the link prior to the CRx. Hence, the NL-induced noise along the link in our experiment was constant. Next, the α_3 term represents the thermal noise which is assumed independent of P_{LO} and P_{SIG} . Then, the α_4 term is due to the shot noise including both the LO and SIG contributions. It is noteworthy that both α_3 and α_4 depend on the responsivity of the CRx beside various other parameters. Finally, the α_5 term represents the residual SIG-SIG beating and hence is proportional to $N_{ch}P_{SIG}^2$ where α_5 includes the impact of the effective CMRR of the signal port and the scaling factor β .

The next step is to estimate $\alpha_1, \alpha_2, \dots, \alpha_5$ in Eq. (4.16) using the experimental data plotted in Fig. 4.8. For the purpose of fitting the model, we use only the experimental data obtained after transmission corresponding to N_{loops} equal to 5, 10 and 15 because at these distances, the scaling factor β saturates to a constant value of 0.55 (see appendix B at the end of this chapter) and

hence α_5 can be assumed constant. Since we have many SNR data points at various operating parameters namely, P_{LO}, P_{SIG}, N_{ch} and N_{loops} , estimating the coefficients $\alpha_1, \alpha_1, \dots, \alpha_5$ requires solving an over-determined system. In order to do so, we use the linear least-squares method where the following two vectors and matrix are formed

$$\mathbf{a} = \begin{bmatrix} \alpha_1 \\ \vdots \\ \alpha_5 \end{bmatrix} \quad \begin{bmatrix} P_{LO_1} P_{SIG_1} / SNR_1 \\ \vdots \\ P_{LO_m} P_{SIG_m} / SNR_m \end{bmatrix} \quad \begin{bmatrix} P_{LO_1} P_{SIG_1} & N_{loops_1} P_{LO_1} P_{SIG_1} & 1 & P_{LO_1} + N_{ch_1} P_{SIG_1} & N_{ch_1} P_{SIG_1}^2 \\ \vdots & \vdots & \vdots & \vdots & \vdots \\ P_{LO_m} P_{SIG_m} & N_{loops_m} P_{LO_m} P_{SIG_m} & 1 & P_{LO_m} + N_{ch_m} P_{SIG_m} & N_{ch_m} P_{SIG_m}^2 \end{bmatrix}$$

where m is the number of data points. Using the least-squares method, an estimate $\hat{\mathbf{a}}$ for the coefficients \mathbf{a} is computed such that $\|\mathbf{a} - \hat{\mathbf{a}}\|^2$ is minimized and will be on the form [84]

$$\hat{\mathbf{a}} = (\mathbf{X}^T \mathbf{X})^{-1} \mathbf{X}^T \mathbf{y}, \quad (4.17)$$

where $\|\mathbf{x}\|$ denotes the norm of a vector \mathbf{x} .

Employing Eq. (4.17) and the experimental data, the vector of fitted coefficients was found to be $\hat{\mathbf{a}} = [0.0159 \quad 0.006 \quad 7.767 \times 10^{-6} \quad 9.743 \times 10^{-6} \quad 0.0069]^T$. By plugging the above estimated coefficients into the SNR model of Eq. (4.16), we now have a known analytical SNR model that can be employed to either verify the experimental data or evaluate the SNR at other operating conditions, e.g. another N_{ch} . Fig. 4.13 shows a comparison between the experimental SNR data and the evaluated SNR data from the fitted analytical model where the SNR is plotted against P_{SIG} for various transmission distances. Fig. 4.13(a) and Fig. 4.13(b) present the data when P_{LO} is set to 12 dBm and N_{ch} is 1 and 16, respectively whereas Fig. 4.13(c) and Fig. 4.13(d) present the data when P_{LO} is set to 3 dBm and N_{ch} is 1 and 16, respectively. In obtaining Fig. 4.13, we performed two least-squares fits of the SNR model: one for the back-to-back case and one for the transmission case, since α_5 is expected to be different in both scenarios. The reason for the expected difference of α_5 between the two scenarios is that α_5 includes the effect of the scaling factor β which is dependent on the amount of CD (see appendix B for more details on the scaling factor β) and hence fitting the SNR model is done for the back-to-back data and transmitted data separately. Indeed, α_5 found from fitting the model to the transmitted data was 1.74 times larger than the fitted α_5 using the back-to-back data. This ratio matches well the expected value based on the theory in appendix B (see Fig. 4.15(c)) if we use β of 0.55 for the

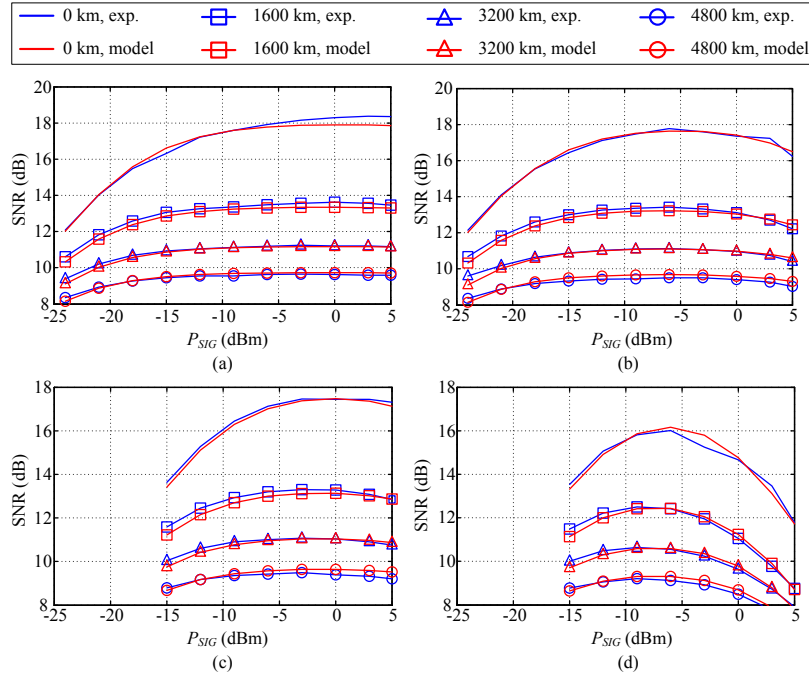


Fig. 4.13. SNR versus P_{SIG} comparing both experimental data points with the points evaluated from the fitted SNR analytical model after 0, 1600, 3200 and 4800 km at the following operating conditions: (a) $P_{LO} = 12$ dBm and $N_{ch} = 1$, (b) $P_{LO} = 12$ dBm and $N_{ch} = 16$, (c) $P_{LO} = 3$ dBm and $N_{ch} = 1$, and (d) $P_{LO} = 3$ dBm and $N_{ch} = 16$.

transmitted data and β of 0.316 for the back-to-back data assuming the worst case polarization orientation of the received signal (45° relative to the PBS of the CRx). Furthermore, we should anticipate that α_5 is the same for all transmitted data since β saturates quickly to a value of 0.55 when the residual CD is more than 3 ns/nm (see Fig. 4.15(c) in appendix B). Looking back at Fig. 4.13, we notice a good agreement between the SNR curves derived from the model compared to the experimental curves which verifies both the validity of the proposed model in Eq. (4.16) and the accuracy of the experimental data.

Besides the agreement between the model and the experimental SNR data, we can also use the estimated value of α_5 (in case of transmitted data) to calculate \overline{CMRR}_{SIG} assuming $\beta = 0.55$ which can be easily done by comparing the last term in the denominators of Eqs. (4.11) and (4.16). We found that \overline{CMRR}_{SIG} obtained from the fitted coefficient is -19 dB. In order to verify this value, we used the analytical definition of \overline{CMRR}_{SIG} presented below Eq. (4.11) in section 4.3 in addition to the CMRR versus frequency curves obtained via characterization of the CRx which were depicted in Fig. 4.2(a) of section 4.2. The value found through the analytical

expression of \overline{CMRR}_{SIG} was -17.5 dB which is in good agreement with the one obtained from fitting.

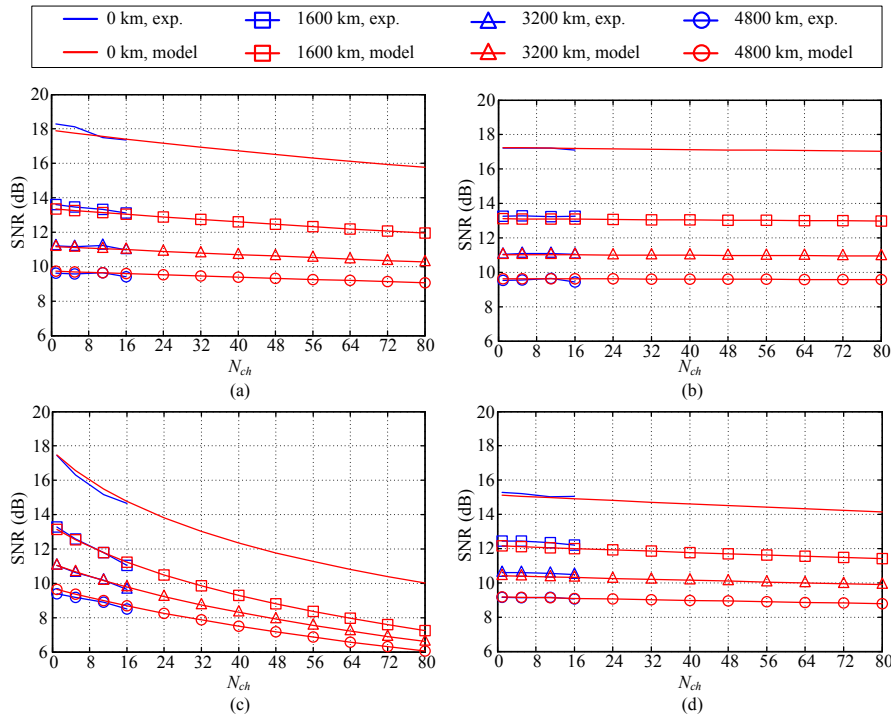


Fig. 4.14. SNR versus N_{ch} comparing the experimental data points with the points evaluated from the fitted SNR analytical model after 0, 1600, 3200 and 4800 km at the following operating conditions: (a) $P_{LO} = 12$ dBm and $P_{SIG} = 0$ dBm, (b) $P_{LO} = 12$ dBm and $P_{SIG} = -12$ dBm, (c) $P_{LO} = 3$ dBm and $P_{SIG} = 0$ dBm, and (d) $P_{LO} = 3$ dBm and $P_{SIG} = -12$ dBm.

Next, we make use of the SNR model found in Eq. (4.16) to predict the SNR performance if the same CRx is used in operating conditions different from those of our experiment. For example, we use the model to predict the performance when the number of WDM channels coincident on the CRx is larger than 16. In Fig. 4.14, we plot the SNR versus N_{ch} after 0, 1600, 3200 and 4800 km transmission for both the model and experiment. It can be observed that the sweep range of N_{ch} is limited to 16 in case of the experimental data whereas we employ the analytical model to predict the SNR if the CRx is used for colorless reception when N_{ch} is up to 80. In Fig. 4.14(a) and Fig. 4.14(b), a high P_{LO} of 12 dBm is chosen and P_{SIG} is set to 0 and -12 dBm, respectively whereas in Fig. 4.14(c) and Fig. 4.14(d) a low P_{LO} of 3 dBm is chosen and P_{SIG} is set to 0 and -12 dBm, respectively. If we compare Fig. 4.14(a)-Fig. 4.14(d), we notice that the impact of increasing N_{ch} on the SNR degradation is the most in Fig. 4.14(c) where the residual SIG-SIG beat noise has the largest impact for small P_{LO} and high P_{SIG} , i.e. small LSR . For example, the SNR after 1600 km transmission degrades by nearly 6 dB as N_{ch} changes from

1 to 80. On the other hand, we observe no impact from varying N_{ch} on the SNR performance in Fig. 4.14(b) when $P_{LO} = 12$ dBm and $P_{SIG} = -12$ dBm. In fact, the model allows us to predict error free operation (SNR > 9.2 dB) after 4800 km transmission when $N_{ch} = 80$. In order to verify that our SNR predictions when $N_{ch} = 80$ are correct from the TIA saturation perspective, we also use Eqs. (4.14) and (4.15) to verify if I_{DC} and I_{ACppd} are going to be below the TIA ratings. Indeed, if we plug the largest P_{SIG} and P_{LO} used in Fig. 4.14 into Eqs. (4.14) and (4.15), i.e. 0 dBm and 12 dBm respectively, and use $N_{ch} = 80$, we obtain $I_{DC} = 2.43$ and $I_{ACppd} = 2.69$ mA which are below the TIA maximum ratings. We finally conclude that all SNR points drawn from the model in Fig. 4.14 are within the linear operation regime of the TIAs.

4.7 Conclusion

In this chapter, we present a comprehensive theoretical and experimental study of the performance of a SiP integrated balanced CRx when employed for colorless reception in a WDM setup. The layout of the CRx chip is depicted and characterization results of its parameters were shown. Then, an analytical SNR expression of the output photocurrent is derived rigorously while pinpointing noise sources in a colorless scheme. Next, experimental results are presented where 16×112 Gbps PDM-QPSK WDM channels are used. We study the impact of varying system parameters on the performance of colorless reception. Results show that the LO beating with incoming optical noise including ASE and NL-induced noises is a dominant noise source regardless of the received signal power. In addition, we identify the SIG-SIG beating due to OOB WDM channels as an additional important noise source in the regime of high received signal power. On the other hand, thermal and shot noises have a significant impact on SNR in the regime of low received signal power. In addition, we conclude that the CMRR and sensitivity are two important CRx specifications that impact significantly the performance at high and low received signal power regimes, respectively. Finally, an excellent match between experimental and analytical SNRs is proven. After fitting the SNR model, we conclude that the SiP CRx is capable of colorless operation with a WDM spectrum comprising 80 channels as long as the LO-to-signal power ratio is properly set.

4.8 Appendix A: Derivation of ACFs, PSDs and powers of various terms in the differential photocurrent

In this appendix, we derive the time-averaged ACFs of all terms in the total differential photocurrent given by Eq. (4.7) from which the PSDs are evaluated through Fourier transformation (FT). Then, the PSDs derived are integrated over frequency to calculate the powers required to evaluate the SNR according to Eq. (4.10). We divide the appendix into four subsections which are laid out for different beating terms of the differential photocurrent given in Eq. (4.7).

4.8.1 Derivation of ACF, PSD and power of the LO-SIG and LO-ON beating terms in the differential photocurrent

We start by neglecting the effect of the impulse responses of $h^P(t)$ and $h^N(t)$. However, we will later modify the final result derived to include their impact. The time averaged ACF of the LO-SIG term in the differential photocurrent in Eq. (4.7) can be calculated starting from the definition of the ACF of $\Delta i_{LO-SIG}(t)$, obtained from the difference between the LO-SIG terms in the P and N photocurrents in Eqs. (4.5) and (4.6), yielding

$$\begin{aligned} \bar{\Gamma}_{\Delta i_{LO-SIG}}(\tau) &= \overline{\langle \Delta i_{LO-SIG}(t) \Delta i_{LO-SIG}(t-\tau) \rangle} \\ &= R_{SIG,s}^P R_{LO,s}^P \overline{\left\langle \text{Re} \left\{ \tilde{E}_{SIG,s} \tilde{E}_{LO}^* \right\} \right\rangle} \\ &\quad + R_{SIG,s}^N R_{LO,s}^N \overline{\left\langle \text{Re} \left\{ \tilde{E}_{SIG,s} \tilde{E}_{LO}^* \right\} \right\rangle} \\ &\quad + \sqrt{R_{SIG,s}^P R_{LO,s}^P R_{SIG,s}^N R_{LO,s}^N} \overline{\left\langle \text{Re} \left\{ \tilde{E}_{SIG,s} \tilde{E}_{LO}^* \right\} \right\rangle} \\ &\quad + \sqrt{R_{SIG,s}^P R_{LO,s}^P R_{SIG,s}^N R_{LO,s}^N} \overline{\left\langle \text{Re} \left\{ \tilde{E}_{SIG,s} \tilde{E}_{LO}^* \right\} \right\rangle}. \end{aligned}$$

Using the relation in Eq. (4.4) to express the product of two real parts and also realizing that the terms having $e^{j2\pi\Delta\nu(2t-\tau)}$ cancel after time averaging as in [121], we arrive at

$$\begin{aligned}
\bar{\Gamma}_{\Delta i_{LO-SIG}}(\tau) &= \frac{1}{2} R_{SIG,s}^P R_{LO,s}^P \operatorname{Re} \left\{ \left\langle \tilde{\mathbf{E}}_{SIG,s} \quad \tilde{\mathbf{E}}_{SIG,s}^* \quad \tilde{\mathbf{E}}_{LO} \quad \tilde{\mathbf{E}}_{LO} \quad \dots \quad \pi \Delta v \tau \right\rangle \right. \\
&\quad + \frac{1}{2} R_{SIG,s}^N R_{LO,s}^N \operatorname{Re} \left\{ \left\langle \tilde{\mathbf{E}}_{SIG,s} \quad \tilde{\mathbf{E}}_{SIG,s}^* \quad \tilde{\mathbf{E}}_{LO} \quad \tilde{\mathbf{E}}_{LO} \quad \dots \quad 2\pi \Delta v \tau \right\rangle \right. \\
&\quad + \frac{1}{2} \sqrt{R_{SIG,s}^P R_{LO,s}^P R_{SIG,s}^N R_{LO,s}^N} \operatorname{Re} \left\{ \left\langle \tilde{\mathbf{E}}_{SIG,s} \quad \tilde{\mathbf{E}}_{SIG,s}^* \quad \tilde{\mathbf{E}}_{LO} \quad \tilde{\mathbf{E}}_{LO} \quad \dots \quad e^{j2\pi \Delta v(\tau+\delta)} \right\rangle \right. \\
&\quad \left. \left. + \frac{1}{2} \sqrt{R_{SIG,s}^P R_{LO,s}^P R_{SIG,s}^N R_{LO,s}^N} \operatorname{Re} \left\{ \left\langle \tilde{\mathbf{E}}_{SIG,s} \quad \tilde{\mathbf{E}}_{SIG,s}^* \quad \tilde{\mathbf{E}}_{LO} \quad \tilde{\mathbf{E}}_{LO} \quad \dots \quad v(\tau-\delta) \right\rangle \right. \right. \quad (4.18)
\end{aligned}$$

Then, if we use the statistical independence between the LO and signal fields, we obtain

$$\begin{aligned}
\bar{\Gamma}_{\Delta i_{LO-SIG}}(\tau) &= \frac{1}{2} R_{SIG,s}^P R_{LO,s}^P \operatorname{Re} \left\{ \bar{\Gamma}_{\tilde{\mathbf{E}}_{SIG} \quad \tilde{\mathbf{E}}_{LO} \quad \dots \quad i2\pi \Delta v \tau} \right\} \\
&\quad + \frac{1}{2} R_{SIG,s}^N R_{LO,s}^N \operatorname{Re} \left\{ \bar{\Gamma}_{\tilde{\mathbf{E}}_{SIG} \quad \tilde{\mathbf{E}}_{LO} \quad \dots \quad i2\pi \Delta v \tau} \right\} \\
&\quad + \frac{1}{2} \sqrt{R_{SIG,s}^P R_{LO,s}^P R_{SIG,s}^N R_{LO,s}^N} \operatorname{Re} \left\{ \bar{\Gamma}_{\tilde{\mathbf{E}}_{SIG} \quad \tilde{\mathbf{E}}_{LO} \quad \dots \quad j2\pi \Delta v(\tau+\delta)} \right\} \\
&\quad + \frac{1}{2} \sqrt{R_{SIG,s}^P R_{LO,s}^P R_{SIG,s}^N R_{LO,s}^N} \operatorname{Re} \left\{ \bar{\Gamma}_{\tilde{\mathbf{E}}_{SIG} \quad \tilde{\mathbf{E}}_{LO} \quad \dots \quad j2\pi \Delta v(\tau-\delta)} \right\}. \quad (4.19)
\end{aligned}$$

The first term in Eq. (4.19) follows directly from the first term in Eq. (4.18) after using the statistical independence between the LO and signal fields. However, the second, third and fourth terms are each obtained as follows

$$\begin{aligned}
&\left\langle \tilde{\mathbf{E}}_{SIG,s} \quad \tilde{\mathbf{E}}_{SIG,s}^* \quad \tilde{\mathbf{E}}_{LO} \quad \tilde{\mathbf{E}}_{LO} \quad \dots \quad \tilde{\mathbf{E}}_{SIG,s} \quad \tilde{\mathbf{E}}_{SIG,s}^* \quad \tilde{\mathbf{E}}_{LO} \quad \tilde{\mathbf{E}}_{LO} \quad \dots \right. \\
&\quad \left. \cdot \left\langle \tilde{\mathbf{E}}_{LO}^* \quad \tilde{\mathbf{E}}_{LO} \quad \dots \right\rangle \right. \\
&= \bar{\Gamma}_{\tilde{\mathbf{E}}_{SIG} \quad \tilde{\mathbf{E}}_{LO} \quad \dots \quad \tilde{\mathbf{E}}_{LO} \quad \tilde{\mathbf{E}}_{LO} \quad \dots} \\
&= \bar{\Gamma}_{\tilde{\mathbf{E}}_{SIG} \quad \tilde{\mathbf{E}}_{LO} \quad \dots} \\
&\left\langle \tilde{\mathbf{E}}_{SIG,s} \quad \tilde{\mathbf{E}}_{SIG,s}^* \quad \tilde{\mathbf{E}}_{LO} \quad \tilde{\mathbf{E}}_{LO} \quad \dots \quad \tilde{\mathbf{E}}_{SIG,s} \quad \tilde{\mathbf{E}}_{SIG,s}^* \quad \tilde{\mathbf{E}}_{LO} \quad \tilde{\mathbf{E}}_{LO} \quad \dots \right. \\
&\quad \left. \cdot \left\langle \tilde{\mathbf{E}}_{LO}^* \quad \tilde{\mathbf{E}}_{LO} \quad \dots \quad \delta \right\rangle \right. \\
&= \bar{\Gamma}_{\tilde{\mathbf{E}}_{SIG} \quad \tilde{\mathbf{E}}_{LO} \quad \dots \quad \tilde{\mathbf{E}}_{LO} \quad \tilde{\mathbf{E}}_{LO} \quad \dots} \\
&= \bar{\Gamma}_{\tilde{\mathbf{E}}_{SIG} \quad \tilde{\mathbf{E}}_{LO} \quad \dots}
\end{aligned}$$

$$\begin{aligned}
& \overline{\langle \tilde{\mathbf{E}}_{SIG,s} \tilde{\mathbf{E}}_{SIG,s}^* \tilde{\mathbf{E}}_{LO} \tilde{\mathbf{E}}_{LO}^* \rangle} = \overline{\langle \tilde{\mathbf{E}}_{SIG,s} \tilde{\mathbf{E}}_{SIG,s}^* \tilde{\mathbf{E}}_{LO} \tilde{\mathbf{E}}_{LO}^* \rangle} \\
& = \overline{\langle \tilde{\mathbf{E}}_{SIG} \tilde{\mathbf{E}}_{SIG}^* \tilde{\mathbf{E}}_{LO} \tilde{\mathbf{E}}_{LO}^* \rangle} \\
& = \overline{\langle \tilde{\mathbf{E}}_{SIG} \tilde{\mathbf{E}}_{SIG}^* \rangle} \overline{\langle \tilde{\mathbf{E}}_{LO} \tilde{\mathbf{E}}_{LO}^* \rangle}
\end{aligned}$$

where the LO field is assumed to be stationary (unmodulated), whereas the signal field is cyclostationary with its time-dependent and lag-dependent (two-argument) ACF being periodic with a period equal to the symbol duration. After time averaging which involves omitting the time variable, it can be shown that $\overline{\langle \tilde{\mathbf{E}}_{SIG}(\tau - \delta) \tilde{\mathbf{E}}_{SIG}^*(\tau + \delta) \rangle}$, and $\overline{\langle \tilde{\mathbf{E}}_{SIG}(\tau - \delta) \tilde{\mathbf{E}}_{SIG}^*(\tau - \delta) \rangle}$ will finally lead to $\overline{\langle \tilde{\mathbf{E}}_{SIG}(\tau + \delta) \tilde{\mathbf{E}}_{SIG}^*(\tau + \delta) \rangle}$ and $\overline{\langle \tilde{\mathbf{E}}_{SIG}(\tau - \delta) \tilde{\mathbf{E}}_{SIG}^*(\tau - \delta) \rangle}$, respectively.

In Eq. (4.19), if we neglect the lineshape of the LO, i.e. $S_{\tilde{\mathbf{E}}_{LO}}(f) = 2P_{LO}\delta(f - \nu_{LO})$, then $\Gamma_{\tilde{\mathbf{E}}_{LO}}(\tau) = 2P_{LO}$. The reason for multiplying P_{LO} by 2 is that the total power of the complex envelope is twice that of the real field [121] since its respective ACF is given by $\Gamma_{\tilde{\mathbf{E}}_{LO}}(\tau) = \frac{1}{2} \text{Re}\{\Gamma_{\tilde{\mathbf{E}}_{LO}}(\tau) e^{j2\pi\nu\tau}\}$. Now if we substitute for $\Gamma_{\tilde{\mathbf{E}}_{LO}}(\tau)$ in Eq. (4.19), we obtain

$$\begin{aligned}
\bar{\Gamma}_{\Delta_{LO-SIG}}(\tau) &= P_{LO} \left(R_{SIG,s}^P R_{LO,s}^P + R_{SIG,s}^N R_{LO,s}^N \right) \cdot \text{Re}\left\{ \bar{\Gamma}_{\tilde{\mathbf{E}}_{SIG}}(\tau) e^{j2\pi\Delta\nu\tau} \right\} \\
&\quad + P_{LO} \sqrt{R_{SIG,s}^P R_{LO,s}^P R_{SIG,s}^N R_{LO,s}^N} \left[\text{Re}\left\{ \bar{\Gamma}_{\tilde{\mathbf{E}}_{SIG}}(\tau + \delta) e^{j2\pi\Delta\nu(\tau + \delta)} \right\} + \text{Re}\left\{ \bar{\Gamma}_{\tilde{\mathbf{E}}_{SIG}}(\tau - \delta) e^{j2\pi\Delta\nu(\tau - \delta)} \right\} \right]. \quad (4.20)
\end{aligned}$$

Then, if we take the FT of ACF, we get the PSD of the LO-SIG term as

$$\begin{aligned}
S_{\Delta_{LO-SIG}}(f) &= \text{FT}\left\{ \bar{\Gamma}_{\Delta_{LO-SIG}}(\tau) \right\} \\
&= P_{LO} \left[\sqrt{R_{SIG,s}^P R_{LO,s}^P} + e^{j2\pi f\delta} \sqrt{R_{SIG,s}^N R_{LO,s}^N} \right]^2 \cdot \frac{1}{2} \left[S_{\tilde{\mathbf{E}}_{SIG}}(f - \nu) + S_{\tilde{\mathbf{E}}_{SIG}}(f - \nu) \right]. \quad (4.21)
\end{aligned}$$

In obtaining the expression in Eq. (4.21), we initially neglected the impulse responses of the P and N paths from the PD outputs up to current subtraction in the TIA which were denoted by $h^P(t)$ and $h^N(t)$. It can be shown that the effects of those two impulse responses can be taken into consideration in the ACF of the LO-SIG as follows

$$\begin{aligned}
\bar{\Gamma}_{\Delta_{LO-SIG}}(\tau) &= P_{LO} R_{SIG,s}^P R_{LO,s}^P \cdot \left(\text{Re} \left\{ \bar{\Gamma}_{\tilde{E}_{SIG}}(\tau) e^{j2\pi\Delta\nu\tau} \right\} \otimes \Gamma_{h^P}(\tau) \right) \\
&\quad + P_{LO} R_{SIG,s}^N R_{LO,s}^N \cdot \left(\text{Re} \left\{ \bar{\Gamma}_{\tilde{E}_{SIG}}(\tau) e^{j2\pi\Delta\nu\tau} \right\} \otimes \Gamma_{h^N}(\tau) \right) \\
&\quad + P_{LO} \sqrt{R_{SIG,s}^P R_{LO,s}^P R_{SIG,s}^N R_{LO,s}^N} \cdot \left(\text{Re} \left\{ \bar{\Gamma}_{\tilde{E}_{SIG}}(\tau) + \delta \right\} e^{j2\pi\Delta\nu(\tau+\delta)} \right) \otimes \Gamma_{h^P h^N}(\tau) \\
&\quad + P_{LO} \sqrt{R_{SIG,s}^P R_{LO,s}^P R_{SIG,s}^N R_{LO,s}^N} \cdot \left(\text{Re} \left\{ \bar{\Gamma}_{\tilde{E}_{SIG}}(\tau) - \delta \right\} e^{j2\pi\Delta\nu(\tau-\delta)} \right) \otimes \Gamma_{h^N h^P}(\tau), \quad (4.22)
\end{aligned}$$

where $\Gamma_{h^P}(\tau)$, $\Gamma_{h^N}(\tau)$, $\Gamma_{h^P h^N}(\tau)$ and $\Gamma_{h^N h^P}(\tau)$ are the deterministic ACFs and cross-correlations of the impulse responses $h^P(t)$ and $h^N(t)$ that can be calculated as follows

$$\begin{aligned}
\Gamma_{h^P}(\tau) &= h^P(\tau) \otimes h^{P*}(-\tau), \quad \Gamma_{h^N}(\tau) = h^N(\tau) \otimes h^{N*}(-\tau), \\
\Gamma_{h^P h^N}(\tau) &= h^P(\tau) \otimes h^{N*}(-\tau), \quad \Gamma_{h^N h^P}(\tau) = h^N(\tau) \otimes h^{P*}(-\tau).
\end{aligned}$$

Taking the FT of the ACF in Eq. (4.22) leads to the PSD of the LO-SIG beating term as

$$S_{\Delta_{LO-SIG}}(f) = P_{LO} \left| H^P(f) \sqrt{R_{SIG,s}^P R_{LO,s}^P} + e^{j2\pi f \delta} H^N(f) \sqrt{R_{SIG,s}^N R_{LO,s}^N} \right|^2 \cdot \frac{1}{2} \left[S_{\tilde{E}_{SIG}}(f) + S_{\tilde{E}_{SIG}}(f) \right], \quad (4.23)$$

where $H^P(f)$ and $H^N(f)$ are the FT pairs of $h^P(t)$ and $h^N(t)$, respectively.

Next, we evaluate the PSD of the received signal field $S_{\tilde{E}_{SIG}}(f)$, which appears in Eq. (4.23).

In fact, this PSD is related to the pulse shape and modulation format used at the transmitter. In fact, we can write the received signal field as

$$\tilde{E}_{SIG}(t) = \sum_{n=-\infty}^{\infty} (aX_n + bY_n) h(t - nT), \quad (4.24)$$

where $h(t) = g(t) \otimes h_{CD}(t)$ is the overall impulse response including the transmitted pulse shape $g(t)$ and CD impulse response $h_{CD}(t)$. Also, X_n and Y_n are the n^{th} information symbols on the

two polarization states, i.e. $X_n, Y_n \in \frac{1}{\sqrt{2}} \{(1+j), (-1+j), (-1-j), (1-j)\}$ in the case of QPSK.

In addition, a and b are the matrix entries of the 2×2 Jones matrix \mathbf{J} representing the polarization rotation due to the misalignment between the state of polarization of the received signal and the axis of the CRx PBS, i.e.

$$\mathbf{J} = \begin{bmatrix} a & b \\ -b^* & a^* \end{bmatrix}. \quad (4.25)$$

Using Eq. (4.24), we find the time averaged ACF of $\tilde{\mathbf{E}}_{SIG}$, denoted by $\bar{\Gamma}_{\tilde{\mathbf{E}}_{SIG}}$, as follows

$$\begin{aligned} \bar{\Gamma}_{\tilde{\mathbf{E}}_{SIG}} &= \overline{\langle \tilde{\mathbf{E}}_{SIG} \tilde{\mathbf{E}}_{SIG}^* \rangle} \\ &= |a|^2 \sum_{n=-\infty}^{\infty} \sum_{m=-\infty}^{\infty} \langle X_n X_m^* \rangle \overline{h(t-nT)h^*(t-\tau-mT)} + |b|^2 \sum_{n=-\infty}^{\infty} \sum_{m=-\infty}^{\infty} \langle Y_n Y_m^* \rangle \overline{h(t-nT)h^*(t-\tau-mT)} \\ &\quad + ab^* \sum_{n=-\infty}^{\infty} \sum_{m=-\infty}^{\infty} \langle X_n Y_m^* \rangle \overline{h(t-nT)h^*(t-\tau-mT)} + a^*b \sum_{n=-\infty}^{\infty} \sum_{m=-\infty}^{\infty} \langle X_n^* Y_m \rangle \overline{h(t-nT)h^*(t-\tau-mT)}. \end{aligned} \quad (4.26)$$

We know that for QPSK modulated symbols on the same polarization, we have

$$\langle X_n X_m^* \rangle = \langle Y_n Y_m^* \rangle = \begin{cases} 1 & n = m \\ 0 & n \neq m \end{cases},$$

and for independent QPSK symbols on different polarizations, we have

$$\langle X_n Y_m^* \rangle = \langle X_n^* Y_m \rangle = 0.$$

Hence, we can substitute with the statistical averages evaluated above into Eq. (4.26) to derive the ACF of the signal field as follows

$$\begin{aligned} \bar{\Gamma}_{\tilde{\mathbf{E}}_{SIG}} &= (|a|^2 + |b|^2) \sum_{n=-\infty}^{\infty} \overline{h(t-nT)h^*(t-\tau-nT)} \\ &= \frac{1}{T} \sum_{n=-\infty}^{\infty} \int_{-T/2}^{T/2} h(t-nT)h^*(t-\tau-nT) dt \\ &= \frac{1}{T} \int_{-\infty}^{\infty} h(t)h^*(t-\tau) dt \\ &= \frac{1}{T} \Gamma_h(\tau), \end{aligned} \quad (4.27)$$

where $\Gamma_h(\tau) = \int_{-\infty}^{\infty} h(t)h^*(t-\tau) dt$ is the deterministic ACF of the overall pulse shape and where

we used the fact that $|a|^2 + |b|^2 = 1$ since J is unitary. The integral in the second line of Eq. (4.27)

comes from the time averaging operator $\overline{f(t)}$ being $1/T \int_{-T/2}^{T/2} f(t) dt$ provided that $f(t)$ is

periodic with a period T . Hence, the PSD of the signal field $S_{\tilde{\mathbf{E}}_{SIG}}$ required in Eq. (4.23) is

given by the FT of the ACF as follows

$$S_{\tilde{E}_{SIG}}(\nu) = \frac{1}{T} |H(f)|^2 = \frac{1}{T} |G(f)|^2, \quad (4.28)$$

where $H(f)$ and $G(f)$ are the FT pairs of $h(t)$ and $g(t)$, respectively. In the second equality of Eq. (4.28), we used the fact that $|H_{CD}(f)|^2 = 1$. Now if we back substitute in Eq. (4.23) after neglecting $\Delta\nu$ (since it will be corrected in DSP afterwards) and integrate over frequency, we get the power of the desired LO-SIG photocurrent term (numerator of the SNR in Eq. (4.10))

$$\begin{aligned} P_{\Delta i_{LO-SIG}} &= P_{LO} \int_{-\infty}^{\infty} \left| H^P(f) \sqrt{R_{SIG,s}^P R_{LO,s}^P} + H^N(f) e^{j2\pi f \delta} \sqrt{R_{SIG,s}^N R_{LO,s}^N} \right|^2 \cdot \frac{1}{T} |G(f)|^2 |H_{rx-DSP}(f)|^2 df \\ &= 2P_{LO} P_{SIG} \frac{\int_{-\infty}^{\infty} \left| H^P(f) \sqrt{R_{SIG,s}^P R_{LO,s}^P} + H^N(f) e^{j2\pi f \delta} \sqrt{R_{SIG,s}^N R_{LO,s}^N} \right|^2 |G(f)|^2 |H_{rx-DSP}(f)|^2 df}{\int_{-\infty}^{\infty} |G(f)|^2 df}, \end{aligned} \quad (4.29)$$

where we employ the fact that the integral of the PSD of the complex envelope of the received signal field in Eq. (4.28) gives $2P_{SIG}$.

Regarding the LO-ON beating term, its ACF and PSD can be derived in a similar way as that used to obtain those quantities for the LO-ON term. In fact, the PSD of the LO-ASE beating will have a similar form to the one derived for the LO-SIG term which was given by Eq. (4.23), and can be expressed as

$$\begin{aligned} S_{\Delta i_{LO-ON}}(f) &= P_{LO} \left| H^P(f) \sqrt{R_{SIG,s}^P R_{LO,s}^P} + H^N(f) e^{j2\pi f \delta} \sqrt{R_{SIG,s}^N R_{LO,s}^N} \right|^2 \\ &\quad \cdot \frac{1}{2} \left[S_{\tilde{E}_{ON}}(\nu) + S_{\tilde{E}_{ON}}(\nu) \right], \end{aligned} \quad (4.30)$$

where $S_{\tilde{E}_{ON}}(\nu)$ is the PSD of the complex envelope of the ASE field within one channel, which can be assumed as that of a narrowband filtered white noise given by

$$S_{\tilde{E}_{ON}}(\nu) = \begin{cases} 2N_o & |f| \leq B_{ch}/2 \\ 0 & |f| > B_{ch}/2 \end{cases}, \quad (4.31)$$

where N_o is the PSD level of the real-valued ASE noise field in W/Hz and B_{ch} is the optical bandwidth of one WDM channel. In Eq. (4.31), we made use of the assumption that the NL-induced noise portion inside \tilde{E}_{ON} can be assumed locally white, i.e. it has an approximately flat spectrum within one WDM channel [118]. Hence, the total optical noise field \tilde{E}_{ON} can be

assumed white. Next, we can easily find the variance (or AC electrical power) of the LO-ON beating photocurrent term in the denominator of the SNR in Eq. (4.10) as follows

$$\sigma_{\Delta i_{LO-ON}}^2 = \frac{2P_{LO}P_{ON} \int_{-B_{ch}/2}^{B_{ch}/2} \left| H^P(f) \sqrt{R_{SIG,s}^P R_{LO,s}^P} + H^N(f) e^{j2\pi f \delta} \sqrt{R_{SIG,s}^N R_{LO,s}^N} \right|^2 |H_{rx-DSP}(f)|^2 df}{B_{ch}}. \quad (4.32)$$

4.8.2 Derivation of ACF, PSD and power of the residual SIG-SIG beating term in the differential photocurrent

Similar to subsection 4.8.1 in this appendix, we begin by neglecting the effect of the impulse responses $h^P(t)$, $h^N(t)$ in Eq. (4.7) and later take them into consideration by modifying the final PSD expression obtained. We start by writing the definition of the time averaged ACF of $\Delta i_{SIG-SIG}(t)$ obtained from the difference between the SIG-SIG beating terms in the P and N photocurrents in Eqs. (4.5) and (4.6), yielding

$$\begin{aligned} \bar{\Gamma}_{\Delta i_{SIG-SIG}}(\tau) &= \overline{\langle \Delta i_{SIG-SIG}(t) \Delta i_{SIG-SIG}(t-\tau) \rangle} \\ &= \frac{1}{4} \left[\begin{aligned} &\sum_{i=1}^{N_{ch}} \sum_{j=1}^{N_{ch}} R_{SIG,i}^P R_{SIG,j}^P \overline{\langle \tilde{\mathbf{E}}_{SIG,i} \dots \tilde{\mathbf{E}}_{SIG,j} \dots \rangle} \\ &+ \sum_{i=1}^{N_{ch}} \sum_{j=1}^{N_{ch}} R_{SIG,i}^N R_{SIG,j}^N \overline{\langle |\tilde{\mathbf{E}}_{SIG,i} \dots \tilde{\mathbf{E}}_{SIG,j} \dots|^2 \rangle} \\ &- \sum_{i=1}^{N_{ch}} \sum_{j=1}^{N_{ch}} R_{SIG,i}^P R_{SIG,j}^N \overline{\langle |\tilde{\mathbf{E}}_{SIG,i} \dots \tilde{\mathbf{E}}_{SIG,j} \dots \delta|^2 \rangle} \\ &- \sum_{i=1}^{N_{ch}} \sum_{j=1}^{N_{ch}} R_{SIG,i}^N R_{SIG,j}^P \overline{\langle \tilde{\mathbf{E}}_{SIG,i} \dots \tilde{\mathbf{E}}_{SIG,j} \dots \rangle} \end{aligned} \right]. \end{aligned}$$

In the above equation, all summation terms where $i \neq j$ will involve the intensities of different channels which can be assumed independent, i.e. the expectation of the product can be evaluated as the product of expectations. Hence,

$$\begin{aligned}
\bar{\Gamma}_{\Delta_{\text{SIG-SIG}}}(\tau) &= \sum_{i=1}^{N_{\text{ch}}} \sum_{\substack{j=1 \\ j \neq i}}^{N_{\text{ch}}} \left(R_{\text{SIG},i}^P R_{\text{SIG},j}^P + R_{\text{SIG},i}^N R_{\text{SIG},j}^N - 2R_{\text{SIG},i}^P R_{\text{SIG},j}^N \right) P_{\text{SIG},i} P_{\text{SIG},j} \\
&\quad + \frac{1}{4} \sum_{i=1}^{N_{\text{ch}}} R_{\text{SIG},i}^P \left| \overline{\tilde{E}_{\text{SIG},i}(\tau)} \right|^2 - \frac{1}{4} \sum_{i=1}^{N_{\text{ch}}} R_{\text{SIG},i}^N \left| \overline{\tilde{E}_{\text{SIG},i}(\tau)} \right|^2 \\
&\quad - \frac{1}{4} \sum_{i=1}^{N_{\text{ch}}} R_{\text{SIG},i}^P R_{\text{SIG},i}^N \left| \overline{\tilde{E}_{\text{SIG},i}(\tau - \delta)} \right|^2 - \frac{1}{4} \sum_{i=1}^{N_{\text{ch}}} R_{\text{SIG},i}^P R_{\text{SIG},i}^N \left| \overline{\tilde{E}_{\text{SIG},i}(\tau + \delta)} \right|^2 \\
&= \sum_{i=1}^{N_{\text{ch}}} \sum_{\substack{j=1 \\ j \neq i}}^{N_{\text{ch}}} \left(R_{\text{SIG},i}^P R_{\text{SIG},j}^P + R_{\text{SIG},i}^N R_{\text{SIG},j}^N - 2R_{\text{SIG},i}^P R_{\text{SIG},j}^N \right) P_{\text{SIG},i} P_{\text{SIG},j} \\
&\quad + \frac{1}{4} \sum_{i=1}^{N_{\text{ch}}} R_{\text{SIG},i}^P \bar{\Gamma}_{|\tilde{E}_{\text{SIG},i}|^2}(\tau) - \frac{1}{4} \sum_{i=1}^{N_{\text{ch}}} R_{\text{SIG},i}^N \bar{\Gamma}_{|\tilde{E}_{\text{SIG},i}|^2}(\tau) \\
&\quad - \frac{1}{4} \sum_{i=1}^{N_{\text{ch}}} R_{\text{SIG},i}^P R_{\text{SIG},i}^N \bar{\Gamma}_{|\tilde{E}_{\text{SIG},i}|^2}(\tau, \delta) - \frac{1}{4} \sum_{i=1}^{N_{\text{ch}}} R_{\text{SIG},i}^P R_{\text{SIG},i}^N \bar{\Gamma}_{|\tilde{E}_{\text{SIG},i}|^2}(\tau, -\delta)
\end{aligned} \tag{4.33}$$

where $\bar{\Gamma}_{|\tilde{E}_{\text{SIG},i}|^2}(\tau)$ is the time averaged ACF of the squared envelope of the electric field of the i^{th} WDM signal which will be derived later. Then, the PSD of the SIG-SIG beating term in the differential photocurrent can be evaluated by taking the FT of its ACF given in Eq. (4.33) and written as

$$\begin{aligned}
S_{\Delta_{\text{SIG-SIG}}}(f) &= \delta(f) \sum_{i=1}^{N_{\text{ch}}} \sum_{\substack{j=1 \\ j \neq i}}^{N_{\text{ch}}} \left(R_{\text{SIG},i}^P R_{\text{SIG},j}^P + R_{\text{SIG},i}^N R_{\text{SIG},j}^N - 2R_{\text{SIG},i}^P R_{\text{SIG},j}^N \right) P_{\text{SIG},i} P_{\text{SIG},j} \\
&\quad + \frac{1}{4} \sum_{i=1}^{N_{\text{ch}}} \left| R_{\text{SIG},i}^P - e^{j2\pi f \delta} R_{\text{SIG},i}^N \right|^2 S_{|\tilde{E}_{\text{SIG},i}|^2}(f).
\end{aligned} \tag{4.34}$$

Now, we can take into consideration the impact of the impulse responses $h^P(t)$ and $h^N(t)$ in a way similar to that described prior to Eq. (4.23), which yields

$$\begin{aligned}
S_{\Delta_{\text{SIG-SIG}}}(f) &= \delta(f) \sum_{i=1}^{N_{\text{ch}}} \sum_{\substack{j=1 \\ j \neq i}}^{N_{\text{ch}}} \left(R_{\text{SIG},i}^P R_{\text{SIG},j}^P + R_{\text{SIG},i}^N R_{\text{SIG},j}^N - 2R_{\text{SIG},i}^P R_{\text{SIG},j}^N \right) P_{\text{SIG},i} P_{\text{SIG},j} \\
&\quad + \frac{1}{4} \sum_{i=1}^{N_{\text{ch}}} \left| H^P(f) R_{\text{SIG},i}^P - H^N(f) e^{j2\pi f \delta} R_{\text{SIG},i}^N \right|^2 S_{|\tilde{E}_{\text{SIG},i}|^2}(f),
\end{aligned} \tag{4.35}$$

where the first term in Eq. (4.35) represents a DC portion that is not of interest while calculating the residual SIG-SIG beat noise power $\sigma_{\Delta_{\text{SIG-SIG}}}^2$ in Eq. (4.10). The second term in Eq. (4.35) represents the sum of the PSDs of the field intensities of all channels scaled by the quantity

$|H^P(f)R_{SIG,i}^P - H^N(f)e^{j2\pi f\delta}R_{SIG,i}^N|^2$ which represents the ability of the CRx to reject the common mode on both the P and N PDs. It is evident that this quantity is frequency dependent due to both the time skew and unequal frequency responses of the P and N paths.

Our next step is to derive the PSD of the field intensity of one channel $S_{|\tilde{E}_{SIG,i}|}^{(f)}$ required in Eq. (4.35). Without loss of generality, we will drop the subscript i and focus on the PSD of the squared envelope of one of the WDM channels $S_{|\tilde{E}_{SIG}|}^{(f)}$. We begin by evaluating the squared envelope of the received signal field given by Eq. (4.24) and then finding the time averaged ACF of the squared field envelope $\bar{\Gamma}_{|\tilde{E}_{SIG}|}^{(\tau)}$ as

$$\begin{aligned} \bar{\Gamma}_{|\tilde{E}_{SIG}|}^{(\tau)} &= \overline{\langle \tilde{E}_{SIG} \tilde{E}_{SIG}^* \tilde{E}_{SIG} \tilde{E}_{SIG}^* \rangle} \\ &= \sum_{n=-\infty}^{\infty} \sum_{m=-\infty}^{\infty} \sum_{l=-\infty}^{\infty} \sum_{k=-\infty}^{\infty} \overline{\langle (aX_n + bY_n)(aX_m + bY_m)^* (aX_l + bY_l)(aX_k + bY_k)^* \rangle} \\ &\quad \times h(t-nT)h^*(t-mT)h(t-\tau-lT)h^*(t-\tau-kT) \end{aligned} \quad (4.36)$$

where the statistical average of the product of four brackets can be evaluated as follows

$$\begin{aligned} \overline{\langle (aX_n + bY_n)(aX_m + bY_m)^* (aX_l + bY_l)(aX_k + bY_k)^* \rangle} &= |a|^4 \langle X_n X_m^* X_l X_k^* \rangle + |b|^4 \langle Y_n Y_m^* Y_l Y_k^* \rangle \\ &\quad + |a|^2 |b|^2 \langle X_n X_m^* Y_l Y_k^* \rangle + |a|^2 |b|^2 \langle Y_n Y_m^* X_l X_k^* \rangle \\ &\quad + |a|^2 |b|^2 \langle Y_n X_m^* X_l Y_k^* \rangle + |a|^2 |b|^2 \langle X_n Y_m^* Y_l X_k^* \rangle \\ &\quad + \text{terms with vanishing statistical averages,} \end{aligned}$$

while noting that

$$\langle X_n X_m^* X_l X_k^* \rangle = \langle Y_n Y_m^* Y_l Y_k^* \rangle = \begin{cases} 1 & n = m \ \& \ l = k \\ 1 & n = k \ \& \ m = l \ \& \ n \neq m, \\ 0 & \text{otherwise} \end{cases}$$

$$\langle X_n X_m^* Y_l Y_k^* \rangle = \langle Y_n Y_m^* X_l X_k^* \rangle = \begin{cases} 1 & n = m \ \& \ l = k \\ 0 & \text{otherwise} \end{cases},$$

$$\langle Y_n X_m^* X_l Y_k^* \rangle = \langle X_n Y_m^* Y_l X_k^* \rangle = \begin{cases} 1 & n = k \ \& \ l = m \\ 0 & \text{otherwise} \end{cases}.$$

Back substituting into Eq. (4.36) yields

$$\begin{aligned}
\bar{\Gamma}_{|\dot{E}_{SIG}}(\tau) &= (|a|^4 + |b|^4) \cdot \left[\sum_{n=-\infty}^{\infty} \sum_{l=-\infty}^{\infty} \overline{|h(t-nT)|^2 |h(t-\tau-lT)|^2} \right. \\
&\quad \left. + \sum_{\substack{n=-\infty \\ n \neq m}}^{\infty} \sum_{m=-\infty}^{\infty} \overline{h(t-nT)h^*(t-mT)h(t-\tau-mT)h^*(t-\tau-nT)} \right] \\
&\quad + 2|a|^2|b|^2 \left[\sum_{n=-\infty}^{\infty} \sum_{l=-\infty}^{\infty} \overline{|h(t-nT)|^2 |h(t-\tau-lT)|^2} \right. \\
&\quad \left. + \sum_{n=-\infty}^{\infty} \sum_{m=-\infty}^{\infty} \overline{h(t-nT)h^*(t-mT)h(t-\tau-mT)h^*(t-\tau-nT)} \right] \\
&= \frac{1}{T} (|a|^4 + |b|^4 + 2|a|^2|b|^2) \sum_{l=-\infty}^{\infty} \Gamma_{|h|^2}(\tau-lT) + \frac{1}{T} (|a|^4 + |b|^4) \sum_{\substack{k=-\infty \\ k \neq 0}}^{\infty} C_h(\tau, k) + \frac{1}{T} 2|a|^2|b|^2 \sum_{k=-\infty}^{\infty} C_h(\tau, k), \quad (4.37)
\end{aligned}$$

where $\Gamma_{|h|^2}(\tau) = \int_{-\infty}^{\infty} |h(t)|^2 |h(t-\tau)|^2 dt$ is the deterministic ACF of the squared envelope of the

overall pulse shape and $C_h(\tau, k) = \int_{-\infty}^{\infty} h(t)h^*(t-\tau)h^*(t-kT)h(t-\tau-kT)dt$. In order to obtain

the last line in Eq. (4.37), we perform some lengthy algebraic manipulations on the two double summations. The first double summation is manipulated as

$$\begin{aligned}
\sum_{n=-\infty}^{\infty} \sum_{l=-\infty}^{\infty} \overline{|h(t-nT)|^2 |h(t-\tau-lT)|^2} &= \frac{1}{T} \sum_{n=-\infty}^{\infty} \sum_{l=-\infty}^{\infty} \int_{-T/2}^{T/2} |h(t-nT)|^2 |h(t-\tau-lT)|^2 dt \\
&= \frac{1}{T} \sum_{n=-\infty}^{\infty} \int_{-T/2}^{T/2} |h(t-nT)|^2 \sum_{l=-\infty}^{\infty} |h(t-\tau-lT)|^2 dt \quad , \text{let } t-nT = z \\
&= \frac{1}{T} \sum_{n=-\infty}^{\infty} \int_{-nT-T/2}^{-nT+T/2} |h(z)|^2 \sum_{l=-\infty}^{\infty} |h(z-\tau-(l-n)T)|^2 dz \\
&= \frac{1}{T} \sum_{l=-\infty}^{\infty} \int_{-\infty}^{\infty} |h(z)|^2 |h(z-\tau-lT)|^2 dz \\
&= \frac{1}{T} \sum_{l=-\infty}^{\infty} \Gamma_{|h|^2}(\tau-lT), \quad \text{where } \Gamma_{|h|^2}(\tau) = \int_{-\infty}^{\infty} |h(t)|^2 |h(t-\tau)|^2 dt
\end{aligned}$$

and the second double summation is evaluated similarly as

$$\begin{aligned}
& \sum_{n=-\infty}^{\infty} \sum_{\substack{m=-\infty \\ n \neq m}}^{\infty} \overline{h(t-nT)h^*(t-mT)h(t-\tau-mT)h^*(t-\tau-nT)} \\
&= \frac{1}{T} \sum_{n=-\infty}^{\infty} \sum_{\substack{m=-\infty \\ n \neq m}}^{\infty} \int_{-T/2}^{T/2} h(t-nT)h^*(t-mT)h(t-\tau-mT)h^*(t-\tau-nT)dt \\
&= \frac{1}{T} \sum_{n=-\infty}^{\infty} \int_{-T/2}^{T/2} h(t-nT)h^*(t-\tau-nT) \left[\sum_{\substack{m=-\infty \\ n \neq m}}^{\infty} h^*(t-mT)h(t-\tau-mT) \right] dt \quad , \text{let } t-nT = z \\
&= \frac{1}{T} \sum_{n=-\infty}^{\infty} \int_{-nT-T/2}^{-nT+T/2} h(z)h^*(z-\tau) \left[\sum_{\substack{m=-\infty \\ n \neq m}}^{\infty} h^*(z-(m-n)T)h(z-\tau-(m-n)T) \right] dz \\
&= \frac{1}{T} \sum_{\substack{k=-\infty \\ k \neq 0}}^{\infty} \int_{-\infty}^{\infty} h(t)h^*(t-\tau)h^*(t-kT)h(t-\tau-kT)dt \\
&= \frac{1}{T} \sum_{\substack{k=-\infty \\ k \neq 0}}^{\infty} C_h(\tau, k), \quad \text{where } C_h(\tau, k) = \int_{-\infty}^{\infty} h(t)h^*(t-\tau)h^*(t-kT)h(t-\tau-kT)dt
\end{aligned}$$

Next, applying the FT to the ACF obtained in Eq. (4.37) yields the desired PSD of the squared envelope (or intensity) of one channel $S_{|\dot{E}_{SIG.}}(f)$ on the form

$$\begin{aligned}
S_{|\dot{E}_{SIG.}}(f) &= \frac{1}{T^2} \cdot \left| FT \{h(t)h^*(t)\} \right|^2 \sum_{l=-\infty}^{\infty} \delta\left(f - \frac{l}{T}\right) \\
&\quad + \frac{1}{T} \sum_{k=-\infty}^{\infty} \left| FT \{h(t)h^*(t-kT)\} \right|^2 - \frac{1}{T} (|a|^4 + |b|^4) \left| FT \{h(t)h^*(t)\} \right|^2 \\
&= \frac{1}{T^2} |H(f) \otimes H^*(-f)|^2 \sum_{l=-\infty}^{\infty} \delta\left(f - \frac{l}{T}\right) \\
&\quad + \frac{1}{T} \sum_{k=-\infty}^{\infty} \left| H(f) \otimes (e^{-j2\pi f k T} H^*(-f)) \right|^2 - \frac{1}{T} (|a|^4 + |b|^4) |H(f) \otimes H^*(-f)|^2, \quad (4.38)
\end{aligned}$$

where in obtaining Eq. (4.38), we first proved and then employed the following FT pairs

$$\begin{aligned}
FT \left\{ \Gamma_{|h|^2}(\tau) \right\} &= \left| FT \{h(t)h^*(t)\} \right|^2 = |H(f) \otimes H^*(-f)|^2, \\
FT \{C_h(\tau, k)\} &= \left| FT \{h(t)h^*(t-kT)\} \right|^2 = \left| H(f) \otimes (e^{-j2\pi f k T} H^*(-f)) \right|^2.
\end{aligned}$$

By carefully examining Eq. (4.38), we notice that the first term of $S_{|\tilde{E}_{SIG,i}}^{AC}(f)$ is a summation of Dirac delta functions at discrete frequencies of l/T where l is an integer. The second and third terms represent the continuous portion of the PSD which depends on the pulse shape, residual CD and polarization orientation. Next, we make use of the derived PSD of the intensity of one channel in Eq. (4.38) to evaluate the PSD of the residual SIG-SIG beating contribution in the differential photocurrent given by Eq. (4.35) while keeping only the relevant AC terms required for the SNR evaluation

$$S_{\Delta I_{SIG-SIG}}^{AC}(f) = \frac{1}{4} \sum_{i=1}^{N_{ch}} \left| H^P(f) R_{SIG,i}^P - H^N(f) e^{j2\pi f \delta} R_{SIG,i}^N \right|^2 S_{|\tilde{E}_{SIG,i}}^{AC}(f), \quad (4.39)$$

where the PSD of the intensity of the i^{th} channel is written based on the form given by Eq. (4.38) in terms of the pulse shape and polarization orientation of the i^{th} channel as follows

$$S_{|\tilde{E}_{SIG,i}}^{AC}(f) = \frac{1}{T} \sum_{k=-\infty}^{\infty} \left| FT \{ h_i(t) h_i^*(t-kT) \} \right|^2 - \frac{1}{T} (|a_i|^4 + |b_i|^4) \left| FT \{ h_i(t) h_i^*(t) \} \right|^2, \quad (4.40)$$

where the subscripts i in Eq. (4.40) take into account the possibility of having different pulse shapes, CD and polarization orientation of different WDM channels. Finally if we integrate the PSD in Eq. (4.39) over frequency, we obtain the variance (AC power) of the residual SIG-SIG beating contribution in the differential photocurrent (required in Eq. (4.10) to evaluate the SNR) as follows

$$\begin{aligned} \sigma_{\Delta I_{SIG-SIG}}^2 &= \frac{1}{4} \sum_{i=1}^{N_{ch}} \int_{-\infty}^{\infty} \left| H^P(f) R_{SIG,i}^P - H^N(f) e^{j2\pi f \delta} R_{SIG,i}^N \right|^2 S_{|\tilde{E}_{SIG,i}}^{AC}(f) |H_{rx-DSP}(f)|^2 df \\ &= \frac{1}{4} N_{ch} \sigma_{|\tilde{E}}^2 \frac{\int_{-\infty}^{\infty} \left| H^P(f) R_{SIG}^P - H^N(f) e^{j2\pi f \delta} R_{SIG}^N \right|^2 S_{|\tilde{E}_{SIG}}^{AC}(f) |H_{rx-DSP}(f)|^2 df}{\int_{-\infty}^{\infty} S_{|\tilde{E}_{SIG}}^{AC}(f) |H^{av}(f)|^2 |H_{rx-DSP}(f)|^2 df}, \end{aligned} \quad (4.41)$$

where in the second equality, we assumed the same responsivity for different WDM channels as well as equal intensity PSDs for various channels, i.e. $S_{|\tilde{E}_{SIG,i}}^{AC}(f)$ is the same for any i which implies assuming the same CD, pulse shape and polarization orientation for different WDM

channels⁴. Also, $\sigma_{|\tilde{E}|}^2 = \int_{-\infty}^{\infty} \sigma_{|\tilde{E}|}^{AC} (f) |H_{rx-DSP}(f)|^2 df$ is the variance (or AC electrical power) of the photocurrent generated by the field intensity of one channel if detected with a single-ended PD having a unity responsivity and frequency response equal to the average frequency responses of the P and N PDs followed by DSP filtering. It is also noticeable that $\frac{1}{4} \sigma_{|\tilde{E}|}^2 = \sigma_{|E_{SIG,se}|}^2$ because the power of the complex field is twice that of the real field. In addition, it can be shown that $\sigma_{|E_{SIG,se}|}^2 = \beta P_{SIG}^2$, where β is a fractional scaling factor defined as the ratio between the AC power of the filtered photocurrent generated by the field intensity of one channel and its DC electrical power (which is the squared DC power of the field itself assuming a unit responsivity). In fact, β was shown by simulations in [108] to be dependent on the residual CD and polarization orientation (see appendix B for further details on the scaling factor β). Later in Appendix B we elaborate more on the dependence of β on CD and the polarization orientation.

4.8.3 Power of thermal and shot noise contributions in the photocurrent difference

Since shot noises generated from P and N PDs are uncorrelated, we can write the variance of their photocurrent difference $\Delta i_{sh}(t) = i_{sh}^P(t) - i_{sh}^N(t)$ assuming, for simplicity, flat responsivity across the WDM spectrum and equal received signal powers for all WDM channels as follows

$$\sigma_{\Delta i_{sh}}^2 = 2e \left[(R_{LO}^N + R_{LO}^P) P_{LO} + N_{ch} (R_{SIG}^N + R_{SIG}^P) P_{SIG} \right] \Delta f \approx 4e \left[R_{LO}^{av} P_{LO} + N_{ch} R_{SIG}^{av} P_{SIG} \right] \Delta f, \quad (4.42)$$

where Δf is the effective BW that depends on the overall frequency response of the receiver including PDs, TIAs, and DSP filtering as well as the transmitted pulse shape. In the second equality, we use the averaged LO and SIG responsivities over both the P and N PDs. Next, we also calculate the variance of the final photocurrent due to thermal noise as follows

$$\sigma_{\Delta i_{th}}^2 = (i_{TIA})^2 \Delta f, \quad (4.43)$$

⁴ Although assuming the same pulse shape, CD and polarization orientation is not true in practice, the discussion in appendix B (see section 4.9) regarding the scaling factor β will show that after a short transmission distance, the PSDs of the intensities of various WDM channels (and hence the power of the SIG-SIG beating) should eventually be the same regardless of the pulse shape, polarization orientation and CD.

where i_{TIA} is the input-referred noise current density which is an important specification for the TIAs, often provided in pA/\sqrt{Hz} .

4.8.4 Expressions of PSDs of the LO-LO, SIG-ON and ON-ON beating contributions in the final differential photocurrent

Although we neglected the LO-LO, SIG-ON and ON-ON beating contributions when evaluating the PSD of the differential photocurrent in Eq. (4.9) since they were found negligible in our experiment, we present hereafter the final expressions of the PSDs of these three beat noise sources for the sake of completeness.

The PSDs of the differential photocurrents $\Delta i_{LO-LO}(t)$, $\Delta i_{SIG-ON}(t)$, and $\Delta i_{ON-ON}(t)$ can be obtained using the same procedure employed for other beating terms, that is by first evaluating the ACF of the photocurrent which, after a FT leads to the PSD. Below are the final expressions of the PSDs of the three beating contributions assuming the same responsivity for all WDM channels

$$S_{\Delta i_{LO-LO}}(f) = |H^P(f)R_{LO}^P - H^N(f)e^{j2\pi f\delta}R_{LO}^N|^2 \cdot P_{LO}^2 (\delta(f) + RIN(f)), \quad (4.44)$$

$$S_{\Delta i_{SIG-ON}}(f) = \frac{1}{4} |H^P(f)R_{SIG}^P - H^N(f)e^{j2\pi f\delta}R_{SIG}^N|^2 N_{ch} \left(S_{\tilde{E}_{SIG}}(f) S_{\tilde{E}_{ON}}(f) \right) \quad (4.45)$$

$$S_{\Delta i_{ON-ON}}(f) = |H^P(f)R_{SIG}^P - H^N(f)e^{j2\pi f\delta}R_{SIG}^N|^2 \left((N_o B_o)^2 \cdot \delta(f) + N_o^2 B_o \text{tri}\left(\frac{f}{B_o}\right) \right), \quad (4.46)$$

where $RIN(f)$ is the spectrum of the relative intensity noise of the LO laser defined as

$$RIN(f) = \text{FT} \left\{ \langle \delta P_{LO}(t) \delta P_{LO}(t-\tau) \rangle / P_{LO}^2 \right\}, \quad (4.47)$$

where $\delta P_{LO}(t)$ denotes the random intensity fluctuations of the LO laser optical power around its average power P_{LO} . Also, the triangular function in Eq. (4.46) is defined as

$$\text{tri}\left(\frac{f}{B_o}\right) = \begin{cases} 1 - \frac{|f|}{B_o} & |f| \leq B_o, \\ 0 & |f| > B_o \end{cases},$$

where B_o is the optical bandwidth of the WDM spectrum.

4.9 Appendix B: Dependence of the scaling factor of the SIG-SIG beating photocurrent on the residual CD and polarization orientation

In this appendix, we study in detail the scaling factor β presented in section 4.3. It is a fractional scaling factor equal to the ratio of the variance (or AC power) of the filtered photocurrent generated by the field intensity of one WDM channel relative to the DC electrical power of the photocurrent (which is the squared average optical power of the field itself assuming unit responsivity). In fact, it can be expressed as follows

$$\beta = \frac{\frac{1}{4} \int_{-\infty}^{\infty} S_{|\tilde{E}_{SIG}|}^{AC}(f) |H^{av}(f)|^2 |H_{rx-DSP}(f)|^2 df}{P_{SIG}^2}, \quad (4.48)$$

where $S_{|\tilde{E}_{SIG}|}^{AC}(f)$ is the AC portion of the PSD of the intensity of the complex envelope of the signal field defined in Eq. (4.38), $H^{av}(f)$ is the average frequency response of the P and N ports of the CRx, $H_{rx-DSP}(f)$ is the frequency response representing all filtering performed at the receiver side DSP, and P_{SIG} is the average optical power of the field of one channel. By looking back at Eq. (4.38), we notice that $S_{|\tilde{E}_{SIG}|}^{AC}(f)$ depends on the pulse shape and the residual CD (included in $h(t)$) as well as on the polarization orientation of the received signal relative to the PBS axis of the CRx (represented by a and b). Hence, the scaling factor β will in turn be dependent on the above parameters. In addition, β also tracks the overlap between the intensity spectrum $S_{|\tilde{E}_{SIG}|}^{AC}(f)$ and the overall transfer function of the receiver side ($H^{av}(f)$ and $H_{rx-DSP}(f)$). In fact, the intensity spectrum is broader than the LO-SIG beating spectrum (desired term) which can be explained in view of Eq. (4.38) as follows: $S_{|\tilde{E}_{SIG}|}^{AC}(f)$ is proportional to $\sum_{k=-\infty}^{\infty} |H(f) \otimes (e^{-j2\pi f k T} H^*(-f))|^2$ meaning that the intensity spectrum is proportional to the squared magnitude of the convolution of the frequency response of the received field with phase shifted versions of itself and hence, the bandwidth of the intensity spectrum is expected to be double that of the received field. Thus, almost one half of the power of the intensity spectrum is

rejected by filtering from the CRx itself and from the receiver DSP since this filtering is designated to pass only the desired signal spectrum.

In order to evaluate the impact of residual CD and polarization orientation on the scaling factor β , simulations are carried using a 28 Gbaud PDM-QPSK signal having 10^5 symbols. First, the symbols were pulse shaped using NRZ pulses at 16 samples/symbol. The NRZ pulse shape used in the simulation produces the QPSK intensity eyediagram shown in Fig. 4.15(a) which matches quite well the experimental intensity eyediagram obtained by direct detection after the single polarization IQ modulator (see Fig. 4.15(b)). After pulse shaping, the waveform was transmitted through various CD amounts ranging from 0 to 5 ns/nm. After CD was applied, the polarization of the waveform was rotated by some Jones angle (θ) by multiplying by the Jones matrix J defined in Eq. (4.25) where $a = \cos(\theta)$ and $b = \sin(\theta)$, in order to simulate the misalignment between the state of polarization of the received signal and the axes of the CRx PBS. Then, the resulting waveform was convolved with the overall receiver's impulse response (assumed to be the matched filter in simulations). Finally, the variance (AC power) of the squared envelope (intensity) of the resulting filtered waveform is calculated and divided by its DC power resulting in the scaling factor β .

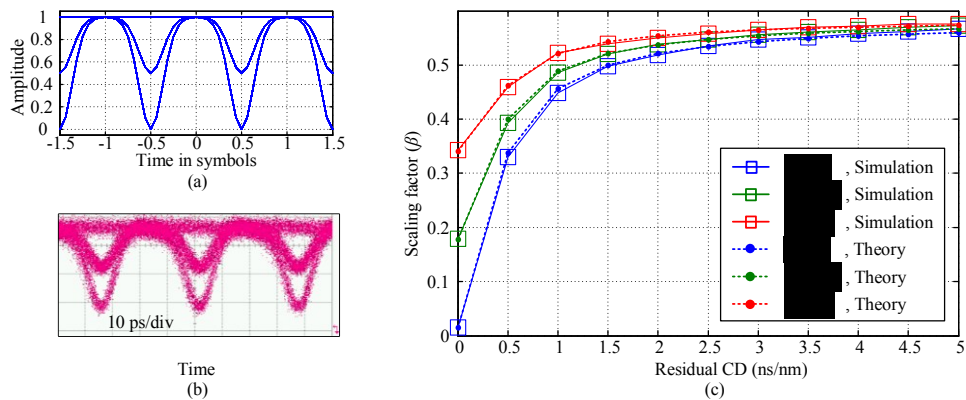


Fig. 4.15. (a) Simulated intensity eyediagram of the single polarization QPSK signal using NRZ pulse shape, (b) experimental intensity eyediagram obtained after the single polarization IQ modulator, (c) scaling factor (β) versus the amount of residual CD for various polarization rotation angles (θ) obtained from simulations and theory on a 28 Gbaud PDM-QPSK signal.

Fig. 4.15(c) plots β as evaluated from the simulation described above versus the amount of CD in ns/nm for various polarization rotation angles θ . For the purpose of comparison, we also plot in Fig. 4.15(c) β versus the amount of CD at different polarization orientations as calculated from our theoretical expression in Eq. (4.48) with the application of Eq. (4.38)

(derived in subsection 4.8.2) that expresses the PSD of the intensity in terms of the pulse shape, CD and polarization orientation. An excellent agreement is observed between the β values calculated from simulation and theory which verifies our analytical expressions. It is also noteworthy that the theoretical expressions derived can be employed to calculate β for any other pulse shape by plugging the impulse response of the pulse shape in Eq. (4.38) and then using Eq. (4.38) into Eq. (4.48). In addition, β can be evaluated for other modulation formats in a similar fashion to the one used for PDM-QPSK, however, a part of the derivation in subsection 4.8.2 has to be re-worked for the desired modulation format, specifically, the statistical average performed on the information symbols in Eq. (4.36), which was evaluated assuming PDM-QPSK modulation, has to be re-calculated for the new format.

Looking back to Fig. 4.15(c), we notice that the impact of the polarization orientation on β is significant for CD values less than 2 ns/nm (which corresponds to ~ 117 km propagation over a fiber with dispersion parameter of 17 ps/(nm.km)). Within this CD range, β is at its maximum when $\theta = \pi/4$ since for this polarization rotation angle, maximum crosstalk (and beating) between the two orthogonal polarizations of the received signal after passing through the PBS of the CRx results. Hence, this maximizes the peak-to-average ratio of the electrical signals at the output of the CRx which in turn increases the AC power of the photocurrent and finally increases β . On the other hand when the residual CD is larger than 2 ns/nm, the impact of θ is less significant. In fact as the residual CD increases beyond 3 ns/nm, β increases until it saturates at a maximum value of around 0.55 regardless of polarization.

Chapter 5

Polarization-Division-Multiplexing in Intensity-Modulation / Direct-Detection Systems Enabled by MIMO DSP

5.1 Overview

As motivated to in section 1.2.2, there is an immense need to develop cost, size and power efficient optics to replace copper in order to solve the intra-datacenter connectivity bottleneck [123]. Recently in IEEE 802.3ba [27], 100 Gb/s transmission of Ethernet frames over 2 to 10 km SMF has been standardized as 100GBASE-LR4 by using 4 colors in the 1300 nm (O-band) on a LAN-WDM grid (4.5 nm channel spacing) with each channel carrying 25 Gb/s of intensity-modulated data. In addition to the LR4 standard, 100GBASE-SR4 provides the specifications for transmitting Ethernet frames over ~100 m of multimode fiber (MMF) using 4 fiber lanes with each carrying 25 Gb/s in the 850 nm window. Commercial 100G transceivers in CFP and CFP2 form factor pluggables [124] following the IEEE 802.3ba standard currently exist on the market. Although WDM or spatial multiplexing, i.e. using multiple fiber lanes, has been adopted to achieve the aggregate total bit rate for the recent 100G Ethernet standard and current commercial products, it is widely agreed that achieving 100 Gb/s on a single wavelength using inexpensive, size and power efficient components is a mandatory building block in order to realize the envisioned future steps of 400 Gb/s and 1 Tb/s [28]. Approaches based on multiplexing lower rates in wavelength (i.e. WDM), e.g. 25 Gb/s or 50 Gb/s, suffer from requiring a large number of laser sources, e.g. 8×50 Gb/s and 20×50 Gb/s to realize 400 and 1 Tb/s respectively, which degrades the overall yield of the transceiver, imposes more stringent requirement on the wavelength stability of the lasers and makes the transceiver packaging (optically and thermally) more challenging. On the other hand, approaches based on spatial multiplexing using multiple fiber lanes per cable would also suffer from packaging and interfacing problems from the parallel fiber lanes into the transceiver and vice versa. Due to all aforementioned arguments, a consensus is expected to be reached that 4×100 Gb/s achieved using 4 colors is the optimal solution to realize 400 Gb/s where each wavelength carries

100 Gb/s. The four wavelengths can be placed on a LAN-WDM (4.5 nm spacing) or CWDM grid (20 nm spacing). In order to scale this to 1 Tb/s, this would require ten lasers to be packaged in a CFP, CFP2 or even CFP4 form factor which seems quite problematic. Also, fitting ten lasers in the O-band on a CWDM grid is not feasible and LAN-WDM will have to be employed. In this case, building uncooled transmitters, i.e. without thermo-electric coolers (TECs), becomes also very difficult because lasers typically have a wavelength temperature coefficient of 0.1 nm/°C [125]. Hence, a solution that allows reducing the number of required colors by increasing the bit rate per wavelength is highly desirable, which is what motivates the current work that exploits another dimension (polarization) to double the achievable bit rate per wavelength, i.e. via polarization division multiplexing (PDM), while maintaining the use of IM/DD.

The recent literature is rich of 100 Gb/s short reach IM/DD transmission experiments that have been reported using various advanced modulation formats, such as 4-level pulse amplitude modulation (PAM-4) with PDM [32], half-cycle Nyquist subcarrier modulated 16-ary quadrature amplitude modulation (16-QAM) with PDM [31], multi-band carrierless amplitude phase modulation (multi-CAP) [126] and discrete multi-tone (DMT) [29]. In the IM/DD experiments in [31, 32], PDM was used to halve the baud rate required to achieve 100 Gb/s with the polarization demultiplexing performed optically at the receiver using a polarization controller, i.e. not using DSP. More recently, 400 Gb/s was also experimentally demonstrated as 4×100 Gb/s using DMT and four directly modulated lasers (DMLs) over 30 km in [127] in the O-band.

In addition to all endeavors above, PDM was also used for the self-coherent system experiment in [128] where the signal was modulated in one polarization (in-phase and quadrature) and a copy of the transmit laser was sent on the other orthogonal polarization to be used as a remote local oscillator (LO) at the receiver. At the receiver, DSP in the Stokes space was used to cancel the unwanted photodetection nonlinearity and enable phase diversity. Also, a recent simulation-based work in [129] proposed a DSP algorithm to perform polarization demultiplexing in the Stokes space for a PDM IM/DD PAM-2 binary signal.

In parallel with the ongoing efforts to select the right signaling format for the future 400 Gb/s and 1 Tb/s short reach links, Silicon photonics (SiP) is rapidly emerging as an inexpensive solution that is suited for both long-haul transport applications [43] and short reach optical interconnects [34]. Among other advantages, Silicon is a useful host material for fabricating

photonic devices (e.g. the modulator, photodiodes, etc.) because of its low cost, high yield, large scale integration, and CMOS compatibility [35].

In [130], we reported 112 Gb/s 10 km transmission using single polarization PAM formats employing a single laser source and a fully packaged SiP modulator [33]. In addition, high speed digital-to-analog and analog-to-digital converters (DAC and ADC) were employed which enables DSP at transmitter and receiver sides to perform, among different other tasks, pulse shaping, pre-compensation and post-compensation of the limited bandwidth of various components.

In this chapter, we propose a PDM IM/DD scheme enabled by novel MIMO DSP based polarization demultiplexing following a DD receiver front-end. An experiment is conducted where we report 224 Gb/s transmission over 10 km using a single 1310 nm laser and the same SiP IM of [33]. To achieve this bit rate on a single wavelength, IM with a 56 Gbaud PAM-4 signal in conjunction with PDM is employed, where polarization demultiplexing at the receiver is performed using a novel DSP that operates in the Stokes space after a direct detection (DD) receiver. In addition, we assume a hard decision FEC with 6.7% overhead which guarantees error free operation ($\text{BER} < 1 \times 10^{-15}$) for an input $\text{BER} < 4.4 \times 10^{-3}$ at the FEC decoder input [131]. To the best of our knowledge, this is the first demonstration of 224 Gb/s (200 Gb/s including 6.7 % FEC overhead in addition to 5% protocol overhead) on a single color using a SiP modulator and MIMO DSP-based transceiver. At the time of the experiment, this was the highest reported bit rate using IM/DD on a single modulated wavelength. In addition to doubling the achievable bit rate, PDM also enables operation at 112 Gb/s using either 56 Gbaud PAM-2 or 28 Gbaud PAM-4 with significantly reduced FEC overhead. When the proposed PDM IM/DD system is used in conjunction with WDM, it requires using only two and five laser sources to achieve aggregate data rates of 400 and 1 Tb/s, respectively; half of the required number of lasers in an equivalent single polarization system.

The remainder of this chapter is organized as follows. Section 5.2 depicts the architecture of the PDM IM/DD transceiver and introduces the concept of the proposed MIMO DSP in Stokes space. Next, section 5.3 shows the experimental setup, the DSP stack at both transmitter and receiver sides and the experimental results. Then, section 5.4 shows simulation results where we study the receiver performance with varying splitting ratios for the couplers employed in the receiver DD front-end. We finally conclude in section 5.5.

5.2 Principle of Stokes space polarization demultiplexing for PDM IM/DD systems

A block diagram of the polarization division multiplexed (PDM) IM/DD system is shown in Fig. 5.1. The transmitter in Fig. 5.1(a) comprises a polarization beam splitter (PBS), two external intensity modulators (IMs) that imprint two independent information streams on the intensity of the two orthogonal states of polarization (SOPs) of the field originating from a single laser before being combined using a polarization beam combiner (PBC) and transmitted. Realizing the proposed PDM system with two external modulators rather than two directly modulated lasers (DMLs) allows the use of a single external laser source whose polarization states are independently modulated externally. The transmitted field can be equivalently represented by a Jones vector $\mathbf{E}^t = [E'_x \quad E'_y]^T$ or a 3-D Stokes vector $\hat{\mathbf{E}}^t = [E'_1 \quad E'_2 \quad E'_3]^T$ where both are related as $E'_1 = |E'_x|^2 - |E'_y|^2$, $E'_2 = 2 \operatorname{Re}\{E'_x E'_y^*\}$, $E'_3 = 2 \operatorname{Im}\{E'_x E'_y^*\}$, where \mathbf{T} denotes vector transpose. In addition to the 1st 2nd and 3rd Stokes parameters E'_1 , E'_2 and E'_3 contained in the Stokes vector $\hat{\mathbf{E}}^t$, the 0th Stokes parameter which represents the total intensity is defined as $E'_0 = |E'_x|^2 + |E'_y|^2$. After propagation, the fiber channel results in a unitary transformation that is modeled by either a 2×2 complex-valued matrix \mathbf{J} or a 3×3 real-valued matrix \mathbf{R} . In the Stokes space, this is written as $\hat{\mathbf{E}}^r = \mathbf{R}\hat{\mathbf{E}}^t = [E'_1 \quad E'_2 \quad E'_3]^T$ where the entries of the matrix \mathbf{R} are unknown. On the other hand, E'_0 is not impacted by the unitary rotation, i.e. $E'_0 = E'_0$. As the proposed system is a PDM IM/DD system where the information is imprinted on the intensity, the only Stokes parameters required to retrieve the information at the receiver are E'_0 and E'_1 , which are the sum and difference of the transmitted intensities on X and Y polarizations, respectively. Since E'_0 is insensitive to the polarization rotation, the task of the receiver MIMO DSP is to recover only E'_1 from the received Stokes vector $\hat{\mathbf{E}}^r$, i.e. from the three received Stokes parameters E'_1 , E'_2 and E'_3 . A functional block diagram of the receiver front-end that extracts the Stokes parameters of the received field is shown in Fig. 5.1(b). A PBS is initially used to split the received signal into two orthogonal polarizations that are further split using 50/50 polarization maintaining couplers

and detected separately to provide $\frac{1}{2}|E_x^r|^2$ and $\frac{1}{2}|E_y^r|^2$ on the upper and lower branches where the excess loss of various components is neglected for simplicity. The detected intensities can then be added and subtracted to obtain $\frac{1}{2}E_0^r$ and $\frac{1}{2}E_1^r$ respectively. In addition, the two polarization tributaries of the received signal at the other outputs of the couplers beat together (after one of them is rotated by 90°) in a 90° hybrid that provides $\frac{1}{2}\text{Re}\{E_x^r E_y^{r*}\}$ and $\frac{1}{2}\text{Im}\{E_x^r E_y^{r*}\}$ after balanced detection on the middle two output branches, i.e. it provides $\frac{1}{4}E_2^r$ and $\frac{1}{4}E_3^r$, respectively. This means that the front-end of Fig. 5.1(b) provides the Stokes parameters of the received signal provided that the two signals at the middle branches resulting from the beating are scaled by a factor of 2. It is noteworthy that the same receiver front-end was used in [128] to detect the Stokes parameters of the received field; however, it was used in a self-coherent scheme where the signal is modulated into one polarization and the other polarization is used to transmit a copy of the laser to be used as a remote LO.

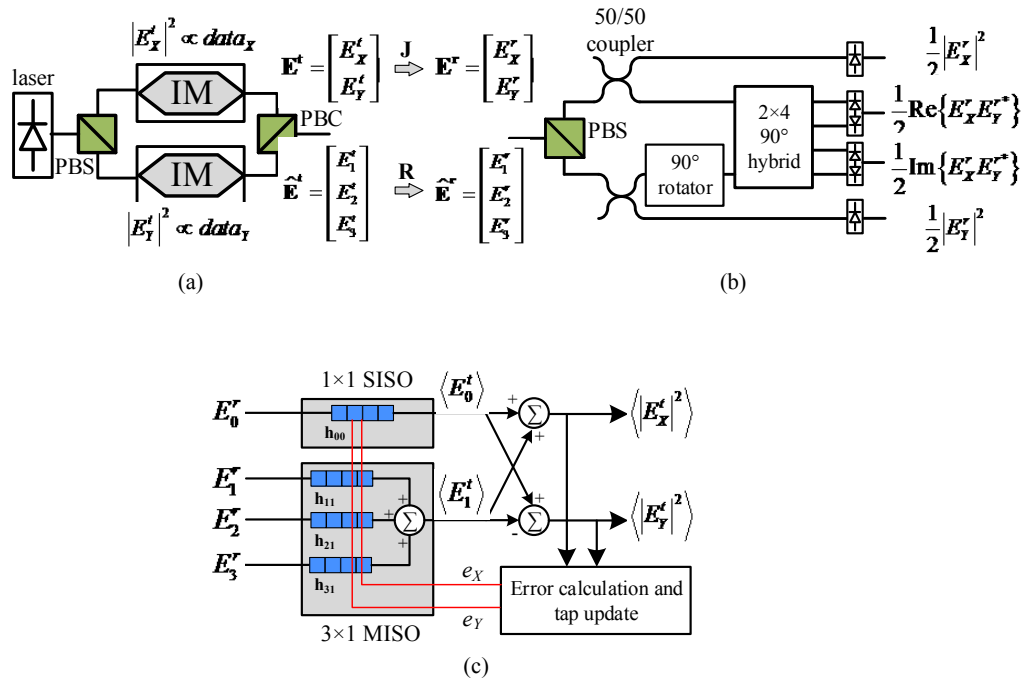


Fig. 5.1. Block diagram of the PDM IM/DD system including (a) transmitter, (b) receiver front-end and (c) MIMO DSP to perform polarization demultiplexing using direct-detected Stokes parameters, (PBS: polarization beam splitter, PBC: polarization beam combiner).

Next, the four detected Stokes parameters are fed into the proposed DSP stack of Fig. 5.1(c) which achieves polarization demultiplexing. First, E_0^r is filtered using a 1×1 single-input and single-output (SISO) finite impulse response (FIR) filter with N real-valued taps \mathbf{h}_{00} to mitigate residual inter-symbol interference (ISI) and provide an estimate of E_0^t denoted by $\langle E_0^t \rangle = \mathbf{h}_{00}^T \mathbf{E}_0^r$, where \mathbf{E}_0^r is an $N \times 1$ tap input vector containing N successive received samples of the 0th Stokes parameter. Also, the lower part of the DSP stack is a 3×1 multiple-input and single-output (MISO) bank of FIR filters \mathbf{h}_{11} , \mathbf{h}_{21} and \mathbf{h}_{31} , each having N real-valued taps, that accepts E_1^r , E_2^r and E_3^r at its input and provides an estimate $\langle E_1^t \rangle = \mathbf{h}_{11}^T \mathbf{E}_1^r + \mathbf{h}_{21}^T \mathbf{E}_2^r + \mathbf{h}_{31}^T \mathbf{E}_3^r$ at its output where \mathbf{E}_k^r represents an $N \times 1$ tap input vector containing N successive received samples of the k^{th} Stokes parameter, i.e. it removes the polarization rotation and mitigates any ISI. In the extreme case of using single tap filters ($N = 1$), \mathbf{h}_{11} , \mathbf{h}_{21} and \mathbf{h}_{31} should represent the first row of the inverse matrix \mathbf{R}^{-1} . Next, the outputs of the 1×1 SISO and 3×1 MISO filters are added and subtracted to retrieve estimates $\langle |E_X^t|^2 \rangle$ and $\langle |E_Y^t|^2 \rangle$ of the transmitted intensities on the X and Y polarizations. Finally, least mean square (LMS) tap adaptation is performed using the two error signals $e_X = \overline{\langle |E_X^t|^2 \rangle} - \langle |E_X^t|^2 \rangle$ and $e_Y = \overline{\langle |E_Y^t|^2 \rangle} - \langle |E_Y^t|^2 \rangle$ where $\overline{\langle |E_X^t|^2 \rangle}$ and $\overline{\langle |E_Y^t|^2 \rangle}$ are maximum likelihood symbol decisions. During the initial equalizer training, decisions are replaced by known training symbols. The equalizers taps \mathbf{h}_{00} , \mathbf{h}_{11} , \mathbf{h}_{21} and \mathbf{h}_{31} at the $(i+1)^{\text{th}}$ symbol are updated from taps at the i^{th} symbol as follows

$$\begin{aligned} \mathbf{h}_{00}^{i+1} &= \mathbf{h}_{00}^{i+1} + \mu(e_X + e_Y) \mathbf{E}_0^r \\ \mathbf{h}_{11}^{i+1} &= \mathbf{h}_{11}^{i+1} + \mu(e_X - e_Y) \mathbf{E}_1^r \\ \mathbf{h}_{21}^{i+1} &= \mathbf{h}_{21}^{i+1} + \mu(e_X - e_Y) \mathbf{E}_2^r \\ \mathbf{h}_{31}^{i+1} &= \mathbf{h}_{31}^{i+1} + \mu(e_X - e_Y) \mathbf{E}_3^r \end{aligned}$$

where μ is the step size parameter that is set to balance the desired polarization tracking speed of the equalizer and the stability of algorithm [84].

5.3 Experimental setup, DSP stacks and results

5.3.1 Experimental setup

Fig. 5.2(a) shows the experimental setup. A 20 mW NEL distributed feedback (DFB) laser at 1310 nm is modulated by a fully packaged SiP IM that was demonstrated in [33]. A differential RF signal is generated from a 70 GSa/s 8-bit digital-to-analog converter (DAC) and amplified using an Inphi linear driver whose output is applied to the SiP modulator which was constantly operated at the quadrature point of the optical transfer function. In addition, the reverse bias voltage of the pn junctions of the SiP modulator was set to 2V. The single polarization modulated signal is then amplified using a Thorlabs booster optical amplifier (BOA) and fed to a PDM emulator to generate a PDM IM signal. The decorrelation delay between the two orthogonal SOPs had to be changed to ensure that it corresponds to an integer number of symbols at the baud rate of operation. Also, the delay had to be sufficiently small (<150 ps) to ensure that the laser phases at both transmitted polarizations are approximately the same which is crucial for the DSP to function reliably. However, this requirement will be inherently fulfilled in a true PDM IM transmitter where two separate modulators are available and no emulation is needed. Next, the signal is filtered using a 1 nm optical filter to reject the out-of-band noise from the BOA. The combination of the BOA and the filter were used to counteract some of the loss of the SiP modulator (IL ~ 13.5 dB at maximum transmission), the PDM emulator (IL ~ 4 dB), and the receiver front-end (IL ~ 7 dB from the PBS input to either one of the photodetectors (PDs) that measures $|E_x^r|^2$ and $|E_y^r|^2$). Next, the signal is launched into either 0, 2, 10 or 20 km of Corning SMF-28e+ fiber. At the receiver, we use the front-end of Fig. 5.1(b) followed by six Picometrix PIN+TIA receivers. It is noteworthy that all passive optical components used at the receiver front-end in the experiment were using polarization maintaining (PM) fiber. Also, the PM VODL at the receiver was used to time align the two polarization tributaries before combining them in the 90° hybrid. The six output electrical waveforms w_1, w_2, \dots, w_6 were then sampled by two Agilent real-time oscilloscopes (RTO) at 80 GSa/s and stored for offline processing.

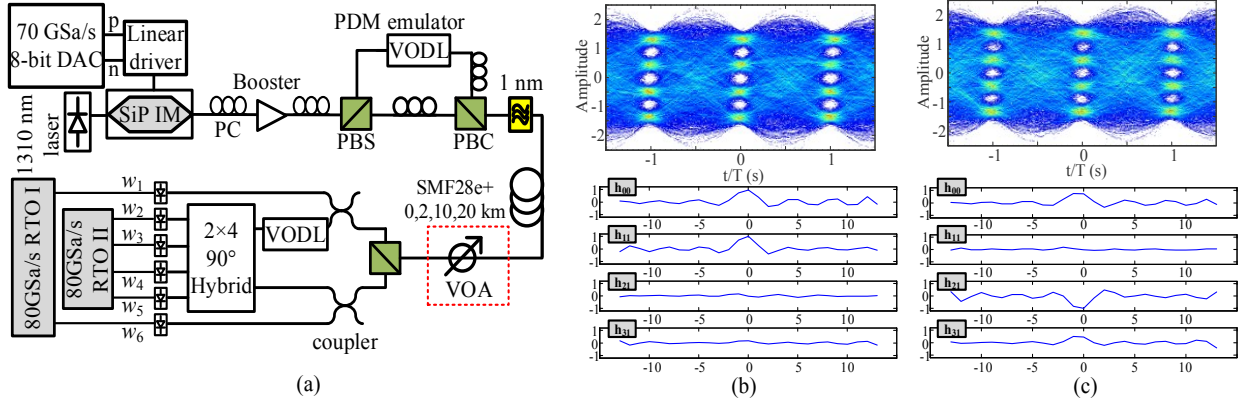


Fig. 5.2. a) Experimental setup, b) and c) Eye diagram after DSP for the X-polarization of a 56 Gbaud PDM PAM-4 signal after 2 km and steady-state MIMO filter taps when received SOP is at 0° (left) and 45° (right) relative to receiver PBS axis.

5.3.2 Offline DSP at transmitter and receiver sides

The transmitter side DSP functions employed are similar to our previous 100 Gb/s demonstration [130] and are depicted in Fig. 5.3(a). This included symbol generation from an alphabet based on the PAM order employed, upsampling to the DAC sampling rate, pulse shaping using a root raised cosine pulse with a roll-off factor (β), precompensation of the nonlinear optical transfer function of the modulator, precompensation of the transmitter limited frequency response. The resulting samples are finally clipped, quantized to 256 levels and loaded to the DAC. It should be noted that in accordance with our work in [130], optimum values of the roll-off factor and clipping ratio had to be obtained for each of the baud rates and PAM orders tested. The optimization procedure was done by simply sweeping these parameters and picking the values leading to the minimum BER.

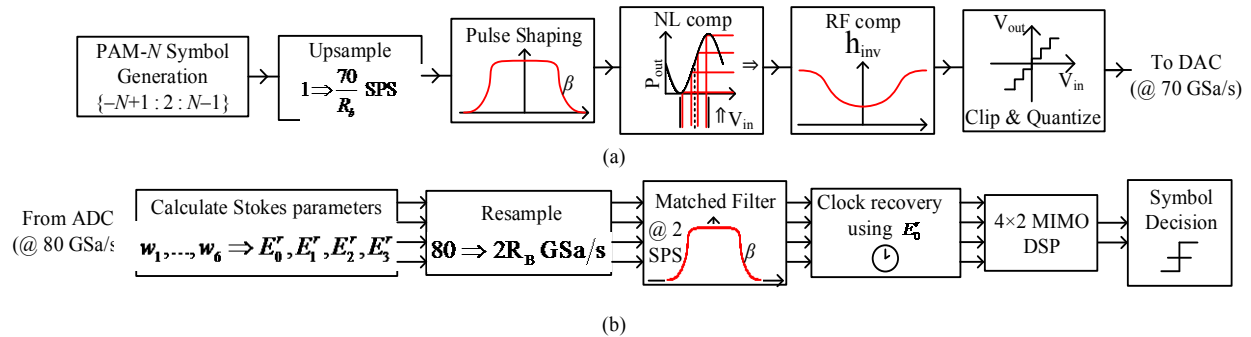


Fig. 5.3. Offline DSP stack employed at a) Transmitter, b) receiver.

At the receiver side, the DSP tasks performed are viewed in Fig. 5.3(b). Offline processing starts by evaluating the Stokes parameters E_0^r , E_1^r , E_2^r and E_3^r from the waveforms w_1, w_2, \dots, w_6

captured by the RTOs as follows $E_0^r = w_1 + w_6$, $E_1^r = w_1 - w_6$, $E_2^r = 2(w_2 - w_3)$ and $E_3^r = 2(w_4 - w_5)$. The last two equations mimic balanced detection to eliminate the direct detection terms by subtracting waveforms at the balanced output pairs of the 2×4 hybrid. Also, the multiplication by 2 in the last two equations is required to scale the signals after subtraction to properly obtain E_2^r and E_3^r as defined in section 5.2. Then, the four waveforms E_0^r , E_1^r , E_2^r and E_3^r are resampled to 2 samples per symbol depending on the baud rate and matched filtered before being fed to the 4×2 MIMO DSP in Fig. 5.1(c) which recovers the transmitted X and Y intensities as explained in section 5.2. Finally, BER is calculated using a sequence of symbol decisions $\langle |E_x^r|^2 \rangle$ and $\langle |E_y^r|^2 \rangle$.

5.3.3 Experimental results

Fig. 5.2(b) shows the resulting eye diagram after DSP for the X-polarization of a 56 Gbaud PDM PAM-4 signal after 2 km as well as the steady-state MIMO filter taps \mathbf{h}_{00} , \mathbf{h}_{11} , \mathbf{h}_{21} and \mathbf{h}_{31} when the SOP of the received signal was manually aligned at 0° with the receiver PBS. Fig. 5.2(c) shows the same results when the SOP of the received signal was at 45° with the receiver PBS axis, i.e. in case of maximum polarization crosstalk. It is clear that as the crosstalk increases, the energy of the taps \mathbf{h}_{11} decreases and becomes more concentrated in \mathbf{h}_{21} and \mathbf{h}_{31} . Also, we notice that the eye in Fig. 5.2(c) is degraded compared to the one in Fig. 5.2(b) which maps to BER increasing from 1.8×10^{-3} to 2.9×10^{-3} . The reason for this degradation in performance as the SOP changes is the degraded receiver sensitivity as the angle between the SOP of the received signal and the PBS axis goes from 0 to 45° . In view of our simulation study that will be presented in section 5.4, the fundamental reason for this degraded sensitivity is the lack of optical power (and hence lower signal-to-noise ratio) at the two middle branches of the receiver that provide $\frac{1}{2} \text{Re}\{E_x^r E_y^{r*}\} = \frac{1}{4} E_2^r$ and $\frac{1}{2} \text{Im}\{E_x^r E_y^{r*}\} = \frac{1}{4} E_3^r$ when compared to the optical power on the upper and lower branches whose sum and difference produce $\frac{1}{4} E_0^r$ and $\frac{1}{4} E_1^r$.

When the receiver thermal noise is added to these signals provided by the optical front-end, this relative difference in optical power among the branches impacts the performance the most when

the angle between the SOP of the received signal and the PBS axis is 45° since the middle two branches carry a lot of information needed by the MIMO equalizer to recover the data in this scenario (\mathbf{h}_{21} and \mathbf{h}_{31} have maximum energy in Fig. 5.2(c)). On the other hand, this relative difference in power favors the scenario in Fig. 5.2(b) because the MIMO equalizer extracts all the information from the upper and lower branches and the middle branches are redundant at this SOP. Hence, in forthcoming results, the reported BERs represent the worst case BERs obtained when the SOP of the signal was aligned at 45° relative to the PBS unless otherwise stated.

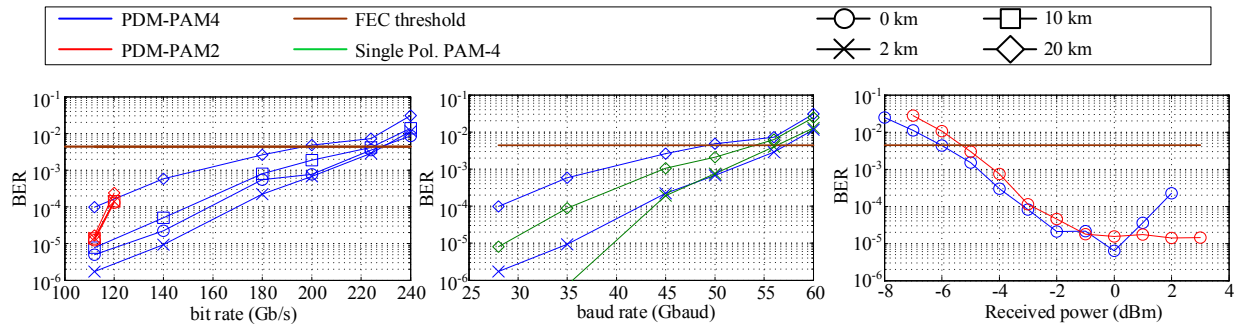


Fig. 5.4. a) BER versus bit rate for PDM PAM-2 and PAM-4 after various distances, b) BER versus baud rate for PDM PAM-4 and single polarization PAM-4, c) BER versus received signal power for 112 Gb/s PDM PAM-4 and PAM-2 in back-to-back.

Fig. 5.4(a) shows the BER versus the total bit rate achieved for both PDM-PAM4 and PDM-PAM2 formats after 0,2,10 and 20 km. To set the bit rate to R_b for either format, the baud rate

was correspondingly set to $\frac{R_b}{2 \log_2 M}$ where M is the PAM order. A bit rate of 224 Gb/s was

achieved at BER of 4.1×10^{-3} after 10 km using 56 Gbaud PDM-PAM4 which is below the FEC threshold of 4.4×10^{-3} assuming the use of the hard decision FEC in [131]. Also, 112 Gb/s at all distances was achieved at BERs below 1.6×10^{-5} and 9×10^{-5} using 56 Gbaud PDM-PAM2 and 28 Gbaud PDM-PAM4, respectively. All points in Fig. 5.4(a) were obtained using optimum roll-off factors for the transmitted pulse shape, which were obtained similar to [130], and optimum received power at the input of the receiver PBS. For PAM-2, the optimum roll-off factor was 0.01 at both 56 and 60 Gbaud whereas for PAM-4, optimum roll-off factors were 0.5, 0.45, 0.15, 0.05, 0.01 and 0.01 for baud rates 28, 35, 45, 50, 56 and 60 Gbaud, respectively. The optimum received power was around 2 dBm for all baud rates but decreased to 0 dBm as the baud rate was lowered to 28 Gbaud as lower baud rates saturate more the TIAs because of the higher AC swing from the transmitter. The gain of the BOA was changed to set the received power to its optimum

value. As an example, the output power of the SiP IM was about -2 dBm for 56 Gbaud PAM-4 and the gain of the BOA was set to have 7.5 dBm out of the 1 nm filter that follows the PDM emulator, producing the optimum received power of 2 dBm at the receiver PBS after 10 km transmission. Next, we plot in Fig. 5.4(b) the BER versus baud rate for PDM PAM-4 and single polarization PAM-4 (with one branch of emulator disconnected) signals after 2 and 20 km in order to verify the penalty of PDM compared to single polarization case operating at the same baud rate, i.e. half the bit rate. We notice no penalty at high baud rates whereas there is a slight increasing penalty as the baud rate decreases due to the saturation of the TIAs that impacts the PDM system because of the increased peak-to-average power ratio (PAPR) of the photocurrents from the PDs. Next, we show in Fig. 5.4(c) the BER versus received signal power at the PBS input for both 28 Gbaud PDM PAM-4 and 56 Gbaud PDM PAM-2 (both delivering 112 Gb/s) in back-to-back with the VOA in Fig. 5.2(a) (enclosed by red line) inserted. For the 28 Gbaud PDM PAM-4 system, we notice the impact of TIA saturation and thermal noise at high and low received powers, respectively. On the other hand, the 56 Gbaud PDM PAM-2 system suffers a BER floor at the high received power end that is mostly due to the higher implementation penalty from the transmitter due to the higher baud rate (not due to TIA saturation). We can also notice that the receiver sensitivity is higher for the 28 Gbaud PDM-PAM-4 when compared to the 56 Gbaud PDM PAM-2 system.

Finally, we show in Fig. 5.5 the back-to-back BER versus received power for both 56 Gbaud PDM PAM-2 (Fig. 5.5(a)) and 28 Gbaud PDM PAM-4 (Fig. 5.5(b)) systems where in each figure we plot all examined cases when the received SOP was at 0° , 30° and 45° relative to the receiver PBS. We enumerate these SOPs as I, II and III, respectively. In both Fig. 5.5(a) and Fig. 5.5(b), we notice that the worst receiver sensitivity is for SOP III which is, as explained earlier in this section, due to lower optical power in the middle two branches of the receiver relative to the upper and lower branches which impacts the performance in case of SOPs II and III at the lower end of received power levels. As the received power increases in Fig. 5.5(a), we observe that all SOPs hit a BER floor that is dictated by the signal quality originating from the transmitter, i.e. the receiver noise has no impact on the performance in this regime. On the other hand, we observe in Fig. 5.5(b) a noticeable degradation at high received power levels for SOPs II and III due to the effect of TIA overload for the signals with high PAPR. This TIA saturation effect

occurs clearly at the low baud rate (Fig. 5.5(b)) as most of the signal spectral content lies within the receiver bandwidth.

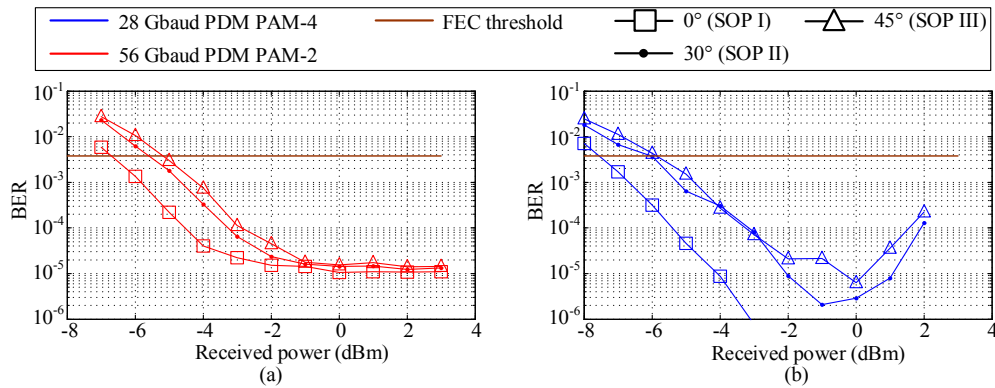


Fig. 5.5. BER versus received signal power when the received SOP was at 0°, 30° and 45° relative to the receiver PBS for both (a) 56 Gbaud PDM PAM-2, (b) 28 Gbaud PDM PAM-4.

5.4 Simulation study of the impact of the coupler splitting ratio

In this section, we present the results obtained from simulations that we performed to further investigate the details of the proposed DD front-end and the MIMO DSP that follows it. In particular, we were interested in exploring the reason for the performance degradation as the angle between the received SOP and the PBS axis goes from 0° to 45°, i.e. from SOP I to SOP III, especially at low received powers.

The system we picked to simulate is a 28 Gbaud PDM PAM-4 system that uses a roll-off factor of 1. The impact of receiver thermal and shot noises were included. Neither the impact of TIA saturation nor the effect of the limited transmitted signal quality were taken into account, i.e. the transmitted signal was assumed to have infinite SNR. The key significant parameter that we were able to sweep in simulations (and not in experiment) is the splitting ratio of the couplers in the upper and lower branches of the receiver front-end. In order to understand the significance of this parameter and how it can make the receiver sensitivity SOP dependent, we look back at Fig. 5.1(b) and assume that the 50/50 couplers in the upper and lower branches are replaced by $\alpha/(1-\alpha)$ couplers, where $(1-\alpha)$ is the ratio of the power going from the input port to the cross output port. Re-working the scaling factors, the output electrical signals after the PDs become $(1-\alpha)|E_X^r|^2$, $(1-\alpha)|E_Y^r|^2$, $\alpha \text{Re}\{E_X^r E_Y^{r*}\}$ and $\alpha \text{Im}\{E_X^r E_Y^{r*}\}$. Since $\alpha = 0.5$ was the value used in the experiment, this resulted in lower optical power on the middle two branches relative to the

outer branches which required the signals on the middle branches to be scaled by 2 (after photodetection and sampling) to obtain the 2nd and 3rd Stokes parameters before entering the MIMO DSP. This meant that the signal-to-noise ratio for the middle two branches into the MIMO DSP, i.e. E_2^r and E_3^r , was always lower than that for the outer branches, i.e. E_0^r and E_1^r , which makes the performance SOP dependent as noticed in the experiment.

To explore this using our simulations, we show in Fig. 5.6(a) the BER versus received power for SOPs I, II and III (having blue, green and red colors, respectively) for two different splitting ratios of $\alpha = 0.5$ and $\alpha = 2/3$. We noticed the same dependence of the performance on the SOP in case of using 50/50 couplers ($\alpha = 0.5$ is represented by solid lines in Fig. 5.6(a)). However, a very interesting finding is that when $\alpha = 2/3$, the performance becomes completely independent on the SOP. This can be very well explained in light of the equations in the previous paragraph by noticing that when $\alpha = 2/3$, the receiver gives $\frac{1}{3}|E_X^r|^2$, $\frac{1}{3}|E_Y^r|^2$, $\frac{2}{3}\text{Re}\{E_X^r E_Y^{r*}\}$ and $\frac{2}{3}\text{Im}\{E_X^r E_Y^{r*}\}$ which readily have the proper scaling factors of the Stokes parameters. This guarantees that the performance will be SOP independent regardless of what will be final taps to which the MIMO filter will converge as can be seen in Fig. 5.6(a) with the markers (no lines) that represent the case of using 67/33 couplers ($\alpha = 2/3$).

Finally, we plot in Fig. 5.6(b) the BER versus α showing individually the BER for SOPs I, II and III at two different received powers of -7 and -8 dBm. We can also see that when $\alpha = 2/3$, all SOPs have the same performance regardless the received power. Also, we noticed that as α decreases below $2/3$, more power is put into the outer branches favoring SOP I which increases the performance gap compared to SOPs II and III. On the other hand, as α increases beyond $2/3$, more power is allocated for the middle branches leading to an advantage for SOPs II and III relative to SOP I. The reason why this advantage of SOPs II and III over SOP I when $\alpha > 2/3$ is not as significant as the advantage SOP I has when $\alpha < 2/3$, is that for SOP I, all the information is contained on the outer branches and the MIMO filter does not make use of any power allocated to the middle branches and hence, the more power on the outer branches the better SOP I will perform. However, for SOPs II and III, the middle branches carry meaningful information that the MIMO needs to retrieve the data, however it still needs at least one of the two outer

branches that will have maximum power while the other outer branch will have zero power. This is why increasing α beyond $2/3$ does not provide improvement and actually makes the overall performance worse. Finally, we conclude that the proper operating point at which the receiver front-end should be implemented is $\alpha = 2/3$ meaning 67/33 couplers are used. This ensures that the receiver operates independent from the received SOP of the signal.

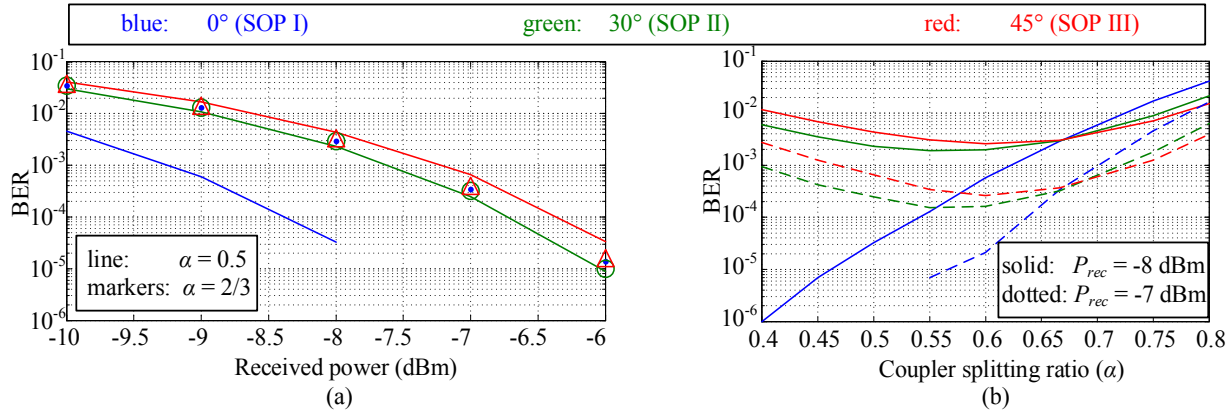


Fig. 5.6. Simulation results for 28 Gbaud PDM-PAM4 system showing: a) BER versus received power for different SOPs and for two different splitting ratios, b) BER versus coupler splitting ratio for different SOPs and at different received powers.

5.5 Conclusion

A PDM IM/DD transceiver is proposed that allows doubling the maximum achievable bit rate of a single wavelength channel, up to 224 Gb/s as demonstrated in this chapter. Also, it enables 112 Gb/s using either PAM-2 or PAM-4 with low BERs ($10^{-5} \sim 10^{-6}$) which reduces significantly the FEC overhead requirement compared to a single polarization system. With the potential improvements of the coupling losses of the SiP modulator and the prospect of integrating all discrete optical components at the receiver on a SiP chip, the losses are expected to decrease, enabling operation without any optical amplifier.

Chapter 6

Conclusion

6.1 Overview

Digital signal processing (DSP) currently plays a paramount role in coherent transceivers in optical transport links over metro / long-haul distances as it enables compensating various transmission impairments, increasing the spectral efficiency, pushing the capacity and reach, and utilizing advanced coding schemes. It is widely believed that the role of DSP in coherent transceivers will only continue to evolve in the future transport networks with an additional challenge of needing to be flexible enough to meet the growing quest for agile coherent transceivers that can adapt to dynamic traffic which imposes varying requirements in reach, capacity and wavelength assignment.

Along with optical transport, DSP is also widely agreed to play a growing role in future low cost IM/DD transceivers for short reach optical interconnects inside modern high speed datacenters. Along with photonic integration, DSP in these short reach interconnects are needed to potentially increase the deliverable bit rates of the IM/DD transceivers, reduce the number of optical components (especially light sources) to achieve a desired throughput, and use lower speed cheaper electronics.

The objective of this thesis spans the two abovementioned networking domains. We introduced advanced technologies for future flexible coherent transceivers; a key enabling technology for future agile transport, and also proposed a novel IM/DD transceiver technology for short reach optical interconnects.

6.2 Summary of original contributions

In Fig. 6.1, we summarize the original contributions achieved in the thesis for both flexible coherent transceivers in optical transport and IM/DD transceivers in short reach optical interconnects inside datacenters. Below, we list each of them highlighting the key results achieved along with the publications produced.

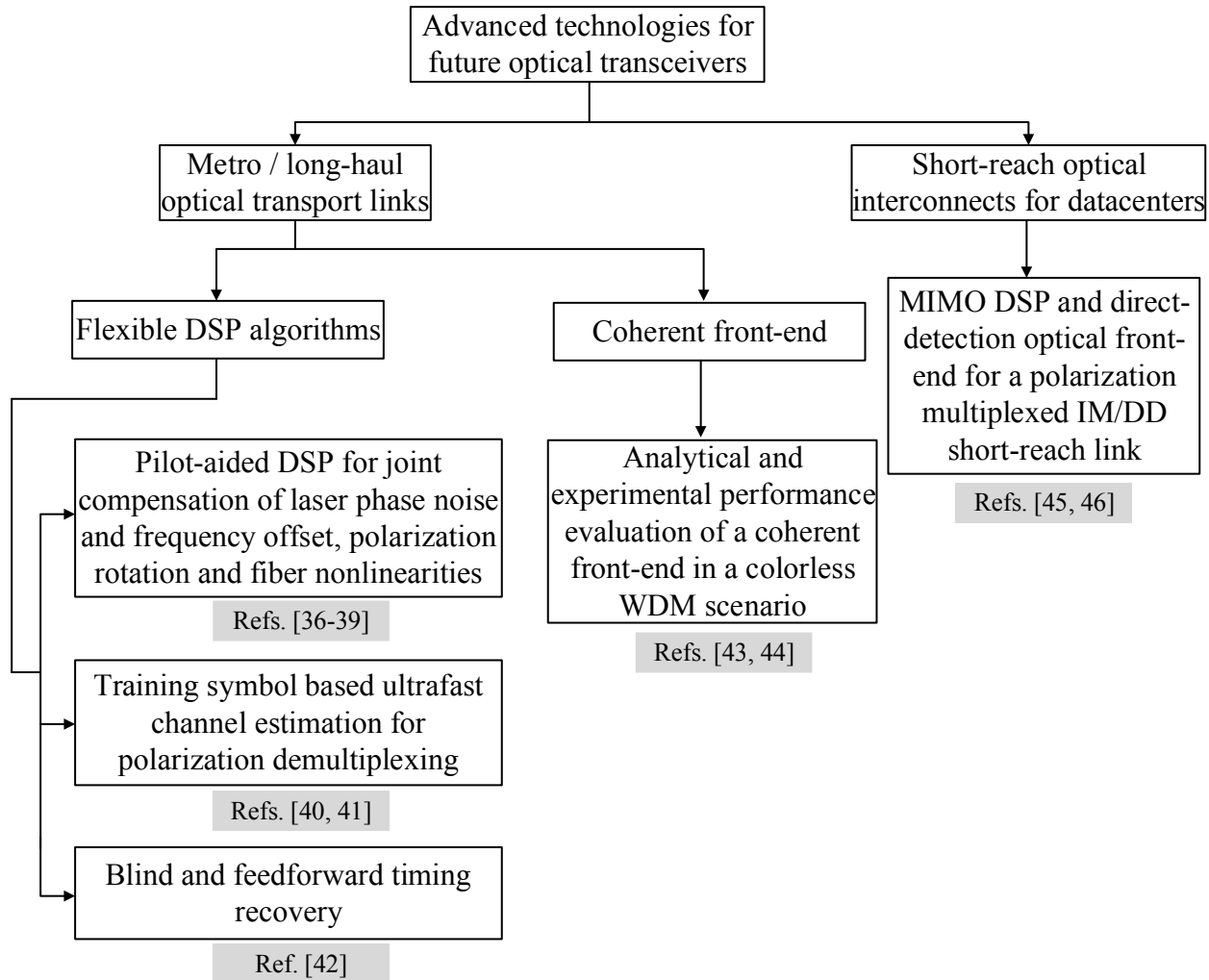


Fig. 6.1. Summary of the original contributions of the thesis.

6.2.1 DSP algorithms for flexible coherent optical transceivers

In Chapter 3, we propose and experimentally verify three DSP algorithms for flexible coherent transceivers to tackle various impairments. All DSP algorithms introduced are transparent to modulation format. Below, we summarize the three schemes highlighting the impairment(s) targeted by each algorithm, the key results achieved and the publications produced.

- We propose pilot-aided (PA) DSP to mitigate *jointly*: a) laser phase noise (PN) from transmitter (Tx) and receiver (Rx) lasers, b) frequency offset (FO) between the two lasers, c) fiber Kerr nonlinearity (NL) induced phase shift, and d) random polarization rotation along the fiber channel. The effectiveness of PA-DSP in compensating laser PN

and fiber nonlinearity is verified by simulations for various modulation formats in [36-38]. In addition, a proof-of-concept experimental verification of PA-DSP is carried out in [39] demonstrating PA-DSP for a 28 Gbaud PDM-QPSK signal in mitigating laser PN and FO in addition to inverting the random polarization rotation along the fiber. The proposed PA-DSP has the following set of advantages at the expense of extra bandwidth overhead allocated for the pilot tone: a) it de-couples carrier recovery from polarization demultiplexing, i.e. PN and FO can be compensated before polarization demultiplexing, b) it does not require synchronization to locate the pilot, and c) the cycle slip problem is eliminated when the pilot is used for CR.

- We present a training symbol (TS) based channel estimation method that uses a very small training overhead to estimate the random polarization rotation along the fiber. Ultrafast initial tracking that is beneficial for system startup is experimentally verified in [40] for both 28 Gbaud PDM-QPSK and PDM-16QAM formats. Using simulations in [41], we also show that the same proposed channel estimation can be used to track fast randomly varying polarization rotation in steady-state operation by sending periodically the TS with a small overhead of just 0.57%.
- We develop a non-data-aided (NDA) feedforward timing recovery scheme for PDM M -QAM signals. The timing estimator operates at 2 samples/symbol and is entirely transparent to modulation format. The estimated timing error is fed to a polynomial interpolator that provides the synchronous symbols correcting– any sampling phase and frequency offsets between the Tx and Rx clocks. The proposed timing recovery is experimentally verified in [42] on 28 Gbaud PDM-QPSK, PDM-16QAM and 7 Gbaud PDM-64QAM signals in back-to-back and transmission scenarios.

6.2.2 Performance of a colorless coherent optical front-end

We carry out in Chapter 4 an extensive theoretical and experimental study of the performance limits of a Si-photonic coherent receiver (CRx) when employed for WDM colorless reception, i.e. without an optical demultiplexing filter prior to the CRx. We first introduce the CRx architecture and some device-level testing results. Secondly, we develop rigorously an analytical expression of the SNR at the CRx output in case of colorless reception taking into consideration all sources of noise specific to the colorless reception scenario. Next, a thorough parametric

experimental study is carried out using 16×112 Gbps PDM-QPSK WDM channels. We study the impact of varying different system parameters on the performance of colorless reception. Results show that the LO beating with incoming optical noise including ASE and NL-induced noises is a dominant noise source regardless of the received signal power. In addition, we identify the signal to signal beating due to out-of-band WDM channels as an additional important noise source in the regime of high received signal power. On the other hand, thermal and shot noises have a significant impact on SNR in the regime of low received signal power. Hence, we identify the CMRR and sensitivity of the CRx as the two important specifications that impact significantly the performance at high and low received signal power regimes, respectively. We finally verify the validity and accuracy of the derived SNR model by fitting it to the experimental data. After the derived model is verified, it was extrapolated to predict the performance of the CRx for colorless selection of the one channel out of a fully populated WDM spectrum. We concluded that the SiP CRx we had in our hands is capable of colorless operation with a WDM spectrum comprising 80 channels as long as the LO-to-signal power ratio is properly set. The entire model derivation and the experimental results formed the material of two journal publications in [43, 44].

6.2.3 MIMO DSP enabling a PDM IM/DD system

In Chapter 5, a polarization-division-multiplexed (PDM) IM/DD transceiver is proposed for short reach optical interconnects in datacenter applications. It allows doubling the maximum achievable bit rate of a single wavelength channel by exploiting two orthogonal polarizations of a single light source. To enable demultiplexing the received signal regardless of the random polarization rotation that occurred along the fiber, we propose a novel MIMO equalizer that operates on the Stokes parameters after a direct-detection receiver to invert the polarization rotation. In [45] using the proposed PDM IM/DD system with the novel MIMO DSP, we report 224 Gb/s transmission of a 56 Gbaud PDM PAM-4 signal over 10 km using a single 1310 nm laser and a SiP IM. At the time of the experiment, this was the world's highest bit rate reported for IM/DD short reach links. More recently in an invited journal publication [46], we performed a more comprehensive simulation-based study of the DD front-end of [45] and concluded that the splitting ratio of the couplers used in the front-end is a key design parameter that changes the performance significantly. It turns out that using 67/33 couplers makes the receiver performance

completely independent from the received state of polarization relative to the receive PBS. With the potential improvements of the coupling losses of the SiP modulator and the prospect of integrating all discrete optical components at the receiver on a SiP chip, the losses are expected to decrease, enabling the operation of the proposed PDM IM/DD scheme without optical amplification.

6.3 Future research avenues

Despite accomplishing the targeted research objectives, there still exists some opportunities for future research that is potentially built upon the work presented in this thesis. Below, we list some of the prospective research avenues derived from each of the topics proposed in the thesis.

DSP Algorithms for flexible coherent optical transceivers

- Extending the experimental investigation that we performed for PA-DSP on a PDM-QPSK signal in subsection 3.2.4 and test the algorithm on higher order QAM signals such as PDM-16QAM and PDM-64QAM.
- Demonstrate experimentally the flexibility of PA-DSP in terms of transparency to modulation format by using the PA scheme for mitigating laser PN, FO and polarization rotation for a time domain hybrid QAM signal in which symbols from different QAM orders are time interleaved to provide flexibility from reach and capacity standpoints [132].
- Experimental verification of the effectiveness of the TS-EST algorithm for tracking time varying random polarization rotation. This has already been done via simulations whose results were presented in subsection 3.3.4.3 and needs to be demonstrated experimentally where the time varying polarization rotations can be introduced via a polarization scrambler added to the recirculating loop in our experimental testbed.

Performance of a colorless CRx front-end

- In Eqs. (4.1) and (4.2), we neglected the SIG-SIG beating between each WDM channel with its neighbors and considered only the beating between each signal with itself which lies within the CRx bandwidth. Although this assumption is true for an NRZ pulse shape where the beating spectral components between two adjacent WDM channels that may fall inside the CRx baseband bandwidth will be negligible, this may not be necessarily

true for other pulse shapes such as Nyquist RRC pulses. For a Nyquist RRC pulse with a roll-off factor close to zero, the spectrum of each WDM signal becomes almost square and the guard bands between these channels are very small, e.g. subchannels within a superchannel that are tightly packed []. Hence, the above assumption needs to be re-visited and the model presented in Chapter 4 needs to be re-worked while taking into consideration the beating between the closest WDM neighbors in calculating the SIG-SIG beating noise in a colorless scenario.

MIMO DSP enabling a PDM IM/DD systems

- Improving the performance of the PDM IM/DD system by compensating the imperfections of the DD front-end (depicted in the experimental setup in Fig. 5.2(a)) at the Rx DSP. These imperfections may include: a) power imbalance that comes from different PD responsivities or unequal losses of the receiver branches, and b) quadrature error due to the hybrid imperfection. The power imbalance can be compensated at the Rx DSP by scaling the photodetected waveforms accordingly and the quadrature error can be mitigated by the use of orthogonalization algorithms as mentioned in subsection 2.4.1.1.
- The experimental demonstration carried out using the setup in Fig. 5.2(a) was just a proof-of-concept of the PDM IM/DD scheme and the novel MIMO DSP. Hence the setup was built from discrete components except for the SiP intensity modulator. Also we had only one copy of the SiP modulator available for the experiment and hence we had to use PDM emulation where the information and its delayed version are imprinted on the two polarizations of the laser. A potential future experimental demonstration is to implement the full PDM IM/DD transceiver in Fig. 5.1(a) and Fig. 5.1(b) on a Silicon chip which also allows to perform a real PDM with two independent information streams encoded on both orthogonal polarizations rather than emulation. Repeating the experiment with the fully integrated SiP version of the transceiver proves the commercial viability of the concept due to its potential for volume production which in turn reduces the cost.
- Performing a study on the computational complexity of the MIMO DSP presented in Fig. 5.1(c). The study aims at evaluating the required number of multiplications, additions and delay elements to implement the proposed MIMO DSP which can be all mapped into resource requirements for a real life ASIC implementation.

- Deriving an analytic model of the SNR (and the BER) for the Stokes vector DD receiver of Fig. 5.1(b). The model should aim at evaluating the receiver sensitivity (BER at a given received optical power) of the DD receiver at any received SOP. The model predictions can be then compared to experimental data to prove its validity.
- Develop a new modulation / demodulation scheme that still employs a DD front-end and is capable of exploiting more degrees of freedom than the current PDM IM/DD scheme which uses two (the two degrees of freedom are the intensities on X and Y polarizations). Being able to encode more than two degrees of freedom and recover the data using a DD front-end will enable increasing the spectral efficiency and hence potentially increasing the deliverable bit rate per wavelength further beyond what was reported in this thesis .

Bibliography

- [1] Cisco Visual Networking Index: Forecast and Methodology, 2013–2018, (Cisco corporation, 2014), http://www.cisco.com/c/en/us/solutions/collateral/service-provider/ip-ngn-ip-next-generation-network/white_paper_c11-481360.html, Accessed April, 2015.
- [2] C. F. Lam, "Chapter 2 - PON Architectures Review," in *Passive Optical Networks*, C. F. Lam, ed. (Academic Press, Burlington, 2007), pp. 19-86.
- [3] WaveLogic 3 Extreme and WaveLogic 3 Nano: New Coherent Chipsets for a Web-scale World (Product brochure), (Ciena corporation, 2015), <http://www.ciena.com/resources/brochures/New-Coherent-Chipsets-Web-scale-World.html>, Accessed April, 2015.
- [4] R. Ryf, N. K. Fontaine, B. Guan, R. J. Essiambre, S. Randel, A. H. Gnauck, S. Chandrasekhar, A. Adamiecki, G. Raybon, B. Ercan, R. P. Scott, S. J. Ben Yoo, T. Hayashi, T. Nagashima, and T. Sasaki, "1705-km transmission over coupled-core fibre supporting 6 spatial modes," in *proceedings of European Conference on Optical Communication (ECOC)*, Paper PD.3.2, 2014.
- [5] J.-X. Cai, H. G. Batshon, M. Mazurczyk, H. Zhang, Y. Sun, O. V. Sinkin, D. Foursa, and A. N. Pilipetskii, "64QAM based coded modulation transmission over transoceanic distance with > 60 Tb/s capacity," in *proceedings of Optical Fiber Communication Conference (OFC)*, Paper Th5C.8, 2015.
- [6] H. Takara, A. Sano, T. Kobayashi, H. Kubota, H. Kawakami, A. Matsuura, Y. Miyamoto, Y. Abe, H. Ono, K. Shikama, Y. Goto, K. Tsujikawa, Y. Sasaki, I. Ishida, K. Takenaga, S. Matsuo, K. Saitoh, M. Koshihara, and T. Morioka, "1.01-Pb/s (12 SDM/222 WDM/456 Gb/s) crosstalk-managed transmission with 91.4-b/s/Hz aggregate spectral efficiency," in *proceedings of European Conference and Exhibition on Optical Communication (ECOC)*, Paper Th.3.C.1, 2012.
- [7] J. Sakaguchi, W. Klaus, J. M. Delgado Mendinueta, B. J. Puttnam, R. S. Luis, Y. Awaji, N. Wada, T. Hayashi, T. Nakanishi, T. Watanabe, Y. Kokubun, T. Takahata, and T. Kobayashi, "Realizing a 36-core, 3-mode fiber with 108 spatial channels," in *proceedings of Optical Fiber Communication Conference (OFC)*, Paper Th5C.2, 2015.
- [8] K. Shibahara, T. Mizuno, H. Takara, A. Sano, H. Kawakami, D. Lee, Y. Miyamoto, H. Ono, M. Oguma, Y. Abe, T. Kobayashi, T. Matsui, R. Fukumoto, Y. Amma, T. Hosokawa, S. Matsuo,

- K. Saitoh, H. Nasu, and T. Morioka, "Dense SDM (12-core \times 3-mode) transmission over 527 km with 33.2-ns mode-dispersion employing low-complexity parallel MIMO frequency-domain equalization," in *proceedings of Optical Fiber Communication Conference (OFC)*, Paper Th5C.3, 2015.
- [9] S. J. Savory, "Digital coherent optical receivers: algorithms and subsystems," *IEEE Journal of Selected Topics in Quantum Electronics* **16**, 1164-1179 (2010).
- [10] S. J. Savory, "Digital filters for coherent optical receivers," *Optics Express* **16**, 804-817 (2008).
- [11] E. M. Ip, and J. M. Kahn, "Fiber impairment compensation using coherent detection and digital signal processing," *Journal of Lightwave Technology* **28**, 502-519 (2010).
- [12] E. Ip, and J. M. Kahn, *Nonlinear impairment compensation using backpropagation* (INTECH Open Access Publisher, 2009).
- [13] E. Ip, A. P. T. Lau, D. J. F. Barros, and J. M. Kahn, "Coherent detection in optical fiber systems," *Optics Express* **16**, 753-791 (2008).
- [14] E. Ip, and J. M. Kahn, "Compensation of dispersion and nonlinear impairments using digital backpropagation," *Journal of Lightwave Technology* **26**, 3416-3425 (2008).
- [15] E. Ip, and J. M. Kahn, "Digital equalization of chromatic dispersion and polarization mode dispersion," *Journal of Lightwave Technology* **25**, 2033-2043 (2007).
- [16] K. Roberts, "100G and beyond," in *proceedings of Opto-Electronics and Communications Conference (OECC)*, 2012.
- [17] K. Roberts, and C. Laperle, "Flexible transceivers," in *proceedings of European Conference on Optical Communication (ECOC)*, Paper We.3.A.3, 2012.
- [18] B. Chatelain, C. Laperle, D. Krause, K. Roberts, M. Chagnon, X. Xian, A. Borowiec, F. Gagnon, J. C. Cartledge, and D. V. Plant, "SPM-tolerant pulse shaping for 40- and 100-Gb/s dual-polarization QPSK systems," *IEEE Photonics Technology Letters* **22**, 1641-1643 (2010).
- [19] K. Roberts, D. Beckett, D. Boertjes, J. Berthold, and C. Laperle, "100G and beyond with digital coherent signal processing," *IEEE Communications Magazine* **48**, 62-69 (2010).
- [20] K. Roberts, M. O'Sullivan, K.-T. Wu, H. Sun, A. Awadalla, D. J. Krause, and C. Laperle, "Performance of dual-polarization QPSK for optical transport systems," *Journal of Lightwave Technology* **27**, 3546-3559 (2009).

- [21] C. Laperle, and M. O'Sullivan, "Advances in high-speed DACs, ADCs, and DSP for optical coherent transceivers," *Journal of Lightwave Technology* **32**, 629-643 (2014).
- [22] R. J. Essiambre, R. Ryf, N. K. Fontaine, and S. Randel, "Breakthroughs in photonics 2012: space-division multiplexing in multimode and multicore fibers for high-capacity optical communication," *IEEE Photonics Journal* **5**, 0701307-0701307 (2013).
- [23] R.-J. Essiambre, G. Kramer, P. J. Winzer, G. J. Foschini, and B. Goebel, "Capacity limits of optical fiber networks," *Journal of Lightwave Technology* **28**, 662-701 (2010).
- [24] D. V. Plant, Z. Qunbi, M. Morsy-Osman, M. Chagnon, X. Xian, and Q. Meng, "Flexible transceivers using adaptive digital signal processing for single carrier and OFDM," in *proceedings of Optical Fiber Communication Conference (OFC)*, Paper OTu2I.5, 2013.
- [25] O. Gerstel, M. Jinno, A. Lord, and S. J. B. Yoo, "Elastic optical networking: a new dawn for the optical layer?," *IEEE Communications Magazine* **50**, s12-s20 (2012).
- [26] M. Jinno, T. Ohara, Y. Sone, A. Hirano, O. Ishida, and M. Tomizawa, "Elastic and adaptive optical networks: possible adoption scenarios and future standardization aspects," *IEEE Communications Magazine* **49**, 164-172 (2011).
- [27] "IEEE Standard for Information technology-- Local and metropolitan area networks-- Specific requirements-- Part 3: CSMA/CD Access Method and Physical Layer Specifications Amendment 4: Media Access Control Parameters, Physical Layers, and Management Parameters for 40 Gb/s and 100 Gb/s Operation," in *IEEE Std 802.3ba-2010 (Amendment to IEEE Standard 802.3-2008)*(2010), pp. 1-457.
- [28] IEEE P802.3bs 400GbE Task Force Public Area, http://www.ieee802.org/3/bs/public/15_03/index.shtml.
- [29] W. Yan, T. Tanaka, B. Liu, M. Nishihara, L. Li, T. Takahara, Z. Tao, J. C. Rasmussen, and T. Drenski, "100 Gb/s optical IM-DD transmission with 10G-class devices enabled by 65 GSamples/s CMOS DAC core," in *proceedings of Optical Fiber Communication Conference (OFC)*, Paper OM3H.1, 2013.
- [30] M. Chagnon, M. Osman, M. Poulin, C. Latrasse, J.-F. Gagné, Y. Painchaud, C. Paquet, S. Lessard, and D. Plant, "Experimental study of 112 Gb/s short reach transmission employing PAM formats and SiP intensity modulator at 1.3 μm ," *Optics Express* **22**, 21018-21036 (2014).

- [31] A. S. Karar, and J. C. Cartledge, "Generation and detection of a 112-Gb/s dual polarization signal using a directly modulated laser and half-cycle 16-QAM Nyquist-subcarrier-modulation," in *proceedings of European Conference on Optical Communication (ECOC)*, Paper Th.3.A.4, 2012.
- [32] R. Rodes, J. Estaran, B. Li, M. Mueller, J. B. Jensen, T. Gründl, M. Ortsiefer, C. Neumeyr, J. Roskopf, K. J. Larsen, M.-C. Amann, and I. Tafur Monroy, "100 Gb/s single VCSEL data transmission link," in *proceedings of Optical Fiber Communication Conference (OFC)*, Paper PDP5D.10, 2012.
- [33] M. Poulin, C. Latrassé, J. F. Gagne, Y. Painchaud, M. Cyr, C. Paquet, M. Morsy-Osman, M. Chagnon, S. Lessard, and D. V. Plant, "107 Gb/s PAM-4 transmission over 10 km using a SiP series push-pull modulator at 1310 nm," in *proceedings of European Conference on Optical Communication (ECOC)*, Paper Mo.4.5.3, 2014.
- [34] P. de Dobbelaere, A. Narasimha, A. Mekis, B. Welch, C. Bradbury, C. Sohn, D. Song, D. Foltz, D. Guckenberger, G. Masini, J. Schramm, J. White, J. Redman, K. Yokoyama, M. Harrison, M. Peterson, M. Mack, M. Sharp, R. LeBlanc, S. Abdalla, S. Gloeckner, S. Hovey, S. Jackson, S. Sahni, S. Yu, T. Pinguet, and Y. Liang, "Silicon photonics for high data rate optical interconnect," in *proceedings of IEEE Optical Interconnects Conference*, Paper WA2, 2012.
- [35] D. Liang, and J. E. Bowers, "Photonic integration: Si or InP substrates?," *Electronics Letters* **45**, 578-581 (2009).
- [36] M. Morsy-Osman, Q. Zhuge, L. R. Chen, and D. V. Plant, "Feedforward carrier recovery via pilot-aided transmission for single-carrier systems with arbitrary M-QAM constellations," *Optics Express* **19**, 24331-24343 (2011).
- [37] M. H. Morsy-Osman, L. Chen, and D. V. Plant, "Joint mitigation of laser phase noise and fiber nonlinearity using pilot-aided transmission for single-carrier systems," in *proceedings of European Conference on Optical Communication (ECOC)*, Paper Tu.3.A.3, 2011.
- [38] M. Morsy-Osman, Q. Zhuge, L. R. Chen, and D. V. Plant, "Joint mitigation of laser phase noise and fiber nonlinearity for polarization-multiplexed QPSK and 16-QAM coherent transmission systems," *Optics Express* **19**, B329-B336 (2011).
- [39] M. Morsy-Osman, Q. Zhuge, M. Chagnon, X. Xu, and D. Plant, "Experimental demonstration of pilot-aided polarization recovery, frequency offset and phase noise mitigation," in *proceedings of Optical Fiber Communication Conference (OFC)*, Paper OTu3I.6, 2013.

- [40] M. H. Morsy-Osman, M. Chagnon, Q. Zhuge, X. Xu, M. Mousa-Pasandi, Z. A. El-Sahn, and D. V. Plant, "Training symbol based channel estimation for ultrafast polarization demultiplexing in coherent single-carrier transmission systems with M-QAM constellations," in *proceedings of European Conference on Optical Communication (ECOC)*, Paper Mo.1.A.4, 2012.
- [41] M. Morsy-Osman, M. Chagnon, Q. Zhuge, X. Xu, M. E. Mousa-Pasandi, Z. A. El-Sahn, and D. V. Plant, "Ultrafast and low overhead training symbol based channel estimation in coherent M-QAM single-carrier transmission systems," *Optics Express* **20**, B171-B180 (2012).
- [42] M. Morsy-Osman, M. Chagnon, Q. Zhuge, X. Xu, and D. V. Plant, "Non-data-aided feedforward timing recovery for flexible transceivers employing PDM-MQAM modulations," in *proceedings of Optical Fiber Communication Conference (OFC)*, Paper W3B.4, 2014.
- [43] M. Morsy-Osman, M. Chagnon, X. Xu, Q. Zhuge, M. Poulin, Y. Painchaud, M. Pelletier, C. Paquet, and D. V. Plant, "Analytical and experimental performance evaluation of an integrated Si-photonic balanced coherent receiver in a colorless scenario," *Optics Express* **22**, 5693-5730 (2014).
- [44] M. Morsy-Osman, M. Chagnon, X. Xian, Z. Qunbi, M. Poulin, Y. Painchaud, M. Pelletier, C. Paquet, and D. V. Plant, "Colorless and preamplifierless reception using an integrated Si-photonic coherent receiver," *IEEE Photonics Technology Letters* **25**, 1027-1030 (2013).
- [45] M. Morsy-Osman, M. Chagnon, M. Poulin, S. Lessard, and D. V. Plant, " $1\lambda \times 224$ Gb/s 10 km transmission of polarization division multiplexed PAM-4 signals using 1.3 μm SiP intensity modulator and a direct-detection MIMO-based receiver," in *proceedings of European Conference on Optical Communication (ECOC)*, Paper PD.4.4, 2014.
- [46] M. Morsy-Osman, M. Chagnon, M. Poulin, S. Lessard, and D. V. Plant, "224-Gb/s 10-km transmission of PDM PAM-4 at 1.3 μm using a single intensity-modulated laser and a direct-detection MIMO DSP-based receiver," *Journal of Lightwave Technology* **33**, 1417-1424 (2015).
- [47] T. H. Maiman, "Stimulated optical radiation in ruby," *Nature* **187**, 493-494 (1960).
- [48] K. C. Kao, and G. A. Hockham, "Dielectric-fibre surface waveguides for optical frequencies," *Proceedings of the Institution of Electrical Engineers* **113**, 1151-1158 (1966).
- [49] F. P. Kapron, D. B. Keck, and R. D. Maurer, "Radiation losses in glass optical waveguides," *Applied Physics Letters* **17**, 423-425 (1970).

- [50] R. J. Mears, L. Reekie, I. M. Jauncey, and D. N. Payne, "Low-noise erbium-doped fibre amplifier operating at 1.54 μ m," *Electronics Letters* **23**, 1026-1028 (1987).
- [51] E. Desurvire, J. R. Simpson, and P. C. Becker, "High-gain erbium-doped traveling-wave fiber amplifier," *Optics Letters* **12**, 888-890 (1987).
- [52] J. X. Cai, D. G. Foursa, C. R. Davidson, Y. Cai, G. Domagala, H. Li, L. Liu, W. W. Patterson, A. N. Pilipetskii, M. Nissov, and N. S. Bergano, "A DWDM demonstration of 3.73 Tb/s over 11,000 km using 373 RZ-DPSK channels at 10 Gb/s," in *proceedings of Optical Fiber Communications Conference (OFC)*, Paper PD22, 2003.
- [53] N. S. Bergano, J. Aspell, C. R. Davidson, P. R. Trischitta, B. M. Nyman, and F. W. Kerfoot, "A 9000 km 5 Gb/s and 21,000 km 2.4 Gb/s feasibility demonstration of transoceanic EDFA systems using a circulating loop," in *proceedings of Optical Fiber Communication Conference (OFC)*, Paper PD13, 1991.
- [54] K. Fukuchi, T. Kasamatsu, M. Morie, R. Ohhira, T. Ito, K. Sekiya, D. Ogasahara, and T. Ono, "10.92-Tb/s (273/spl times/40-Gb/s) triple-band/ultra-dense WDM optical-repeated transmission experiment," in *proceedings of Optical Fiber Communication Conference (OFC)*, Paper PD24, 2001.
- [55] T. Okoshi, *Coherent optical fiber communications* (Springer Science & Business Media, 1988).
- [56] T. Okoshi, "Recent advances in coherent optical fiber communication systems," *Journal of Lightwave Technology* **5**, 44-52 (1987).
- [57] S. B. Leonid Kazovsky, Alan E. Willner, *Optical Fiber Communication Systems* (Artech House, 1996).
- [58] S. J. Savory, "Coherent detection - why is it back?," in *proceedings of IEEE Lasers and Electro-Optics Society (LEOS)*, Paper TuH1, 2007.
- [59] G. Li, "Recent advances in coherent optical communication," *Advances in Optics and Photonics* **1**, 279-307 (2009).
- [60] P. J. Winzer, and R. Essiambre, "Advanced optical modulation formats," *Proceedings of the IEEE* **94**, 952-985 (2006).
- [61] G. P. Agrawal, "Lightwave Technology: Telecommunication Systems," (Wiley, 2005).

- [62] A. Gnauck, P. Winzer, S. Chandrasekhar, X. Liu, B. Zhu, and D. Peckham, "Spectrally efficient long-haul WDM transmission using 224-Gb/s polarization-multiplexed 16-QAM," *Journal of Lightwave Technology* **29**, 373-377 (2011).
- [63] P. J. Winzer, A. H. Gnauck, G. Raybon, M. Schnecker, and P. J. Pupalais, "56-Gbaud PDM-QPSK: coherent detection and 2,500-km transmission," in *proceedings of European Conference on Optical Communication (ECOC)*, Paper PD2.7, 2009.
- [64] P. J. Winzer, A. H. Gnauck, S. Chandrasekhar, S. Draving, J. Evangelista, and B. Zhu, "Generation and 1,200-km transmission of 448-Gb/s ETDM 56-Gbaud PDM 16-QAM using a single I/Q modulator," in *proceedings of European Conference on Optical Communication (ECOC)*, Paper 1-3, 2010.
- [65] R. Schmogrow, M. Winter, M. Meyer, D. Hillerkuss, S. Wolf, B. Baeuerle, A. Ludwig, B. Nebendahl, S. Ben-Ezra, J. Meyer, M. Dreschmann, M. Huebner, J. Becker, C. Koos, W. Freude, and J. Leuthold, "Real-time Nyquist pulse generation beyond 100 Gbit/s and its relation to OFDM," *Optics Express* **20**, 317-337 (2012).
- [66] J. G. Proakis, *Digital Communications* (McGraw-Hill, Boston, 2001).
- [67] Y. Gao, J. C. Cartledge, A. S. Karar, S. S. H. Yam, M. O'Sullivan, C. Laperle, A. Borowiec, and K. Roberts, "Reducing the complexity of perturbation based nonlinearity pre-compensation using symmetric EDC and pulse shaping," *Optics Express* **22**, 1209-1219 (2014).
- [68] J. Bromage, "Raman amplification for fiber communications systems," *Journal of Lightwave Technology* **22**, 79-93 (2004).
- [69] F. M. Gardner, "Interpolation in digital modems. I. Fundamentals," *IEEE Transactions on Communications* **41**, 501-507 (1993).
- [70] L. Erup, F. M. Gardner, and R. A. Harris, "Interpolation in digital modems. II. Implementation and performance," *IEEE Transactions on Communications* **41**, 998-1008 (1993).
- [71] I. Fatadin, S. J. Savory, and D. Ives, "Compensation of quadrature imbalance in an optical QPSK coherent receiver," *IEEE Photonics Technology Letters* **20**, 1733-1735 (2008).
- [72] J. R. Barry, and E. A. Lee, "Performance of coherent optical receivers," *Proceedings of the IEEE* **78**, 1369-1394 (1990).
- [73] T. Pfau, S. Hoffmann, and R. Noé, "Hardware-efficient coherent digital receiver concept with feedforward carrier recovery for M -QAM constellations," *Journal of Lightwave Technology* **27**, 989-999 (2009).

- [74] G. P. Agrawal, *Fiber-Optic Communication Systems* (Wiley, 2002).
- [75] P. K. A. Wai, and C. R. Menyuk, "Polarization mode dispersion, decorrelation, and diffusion in optical fibers with randomly varying birefringence," *Journal of Lightwave Technology* **14**, 148-157 (1996).
- [76] C. D. Poole, and R. E. Wagner, "Phenomenological approach to polarisation dispersion in long single-mode fibres," *Electronics Letters* **22**, 1029-1030 (1986).
- [77] Y. Gao, J. H. Ke, K. P. Zhong, J. C. Cartledge, and S. S. Yam, "Assessment of intrachannel nonlinear compensation for 112 Gb/s dual-polarization 16QAM systems," *Journal of Lightwave Technology* **30**, 3902-3910 (2012).
- [78] T. Zhenning, D. Liang, Y. Weizhen, L. Lei, T. Hoshida, and J. C. Rasmussen, "Multiplier-free intrachannel nonlinearity compensating algorithm operating at symbol rate," *Journal of Lightwave Technology* **29**, 2570-2576 (2011).
- [79] Q. Zhuge, M. Reimer, A. Borowiec, M. O'Sullivan, and D. V. Plant, "Aggressive quantization on perturbation coefficients for nonlinear pre-distortion," in *proceedings of Optical Fiber Communication Conference (OFC)*, Paper Th4D.7, 2014.
- [80] A. Mecozzi, C. B. Clausen, and M. Shtaif, "Analysis of intrachannel nonlinear effects in highly dispersed optical pulse transmission," *IEEE Photonics Technology Letters* **12**, 392-394 (2000).
- [81] W. Shieh, and I. Djordjevic, *OFDM for Optical Communications* (Academic Press, Oxford, 2010).
- [82] A. Oppenheim, and R. Schaffer, *Discrete-Time Signal Processing* (Prentice-Hall, New Jersey, 1999).
- [83] S. Qi, A. P. T. Lau, and L. Chao, "Fast and robust blind chromatic dispersion estimation using auto-correlation of signal power waveform for digital coherent systems," *Journal of Lightwave Technology* **31**, 306-312 (2013).
- [84] S. Haykin, *Adaptive Filter Theory* (Prentice Hall, 1996).
- [85] F. M. Gardner, "A BPSK/QPSK timing-error detector for sampled receivers," *IEEE Transactions on Communications* **34**, 423-429 (1986).
- [86] M. Oerder, and H. Meyr, "Digital filter and square timing recovery," *IEEE Transactions on Communications* **36**, 605-612 (1988).

- [87] L. Seung Joon, "A new non-data-aided feedforward symbol timing estimator using two samples per symbol," *IEEE Communications Letters* **6**, 205-207 (2002).
- [88] A. Viterbi, "Nonlinear estimation of PSK-modulated carrier phase with application to burst digital transmission," *IEEE Transactions on Information Theory* **29**, 543-551 (1983).
- [89] A. N. D. A. Umberto Mengali, *Synchronization Techniques for Digital Receivers* (Springer US, 1997).
- [90] T. Pfau, Noe, x, and R., "Phase-noise-tolerant two-stage carrier recovery concept for higher order QAM formats," *IEEE Journal of Selected Topics in Quantum Electronics* **16**, 1210-1216 (2010).
- [91] P. Ciblat, and M. Ghogho, "Blind NLLS carrier frequency-offset estimation for QAM, PSK, and PAM modulations: performance at low SNR," *IEEE Transactions on Communications* **54**, 1725-1730 (2006).
- [92] I. Fatadin, D. Ives, and S. J. Savory, "Compensation of frequency offset for differentially encoded 16- and 64-QAM in the presence of laser phase noise," *IEEE Photonics Technology Letters* **22**, 176-178 (2010).
- [93] S. Yamamoto, N. Edagawa, H. Taga, Y. Yoshida, and H. Wakabayashi, "Analysis of laser phase noise to intensity noise conversion by chromatic dispersion in intensity modulation and direct detection optical-fiber transmission," *Journal of Lightwave Technology* **8**, 1716-1722 (1990).
- [94] I. Fatadin, D. Ives, and S. J. Savory, "Laser linewidth tolerance for 16-QAM coherent optical systems using QPSK partitioning," *IEEE Photonics Technology Letters* **22**, 631-633 (2010).
- [95] Z. Xiang, and S. Yifan, "Low-complexity, blind phase recovery for coherent receivers using QAM modulation," in *proceedings of Optical Fiber Communication Conference (OFC)*, Paper OMJ3, 2011.
- [96] A. P. T. Lau, T. S. R. Shen, W. Shieh, and K.-P. Ho, "Equalization-enhanced phase noise for 100Gb/s transmission and beyond with coherent detection," *Optics Express* **18**, 17239-17251 (2010).
- [97] W. Shieh, and K.-P. Ho, "Equalization-enhanced phase noise for coherent-detection systems using electronic digital signal processing," *Optics Express* **16**, 15718-15727 (2008).

- [98] M. G. Taylor, "Coherent detection method using DSP for demodulation of signal and subsequent equalization of propagation impairments," *IEEE Photonics Technology Letters* **16**, 674-676 (2004).
- [99] P. J. Winzer, A. H. Gnauck, C. R. Doerr, M. Magarini, and L. L. Buhl, "Spectrally efficient long-haul optical networking using 112-Gb/s polarization-multiplexed 16-QAM," *Journal of Lightwave Technology* **28**, 547-556 (2010).
- [100] L. Ling, T. Zhenning, Y. Weizhen, S. Oda, T. Hoshida, and J. C. Rasmussen, "Initial tap setup of constant modulus algorithm for polarization de-multiplexing in optical coherent receivers," in *proceedings of Optical Fiber Communication Conference (OFC)*, Paper OMT2, 2009.
- [101] M. G. Taylor, "Phase estimation methods for optical coherent detection using digital signal processing," *Journal of Lightwave Technology* **27**, 901-914 (2009).
- [102] Q. Zhuge, X. Xu, Z. A. El-Sahn, M. E. Mousa-Pasandi, M. Morsy-Osman, M. Chagnon, M. Qiu, and D. V. Plant, "Experimental investigation of the equalization-enhanced phase noise in long haul 56 Gbaud DP-QPSK systems," *Optics Express* **20**, 13841-13846 (2012).
- [103] I. Fatadin, D. Ives, and S. J. Savory, "Blind equalization and carrier phase recovery in a 16-QAM optical coherent system," *Journal of Lightwave Technology* **27**, 3042-3049 (2009).
- [104] L. Nelson, "Polarization effects in coherent systems," in *proceedings of Optical Fiber Communication Conference (OFC)*, Paper OTu1A.4, 2012.
- [105] L. E. Nelson, M. Birk, S. L. Woodward, and P. Magill, "Field measurements of polarization transients on a long-haul terrestrial link," in *proceedings of IEEE Photonics Conference (IPC)*, Paper ThT5, 2011.
- [106] NeoPhotonics External Cavity micro-ITLA product webpage, (NeoPhotonics Corporation, 2015), http://www.neophotonics.com/products/product_193.aspx, Accessed April, 2015.
- [107] L. G. Kazovsky, "Multichannel coherent optical communications systems," *Journal of Lightwave Technology* **5**, 1095-1102 (1987).
- [108] L. E. Nelson, S. L. Woodward, S. Foo, M. Moyer, D. J. S. Beckett, M. O'Sullivan, and P. D. Magill, "Detection of a single 40 Gb/s polarization-multiplexed QPSK channel with a real-time intradyne receiver in the presence of multiple coincident WDM channels," *Journal of Lightwave Technology* **28**, 2933-2943 (2010).

- [109] C. Xie, P. J. Winzer, G. Raybon, A. H. Gnauck, B. Zhu, T. Geisler, and B. Edvold, "Colorless coherent receiver using 3x3 coupler hybrids and single-ended detection," *Optics Express* **20**, 1164-1171 (2012).
- [110] B. Zhang, C. Malouin, and T. J. Schmidt, "Towards full band colorless reception with coherent balanced receivers," *Optics Express* **20**, 10339-10352 (2012).
- [111] L. E. Nelson, X. Zhou, R. Isaac, Y. Lin, J. Chon, and W. I. Way, "Colorless reception of a single 100Gb/s channel from 80 coincident channels via an intradyne coherent receiver," in *proceedings of IEEE Photonics Conference (IPC)*, Paper TuE4, 2012.
- [112] C. R. Doerr, P. J. Winzer, Y.-K. Chen, S. Chandrasekhar, M. S. Rasras, L. Chen, T.-Y. Liow, K.-W. Ang, and G.-Q. Lo, "Monolithic polarization and phase diversity coherent receiver in silicon," *Journal of Lightwave Technology* **28**, 520-525 (2010).
- [113] Y. Painchaud, M. Pelletier, M. Poulin, F. Pelletier, C. Latrasse, G. Robidoux, S. Savard, J.-F. Gagné, V. Trudel, M.-J. Picard, P. Poulin, P. Sirois, F. D'Amours, D. Asselin, S. Paquet, C. Paquet, M. Cyr, M. Guy, M. Morsy-Osman, Q. Zhuge, X. Xu, M. Chagnon, and D. Plant, "Ultra-compact coherent receiver based on hybrid integration on silicon," in *proceedings of Optical Fiber Communication Conference (OFC)*, Paper OM2J.2, 2013.
- [114] C. R. Doerr, L. Zhang, P. J. Winzer, N. Weimann, V. Houtsma, T. Hu, N. J. Sauer, L. L. Buhl, D. T. Neilson, S. Chandrasekhar, and Y. K. Chen, "Monolithic InP dual-polarization and dual-quadrature coherent receiver," *IEEE Photonics Technology Letters* **23**, 694-696 (2011).
- [115] A. Matiss, R. Ludwig, J. K. Fischer, L. Molle, C. Schubert, C. C. Leonhardt, H. Bach, R. Kunkel, and A. Umbach, "Novel integrated coherent receiver module for 100G serial transmission," in *proceedings of Optical Fiber Communication Conference (OFC)*, Paper PDPB3, 2010.
- [116] C. R. Doerr, L. L. Buhl, Y. Baeyens, R. Aroca, S. Chandrasekhar, X. Liu, L. Chen, and Y. K. Chen, "Packaged monolithic silicon 112-Gb/s coherent receiver," *IEEE Photonics Technology Letters* **23**, 762-764 (2011).
- [117] A. Carena, V. Curri, G. Bosco, P. Poggiolini, and F. Forghieri, "Modeling of the impact of nonlinear propagation effects in uncompensated optical coherent transmission links," *Journal of Lightwave Technology* **30**, 1524-1539 (2012).
- [118] P. Poggiolini, "The GN model of non-linear propagation in uncompensated coherent optical systems," *Journal of Lightwave Technology* **30**, 3857-3879 (2012).

- [119] P. Poggiolini, A. Carena, V. Curri, G. Bosco, and F. Forghieri, "Analytical modeling of nonlinear propagation in uncompensated optical transmission links," *IEEE Photonics Technology Letters* **23**, 742-744 (2011).
- [120] Y. Painchaud, M. Poulin, M. Morin, and M. Têtu, "Performance of balanced detection in a coherent receiver," *Optics Express* **17**, 3659-3672 (2009).
- [121] M. Nazarathy, W. V. Sorin, D. M. Baney, and S. A. Newton, "Spectral analysis of optical mixing measurements," *Journal of Lightwave Technology* **7**, 1083-1096 (1989).
- [122] "ITU-T G.975.1, Forward error correction for high bit-rate DWDM submarine systems," (2004).
- [123] L. Paraschis, "Advancements in data-center networking, and the importance of optical interconnections," in *proceedings of European Conference on Optical Communication (ECOC)*, Paper Th.2.F.3, 2013.
- [124] CFP Module Multi-source Agreement public area, (2013), <http://www.cfp-msa.org/index.html>.
- [125] M. Funabashi, H. Nasu, T. Mukaihara, T. Kimoto, T. Shinagawa, T. Kise, K. Takaki, T. Takagi, M. Oike, T. Nomura, and A. Kasukawa, "Recent advances in DFB lasers for ultradense WDM applications," *IEEE Journal of Selected Topics in Quantum Electronics* **10**, 312-320 (2004).
- [126] M. I. Olmedo, Z. Tianjian, J. B. Jensen, Z. Qiwen, X. Xiaogeng, S. Popov, and I. T. Monroy, "Multiband carrierless amplitude phase modulation for high capacity optical data links," *Journal of Lightwave Technology* **32**, 798-804 (2014).
- [127] T. Tanaka, M. Nishihara, T. Takahara, W. Yan, L. Li, Z. Tao, M. Matsuda, K. Takabayashi, and J. Rasmussen, "Experimental demonstration of 448-Gbps+ DMT transmission over 30-km SMF," in *proceedings of Optical Fiber Communication Conference (OFC)*, Paper M2I.5, 2014.
- [128] D. Che, A. Li, X. Chen, Q. Hu, Y. Wang, and W. Shieh, "Stokes vector direct detection for short-reach optical communication," *Optics Letters* **39**, 3110-3113 (2014).
- [129] K. Kikuchi, "Electronic polarization-division demultiplexing based on digital signal processing in intensity-modulation direct-detection optical communication systems," *Optics Express* **22**, 1971-1980 (2014).

- [130] M. Chagnon, M. Osman, M. Poulin, C. Latrassé, J.-F. Gagné, Y. Painchaud, C. Paquet, S. Lessard, and D. Plant, "Experimental study of 112 Gb/s short reach transmission employing PAM formats and SiP intensity modulator at 1.3 μm ," *Optics Express* **22**, 21018-21036 (2014).
- [131] M. Scholten, T. Coe, and J. Dillard, "Continuously-interleaved BCH (CI-BCH) FEC delivers best-in-class NECG for 40G and 100G metro applications," in *proceedings of Optical Fiber Communication Conference (OFC)*, Paper NTuB3, 2010.
- [132] Q. Zhuge, M. Morsy-Osman, X. Xu, M. Chagnon, M. Qiu, and D. V. Plant, "Spectral efficiency-adaptive optical transmission using time domain hybrid QAM for agile optical networks," *Journal of Lightwave Technology* **31**, 2621-2628 (2013).